CHARACTERIZATION OF A TAYLOR-COUETTE VORTEX FLOW REACTOR

by

CHRISTINE M. V. MOORE

Submitted to the Department of Chemical Engineering
in partial fulfillment of the requirements for the degree of

DOCTOR OF PHILOSOPHY

in

CHEMICAL ENGINEERING

at the

MASSACHUSETTS INSTITUTE OF TECHNOLOGY

September 1994

Signature of Author ....
Department of Chemical Engineering
September 2, 1994

Certified by................
Charles L. Cooney
Thesis Supervisor, Department of Chemical Engineering

Accepted by ....
Robert E. Cohen
Chairman, Committee for Graduate Students

Characterization of a Taylor-Couette Vortex Flow Reactor

Christine M. V. Moore

Submitted to the Department of Chemical Engineering
on September 2, 1994 in partial fulfillment of the
requirements for the degree of
Doctor of Philosophy in Chemical Engineering

Abstract

The vortex flow reactor (VFR) is a new solid-liquid reactor with applications in biochemical reaction and separation. Through the use of a secondary flow, called Taylor-Couette vortex flow, the VFR provides high mass transfer rates and good mixing properties while performing well with shear sensitive biological components, such as blood. This thesis presents work on characterization of the VFR for catalytic reaction and adsorptive separation.

A mathematical model of reactor conversion is developed based on the one-dimensional convection-dispersion equation and its limitations are discussed. The model inputs include macrotransport parameters (i.e. axial dispersion and mass transfer to the active surface) and kinetic parameters, both of which are independently determined. Whereas published correlations exist for mass transfer to the cylinder walls, no previous studies have comprehensively described either axial dispersion or mass transfer to suspended particles in Taylor-Couette vortex flow. Therefore, results from residence time distribution studies are presented examining axial dispersion in the VFR. Dispersion properties are found to strongly vary with rotation rate from near plug flow performance at low rotation rates to well stirred behavior at high rotation rates. Mass transfer to suspended particles is examined experimentally through benzoic acid dissolution studies. The results from the axial dispersion and mass transfer experiments are incorporated into dimensionless correlations relating the transport properties to VFR operational and design parameters. The mathematical model and the concept of the VFR are validated through experiments using immobilized alkaline phosphatase: 1) on a membrane attached to the inner cylinder and 2) on particles suspended in the reactor annulus.

Model simulations and experimental results reveal the tradeoffs between mass transfer and axial dispersion in the reactor. Unlike most biochemical reactors in which conversion is determined solely by axial flow rate, the VFR has two operating parameters of axial flow rate and rotation rate which may be independently adjusted to vary the conversion.

Further experiments of protein adsorption in VFR demonstrate the feasibility of the VFR as an adsorber. The VFR is found to work with high particle loadings providing performance equal to or exceeding a traditional fluidized bed adsorber.

Thesis Supervisor: Charles L. Cooney
Professor of Chemical and Biochemical Engineering

Characterization of a Taylor-Couette Vortex Flow Reactor

Christine M. V. Moore
Thesis Advisor: Charles L. Cooney
September 2, 1994

Technical Summary

The vortex flow reactor (VFR) is a new solid-liquid reactor with applications in biochemical reaction and separation. Through the use of Taylor-Couette vortex flow, induced by rotating the inner cylinder of an annulus, the VFR provides high mass transfer rates and good mixing while performing well with shear sensitive biological cells. The active surface in the VFR is located either on the cylinder walls or on particles suspended within the annulus. This thesis characterizes VFR performance as a function of operational and design parameters and demonstrates the utility of the VFR for immobilized enzymatic reaction and for protein adsorption. A result of the work is a mathematical model which predicts VFR conversion for given reaction constants and operating conditions. While the VFR may be used for any solid-liquid reaction, the reactor is particularly useful for difficult feed streams such as those containing high viscosity, suspended solids or biological cells. Some biological applications include adsorption of a product from a cell culture broth or cell homogenate and reaction with a blood component as an extracorporeal reactor.

The first step in understanding the performance of the VFR is characterizing transport phenomena in Taylor-Couette vortex flow. One of the most extensively studied areas of Taylor-Couette flow is mass transfer to the cylinder walls. The works of several independent research groups were compiled into a consensus correlation describing transport to a cylinder with an active surface. Other transport phenomena such as axial dispersion and mass transfer to suspended particles have previously received little attention. To fill in these information gaps, axial dispersion is examined through residence time distribution studies, and mass transfer to suspended particles is studied through benzoic acid dissolution experiments.

Mixing in the VFR is described using a one-dimensional dispersion coefficient. The one-dimensional assumption is valid because mixing in the radial and azimuthal directions is fast as compared to the axial direction. The axial dispersion is examined experimentally over a wide range of operating conditions and reactor geometries. The dispersion coefficients, ranging from 0.01 cm^2/s to 10 cm^2/s, are several orders of magnitude greater than the molecular diffusivity indicating the importance of convection in the reactor. The mixing behavior in the VFR ranges from a well mixed, stirred tank reactor (CSTR) at high rotational Reynolds number to near plug flow (PFR) at low rotational Reynolds number. Dispersion is strongly dependent upon rotation rate with only slight dependence upon axial velocity and reactor geometry.

Mass transfer from suspended particles is studied through experiments using dissolution of benzoic acid particles suspended within the annulus. Mass transfer is examined as a function of operating parameters by varying rotation rates, axial flow rates,

reactor geometries, and fluid properties. The results from these experiments are incorporated into a dimensionless correlation. As expected, mass transfer rates in the VFR are significantly higher than those in a conventional fluidized bed operating at the same axial velocity.

The dimensionless correlations for dispersion and mass transfer are incorporated into the mathematical model of the VFR. The mathematical model is based on the one dimensional convective-dispersion equation with reaction. The inputs to the model are the design parameters (i.e. reactor geometry), operational parameters (rotation rate and axial flow rate) and intrinsic kinetics of adsorption or reaction. Model simulations reveal that the most important operational parameters influencing performance of the VFR are the rotation rate and the axial flow rate. Trade-offs between these operational parameters exist. For example, increasing rotation rates increases both mass transfer to the active surface and dispersion. The increasing mass transfer tends to increase conversion, while the increasing dispersion tends to lower conversion. One result of having the two important process variables is increased degree of control over the system. The VFR with its two independent process control variables (axial flow rate and rotation rate) has greater flexibility in operation than traditional solid-liquid reactors (i.e. traditional fluidized beds , hollow fibers) which have only one process variable- axial flow rate.

The mathematical model of the VFR is validated through experiments using immobilized alkaline phosphatase: 1) on a membrane attached to the inner cylinder and 2) on particles suspended in the reactor annulus. Reactor conversion is compared to model predictions obtained using independently determined parameters. Excellent agreement is found between the experimental results and the model predictions for both for transient and steady-state operation. The steady state experiments reveal the effects of mass transfer, dispersion, and reaction rates on conversion in the VFR.

The immobilized enzyme experiments demonstrate the feasibility of the VFR as an solid-liquid reactor. Further experiments with protein adsorption on ion exchange particles demonstrate the utility of the VFR as an adsorber. The dynamic capacity in the VFR is examined by protein breakthrough curves. Protein adsorption is found to be internally mass transfer limited, a condition which typically defines the limits of reactor performance. However, the reactor performance in the VFR can be adjusted by altering the particle volume fraction. Because the VFR is capable of working with high particle volume fractions of up to 0.50, VFR performance can exceed traditional fluidized bed adsorbers which use lower particle loadings.

The mathematical model, developed and validated as described above, allows for reactor conversion to be predicted for nearly any reaction or adsorption in the VFR. One such application of great research interest is the use of immobilized heparinase in the VFR to neutralize heparin following extracorporeal therapy. Reactor design calculations are presented both for vortex flow reactors with immobilized heparinase on suspended particles and on cylinder walls. The model predictions illustrate the system's limitations and point out the critical areas for future research.

Acknowledgments

I would like to thank my many collaborators and colleagues for their contributions and advice during the past five years. In particular, I wish to acknowledge Thomas Aicher who performed most of the experiments of mass transfer from benzoic acid particles, and Dominique Maugeais who helped in the particle fluidization studies and the kinetic studies on immobilized alkaline phosphatase particles. In addition, I wish to thank the undergraduates who contributed to several areas of this thesis. These students include Anne Bisagno who helped in developing methods for residence time distribution studies, Ricardo Calderon who assisted in particle characterization studies, and Loren Baugh who helped in particle visualization studies and in kinetic studies with the agarose-silica particles.

I am also grateful to several companies for their donations or loans of supplies and materials not yet commercially available. The motors and cylinders used in the vortex flow reactor were generously loaned or donated from Membrex, Inc. The azlactone-functionalized membranes were provided by 3M, and the agarose-silica particles were donated by Pharmacia. Just as important as these materials was the invaluable advice and encouragement from the company representatives. Thanks go to Phil Rolchigo (Membrex) for his expert advice on vortex flow, Bob Kennedy (currently at Pharmacia, formerly at Membrex) for being my reliable contact man at both of his jobs, and Dave Gagnon and Pat Coleman at 3M for their helpful advice on immobilization techniques and assay protocols.

I also wish to thank Rob Davis (University of Colorado) for his valuable suggestions on fitting residence time distribution curves, and Gil Iosilevskii for his work and suggestions on modeling transport and reaction in Taylor-Couette flow. Many of the ideas incorporated into the heparinase reactor concept and calculations are largely due to suggestions from Lisa Freed, Gordana Vunjak-Novakovic, Ram Sasisekharan, Ganesh Venkataraman, Steffen Ernst, William Harmon (Childrens Hospital) and Joe Zimmerman (IBEX Technologies). Furthermore, I wish to thank Stefan Weissflog, Kai-Chee Loh and Guillermo Ameer for proofreading parts of this thesis. Finally, deepest appreciation is extended to my thesis advisor, Charles Cooney, for his guidance, support and confidence in my abilities. I am also very grateful to my thesis committee of Howard Brenner, Alan Hatton, Bob Langer and Greg Stephanopoulos for their insightful and constructive comments.

Financial Support for this thesis was provided from a Merck Manufacturing Division Fellowship, from the National Science Foundation to the Biotechnology Processing Engineering Center under the Engineering Research Center Initiative (Cooperative Agreement ECD-88-03014), and from the National Institutes of Health under the Interdepartmental Biotechnology Training Grant (#5 T32 GM08334) and under Public Service Grant 1R01 GM25810-01.

On a more personal level, I wish to acknowledge my friends and co-workers at MIT who provided support and advice. Most important are the contributions of my labmates and officemates: Kai-Chee Loh, Eric Scharin and Margaret Speed. Graduate school would not have been the same without their friendship and listening ears. I'll never forget the good times, the valuable (and sometimes the pointless) discussions, and the friendship we've shared. My other Building 16 colleagues have also been a constant source of encouragement, advice and friendship. Thanks go to Thomas Aicher, Chris Dowd, Alex Engel, John Konz, Dominique Maugeais, G. K. Raju, Cliff Rutt, Stefan (FTN) Weissflog, Stefan (the Bavarian) Winkler and especially to: Joya Gargano for doing a thankless job so well, Jean-François Hamel for always being there, Jack Prior for bailing me out of my IBM problems, and Bob Murray for always having a trivia question handy. I also extend my appreciation to the last group of Building 16 students who introduced me to laboratory procedures with patience and helpfulness, especially Neal Gordon, Anna Hagen, Jeff Cleland, Greg O'Connor, Max Kennedy, and Ulrich Holeschovsky. Not to be forgotten are the newest Building 16 members, the Cima-ites who kept me company late at night in the lab and in the computer room: Scott Borland, Erik Hancock, Sue Hobbs, Philip Kuhl, Stephanie Lopina, Ann Park, Mark Powers, and Jeff Sperinde. Finally, I want to thank my Building 20 colleagues past and present - who are too numerous to mention - but especially Ed Osawa and Brian Kelly who always made me feel welcome on my visits.

At last, I wish to acknowledge the most important contributor to my thesis, my husband Thomas, to whom this thesis is dedicated. I could never thank him enough for his love, support, patience and friendship throughout the years. Whether the task was helping me solve a differential equation or bringing me dinner when I was stuck in the lab, I could always count on him. I look forward to many more years of the Dr. Moore and Dr. Moore collaboration.

Table of Contents

List of Figures

Chapter 1 Introduction

Chapter 2 Review of Taylor-Couette Vortex Flow

Chapter 3 Mathematical Model of the Vortex Flow Reactor

Chapter 4 Materials and Methods

Chapter 5 Mass Transfer in Taylor-Couette Vortex Flow

Chapter 6 Mathematical Model Simulations

Chapter 7 Characterization of a VFR with an Immobilized Alkaline Phosphatase Membrane

Chapter 8 Characterization of a Vortex Flow Reactor Containing Suspended Particles

Appendix A Reactor Design Calculations for a Vortex Flow Reactor with Immobilized Heparinase

List of Tables

Chapter 1 Introduction

Chapter 2 Review of Taylor-Couette Vortex Flow

Chapter 3 Mathematical Model of the Vortex Flow Reactor

Chapter 4 Materials and Methods

Chapter 5 Mass Transfer in Taylor-Couette Vortex Flow

Chapter 1 -

Introduction

The flow between rotating concentric cylinders known as Taylor vortex flow, or more generally as Taylor-Couette flow, has for many years intrigued both theoreticians and experimentalists. The periodic vortices were first described thoroughly by G. I. Taylor in 1923. The following 70 years have provided an abundance of research on the hydrodynamics, transport properties and applications of the vortex columns.

Recently, there has been a strong interest in Taylor-Couette flow applications in specialty fields such as biotechnology. The interest in vortex flow is due in part to its ability to handle difficult process streams, such as those containing suspended solids or high viscosities. The ability to handle difficult materials is readily shown in vortex flow filtration, which can successfully filter cell homogenates (Kroner *et al.* , 1987), high solid content food products (DeStefano *et al.*, 1991), and oily wastes (Vigo *et al.*, 1985). Other filtration applications, such as blood plasmapheresis (Beaudoin and Jaffrin, 1987) and continuous cell culture (Tramper *et al.*, 1986), demonstrate the ability of the vortices to work with shear sensitive biological process streams.

Applications of Taylor-Couette flow are not limited to filtration devices. Some novel uses of vortex flow include plant cell culture (Miller *et al.*, 1964), blood oxygenation (Strong and Carlucci, 1976), gaseous catalytic reaction (Moalem Maron, 1983), and isoelectric focusing (Grutzner and Pellechia, 1990) where molecules are separated by their isoelectric points in an electric field. The use of Taylor-Couette flow in these applications is motivated by the unique characteristics of the flow profile. The vortices provide good mixing (dispersion) properties along with excellent heat and mass transfer to the cylinder walls. The combination of good mixing and mass transfer allow vortex flow systems to achieve near ideal performance for most chemical or biochemical reactions. In addition, the controllable shear environment of Taylor-Couette flow permits the processing of many biological components.

Although many applications of Taylor-Couette flow have been developed and many more are anticipated, little progress has been made previously in quantitatively describing transport and reaction in the vortex columns. Without a thorough description of transport phenomena and reaction behavior in the vortices, it is not possible to predict operating performance of Taylor-Couette systems. Therefore, the main goal of this thesis is to characterize transport phenomena in a Taylor-Couette flow reactor. By incorporating the results into a mathematical model, a framework is developed for calculation of design, scale-up, and optimization of vortex flow reactors.

The device chosen for these studies, called the vortex flow reactor (VFR), is a solid-liquid contactor containing an active surface located either on particles suspended within the annulus or on one or both of the cylinder walls, as illustrated in Figure 1.1. The active surface may be a catalyst, such as an immobilized enzyme, or an adsorbent. While the vortex flow reactor may be used for any solid-liquid reaction or adsorption, it is most useful in applications which include feed streams containing high solids content, high

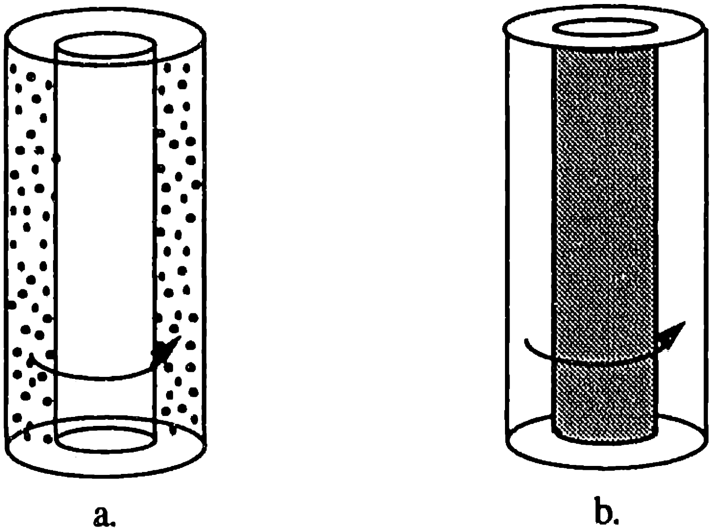

Figure 1.1: Vortex flow reactor configurations: (a) with active surface on suspended particles and (b) with active surface on cylinder wall(s).

viscosity, or shear sensitive biologicals. Two apparent applications are (1) an adsorber to remove products or wastes from cell broths or cell homogenates, and (2) an extracorporeal reactor for removal of a toxin or for reaction with a blood component.

By using a VFR containing an adsorbent during a purification with a solute capture step, the VFR can achieve simultaneous purification of a product and clarification of the solids from a cell homogenate. In most purification schemes, the homogenate is first clarified by centrifugation or ultrafiltration to remove solids, then the clarified stream is further processed to purify and concentrate the product. By replacing the two or three processing steps with a single step VFR, a decrease in product losses and an economy of operation is expected to result. Of course, direct capture from a cell homogenate is not limited to the VFR; conventional fluidized beds (Buijs and Wesselingh, 1980; Burns and Graves, 1985) and stirred tanks (Pungor *et al.*, 1987; Afeyan *et al.*, 1989; Gordon *et al.*, 1990) have worked successfully in this operation. The optimal reactor for the process would be able to handle suspended solids (unlike a packed bed), have low dispersion to achieve plug-flow behavior, and have high mass transfer to the active surface. The VFR with its good dispersion and mass transfer properties fits this description. The fundamental studies of transport and reaction presented in this thesis provide the groundwork for designing VFR adsorbers.

The second application of the solid-liquid VFR is an extracorporeal reactor for processing blood. Taylor-Couette devices have been previously shown to work well with blood in plasmapheresis and oxygenation applications. One such blood plasmapheresis device (Baxter; Deerfield, IL) has obtained FDA approval and is commercially available. In addition to good blood compatibility, the VFR offers excellent mixing and transport properties. A VFR containing immobilized enzyme or adsorbent can be used to remove or react with a blood component. In one specific example, described later, the VFR is used as an extracorporeal reactor with immobilized heparinase to enzymatically degrade the anticoagulant heparin into small inactive fragments. By neutralizing the anticoagulent heparin during dialysis or membrane oxygenation, the heparinase VFR has the potential to reduce post-surgical hemorrhaging complications. The advantage of the VFR over other extracorporeal device lies in the good transport properties and controllable shear provided by the vortices.

The adsorber and extracorporeal reactor described above are just two applications of Taylor-Couette vortex flow reactors. In general, the knowledge obtained in the characterization of the solid-liquid VFRs is applicable to any vortex flow application. By obtaining a fundamental understanding of transport and reaction in the vortices, it is possible to design, scale-up and optimize any reactive vortex flow system. The specific goals needed to fully characterize the vortex flow reactor are described below.

The overall goal for this thesis is to characterize the vortex flow reactor for catalytic reactions and adsorptive separations. The specific goals for characterization include:

1) Develop a prototype vortex flow reactor for solid-liquid reaction and examine the range of feasible operation. Two reactors are examined - one with the active surface on the cylinder walls and one with the active surface on particles suspended within the annulus.

2) Describe mixing (dispersion) in the vortex flow reactor as a function of operational and design parameters.

3) Describe mass transfer to the active surfaces in the VFR as a function of operational and design parameters.

4) Develop a mathematical model to describe reaction and transport in the VFR.

5) Validate the mathematical model using a model immobilized enzymatic reaction.

6) Demonstrate the utility of the VFR as an immobilized enzyme reactor and as an adsorber.

7) Use the model to calculate optimal design parameters for an immobilized heparinase reactor.

This thesis contains the theory and experiments necessary to characterize the vortex flow reactor. A thorough analysis of the published literature provides information for reactor design and operation. A mathematical model predicting conversion in the VFR is presented along with supporting experiments to determine the model parameters. Immobilized enzymes are used in the VFR to validate the reactor concept and the mathematical model. The utility of the VFR is demonstrated both for immobilized enzymatic reaction and for protein adsorption. Finally, directions for further VFR studies are discussed. The thesis concludes with design estimates of an immobilized heparinase reactor for use in neutralization of heparin in blood.

Chapter 2 -

Review of Taylor-Couette Vortex Flow

The knowledge accumulated throughout the past seven decades of research on Taylor-Couette flow provides a foundation for the characterization of the VFR. The research examining the hydrodynamics of the vortices establishes the operational limits of the VFR. Furthermore, information on transport properties aids in relating mass transfer to operational parameters. This review summarizes the literature on transport phenomena and applications using Taylor-Couette flow. A quantitative approach is used by compiling and comparing experimental results and derived correlations from different authors. In many cases, a consensus is obtained from the literature allowing the correlation of a transport property with the system's operational parameters. In some cases, the resulting transport correlation can be incorporated directly into the mathematical model. In other cases, analysis of the literature suggests areas of further experimentation.

The following review examines momentum, mass and heat transfer in Taylor-Couette flow and the unique features these transport properties impart on vortex flow applications. While this review does not focus on the hydrodynamic aspects of vortex flow, enough detail is included to appreciate the impact of vortex hydrodynamics on transport phenomena and applications. A notable result from compiling the diverse studies on Taylor-Couette flow is the development of consensus correlations relating transport properties to operational parameters. Although the information in the correlations is present in the works of individual authors, the exhaustive compilations presented here make apparent several trends which are not evident by examining one or two individual works. The consensus correlations aid both in the fundamental understanding of Taylor-Couette flow and in the design of vortex flow reactor.

2.1. Applications of Taylor-Couette Flow

Application of Taylor-Couette flow to engineering problems has been as periodic as the flow profile itself. During the early years following Taylor's discovery (Taylor, 1923, 1935), many researchers examined the fundamentals of transport phenomena in Taylor-Couette flow by focusing on heat transfer in rotating machinery (Gazley, 1958; Kaye and Elgar, 1958; Bjorklund and Kays, 1959; Tachibana *et al.*, 1960; Haas and Nissan, 1961; Becker and Kaye, 1962a; Ho *et al.*, 1964) and mass transfer enhancement in rotating electrolytic reactors (Eisenberg *et al.*, 1954, 1955; Bennett and Lewis, 1958; Sherwood and Ryan, 1959; Arvia and Carozza, 1962).

In addition to such straightforward applications of Taylor-Couette vortex flow, a number of creative applications were being explored. A summary of these applications appear in Table 2.1. Among the earliest developments was the spinner column for liquid-liquid extraction (Ney and Lochte, 1941; Maycock, 1949; Short and Twigg, 1951; Davis and Weber, 1960). In this device, heavy and light phases were introduced into an annular

TABLE 2.1 - APPLICATIONS OF TAYLOR-COUETTE FLOW SYSTEMS

Application	References
Liquid-Liquid Extraction	Ney and Lochte - 1941 Maycock - 1949 Short and Twigg - 1951, Davis and Weber - 1960
Solid-Liquid Adsorption	Olin, et al. - 1954
Gas Phase Catalytic Reactor	Yacoub and Moalem Maron - 1984
Viscosity Measurement	Vera and Grutzner - 1986
Isoelectric Focusing	Grutzner and Pellechia - 1990 Ivory *et al.* - 1992
Plant Cell Culture	Miller *et al.* - 1964 Thomas and Janes - 1987
Mammalian Cell Culture	Mered *et al.* - 1992 Rolchigo - 1992
Blood Oxygenation	Strong and Carlucci - 1976 Gaylor and Smeby - 1976 Mendler *et al.* - 1976 Mottaghy and Hanse - 1985
Blood Plasmapheresis	Beaudoin and Jaffrin - 1987, 1989 Fischel *et al.* - 1988 Jaffrin - 1989 Ohashi *et al.* - 1988
Filtration	Sherwood *et al.* - 1967 Lieberherr - 1978 , Hallstrom and Lopez-Levia - 1978 Lopez-Levia - 1979, 1980a, 1980b, Tobler - 1979, 1982 Rebsamen - 1983 Rebsamen *et al.* - 1985 Vigo *et al.* - 1985, 1986 Goldinger *et al.* - 1986 Kroner - 1987 Kroner and Nissinen - 1986, 1987, 1988 Kroner *et al.* - 1987 van Hemert, and Tiesjema - 1987 Rolchigo *et al.* - 1988, Turkson *et al.* - 1989a, 1989b, DeStefano *et al.* - 1991, Holeschovsky and Cooney - 1991, Paul *et al.* - 1991 Jiang *et al.* - 1992 Balakrishnan *et al.* - 1993 Belfort *et al.* - 1993a, 1993b Tsai *et al.* - 1993

column in counter-current directions. Rotation of the inner surface of the annular column caused the fluid phases to mix vigorously when the column was operated within the vortex flow regime. Contacting between the phases was shown to be extremely efficient, with height equivalent to a theoretical stage value of 6 to 8 cm.

As an extension of the liquid-liquid spinner column, similar columns were developed for solid-liquid contacting (Koenig *et al.*, 1954; Olin *et al.*, 1954). Two columns were used in these studies: one for adsorption, the other for desorption and regeneration. In this set-up, ion exchange resins were contacted with an aqueous stream in counter current directions. It was concluded from this study that the mass transfer rate to and from the suspended adsorbent was increased significantly (i.e., height equivalent to theoretical stage value was low). Maximum values of the mass transfer coefficient were found to coincide with or slightly exceed the Taylor instability. At high Taylor Numbers, excessive axial dispersion occurred, reducing the overall liquid mass transfer coefficients. At rotation rates insufficient to produce the vortex flow profile, serious channeling was observed. The major disadvantage of this type of column is its low capacity.

A more intriguing process involved Taylor-Couette vortex flow to enhance the photosynthetic rate in algal reactors (Miller *et al.*, 1964; Howell *et al.*, 1966). In this bioreactor, algal cells were suspended at high densities within an annular column. The inner surface of the annulus rotated at rates high enough to produce the Taylor vortex structure and a flashing light source was introduced at either of the annular surfaces to stimulate photosynthesis. The excellent mixing of the algal cells within the vortex allowed for uniform exposure of the cells to the light source. Overall, a 100% increase in the photosynthetic rate was observed over the control condition without rotation. An interesting conclusion of the work was that a reactor 3 feet in diameter, 6 feet high with a

1 inch annular gap width could produce 900 grams of oxygen per day, an amount sufficient for one person.

Through the 1960's and into the mid 1970's, applications activity in Taylor-Couette flow waned slightly, and most efforts focused on more basic issues such as modeling of the flow structure. From the mid 1970's to date, however, interest in fundamental and applied Taylor-Couette flow has been revitalized. Fundamental research aimed at further understanding and controlling heat and mass transfer problems encountered in rotating equipment was undertaken by many scientists including Kataoka (Kataoka, 1975; Kataoka *et al.*, 1975, 1984), Legrand and Coeuret (Coeuret and Legrand, 1980, 1981; Legrand *et al.*, 1980; Legrand and Coeuret, 1984) and Gu and Fahidy (1982, 1985a, 1985b, 1986).

On the applied side, researchers have exploited the enhanced mass transfer rates induced by the Taylor-Couette flow profile to improve the efficiency of blood oxygenation (Gaylor and Smeby, 1976; Mendler *et al*., 1976; Strong and Carlucci, 1976; Mottaghy and Hanse, 1985). In these devices, a gas permeable membrane is placed on the rotating surface of the annulus while blood is transported axially though the annular gap. Order of magnitude increases in oxygen transfer rates over non-rotating membrane contactors were observed.

The next and perhaps most commercial application of Taylor-Couette flow to engineering problems is aimed at reducing the concentration polarization problems associated with microfiltration and ultrafiltration. In these devices, a filtration membrane is placed on either the rotating or stationary surface of the annulus and the feed material to be filtered is transported axially though the annular gap. The enhanced mass transfer rates provided by the vortex flow profile increases filtration flux (i.e., filtrate flow rate normalized to a unit of active filter area) by a factor of ten over conventional tangential flow filtration methods.

While the earliest paper on vortex flow filtration was published by Sherwood *et al.* (1967), the start of the applications wave was initiated in the late 1970's by two independent research groups in Switzerland (Lieberherr, 1978) and Sweden (Hallstrom and Lopez-Levia, 1978; Lopez-Levia, 1979, 1980a, 1980b). Early filtration studies used vortex flow filtration to concentrate milk (Lopez-Levia, 1980b) and to separate oil-water emulsions (Vigo *et al.*, 1985; Vigo and Uliana, 1986). Lieberherr's work formed the basis for a vortex flow filtration system developed by Escher Wyss Limited of the Sulzer Group. This device, called the "Dynamic Pressure Filter", was applied to diverse applications including the clarification of animal and microbial cell fermentations (Tobler, 1979, 1982; Rebsamen, 1983; Rebsamen *et al.*, 1985; Goldinger *et al.*, 1986; Kroner and Nissinen, 1986, 1987, 1988; Kroner, 1987; Kroner *et al.*, 1987; van Hemert and Tiesjema, 1987). A further commercialization of this approach is currently being pursued by Membrex, Inc. (Rolchigo *et al.*, 1988). Several recent studies have examined the mechanisms of fouling (Turkson *et al.*, 1989a, 1989b; Holeschovsky and Cooney, 1991; Belfort *et al.*, 1993a, 1993b) and protein transmission (Balakrishnan *et al.*, 1993) in vortex flow filtration.

Applications of Taylor-Couette systems are best developed by exploiting the benefits of the vortex flow profile while considering the system's limitations. For example, a limitation of the vortex flow filtration is the decreasing surface area to volume ratio as the system is scaled radially. Therefore, applications are aimed at low volume streams such as those found in biotechnology. Of particular importance is the conversion of batch bioreactors to continuous perfusion reactors. In perfusion reactors, a filtration system is connected to the reactor allowing nutrients to be replenished while removing bioproducts or wastes. While the vortex flow profile provides excellent resistance to fouling of the filter, it also has been shown to be a relatively gentile environment for the suspended cells (Rebsamen *et al.*, 1985; Tramper *et al.*, 1986; Abu-Reesh and Kargi, 1989). This approach has greatly increased reactor productivity since the reactors can run continuously for over 20 days (Janes *et al.*, 1987; Thomas and Janes, 1987; Mered *et al.*, 1992; Rolchigo, 1992).

A practical extension of vortex flow filtration is to plasmapheresis. A device designed for this application developed by Hemasciences (Shoendorfer, 1987; Shooneman, 1988) utilizes a membrane filter positioned on the rotating surface. Several excellent studies illustrate the advantages of the Taylor-Couette flow filtration system for plasmapheresis (Beaudoin and Jaffrin, 1987, 1989; Fischel *et al.*, 1988; Ohashi *et al.*, 1988; Jaffrin, 1989).

One of the major drawbacks in the application of Taylor-Couette flow to filtration processes is the inherent geometric limitation to scaling. On the other hand, the geometry is ideal for miniaturization and sampling applications. Large volumes of sample feeds can be concentrated by over 100-fold in the gap. The vortex action maintains high filtration fluxes throughout the concentration procedure and enables nearly total recovery of product from either the clarified or concentrated feed. In the case of sugar cane sampling, the product is in the clarified stream (DeStefano *et al.*, 1991). In contrast, determination of bioburdens in foods and beverages requires analysis of the concentrate. Potential food spoilage organisms can be concentrated highly (> 100-fold), providing samples for simple, rapid testing to monitor and improve product quality. An analogous approach has been used to concentrate both ocean water samples and municipal water supplies to monitor for infectious organisms such as viruses and bacteria (Paul *et al.*, 1991; Jiang *et al.* , 1992; Tsai *et al.*, 1993).

The final application examples of Taylor-Couette flow deal with reactors. Grutzner *et al.* (1988) developed a variation on the early spinner columns. In this study, the vortex flow profile was used to stabilize discrete pH bands positioned and held by each vortex ring. The stable columns are speculated to be useful for several applications including separations and interfacial reactions. By placing electrodes at the ends of the cylinders, the device can be used to separate proteins and other molecules by isoelectric focusing (Grutzner and Pellechia 1990). Ivory *et al* (1992) has extended this approach to examine continuous zone electrophoresis in Taylor vortex systems. Similar devices use the feature of low axial dispersion to observe patterns from spatiotemporal reactions (Ouyang *et al.*., 1989; Tam *et al.*, 1988). Moalem Maron and co-workers carried out gaseous reactions in a vortex flow reactor (Cohen and Moalem Maron, 1983; Moalem Maron, 1983; Yacoub and Moalem Maron, 1984); the inside surface was used as a catalyst and the outside cylinder was used for heat transfer. The reactor obtained a higher conversion yield at a smaller reactor size than tubular reactors due to the high mass transfer, high heat transfer, and efficient mixing of the vortices.

Several of the reactors discussed above are similar to the vortex flow reactor examined in this thesis. The solid liquid ion exchanger of Olin *et al.* (1954) and the gaseous catalytic reactor of Moalem Maron (1983) closely resemble the particle and wall VFR configurations, respectively. This section also outlines other industrial and commercial applications of Taylor-Couette flow, many of which have just started to be explored. Whereas there have been numerous examples of the vortex flow reactors, there has been no previous systematic and comprehensive study of the reactor behavior.

The following sections, which describe hydrodynamics and transport phenomena of Taylor-Couette flow in detail, lay a foundation for full characterization of the vortex flow reactor. The unique features of the vortices are examined and their benefits to practical applications are discussed. The quantitative approach is directly applicable in design, operation and modeling of the VFR.

2.2 Description of Taylor-Couette Flow (Without Axial Flow)

2.2.1 Stability Criteria

The first thorough description of the stability of flow between cylinders was provided by Taylor (1923), who examined the onset of vortices within concentric cylinders for the inner and the outer cylinders rotating either at the same time or independently. Taylor showed that rotation of the inner cylinder above a critical rotation rate produces a secondary (vortex) flow, whereas rotation of the outer cylinder alone does not produce vortices. The flow made by the rotating inner cylinder and stationary outer cylinder above the critical rotation rate, shown in Figure 2.1, is now called laminar Taylor-Couette vortex flow or simply Taylor vortex flow. Through linear stability analysis, Taylor was able to mathematically explain his experimental observations.

The mathematical description of vortex flow usually involves a dimensionless group, the Taylor number, which describes the ratio of rotational to viscous forces. In its most general form, a modified Taylor number, Ta_m, is described as

$$Ta_m = \frac{\omega b r_i}{\nu}\left(\frac{b}{r_i}\right)^{0.5}\left(\frac{1}{F_g}\right) \tag{2.1a}$$

where ω is the rotation rate, b is the gap width between the cylinders, and r_i.is the inner radius. The correction factor F_g is given by

$$F_g = \frac{\pi^2}{41.2}\left(1 - \frac{b}{2r_i}\right)^{-1} P^{-0.5} \tag{2.1b}$$

and incorporates a parameter P,

$$P = 0.0571\left(1 - 0.652\frac{b}{r_i}\right) + 0.00056\left(1 - 0.652\frac{b}{r_i}\right)^{-1} \quad . \tag{2.1c}$$

The stability limits for laminar flow with no axial flow, as determined by Taylor, can be expressed by the critical Taylor number $Ta_{m,cr}$ as (Stuart, 1986)

$$Ta_{m,cr} = \frac{\pi^2}{\sqrt{P}} \quad . \tag{2.2}$$

Details of the linear stability analysis used to calculate (2.2) can be found in Taylor's original paper (Taylor, 1923) and in reviews by Schlichting (1955), Kataoka (1986) and DiPrima and Swinney (1981).

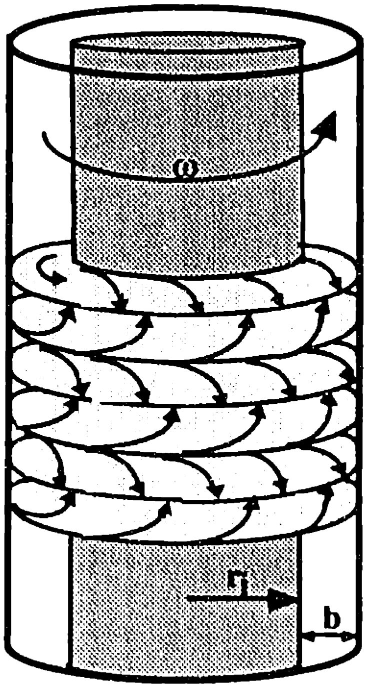

Figure 2.1: Schematic of laminar Taylor-Couette vortex flow.

In the narrow gap limit, where $b/r_i \rightarrow 0$, the correction factor F_g is unity the parameter P tends to 0.05766 and critical Taylor number found from (2.2) tends to 41.2. For the narrow gap case, the Taylor number can be expressed as

$$Ta = \frac{\omega b r_i}{\nu}\left(\frac{b}{r_i}\right)^{0.5}. \tag{2.3}$$

For consistency in the literature review, Taylor numbers from cited references will be converted to the definitions in (2.1a) and (2.3) whenever possible. Several other definitions exist for the Taylor number; one commonly used variation utilizes the square of (2.3). Throughout this thesis, the definitions for the Taylor number in (2.1a) and (2.3) are used in describing the VFR and (2.2) is used to calculate the critical rotation rate of Taylor vortex flow without axial flow.

Many researchers have since elaborated on the work of G.I. Taylor, to show the impact of other variables on vortex stability. The stability limits of Taylor vortex flow for larger gap ratios of $b/r_i \approx 1.0$ were examined by Chandrasekhar (1958) . Axial flow tends to stabilize the laminar flow and delays the onset of the vortices. The modified stability criterion for axial flow is discussed in Section 2.3.1. Another factor affecting the critical Taylor number is the buoyancy of the fluid. Heat applied to the inner cylinder tends to stabilize laminar flow, whereas heat applied to the outer cylinder stabilizes vortex flow (Becker and Kaye, 1962a; Sorour and Coney, 1979b). Other forces impacting vortex stability include a magnetic field applied on a conducting fluid (Chandrasekhar, 1961), and a Coriolis force external to the cylinders (Wiener *et al.*, 1990). Many of these and other advances on determining vortex stability are summarized by Donnelly (1991).

2.2.2 Higher Order Taylor-Couette Flows

The picture of Taylor-Couette flow in Figure 2.1 is typical of the behavior just above the critical rotation rate. As the rotation rate is increased further, the vortices transition into higher order flow patterns. There is a large amount of literature describing the stability and transitions of the many flow regimes above laminar Taylor vortex flow. Reviews by DiPrima and Swinney (1981) and Katoaka (1986) nicely summarize the published theoretical and experimental work. Experimental methods for examination of vortex structure include: (1) visual observation using dye (Taylor, 1923), smoke (Kaye and Elgar, 1958), suspended particles (Coles, 1965) or a chemical reaction product (Gu and Fahidy, 1985c), (2) internal measurement of velocity from hot-wire anemometers or pitot tubes (Smith and Townsend, 1982), (3) external measurement using NMR (Vera and Grutzner, 1986), light scattering (Gorman and Swinney, 1982), or laser Doppler velocimetry (Fenstermacher *et al.*, 1979).

Wavy Vortex Flow

For small gap geometry, a time dependent flow called wavy vortex flow occurs above the critical Taylor number. The wavy vortex flow pattern, sketched in Figure 2.2, was noted first by Taylor (1923), and systematically studied first by Coles (1965). Upon increasing the rotation rate, the vortex shape gradually changes from the doughnut shape pictured in Figure 2.1 to wavy bands with superimposed azimuthal (or circumferentially traveling) wave or waves. The number of azimuthal waves and the individual vortex length is dependent upon the gap to radius ratio, the rotation rate and the cylinder length (DiPrima and Swinney, 1981; Bühler *et al.*, 1986); increasing the rotation rate tends to increase the number of waves and the length of a single vortex (Coles, 1965). An interesting aspect of this flow is the non-uniqueness of wavy vortex flow; the number of azimuthal waves and length of a vortex is dependent on the start-up conditions of the rotating cylinder. An additional transition may occur in wavy vortices at high rotation rates. In this flow pattern, called modulated wavy vortex flow or double periodic wavy vortex flow, both the position and amplitude of the traveling waves vary with time (Gorman and Swinney, 1982).

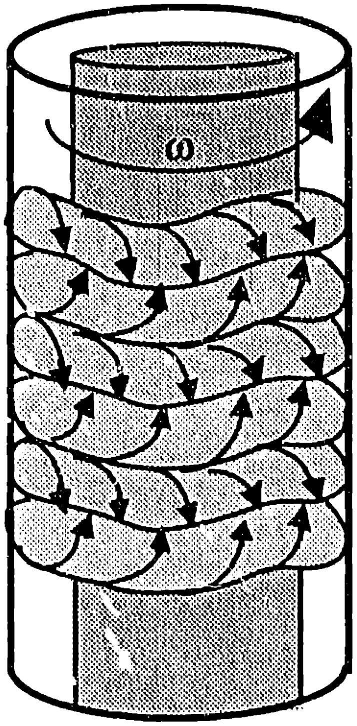

Figure 2.2: Schematic of Taylor-Couette flow with circumferential traveling (wavy Taylor-Couette vortex flow).

The critical Taylor number for wavy vortex flow depends largely upon the gap ratio. For example, experimental results (DiPrima and Swinney, 1981) show $Ta_{cr,wavy} \approx 1.08\ Ta_{cr}$ for $b/r_i = 0.05$ and increases with gap ratio to $Ta_{cr,wavy} \approx 10\ Ta_{cr}$ for $b/r_i = 1.0$. While this data provides a guide for flow transition, no general correlation exists for the onset of wavy vortex flow.

Turbulent Vortex Flow.

No clear criteria exists for defining either the initiation of turbulent vortices or the transition from turbulent vortices to fully turbulent flow. Turbulence in wavy vortex flows is observed first as irregular motion appears within the wavy vortices. This is first present at speeds 10 times the critical rotation rate (Coles, 1965) for a gap ratio of $b/r_i=0.14$. As the rotation rate increases, the flow gradually becomes increasing turbulent. The axial periodicity of the vortices still holds while the azimuthal waves disappear. For a gap ratio of $b/r_i = 0.33$, Smith and Townsend (1982) report the persistence of vortex structure up to 500 times the critical rotation rate and turbulence without vortex structure at rotation rates over 700 times critical.

2.2.3 Vortex Velocity Profiles

An analytical solution of the Navier-Stokes equations does not exist for Taylor vortex flow. Methods for experimentally measuring the radial, axial and tangential components of the vortex velocity profile include hot wire anemometer measurements (Simmers and Coney, 1979a; Simmers and Coney, 1980), particle visualization techniques (Mizushina *et al.*, 1971; Kataoka, 1975) , and pressure measurements using pitot tubes (Taylor, 1935). Experimental and computational results show that the tangential velocity is the dominant velocity component with the radial velocity at least an order of magnitude smaller (Majumdar and Spalding, 1977; Simmers and Coney, 1980). A sketch of the tangential velocity profile for Taylor vortex and laminar (Couette) flow between rotating cylinders is shown in Figure 2.3 . In laminar Couette flow a linear velocity gradient is present, whereas in vortex flow, the tangential profile is relatively constant across the gap except at the walls where sharp gradients exists.

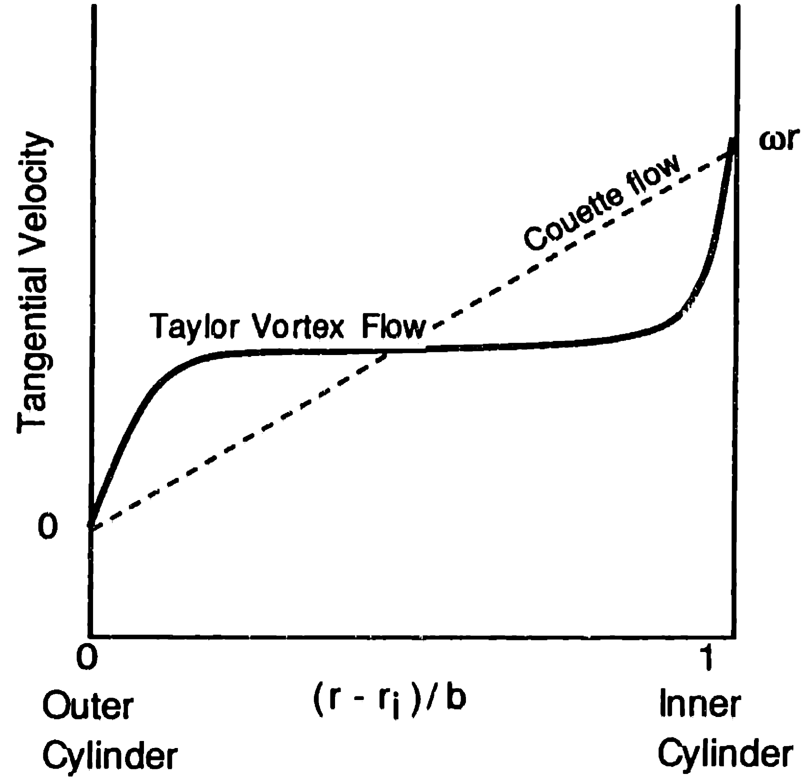

Figure 2.3: Tangential velocity profiles for Taylor vortex flow (solid line) and for non-vortex Couette flow (dashed line).

The velocity profiles also can be determined numerically. A numerical solution of the Navier-Stokes equations has been presented (Majumdar and Spalding, 1977) for Taylor numbers just above Ta_{cr}. Jones (1981) obtained a nonlinear steady solution for laminar vortices at high Taylor number as a first step in calculating the transition to wavy vortices. Computational methods also have been developed to solve Navier-Stokes equation for the more complicated wavy vortex flow (Marcus, 1984a, 1984b).

2.3. Description of Taylor-Couette Flow with Axial Flow

2.3.1 Stability Criteria

Axial flow tends to stabilize laminar flow and delay the onset of vortices, thus increasing the critical Taylor number. Upon introduction of a low axial velocity there is a sudden increase in Ta_{cr}. Theoretical (Chandrasekhar, 1962; Krueger and DiPrima, 1964; Datta, 1965) and experimental (Snyder, 1962) analyses have been conducted to examine this increase in Ta_{cr} at very low axial Reynolds numbers (Re_z). Datta (1965) described the relationship between critical Taylor number and axial Reynolds number for $Re_z<2.5$ as

$$Ta^*_{cr} = 1707.8 + 0.33 Re_z^2 \tag{2.4}$$

where Ta^* is an alternate Taylor number ($Ta^*=(2\, r_i^2\, b^4\, \omega^2)/(\nu^2\, (r_o^2 - r_i^2))$).

The dependence of Ta_{cr} on Reynolds number at moderate axial flow rates has been studied extensively. Chandrasekhar (1960) and DiPrima (1960) used stability theory to study the effect of axial flow on Taylor vortices; the results agree well with the experimental measurements of Donnelly and Fultz (1960) for Ta_{cr} with axial Reynolds numbers[†] between 10 and 50. Gu and Fahidy (1986) derived a correlation for Ta_{cr},

$$Ta_{cr} = 43.61 + 0.344 Re_z \tag{2.5}$$

from experimental data for b/r_i values of 0.12 and 0.167 and with axial Reynolds numbers up to 50. Several studies (Chung and Astill, 1977; Hansoon and Martin, 1977) have attempted to determine the critical Taylor number at high Re_z; in some cases good agreement has been found with experimental data (Gravas and Martin, 1978).

[†] Axial Reynolds numbers are given as $Re_z = 2b\, u_{avg}/\nu$, values for Reynolds numbers from other authors have been converted to this basis.

In general, the onset of Taylor vortex instability is well described for zero to moderate axial flow rates. As the operating conditions for the VFR is for axial Reynolds numbers below 50, equations (2.2), (2.4) and (2.5) are used in determining the critical rotation rate for the onset of vortices, and thus the lower operating limit of the VFR.

The onset of the flow transitions beyond Ta_{cr} are less well described than for the initial vortex instability. Kaye and Elgar (1958) were the first to describe combined axially and rotational flow as four flow regimes - laminar, laminar vortices, purely turbulent flow, and turbulent vortices. The location of the flow regimes are presented schematically in Figure 2.4 as a function of axial flow rate and rotation rate. Although graphs such as Figure 2.4 have been used by many authors to describe combined flow, they are technically incorrect. As in Taylor vortex flow without axial flow, there are actually several different flow patterns possible between the purely laminar vortices and the turbulent vortices. As the axial Reynolds number increases, the vortices shift from doughnut-shaped, torroidal cells to inclined, spiraling cells (Snyder, 1962; Gu and Fahidy, 1985a 1985b, 1986) and individual vortex cells begin to overlap. Individual researchers have examined experimentally the shift from laminar to wavy vortex flow and from wavy vortex to turbulent flow. In general, however, there are no clear criteria to predict the transition to wavy vortices or the transition to turbulence

2.3.2 Entrance Length.

The entrance length, or the region over which the vortices become fully developed, is an important parameter in determining the behavior of combined axial and vortex flow. In purely rotational Taylor vortex flow (i.e. without axial flow), entrance effects are found to be negligible (Snyder, 1969) as long as the ratio of cylinder length to gap width, L/b, is greater than 10. In combined rotational and axial flow, an entrance region exists where the tangential velocity components of the vortices develop (Astill, 1964; Astill *et al.*, 1968; Simmers and Coney, 1979a; Sorour and Coney, 1979a). The vortices begin to develop at the inner rotating surface and grow to extend completely to the outer, stationary cylinder at the hydrodynamic entrance length. The hydrodynamic development length is known to decrease with increasing Taylor number or decreasing axial Reynolds numbers (Astill, 1964). Simmers and Coney found (1979a) the distance for the development of the entrance region to vary as Re^2/Ta. This guideline is useful in scale-up design of vortex flow systems.

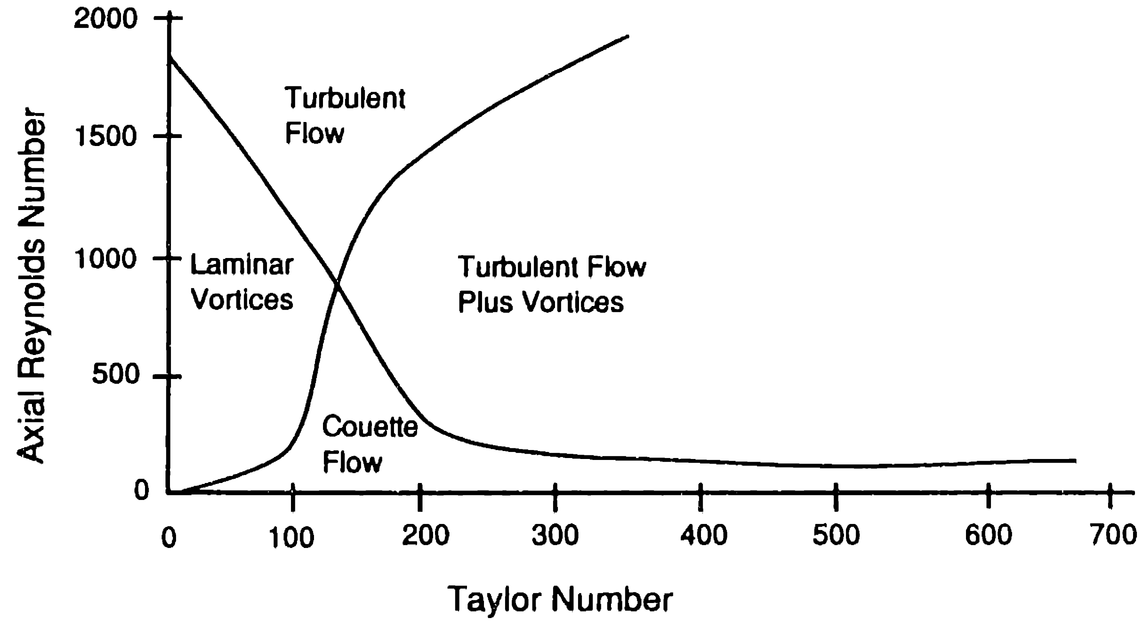

Figure 2.4: Schematic of the four flow regimes in Taylor-Couette flow with axial flow, as described by Kaye and Elgar (1958).

2.4. Torque, Friction Factors and Wall Shear in Taylor-Couette Flow

The various frictional effects in Taylor vortex systems have been studied by many experimenters, primarily for the design of rotating machinery. Studies on frictional effects can further be used to predict power consumption of Taylor-Couette flow applications (Sinevic *et al.*, 1986). The information from torque studies also serves as a useful comparison with studies on hydrodynamic structure and with experimental measurements of heat and mass transfer. This section describes the available correlations on torque, friction factor and wall shear effects.

Beaudoin and Jaffrin (1989) fit data from G. I. Taylor's torque studies (Taylor, 1936) to obtain a correlation for shear rate at the inner cylinder wall, γ_w:

$$\gamma_w = 0.23 Ta^{0.5} \frac{\omega r_i}{b} \,. \tag{2.6}$$

The viscous and geometric terms in (2.6) can be rearranged to relate shear stress, τ, to the Taylor number as: $\tau \propto Ta^{1.5}$. Coney and Simmers (1979) examined shear stress at the outer wall for vortices with axial flow. Shear stress was related with the critical Taylor number and the corresponding shear stress for laminar Poiseuille flow, τ_{pois}.

$$\frac{\tau}{\tau_{pois}} = \left(\frac{Ta}{Ta_{cr}}\right)^{1.57} \tag{2.7}$$

In the range of Taylor numbers studied ($Ta = 600\text{-}3200$), the only dependence on axial flow rate is contained in the variation of Ta_{cr} with axial flow. A second study by Abdallah and Coney (1988) on combined axial and vortex flow presents a different functional dependency of shear stress on the Taylor number.

$$\tau^{1/3} = n \ln(Ta) + const. \tag{2.8}$$

In this work, three flow regimes were characterized by observation of the shear stress curves. At low axial flow rates (laminar flow), the shear is constant with Taylor number but increases with increasing axial flow. In the secondary regime, the coefficient, n, in (2.8) was found to vary from 1.0 to 1.12. A tertiary regime was apparent at even higher rotation rates; the coefficient n varies from 1.4-1.6 in this regime. The authors interpreted the secondary and tertiary flow regimes to indicate the presence of wavy vortex flow and turbulent vortex flow, respectively.

Bjorklund and Kays (1959) fit friction factor data for Taylor vortex flow without axial flow to obtain the correlations

$$\frac{fTa}{(fTa)_{lam}} = 0.0388 Ta^{0.877} \qquad Ta_{cr} < Ta < 90 \qquad (2.9a)$$

$$\frac{fTa}{(fTa)_{lam}} = 0.19 Ta^{0.52} \qquad 90 < Ta < 8000 \qquad (2.9b)$$

where the friction factor is related to shear stress and torque, G, by:

$$f = \frac{2\tau}{\rho(\omega r_i)^2} = \frac{G}{\pi L \rho (r_i \omega)^2 r_i^2} \qquad (2.9c)$$

The friction factor for laminar flow, $(f\,Ta)_{lam}$, is a geometric parameter expressed as:

$$(fTa)_{lam} = \frac{4(b/r_i)^{3/2}}{1-(r_i/r_o)^2}. \qquad (2.9d)$$

Note that by substitution of (2.9c), (2.9d) and (2.1) into (2.9b), it can be shown that $\tau \propto Ta^{1.52}$ which is in good agreement with the other wall shear correlations.

Torque, G, in Taylor vortices without axial flow has been described by the equation:

$$G = a\omega^{-1} + b\omega^{m} \qquad (2.10)$$

where ω is the rotation rate and a and b are geometric constants. For Taylor numbers just above critical, Stuart (1958) found the exponent $m=1$ via a theoretical analysis with experimental confirmation. Donnelly and Simon (1960) found $m=1.36$ for low rotational speeds ($Ta< 10\,Ta_{cr}$) and $m=1.5$ at higher rotation rates. Nakabayashi *et al.* (1982) also found torque data to correlate to equation (2.10) with $m=1.36$ at low rotation rates. Wendt (1933) found torque data to correlate to $m=$ 1.5 for rotation rates approximately 4 to 150 times critical. Above this rotation rate, torque varied as $m=1.7$. Through a theoretical analysis of torque in wavy vortices, Eagles (1974) obtained results which corresponded with Donnelly and Simon's measurements and determined that torque in wavy vortex flow is less than the torque in the corresponding non-wavy Taylor vortex flow.

The above correlations show a remarkable consistency at rotation rates above $Ta> 10Ta_{cr}$ (approximately $Ta>500$). As discussed earlier, equations (2.6), (2.7) and (2.9b) can be rearranged to show the dependence of shear stress on Taylor number. In addition, equation (2.10) can be rearranged by noticing that at high rotation rate the second term is dominant, and that torque is geometrically related to shear stress. A summary of the correlations in the form

$$\tau \propto Ta^m \tag{2.11}$$

is shown in Table 2.2. It is evident that shear stress in Taylor-Couette flow at moderate to high rotation rates can be described well by equation (2.11) with $m=1.5$. A full description of shear stress may require additional geometric parameters, such as the gap ratio (b/r_i) and the aspect ratio (L/b).

The result of $m = 1.5$ for high Taylor number was predicted theoretically by G. K. Batchelor through scaling arguments. Batchelor, in an appendix to Donnelly and Simon's paper (1960), showed that at high rotation rates the dimensionless boundary layer at the wall, δ/b, varies as

$$\delta / b \propto Ta^{-1/2} \, . \tag{2.12}$$

With the boundary layer known, the relationship $G \propto Ta^{1.5}$ is obtained; consequent manipulations yield equation (2.11) with $m=1.5$.

Reference	Taylor Number Exponent, m
Beaudoin and Jaffrin (1989)	1.5
Coney and Simmers (1979)	1.57
Bjorklund and Kays (1959)	1.52
Wendt (1933)	1.5
Donnelly and Simon (1960)	1.5

Table 2.2: Summary of shear stress correlations for moderate to high Taylor number. Shear rate, torque and friction factor data were rearranged to fit the expression $\tau \propto Ta^m$

Compilation of the available experimental and theoretical work allows us to draw conclusions of how frictional factors vary with rotational and viscous forces. In the region of moderate to high rotation rate, experimental and theoretical studies reveal that shear stress (and torque) can be explained by (2.11) with an exponent of $m = 1.5$.

Physically, this region can be interpreted as corresponding to wavy vortex flow or turbulent vortex flow. At lower rotation rates, when laminar vortices are present, torque scales with a smaller exponent of $m \approx 1.3$. At higher rotation rates where non-vortex turbulent flow occurs, torque scales as $m > 1.5$. Similar results were observed by Lathrop and coworkers (1992a, 1992b) in high precision studies of torque on rotating cylinders. They did not find a constant value of m, but rather found m to increase with increasing rotation rate with values ranging from $m = 1.23$ at $Ta = 1700$, to $m = 1.87$ at $Ta = 7 \times 10^5$. The values of the exponent are consistent with those found by other workers in each range of Taylor numbers. As expected, the values for m lie below the theoretical maximum of $m = 2.0$ for isotropic, Kolmogorov turbulence (Lathrop *et al.*, 1992b) .

2.5. Mass Transfer in Taylor-Couette Vortex Flow

Mass transfer is one of the most intensively investigated aspects of Taylor vortex flow. Two aspects of mass transfer are discussed in this section: mass transfer from the vortices to the cylinder walls and mass transfer within vortices. Mass transfer characterization typically employs dimensional analysis to correlate a mass transfer parameter, such as the Sherwood number, to experimental data. Summaries of mass transfer correlations are presented in Tables 2.3, 2.4 and 2.5. Because the correlations in the literature are often in diverse functional form, they have been rearranged to present a mass transfer parameter as the product of up to three terms: a Schmidt number exponential, a Taylor number exponential and, in some cases, a geometric exponential. In Table 2.3 and 2.4, as well as in the rest of this review, the original correlations may have been rewritten to correspond to the Taylor number definition in (2.3) and the axial Reynolds number definition of $Re_z = 2u \;\; b/\nu$.

2.5.1 Mass Transfer to the Rotating Cylinder - Wide Gap/Turbulent Vortices

A large portion of the published works on mass transfer to the cylinder walls comes from rotating cylinder electrodes; these works are summarized in reviews by Gabe (Gabe, 1974; Gabe and Walsh, 1983). The four correlations in Table 2.3 (equations T3.1 through T3.4) are for turbulent mass transfer at the inner rotating cylinder. The studies used cylinders with large gap to radius ratio (e.g. $b/r_i >> 1$) and small aspect ratio (typically $L/b < 10$) to achieve turbulent flow. The degree of turbulence present in the experiments is difficult to ascertain since flow visualization studies unfortunately were not included in these works.

The most widely accepted correlation for mass transfer in turbulent vortices was presented by Eisenberg *et al.* (1954) and since has been validated experimentally by numerous authors. Mass transfer systems used in the validation include benzoic acid dissolution (Eisenberg *et al.*, 1955; Sherwood and Ryan, 1959), ferranocyanide reduction (Eisenberg *et al.*, 1955), and steel corrosion (Ellison and Schmeal, 1978; Shirkhanzadeh, 1987). Arvia and Carrozza (1962) explained mass transfer at the outer cylinder with the addition of a geometric factor (equation T3.2). Roughness of the rotating cylinder can have a marked effect on mass transfer (Kappesser *et al.*, 1971; Eklund and Simonsson, 1988); increased roughness enhances mass transfer due to both increased effective surface area and greater shear at the surface (Gabe and Walsh, 1983).

The original form of many of the correlations in Table 2.3 are in terms of the rotational Reynolds number, $Re_r = 2\omega r_i^2/\nu$, illustrating the independence of mass transfer from the gap width and outer wall geometry. The lack of dependence on outer cylinder geometry is expected as large gap widths make the experimental systems resemble a rotating cylinder in an infinite medium. Thus, it is not surprising that correlations for

Reference - system used	$\frac{b}{r_i}$	$\frac{L}{b}$	Ta	Sc	Original Correlation	Rearranged Correlation	Equation number
Eisenberg *et al.* (1954, 1955) - benzoic acid - ferricyanide reduction	0.21 - 6.8	2.4 - 29	470- 290,000	800- 11,500	$jD' = \frac{k_s}{\omega r_i} Sc^{0.644} = 0.0791\,Re_r^{-0.3}$	$Sh = 0.1285\,Sc^{0.356}\,Ta^{0.7}\left(\frac{b}{r_i}\right)^{-0.05}$	T3.1
Arvia&Carozza (1962) - copper electrodeposition	0.46 - 3.45	2.4 - 5.8	1500- 42,000	2450	$jD' = 0.0791\,Re_r^{-0.3}\left(\frac{r_i}{r_o}\right)^{0.7}$	$Sh{=}0.1285\,Sc^{.356}\,Ta^{.7}\left(\frac{r_i}{r_o}\right)^{.7}\left(\frac{b}{r_i}\right)^{-.05}$	T3.2
Singh&Mishra† (1980) - benzoic acid in benzene+water - salicylic acid in benzene+water - 2-napthol	—	—	—	2.4- 3200 Pr=0.7 -676	$Sh_d = 0.184\,Sc^{1/3}\,Re_r^{0.62}$	$Sh = 0.12\,Sc^{1/3}\,Ta^{0.62}\left(\frac{b}{r_i}\right)^{0.07}$	T3.3
Bennett &Lewis (1958) - benzoic acid	2.0	2.5	420- 2800	400- 3000	$Sh_d = 0.135\,Re_r^{0.6}\,Sc^{-0.6}$	$Sh = 0.523Sc^{0.4}Ta^{0.6}\left(\frac{b}{r_i}\right)^{0.10}$	T3.4

† Incorporates both heat and mass transfer data from other researchers.

Table 2.3 Correlations for mass transfer from cylinder wall in Taylor-Couette flow for wide gap vessels.

mass transfer from a rotating cylinder to an infinite medium (Kappesser *et al.*, 1971) closely resembles the Eisenberg correlation for mass transfer in wide gap vessel.

As seen in Table 2.3, mass transfer in turbulent vortices can be expressed by:

$$Sh = ARe_r^{\alpha} Sc^{\beta}$$

where A is a geometric constant, and the exponents α and β are experimentally determined parameters. In an extensive review of the rotating cylinder electrode, Gabe (1974) reveals that experimentally determined values of the Re_r exponent vary from 0.6 to 0.7, while reported values of the Sc exponent vary from 0.33 to 0.41.

2.5.2 Mass Transfer to Rotating Cylinder - Narrow Gaps

Unlike the very wide gap studies mentioned in Section 2.5.1, the correlations in Table 2.4 are obtained under experimental conditions similar to those used in most stability studies and to those encountered in practical applications. The mass transfer experiments are conducted with narrow gap ratios (b/r_i,< 0.5), large aspect ratios (typically L/b > 20) and small or zero axial flow. It can be seen easily that Taylor number exponents near 0.5 are obtained in most of the correlations in Table 2.4. This exponent of 0.5 is smaller than the exponent of 0.7 for turbulent flow indicating that mass transfer in laminar vortex flow is less dependent on rotation rate than mass transfer in turbulent flow.

The correlations in Table 2.4 also reveal that the axial Reynolds number, Re_z, has little or no effect on mass transfer over a wide range of Reynolds numbers. For example, the correlations T4.3, T4.5, T4.6 and T4.9 have no dependence on axial flow rate. As seen in T4.7 and T4.8, Legrand and Coeuret (Legrand *et al.*, 1980; Coeuret and Legrand, 1981) found no mass transfer dependence on axial flow for Re_z less than 300 and

Reference - system used	$\frac{b}{r_i}$	$\frac{L}{b}$	Ta	Re_z	Sc	Original Correlation	Rearranged Correlation	Equation Number
Coeuret & Legrand (1980) - ferricyanide reduction	0.14-0.43	39.5-118	200-4000	0	1380	$Sh = 0.74 \left(\frac{Ta}{2}\right)^{1/2} Sc^{1/3}$	$Sh = 0.523\, Sc^{1/3}\, Ta^{1/2}$	T4.1
Mizushina (1971) - copper electrodeposition	0.62-1.0	16-22	59-19500	0	3000-770000	$Sh = 0.74\, Ta^{1/2}\, Sc^{1/3}$	$Sh = 0.74\, Sc^{1/3}\, Ta^{1/2}$	T4.2
Flower *et al* (1969) (Shell Data) - n-butanol/air	0.15		200-2000	140-2600	1.74	$Sh = 0.702\, Ta^{0.52} \left(\frac{r_o}{r_i}\right)^{0.52}$	$Sh = 0.702\, Ta^{0.52} \left(\frac{r_o}{r_i}\right)^{0.52}$	T4.3
Flower & Macleod (1969) - n-heptane/air - mercury/air - water/air	0.11-0.42		0-2600	200-2000	0.6-1.9	$Sh{=}1.0\, Ta^{.52} Sc^{.33} Re_z^{-0.1} \left(\frac{r_o}{r_i}\right)^{.52}$	$Sh{=}1.0\, Sc^{.33} Ta^{.52} Re_z^{-0.1} \left(\frac{r_o}{r_i}\right)^{.52}$	T4.4
Macleod & Ruess (1975) - ethyl salicylate	0.312	96.0	210-680	33-100	1260	$Sh = 1.91\, Ta^{0.7}$	$Sh = 1.91\, Ta^{0.7}$	T4.5
Kataoka (1977) - copper electrodeposition	0.62	21.1	35-9200	0-260	3000-800000	$Sh = 0.43\, Ta^{0.49}\, Sc^{0.33}$ extrapolated from graph, from (Lopez-Levia, 1979)	$Sh = 0.43\, Sc^{0.33}\, T\varepsilon^{0.49}$	T4.6
Legrand (1980); **Coeuret&Legrand** (1981) - ferricyanide reduction	0.14, 0.286	63, 126	130-1600	25-300	1380-6500	$Sh = 0.38\, Ta^{1/2}\, Sc^{1/3}$	$Sh = 0.38\, Sc^{1/3}\, Ta^{1/2}$	T4.7a
				300-810	1380-6500	$Sh = 0.12\, Re_z^{1/3}\, Ta^{0.4}\, Sc^{1/3}$	$Sh = 0.12\, Sc^{1/3}\, Ta^{0.4}\, Re_z^{1/3}$	T4.7b
Coeuret&Legrand (1981) - ferricyanide reduction	0.429	42	700-3700	25-300	1380	$Sh = 0.59\, Ta^{1/2}\, Sc^{1/3}$	$Sh = 0.59\, Sc^{1/3}\, Ta^{1/2}$	T4.8a
				300-720	1380	$Sh = 0.08\, Re_z^{1/3}\, Ta^{0.4}\, Sc^{1/3}$	$Sh = 0.08\, Sc^{1/3}\, Ta^{0.4}\, Re_z^{1/3}$	T4.8b
Holeschovsky & Cooney (1991) - filtration	0.04-0.148	52-189	65-9700	25-200		$Sh = 0.75\, Re_\theta^{0.5} \left(\frac{2b}{r_i}\right)^{0.42} Sc^{0.33}$	$Sh = 1.42 Sc^{0.33} Ta^{0.5} \left(\frac{b}{r_i}\right)^{0.17}$	T4.9

Table 2.4 Correlations for mass transfer from cylinder wall in Taylor-Couette flow in narrow gap vessels.

thereafter an increase in mass transfer with increasing axial flow. Katoaka (1977) found an initially rapid drop in mass transfer occurs just above $Re_z=0$ followed by a very slight decrease in mass transfer with increasing axial velocity.

A few mass transfer studies require special note. Several of the mass transfer correlations in Table 2.4 were measured at the outer cylinder; these include the studies of Mizushina, Flower (and Shell data), and Macleod (equations T4.2, T4.3, T4.4, and T4.5, respectively). In general, for mass transfer at the outer cylinder, the exponential form of the correlation remains the same while the magnitude of mass transfer increases (Macleod and Ruess, 1975; Legrand *et al.*, 1980; Coeuret and Legrand, 1981). The work of Holeschovsky and Cooney (1991), in Table 2.4, describes mass transfer from the concentration polarization layer on a rotating cylinder during filtration. By assuming the concentration polarization model, mass transfer coefficients were obtained from the filtrate flux at high pressures in the pressure independent region.

Not included in Table 2.4 are studies which examine local mass transfer behavior (Kataoka *et al.*, 1977; Legrand *et al.*, 1983; Kataoka *et al.*, 1984; Gu and Fahidy, 1985b) over the length of a single vortex. These researchers found that mass transfer in a laminar vortex pair varied sinusoidally, with the maxima occurring at the boundary where the vortices join and impinge on the cylinder wall, as shown in Figure 2.5. Legrand and Coeuret (1987) found that mass transfer from the cylinder wall increased 60% to 100% with the presence of a two phase liquid emulsion. The change in mass transfer was attributed to mechanical deformation of liquid droplets at the wall surface and to observed modifications of the vortex structure. Also noticeable absent from Table 2.4 is the work Holman and Ashar (1971). While these authors published a thorough study of mass transfer from a rotating cylinder, they used the wrong viscosity for water, thus the derived correlations are incorrect. Nevertheless, when data sets with the same viscosity were correlated to a Taylor number exponential, the exponents were found to range from 0.40 to 0.49, in close agreement with the correlations in Table 2.4.

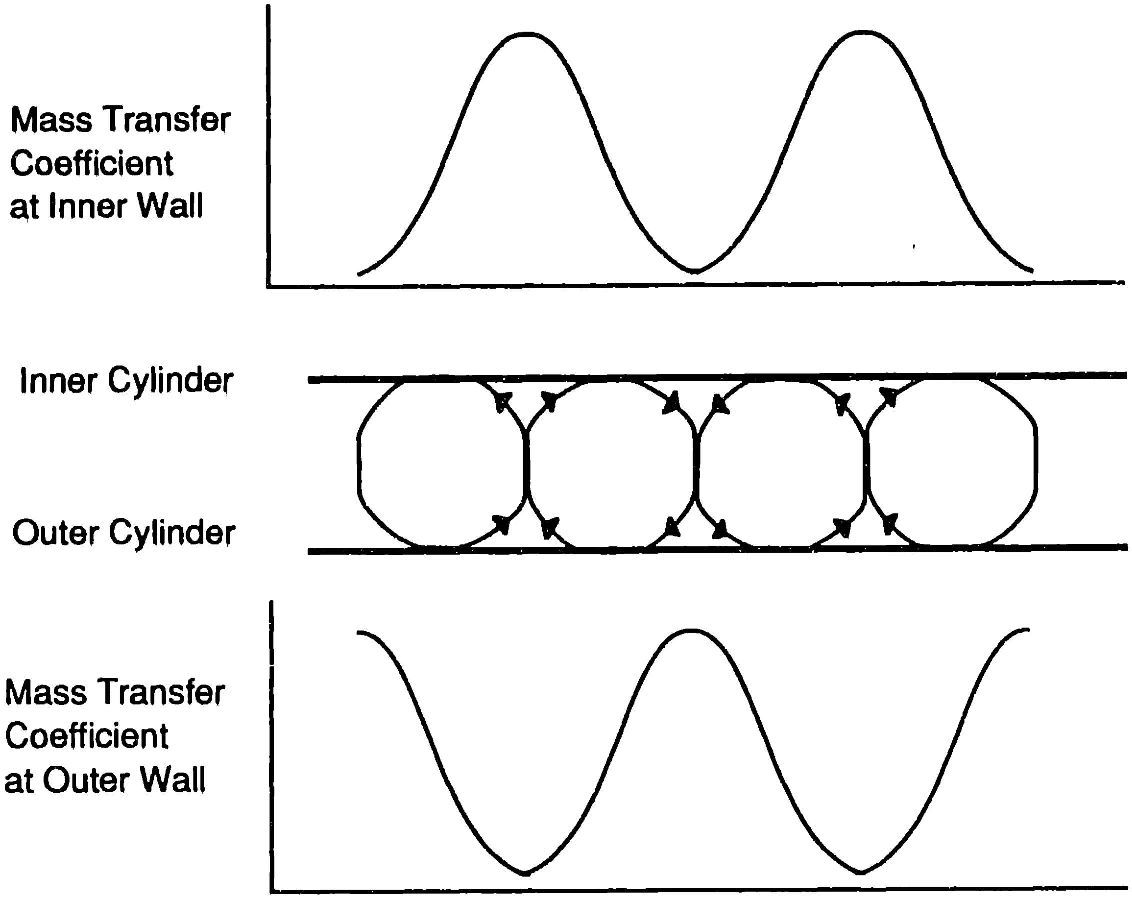

Figure 2.5: Variation of local mass transfer coefficient with vortex position for laminar Taylor vortex flow.

Numerous authors have attempted to find an analogy between mass transfer from the rotating surface and frictional effects. Eisenberg (1955) was able to describe mass transfer in turbulent vortices in close correspondence to the Chilton-Colburn analogy.

Several authors have modeled vortices in narrow gap systems as a turbulent vortex core with laminar sublayers in an effort to relate mass (Sherwood and Ryan, 1959; Singh and Mishra, 1980) and heat (Gazley, 1958; Bjorklund and Kays, 1959; Simmers and Coney, 1979b) transfer to momentum transfer. A more reasonable approach, as pointed out by Flower and Macleod (1969), is to analyze the vortices not as turbulent flow but as large laminar flow cells. Perhaps the simplest and most effective theoretical description of transport to the rotating surface is derived from Batchelor's scaling arguments (cf. Section 2.4). By the Prandtl analogy, the Sherwood number is expected to vary as:

$$Sh = \frac{b}{\delta_{mt}} \propto \frac{b}{\delta} Sc^{1/3} \tag{2.13}$$

at high rotation rates, where δ_{mt} is the mass transfer boundary layer. Upon substitution of (2.12) into (2.13) we find the result

$$Sh \propto Sc^{1/3} Ta^{1/2}. \tag{2.14}$$

Equation (2.14) can be considered a "consensus correlation" for mass transfer in narrow gaps. The correlation has been obtained experimentally by several independent researchers and also has a theoretical basis. This simple correlation is a powerful tool for the design of vortex flow devices, as it allows the researcher to determine mass transfer to the rotating surface within a multiplicative constant. The constant, although not uniquely determined, has been found to range from 0.1 to 1.2 with a median value of around 0.5. Another striking feature observed from the literature is that mass transfer to the rotating surface is independent of axial flow for axial Reynolds number below 300. An important consequence of the independence of mass transfer on axial Reynolds number is that mass transfer in a vortex flow system can be adjusted separate from the flow rate.

2.5.3 Mass Transfer Between Vortices

Transport of a material within vortices occurs in three directions - radially, circumferentially and axially. Radial and circumferential mixing occur within a single vortex whereas axial mixing occurs between vortices. Researchers have examined all three forms of mixing, with most of the studies focusing either on laminar vortex flow at low Taylor numbers or on turbulent vortex flow at very high Taylor numbers. Since transport of material within the vortices is closely related to vortex structure, many of the studies include visual observations of the vortices.

Many interesting mixing properties are found in laminar Taylor vortices (Figure 2.1) at low rotation rates of the inner cylinder and no axial flow. In this flow regime, sharp boundaries exist between the vortices and little intermixing occurs between individual vortex pairs. Kataoka and coworkers (1975) studied all three components of mixing in Taylor vortices. They found radial mixing in an individual vortex was fast as compared to circumferential mixing or axial mixing. Legrand and coworkers (Legrand and Coeuret, 1984; Guihard *et al.*, 1989) found that the circumferential mixing in Taylor vortices was slight but not negligible. They modeled circumferential mixing as a single vortex consisting of 40 to 60 stirred tanks with complete recirculation. For $Ta = 435$ to 2000, complete mixing was obtained in a vortex within 15 to 20 revolutions or 1 to 3 minutes. The tracer was completely contained within the single vortex, illustrating that circumferential mixing is fast compared to axial mixing. In addition, mixing increased (or the number of stirred tanks decreased) when multi-phase systems were used.

Because the mixing in laminar Taylor vortices tends to be slowest in the axial direction, the flow can be described by the plug flow model (i.e. no back-mixing) under certain conditions. Kataoka *et al.* (1975) found flow in the axial direction resembled ideal plug flow at $Ta_{cr}<Ta<640$ and $0<Re_z<90$ for a vessel geometry of $b/r_i=0.33$. Deviations from ideal plug flow behavior at low rotation rates and axial flow rates have been described by the tanks-in-series model (Kataoka and Takigawa, 1981) and by the axial dispersion model (Pudjiono *et al.*, 1992). The ability of Taylor vortex systems to work at or near plug flow performance is a valuable asset for vortex flow reactors. For normal reactions, where rate decreases with conversion, a maximum overall conversion is obtained under plug flow operation (Carberry, 1976).

The axial dispersion model, which describes axial mixing by a one-dimensional dispersion coefficient, has been used extensively to describe mixing in turbulent Taylor-Couette flow. The one-dimensional model is justified for non-reactive tracers (Tam and Swinney, 1987) and for reactive mixtures (Iosilevskii *et al.*, 1993) due to the spatial periodicity of Taylor-Couette flow. The dispersion experiments are run under conditions where the tracer is well mixed in the radial and circumferential direction. Tam and Swinney (1987) used the equation

$$D^* = ATa^B \tag{2.15}$$

to describe the dispersion coefficient, D^*, in turbulent vortex flow. The constant A was found to be dependent upon the ratio of the gap width to vortex height; different vortex sizes were obtained by varying the rotation rate ramping procedure. Subsequent papers were able to relate dispersion results to torque measurements (Lathrop *et al.*, 1992a, 1992b). Enokida and co-workers (1989) presented correlations for axial dispersion in Taylor-Couette flow at lower rotation rates. Their results, for vortices with no axial flow, can be written in the form of (2.15) and are presented along with Tam and Swinney's results in Table 2.5. An extensive study of axial dispersion in Taylor-Couette flow was performed by Croockewit *et al.* (1955). No correlations were presented, but their complete data set was published. Included in Table 2.5 is a least squares fit of (2.15) calculated for Croockewitt's published data.

Reference	Original Correlation	Rearranged Correlation	$\frac{b}{r_i}$	$\frac{L}{b}$	Ta	Re_z	A	B
Croockewit, *et al.* (1955)	$D^*=A\,Ta^B$	$D^*=A\,Ta^B$	1.23	15.3	1300-4300	100-350	8.2×10^{-3}	0.76
			0.532	24.2	780-26000	63-220	1.1×10^{-2}	0.78
			0.205	49.4	1850-10000	31-110	3.0×10^{-4}	1.05
			0.127	74.5	170-56000	20-70	2.6×10^{-2}	0.81
Tam and Swinney (1987)	$D^*=A\left(\frac{\lambda}{2b}\right)Ta^a$	$D^*=A\left(\frac{\lambda}{2b}\right)Ta^B$	1.024	20	6800-68000	0	2.4×10^{-3}	0.69
			0.585	28	2810-54000	0	1.6×10^{-3}	0.77
	NOTE:		0.370	38	3800-35000	0	2.7×10^{-3}	0.75
	$\lambda/2b = 0.9\text{-}1.6$		0.143	82	2200-12600	0	1.5×10^{-3}	0.85
Enokida, *et al.* (1989)	$D^*=(Re\ \omega^2)^{0.405}$	$D^*=A\,Ta^B$	0.316	22	2800-17000	0	2.2×10^{-4}	0.81
			0.685	16	1450-8700	0	3.6×10^{-4}	0.81

Table 2.5: Correlations for axial dispersion in Taylor-Couette flow without axial flow.

Unlike mass transfer to the cylinder walls, a consensus on mass transfer within vortices has not been achieved yet. Furthermore, most of the studies on dispersion in turbulent vortices presented above, along with many of the studies on mixing in laminar Taylor vortex flow, do not include axial flow. In addition, none of the above studies systematically examine the effect of all operational parameters on mixing in Taylor-Couette flow. These issues are addressed in the dispersion experiments presented in Chapter 5.

Even though dispersion in Taylor-Couette flow is not totally understood, several characteristics of mass transfer between the vortices are accepted. In general, mixing time scales for the three dimensions in Taylor -Couette vortex flow can be expressed as:

$$\begin{matrix}\text{rate of} & & \text{rate of} & & \text{rate of} \\ \text{radial mixing} & > & \text{circumferential mixing} & > & \text{axial mixing}\end{matrix} .$$

At low axial flow rates in the laminar Taylor vortex regime, axial dispersion is almost nonexistent and the flow resembles ideal plug flow. As the flow rate or rotation rate is increased, axial dispersion increases. Although many researchers have examined axial dispersion both in laminar and turbulent Taylor-Couette flow, a common correlation has not emerged. The lack of agreement is not surprising since transport within vortices may be as complicated as the vortex patterns themselves. For example, each mode of wavy vortex flow may have its own transport characteristic in the radial, circumferential and axial directions. The presence of axial flow further complicates matters.

One approach to describing dispersion for the many flow states and possible flow patterns is presented later in this thesis. In this study, data from a wide operating range is incorporated into a single dispersion correlation. This type of correlation is the most useful for preliminary design and performance estimates of vortex flow reactors. An alternative approach was taken by Swinney's group (Tam and Swinney, 1987, Lathrop *et al.* , 1992a, 1992b) who examined mixing on a more microscopic scale by including vortex size in their dispersion correlations for turbulent vortex flow. The authors point out that extending this approach to wavy vortex flow regime would require additional knowledge of vortex wave numbers. The microscopic approach to analyzing mixing within Taylor-Couette flow is much more experimentally difficult than the lumped parameter approach, but it allows for a more fundamental understanding of the physical mechanisms of transport. Future studies will likely continue in this direction, especially examining the complicated flow patterns and mixing behaviors of wavy vortex flow and of combined axial and vortex flow.

2.6. Heat Transfer to Cylinder Walls

Heat removal from concentric rotating cylinders is a common problem in mechanical design. Taylor-Couette systems have been studied extensively to enhance understanding of heat transfer from rotating equipment. A compilation of heat transfer correlations from a rotating inner cylinder is presented in Table 2.6. Whenever possible, the correlations have been rearranged into a form including a Taylor number exponential. In general, these correlations are developed for vortex flow with narrow gap geometry and long cylinders. In several of the correlations, the Nusselt number, Nu, is scaled to the Nusselt number for pure conduction, such as in laminar Couette flow. The theoretical value for Nu_{cond} is 2.0.

Thermal properties of the fluid, as described by the Grashof number and/or the Prandtl number, are incorporated into the correlation in two different manners. Haas and Nissan (1961) and Ho *et al.* (1964) present correlations (equations T6.2 and T6.4, respectively) which incorporate fluid properties into the exponent on the Taylor number. The second type of correlation (i.e. equations T6.6 and T6.7) contains the term $Ta^{0.5}$ along with a Prandtl number exponent.

The latter form of the heat transfer correlations closely resembles the correlations for mass transfer in laminar vortex flow as seen in Table 2.4. Both contain the term $Ta^{0.5}$ and a Prandtl or Schmidt number with an exponent ranges in the range of 0.25 to 0.33. The correlations of Bjorklund and Kays (1959) and Becker and Kaye (1962b) (equations T5.1 and T5.3b, respectively) also have Taylor number exponents near 0.5. The similarity between mass transfer and heat transfer correlations is not unexpected; heat and mass transfer are described by mathematically identical equations and boundary conditions. The similarity between mass and heat transfer is found in both the laminar and turbulent vortex flow regimes. The second correlation from Tachibana and Fukui

Reference - system used	$\frac{b}{r_i}$	$\frac{L}{b}$	Ta	ΔT (°C)	Pr	**Original Correlation**	**Rearranged Correlation**	**Equation Number**
Bjorklund & Kays (1959) - air	0.054-0.25	66-300	0-2000	7	0.7	$\frac{Nu}{Nu_{cond}} = 0.175\ Ta^{1/2}$	$\frac{Nu}{Nu_{cond}} = 0.175\ Ta^{1/2}$	**T6.1**
Haas & Nissan (1961) - air, water	0.11-0.167	17-25	50-4000	10	0.7,6.0	$\frac{Nu}{Nu_{cond}} = 1.0 \left(\frac{P}{P_c}\right)^m$ m=0.7 air; m=0.22 water	$\frac{Nu}{Nu_{cond}} = 1.0 \left(\frac{Ta}{Ta_c}\right)^m$ m=0.7 air; m=0.22 water	**T6.2**
Becker & Kaye (1962b) - air	0.239	172	Ta_m= 41-100	10	0.7	$Nu = 0.128\ Ta_m^{0.734}$	$Nu = 0.128\ Ta_m^{0.734}$	**T6.3a**
			Ta_m= 100-3200	10	0.7	$Nu = 0.409\ Ta_m^{0.482}$	$Nu = 0.409\ Ta_m^{0.482}$	**T6.3b**
Ho *et al.*† (1964) - water, air, mercury, glycerol/water	0.082	53	$1 < \frac{Ta}{Ta_c} < 100$	-	Pr/Gr= 10^{-7}-40	$\frac{Nu}{Nu_{cond}} = \left(\frac{P}{P_c}\right)^m$ $m = \left(\frac{Pr}{Gr}\right)^{1/6}$	$\frac{Nu}{Nu_{cond}} = \left(\frac{Ta}{Ta_c}\right)^m$ $m = \left(\frac{Pr}{Gr}\right)^{1/6}$	**T6.4**
Ball *et al.* (1989) - air	0.524-1.29	31-77	21-460	<20	0.7	$Nu^* = 0.069 \left(\frac{r_i}{r_o}\right)^{-2.9} Re_t^{.46 \ln(3.34\ ri/ro)}$	$Nu_r = 0.069 \left(\frac{r_i}{r_o}\right)^{-2.9} Re_t^{.46 \ln(3.34\ ri/ro)}$	**T6.5**
Aoki *et al.* (1967) - air, spindle oil, isobutyl alcohol, water	0.055-0.13	106-238	70-450	10-53	0.7-200	$Nu^* = 0.22\ Ta_m^{0.5}\ Pr^{0.3}$	$Nu_r = 0.22\ Ta_m^{0.5}\ Pr^{0.3}$	**T6.6**
Tachibana *et al.* (1960) - air, spindle oil mobile oil	0.015-0.92	3.8-477	0.5-45000	20-30		$\frac{Nu}{2} = 0.21\ (Ta^2\ Pr)^{1/4}$	$Nu = 0.42\ Ta^{0.5}\ Pr^{0.25}$	**T6.7**
Tachibana & Fukui (1964) - air (turbulent flow)	0.067-0.33	2.3-11.3	$2x10^4$-$6x10^5$		0.73	$\frac{Nu}{2} = 0.046\ (Ta^2\ Pr)^{1/3}$	$Nu = 0.92\ Ta^{0.66}\ Pr^{0.33}$	**T6.8**

†Correlation includes heat transfer data from other researchers.

Table 2.6 Correlations for heat transfer in Taylor-Couette flow.

(1964) , equation T6.8, occurs in the turbulent vortex flow regime and bears a close resemblance to the Eisenburg correlation (Eisenberg *et al.*, 1954) (T3.1) for mass transfer in turbulent vortex flow.

Relatively few works have dealt with heat transfer from a rotating cylinder with superimposed axial flow; no correlations were found in a thorough literature search. Gardiner and Sabersky (1978) report little effect of axial flow on heat transfer for Reynolds number up to 1000. Data from Becker and Kaye(1962b) reveal that for $Re<1600$, there is a slight decrease in heat transfer with increased axial flow rate. The small dependence of low axial flow on surface transport is consistent with mass transfer findings.

In general, the published heat transfer correlations are consistent with the mass transfer relationships. That is, transport to the rotating surface can be written as:

$$Nu \propto Ta^{0.5} Pr^{0.33} \tag{2.16}$$

in analogy to (2.14) for mass transfer. An imposed axial flow up to $Re_z = 1000$, has little effect on heat transfer to the cylinder walls.

2.7. Conclusions

This review surveys the published literature on transport properties and applications of Taylor-Couette flow. Through a detailed examination of compiled data and observations from many sources, agreement among the published literature becomes evident. With the exception of mass transfer within vortices, all transport properties can be described by dimensionless correlations which have been validated by independent researchers. A summary of the relationships for the transport properties of frictional factors, mass transfer to the cylinder walls, and heat transfer are presented below.

1.) Frictional Factors - Shear stress in Taylor-Couette flow at moderate to high rotation rates is described by $\tau \propto Ta^m$ with $m = 1.5$. The exponent m is less than 1.5 for lower rotation rates where laminar vortex flow is present, and slightly higher than 1.5 at very high rotation rates where turbulent non-vortex flow exists. The properties of torque, friction factor and shear rate can be related to the expressions for shear stress by geometric factors.

2.) Mass Transfer - Mass transport to the cylinder walls can be expressed by $Sh = A\ Re_r^{\alpha} Sc^{\beta}$ for turbulent flow in vessels with wide gap ratios. The exponents $\alpha = 0.7$ and $\beta = 0.33$ are the most commonly accepted values, although some experimenters found slightly higher or lower values. For mass transfer in narrow gaps, $Sh = A\ Ta^{\alpha}\ Sc^{\beta}$ with $\alpha = 0.5$, $\beta = 0.33$ and $A \approx 0.5$. In most cases, mass transfer to the cylinder walls is independent of axial flow rate.

3.) Heat Transfer - Heat transport from the cylinder walls can be expressed in two different types of correlations (cf. Table 2.5), one of which is $Nu \propto Ta^{0.5}\ Pr^{0.33}$ in analogy to the mass transport correlation.

The consensus correlations presented above aid in the development of the vortex flow reactor. Correlations on friction factors and heat transfer are used to estimate the power consumption and cooling capacity needed in VFR design. The mass transfer correlation is used in this work for the mathematical modeling of reaction or adsorption on the cylinder walls. The literature review further reveals areas which require additional study. For example, while mass transfer between vortices (i.e. dispersion) has been previously studied, no systematic study of all process variables had been undertaken. Additionally, the thorough literature search revealed little information on mass transfer to particles suspended within the annulus. Therefore, the problems of dispersion and mass transfer to suspended particles were examined experimentally; the results are presented in Chapter 5.

A single communality exists in the development of the above consensus correlations. In these studies, experimenters examined a specific property over a range of operational and design parameters and fit the data with dimensionless equations. In most cases a single equation was developed, usually with disregard for the vortex structure. In some cases, multiple equations were obtained representing different operational regimes corresponding to the Taylor-Couette flow structure. However, full agreement between theory and experiment has not yet been achieved. The problem lies in the complexity of Taylor-Couette flow at higher rotation rates, where non-laminar vortices exist. The non-unique flow patterns of wavy vortex flow and the structure of combined vortex and axial flow are very difficult to describe mathematically. Considering the complicated hydrodynamics of higher order Taylor-Couette flows it is somewhat remarkable that common correlations, such as those presented above, can be developed. A great challenge remains in determining the effect of the different forms of Taylor-Couette flow on transport properties.

Chapter 3 -

Mathematical Model of the Vortex Flow Reactor

3.1 Formulation of Model Equations

Transport and reaction in the vortex flow reactor is governed by (Bird *et al.*, 1960)

$$\frac{\partial C(\boldsymbol{r},t)}{\partial t}+v(\boldsymbol{r})\cdot\nabla C(\boldsymbol{r},t)-D\nabla^2 C(\boldsymbol{r},t)=R(\boldsymbol{r},C) \tag{3.1}$$

for an incompressible fluid with concentration $C(\boldsymbol{r},t)$, fluid velocity $v(\boldsymbol{r})$, molecular diffusion coefficient D and reaction or adsorption rate $R(\boldsymbol{r},C)$. The transport equation (3.1) is highly complex; it contains three spatial dimensions $\boldsymbol{r} = (r,\theta, z)$ and variable coefficients. In addition, the velocity coefficient, $v(\boldsymbol{r},t)$ is a function of the complicated Taylor-Couette flow profile (cf. Section 2.2 and 2.3). As a consequence of its complexity, solving (3.1) would be a monumental task in numerical analysis. Fortunately, under certain conditions, equation (3.1) can be simplified to a more tractable form.

The method for simplifying a complex transport equation is described by Macrotransport Theory as developed by Brenner (1980a, 1980b), following earlier developments of G. I. Taylor (1953), Aris (1956) and Horn (1971). In general, the theory describes how an n-dimensional microtransport equation, such as (3.1), can be reduced into a one-dimensional macrotransport equation with constant coefficients. For the vortex flow reactor, this translates into transforming the three dimensional equation (3.1) into an equation with just one spatial dimension - the axial direction, z.

There are three main limitations in applying the Macrotransport Theory to (3.1):

(1) The reaction rate or adsorption isotherm must be linear for all reactants and products such that $R(r,C_i) = k_i(r)\, C_i$ for all components C_i.

(2) The velocity coefficient $v(r)$ and the reaction rate coefficient, $k_i(r)$ must either not vary with the macrotransport parameter z or vary with z in a periodic manner.

(3) The "long term limit" must be satisfied, requiring a long enough residence time such that all molecules have the opportunity to sample the entire vessel cross-section (r and θ directions), traveling either by diffusion or convection.

These three limitations can be satisfied in the VFR experiments. The model validation experiments and the heparinase simulations are conducted in the first order limit where the substrate concentration is much less than the Michaelis constant, K_m. Both the velocity profile and the enzyme distribution (and thus reaction rate) are spatially periodic in the axial direction, satisfying the second condition. Finally, the long term limit in the VFR is determined experimentally during residence time distribution experiments as described in Section 5.1.1.

For a first order reaction of $R(r,C) = k(r)\, C$, the corresponding one-dimensional transport equation of (3.1) is

$$\frac{\partial \overline{C}(z,t)}{\partial t} + U^{*} \frac{\partial \overline{C}(z,t)}{\partial z} - D^{*} \frac{\partial^{2} \overline{C}(z,t)}{\partial z^{2}} = K^{*} \overline{C} \tag{3.2}$$

where $\overline{C}(z,t)$ is the vortex-averaged concentration of tracer at axial position z, U^{*} is the mean solute velocity, K^{*} is the macrotransport volumetric reaction coefficient, and D^{*} is the effective diffusivity or dispersion coefficient. The macrotransport parameters U^{*}, D^{*} and K^{*} in (3.2) have been mathematically related to physical parameters in spatially periodic systems such as Taylor-Couette flow for cases: (i) without reaction (Brenner, 1980b); (ii) with reaction on the walls (Shapiro and Brenner, 1988); and (iii) with reaction on particles suspended in the annulus (Iosilevskii *et al.*, 1993).

Through these analyses, certain generalizations can be made regarding the macrotransport parameters. For example, the mean velocity U^{*} is simply the average fluid velocity, U, in a non-reactive system with a Brownian tracer (i.e. a molecule having negligible size compared to vessel cross-sectional dimensions). For a homogeneous reaction (Shapiro and Brenner, 1986), the species velocity U^{*} is equal to the mean velocity of the inert carrier fluid U, the reaction coefficient is constant and is equivalent to the microtransport reaction parameter (i.e. $K^{*} = k_{1} = constant$), and the dispersion coefficient is equal to the non-reactive dispersion coefficient, D^{*}_{nr}. Consequently, for homogeneous reactions, the macrotransport parameters can be determined experimentally as: the average velocity U, the microtransport reaction rate k_{1}, and the non-reactive dispersion coefficient D^{*}_{nr}. However, for non-homogeneous reactions such as the solid-liquid VFR, the phenomenological coefficients U^{*}, K^{*} and D^{*} can greatly vary from the known parameters of U , k_{1} and D^{*}_{nr}.

Although solutions exist for obtaining the unknown coefficients U^*, D^* and K^* in (3.2), solving the equations for the macrotransport parameters still involves complicated numerical calculations requiring detailed knowledge of the vortex velocity profile. An analytical solution for the macrotransport parameters is feasible for Taylor vortex flow just above the critical rotation rate where the flow pattern is relatively well defined. However, in order to provide good mass transfer to the active surface, the VFR typically operates at higher RPM where wavy vortex or turbulent vortex flow is present. The vortices retain their spatial periodicity and the macrotransport approach is still valid, but an analytical solution becomes taxing. A simpler approach is to determine the macrotransport coefficients from independent experiments. The coefficient D^*_{nr} can be determined for a non-reactive VFR through residence time distribution experiments as discussed in Sections 4.1 and 5.1. The microtransport coefficient k_1 can be determined as outlined in Sections 3.3 and 4.4. However, as discussed above, the parameters D^*_{nr} and k_1 are not necessarily the same as D^* and K^* observed in the reactive case. Fortunately, in the limit of slow reaction as compared to diffusion to the active site (Shapiro and Brenner, 1988), D^* is the same as that without reaction, U^* is the same as the average fluid velocity U, and K^* is the same as the average volumetric reaction rate such that

$$K^* = k_1 = \frac{1}{V}\int_V k(r)d^3r \quad . \tag{3.3}$$

The limit of slow reaction compared to diffusion occurs when internal mass transfer resistances can be neglected, as described by a small Damkohler number ($Da \ll 1$). The Damkohler number in the VFR is defined as

$$Da = \frac{overall\ reaction\ rate}{axial\ dispersion\ rate} = \frac{k'_{ex} l^2}{D_{eff}} \tag{3.4a}$$

where l is the characteristic length of the solid support (i.e. membrane thickness or particle radius) and D_{eff} is the effective diffusivity defined by

$$D_{eff} = \frac{D\varepsilon}{\tau} \tag{3.4b}$$

for a solid with a porosity of ε and a tortuosity of τ. The constant k'_{ex} is a lumped reaction rate constant including the intrinsic kinetic rate k' and the external mass transfer coefficient k_{mt} as given by

$$k'_{ex} = \frac{k'k_{mt}}{k'V_s / A_s + k_{mt}} \quad . \tag{3.4c}$$

The Damkohler number defined in (3.4a) compares the rate of diffusion in the solid support to the slower of the reaction rate and external mass transfer rate. In the limit of low Damkohler number, the solid-liquid reaction appears to occur uniformly across the reactor cross-section. Consequently, as in the case of homogenous reactions, the parameters D^* and U^* are the same as the non-reactive parameter D^*_{nr} and U, respectively. The immobilized enzyme experiments in the VFR, presented in Chapters 7 and 8, occur under the conditions of low Damkohler number. Therefore, the average velocity U, the experimentally determined value of D^*_{nr} from the non-reactive tracer studies, and the value of K^* from the kinetic studies were used in solving equation (3.2). In contrast, the protein adsorption studies presented in Chapter 8 occur in the internally mass transfer limited region. The deviation of the dispersion coefficient D^* from the non-reactive dispersion coefficient D^*_{nr} is evident in these experimental results.

3.2 Solutions of the Model Equation

The convection-dispersion-reaction equation (3.2) is commonly encountered in chemical engineering; solutions exist in the published literature for a variety of boundary and initial conditions. The first two solutions of interest are for a non-reactive tracer ($K^* = 0$) introduced into the reactor as a perfect pulse (delta function) or as a step change. The closed boundary conditions,

$$-D^* \frac{\partial \bar{C}(0,t)}{\partial z} + U\bar{C}(0,t) = 0 \tag{3.5a}$$

and

$$-D^* \frac{\partial \bar{C}(L,t)}{\partial z} = 0 \ , \tag{3.5b}$$

are used (Levenspiel, 1972) which assume there is no back flow across the inlet and outlet ports or in the short sections of tubing before or after the vessel. The boundary conditions are representative of the experimental set-up (cf. Section 4.1). For an instantaneous pulse of tracer, $\bar{C}(z,0) = \delta(z)C_{in}$, the concentration profile at the vessel outlet is given by (Yagi and Miyauchi, 1953),

$$\frac{\bar{C}(L,t)}{C_{in}} = \sum_{i=1}^{\infty} A_i \exp(-\alpha_i \bar{t}) \tag{3.6}$$

where

$$\cot \lambda_i = (\lambda_i / Pe - Pe / 4\lambda_i) \ , \tag{3.7a}$$

$$A_i = \frac{\lambda_i (Pe \sin \lambda_i + 2\lambda_i \cos \lambda_i)}{\left(\frac{Pe}{2}\right)^2 + Pe + \lambda_i^2} \exp\left(\frac{Pe}{2}\right) \ , \tag{3.7b}$$

$$\alpha_i = \frac{Pe}{4} + \frac{\lambda_i^2}{Pe} \ , \tag{3.7c}$$

$Pe=UL/D^*$ is the Peclet number, and $\bar{t}$ is the time normalized by the residence time (i.e. nominal holdup time). The concentration profile (3.6) is used in reconstruction of residence time distribution curves in Section 5.1. The second solution for $K^* = 0$ is for a step change input, where $\bar{C}(z,t)=0$ for $t< 0$ and $\bar{C}(0,t) = C_{in}$ for $t>0$. The step change solution,

$$\frac{\overline{C}(L,t)}{C_{in}} = \sum_{i=1}^{\infty} \frac{A_i}{\alpha_i}\left(1 - e^{-\alpha_i \bar{t}}\right) \tag{3.8}$$

uses boundary conditions (3.5) and the definitions of λ_i, A_i and α_i in (3.7).

The step change solution for a first order reaction ($K^* \neq 0$) can be obtained by transforming the nonreactive solution (3.8) by Dankwerts' method (Crank, 1975). The same boundary conditions (3.5) are used. Dankwerts' method states that if a solution, $\overline{C}$, for the non-reactive case is known, then the solution for a first order reaction is given by:

$$\tilde{C} = K^* \int_0^t \overline{C} e^{-K^* t'}\, dt' + \overline{C} e^{-K^* t} \ . \tag{3.9}$$

The above equation can be shown to be valid by substituting (3.9) into the original equation (3.2) and the boundary conditions (3.5). The substrate concentration is obtained by solving (3.9) using the non-reactive solution (3.8) to obtain

$$\frac{\overline{C}(L,t)}{C_{in}} = \sum_{i=1}^{\infty} \frac{A_i}{\alpha_i + K^*}\left(1 - e^{-(\alpha_i + K^*)\bar{t}}\right) \ . \tag{3.10}$$

The product concentration, $\overline{C}_p$, is obtained from the difference between the non-reactive concentration profile (3.8) and the reactant concentration profile (3.10) as

$$\frac{\overline{C}_p(L,t)}{C_{in}} = \sum_{i=1}^{\infty} \frac{A_i}{\alpha_i(\alpha_i + K^*)}\left[k\left(1 - e^{-\alpha_i \bar{t}}\right) - \alpha_i e^{-\alpha_i \bar{t}}\left(1 - e^{-K^* \bar{t}}\right)\right] \ . \tag{3.11}$$

The substrate steady-state solution at the reactor outlet is obtained by solving (3.2) with $d\overline{C}/dt = 0$ and with boundary conditions (3.5). For an inlet concentration of C_{in}, the steady state solution is given by (Dankwerts, 1952)

$$\frac{\overline{C}}{C_{in}} = \frac{4a}{(1 + a^2)\exp\left[-\frac{Pe}{2}(1 - a)\right] - (1 - a^2)\exp\left[-\frac{Pe}{2}(1 + a)\right]} \tag{3.12}$$

where $a=\sqrt{1+4K^{*}D^{*}/U^{*2}}$. Although not intuitively obvious, (3.12) is equivalent to (3.10) in the limit of $\bar{t}\rightarrow\infty$. In the limits of Pe=0 and ∞, (3.12) reduces to the equations for a stirred tank reactor and a plug flow reactor, respectively.

The solutions to the VFR model equations presented in this section assume a first order irreversible reaction rate. The same conditions are used in the experimental studies and in the simulations of the VFR presented in the following chapters. Other cases such as parallel first order reactions of multiple species also can be solved using a similar approach. An important point to note is that the simplification of (3.1) to (3.2) is valid for any set of first order equations. Biological systems, however, frequently exhibit non-linear kinetics; such cases include: Michaelis-Menton enzymatic reaction, Langmuir-Hinshelwood type adsorption, and enzymatic reaction with product or substrate inhibition. Often non-linear kinetics may be simplified to first-order under a limiting condition such as low substrate or product concentration. In cases where linearization of the reaction kinetics is not feasible, the macrotransport model may be extrapolated to the non-linear kinetics under the constraint of low Damkohler number. If the reaction rate is slow compared to the internal diffusion rate (Da << 1), the reactor concentration appears to be uniform across the reactor cross section. For first order reactions, macrotransport theory rigorously shows that the dispersion behavior does not vary from the non-reactive dispersion behavior and the overall kinetic rate is simply the average kinetic rate over the cross sectional area. In other words, the dispersion is independent of the reaction rate and the overall reaction rate is unaffected by the dispersion for low reaction rate. Similar independence between dispersion and reaction rate is expected for non-linear kinetics at low Damkohler number. Therefore, in the limit of low Damkohler number, the non-reactive dispersion coefficient and the overall reaction rate may be used in solving the one-dimensional macrotransport equation for non-linear kinetics. Numerical methods would be required to solve the equation as the solution for the non-linear kinetics cannot be written in a simple closed form expression like that presented above for the linear case.

3.3 Evaluation of Model Parameters

The previous sections show the formulation and the solutions of the constitutive equation for transport in the VFR. In order to utilize these equations, the unknown coefficients, U^*, D^* and K^* need to be determined. The model validation experiments with immobilized alkaline phosphatase operate in the limit of slow reaction rate compared to internal diffusion (i.e. internal mass transfer resistances are negligible). Therefore, the velocity parameter U^* is simply the average velocity, and the dispersion coefficient D^* is the same as in the non-reactive coefficient; both of these parameters can be determined experimentally. The third coefficient K^* is more complex as it contains both the effects of kinetics and mass transfer resistances. The relationship between the three coefficients and the VFR model is illustrated in Figure 3.1.

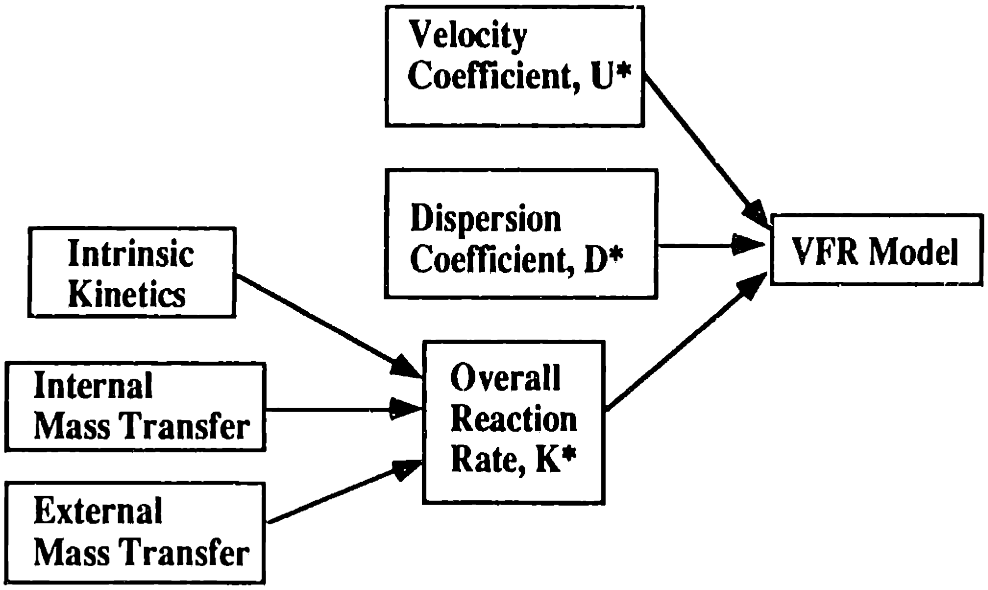

Figure 3.1: Inputs into VFR mathematical model.

As shown in Figure 3.1, the coefficient K^* is a function of intrinsic kinetics, internal mass transfer resistances, and external mass transfer resistances. The intrinsic kinetic rate is the local reaction rate at the active site. This section considers immobilized enzymatic reactions as described by Michaelis-Menton kinetics (Bailey and Ollis, 1986),

$$rate = \frac{V_{max} C'}{K_m + C'} \quad . \tag{3.13}$$

where C' is the local (internal) substrate concentration and K_m is the Michaelis constant. V_{max} is the maximum volumetric kinetic rate and is equal to

$$V_{max} = ES \tag{3.14}$$

where E is the immobilized enzyme activity (Units enzyme/cm^3 support) and S is the specific activity (μmol substrate/time/Unit enzyme). When the substrate concentration is low, such that $C' << K_m$, the reaction rate may be described as first order with

$$rate = \frac{V_{max}}{K_m} C' = k'C' \tag{3.15}$$

where k' is the first order volumetric reaction rate. The first order limit is used both in the model validation experiments and in the simulations of a VFR containing immobilized heparinase. Prior to solving the model equations as described in Section 3.2, it is necessary to relate the intrinsic rate constant k' to the macrotransport rate constant K^* by examining mass transfer limitations in solid-liquid reactions.

Two types of mass transfer (internal and external) occur in solid-liquid reactions as illustrated in Figure 3.2. The external mass transfer describes transport from the bulk solution with concentration $\overline{C}$ to the active surface (either the cylinder walls or suspended particles) at concentration C_s whereas internal mass transfer describes diffusion into the

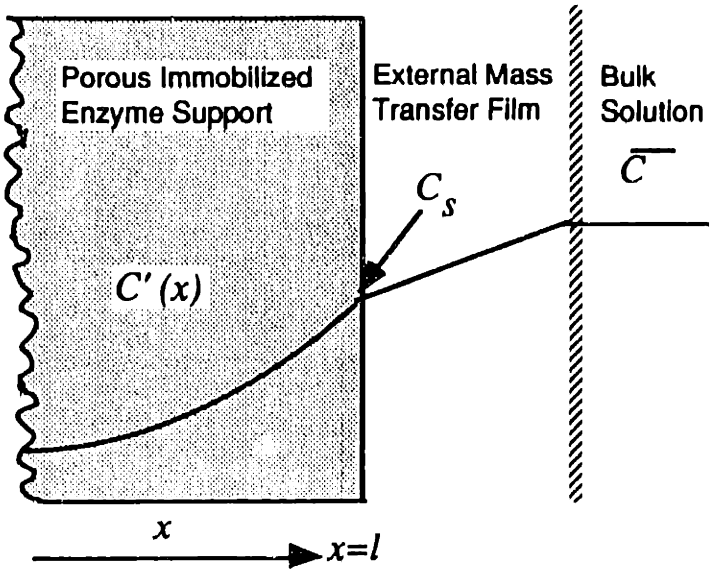

Figure 3.2 - Diagram of mass transfer resistances and kinetics in a porous immobilized enzyme support.

pores of the solid support. Two cases are considered for the VFR - flat plate and spherical geometry, representing the wall reactor and the particle reactor, respectively. The mathematical treatment is identical except for the choice of coordinate systems. The approach follows the standard chemical engineering analysis for mass transfer and reaction in a porous catalyst (Carberry, 1976).

External mass transfer is modeled as a thin stagnant layer at the active surface where transport occurs by diffusion alone. The flux at the surface, N_S, is described using the mass transfer coefficient, k_{mt},

$$N_s = k_{mt}(\bar{C} - C_s) \quad . \tag{3.16}$$

The internal mass transfer resistance represents diffusion in the pores of the support and is described, for a first order reaction, by

$$\frac{\partial C'}{\partial t} = D_{eff}\nabla^2 C' - k'C' \tag{3.17}$$

where C' is the concentration of substrate in the pores of the support, k' is the intrinsic reaction rate, and D_{eff} is given by (3.4b).

The following derivation assumes that the concentration inside the solid support, C', is in equilibrium with the surface concentration. This assumption is valid: 1) during steady state operation or 2) when internal mass transfer resistances are negligible, such that the time for transport into the solid is less than either the time for reaction in the pores or transport through the external mass transfer film. Using the equilibrium condition, ($\partial C'/\partial t=0$), equation (3.17) can be solved with the boundary conditions:

$$\text{at } x=0 \qquad \nabla C'=0 \tag{3.18a}$$

$$\text{at } x=l \qquad -D_{eff}\nabla C'=k_{mi}(\overline{C}-C') \tag{3.18b}$$

For flat plate geometry, such as that present at the wall VFR, the parameter l in (3.18b) equals the wall thickness, w. For spherical geometry, like the particle VFR, l is the particle radius, $d_p/2$. The boundary condition (3.18b) represents matching flux at the outer surface whereas (3.18a) represents no flux at the inner wall for the flat plate geometry and symmetry for the case of spherical geometry. In either the wall reactor or the particle reactor, the equations describing reaction rate are independent of axial position, z.

The solution to (3.17) using (3.18) with flat plate geometry is

$$C'=\frac{Bi\overline{C}\cosh(\phi x/w)}{\phi\sinh\phi+Bi\cosh\phi} \tag{3.19}$$

where $Bi=k_{mi}w/D_{eff}$ is the Biot number and $\phi=w\sqrt{k'/D_{eff}}$ is the Thiele modulus. Note that for negligable external mass transfer resistances $Da=\phi^2$. The intrinsic reaction rate is related to the overall reaction parameter K^* by

$$\textit{reaction rate}=K^*\overline{C}=\eta k'\frac{V_s}{V_l}\overline{C} \quad . \tag{3.20}$$

where η is the effectiveness factor. The effectiveness factor describes the ratio of the observed reaction rate to the reaction rate with no mass transfer resistances,

$$\eta = \frac{\frac{1}{w}\int_0^l k'C'dx}{k'\overline{C}} = \frac{1}{w\overline{C}}\int_0^l C'dx \ . \tag{3.21}$$

Upon substituting (3.19) into (3.21) and integrating,

$$\eta = \frac{\tanh\phi}{\phi\left[1+\phi\tanh\phi/Bi\right]} \tag{3.22}$$

is obtained for flat plate geometry. By rearranging (3.22) and by substituting in the definitions for ϕ and Bi, a more revealing form of the equation,

$$\frac{1}{\eta} = \frac{\phi}{\tanh\phi} + \frac{wk'}{k_{ml}} \ , \tag{3.23}$$

illustrates the overall effectiveness factor as a sum of resistances from internal mass transfer (first term) and external mass transfer (second term). If wk'/k_{ml}<<1 the influence of external film resistance is negligible. If the reaction rate is slow compared to diffusion, such that ϕ<<1, then $\phi/\tanh\phi$=1, and internal mass transfer resistances are negligible. The overall reaction rate is obtained from (3.20) and (3.22) as

$$K^* = \frac{\tanh\phi}{\phi\left[1+\phi\tanh\phi/Bi\right]}\left(\frac{V_s}{V_l}\right)k' \tag{3.24}$$

A similar approach may be taken for spherical geometry to obtain an overall effectiveness factor expressed as

$$\frac{1}{\eta} = \frac{\phi^2\tanh\phi}{3(\phi-\tanh\phi)} + \frac{\phi^2}{3Bi} \tag{3.25}$$

where $\phi = \frac{d_p}{2}\sqrt{k'/D_{eff}}$ and $Bi = k_{ml}d_p/2D_{eff}$.

Often, it is difficult to isolate the effects of internal and external mass transfer resistances. External mass transfer resistances can be altered by changing the operational parameters such as stirring rate or fluid velocity. The internal mass transfer, however, is a function of the support geometry and is often difficult to elucidate. It is therefore instructive to define an effectiveness factor incorporating the effects of internal mass transfer resistances as

$$\eta_{int} = \frac{\tanh\phi}{\phi} \qquad \text{for flat plate geometry} \tag{3.26a}$$

and

$$\eta_{int} = \frac{3}{\phi}\left(\frac{1}{\tanh\phi} - \frac{1}{\phi}\right) \qquad \text{for spherical geometry.} \tag{3.26b}$$

The overall kinetic rate may be written as

$$K^{*} = \left(\frac{V_s}{V_l}\right)\frac{k_{mt}k_{int}}{k_{mt} + k_{int}V_s / A_s} \tag{3.27}$$

for either geometry where $k_{int} = k'\eta_{int}$ is an observed first order rate constant incorporating the effects of internal mass transfer limitations. If internal mass transfer resistances are negligible, $k_{int} = k'$. Equation (3.27) is found to be useful in both the immobilized enzyme studies and model validation experiments. In these experiments the support geometry is kept constant such that k_{int} is constant and the mass transfer coefficient is changed by varying the operational parameters.

The above equations for the effectiveness factor and the overall kinetic rate assume that the concentration gradient within the solid support does not change over time. The equilibrium assumption used in deriving the equations is useful in diagnosing internal mass transfer limitations. If internal mass transfer limits are negligible, the effectiveness factor and the Damkohler number are small and $\eta_{int} \cong 1$. Furthermore, the non-reactive values for the dispersion and the velocity may be used in solving the model equations, as discussed in Section 3.1. However, if internal mass transfer is rate limiting, the dispersion and velocity will not display their corresponding non-reactive behavior during transient operation. Upon a change in bulk fluid concentration, the substrate molecules will take a longer time to reach the reaction site and to react than predicted by the model. Therefore, the mean solute velocity will decrease and the apparent solute dispersion will increase. However, when an internally mass transfer limited reactor is in steady state operation, the concentration gradient across the solid support does not change with time. The reaction appears to be first-order as described by (3.20) and the dispersion and velocity parameters are expected to be the same as those in the non-reactive case.

Chapter 4 -

Materials And Methods

4.1. Reactor Design

The vortex flow reactor design is based on the Membrex Benchmark® filtration system, pictured in Figure 4.1. The VFR utilizes two concentric cylinders forming an annulus . The outer polysulfone cylinder is stationary and the inner polypropylene cylinder is rotated with a variable speed motor. Rotation rates from 0 to 2000 RPM are obtained with a Membrex motor connected to a separate controller (Electro-Craft E652-M). The motor and controller of the commercial Membrex filtration unit are used to achieve rotation rates between 2000 and 4000 RPM. The cylinder rotation rate, determined with a tachometer, varied less than 1% over the course of an experiment. For low rotation rates (< 100 RPM), the tachometer reading was validated against visual observations. For higher rotation rates, the tachometer was validated by comparison to the gauge on the Membrex unit. Temperature in the VFR is monitored by a screw-type thermistor probe (Cole-Parmer) mounted flush with the inside of the outer cylinder wall. The section of the probe external to the VFR was insulated with silicone rubber to eliminate the effect of the

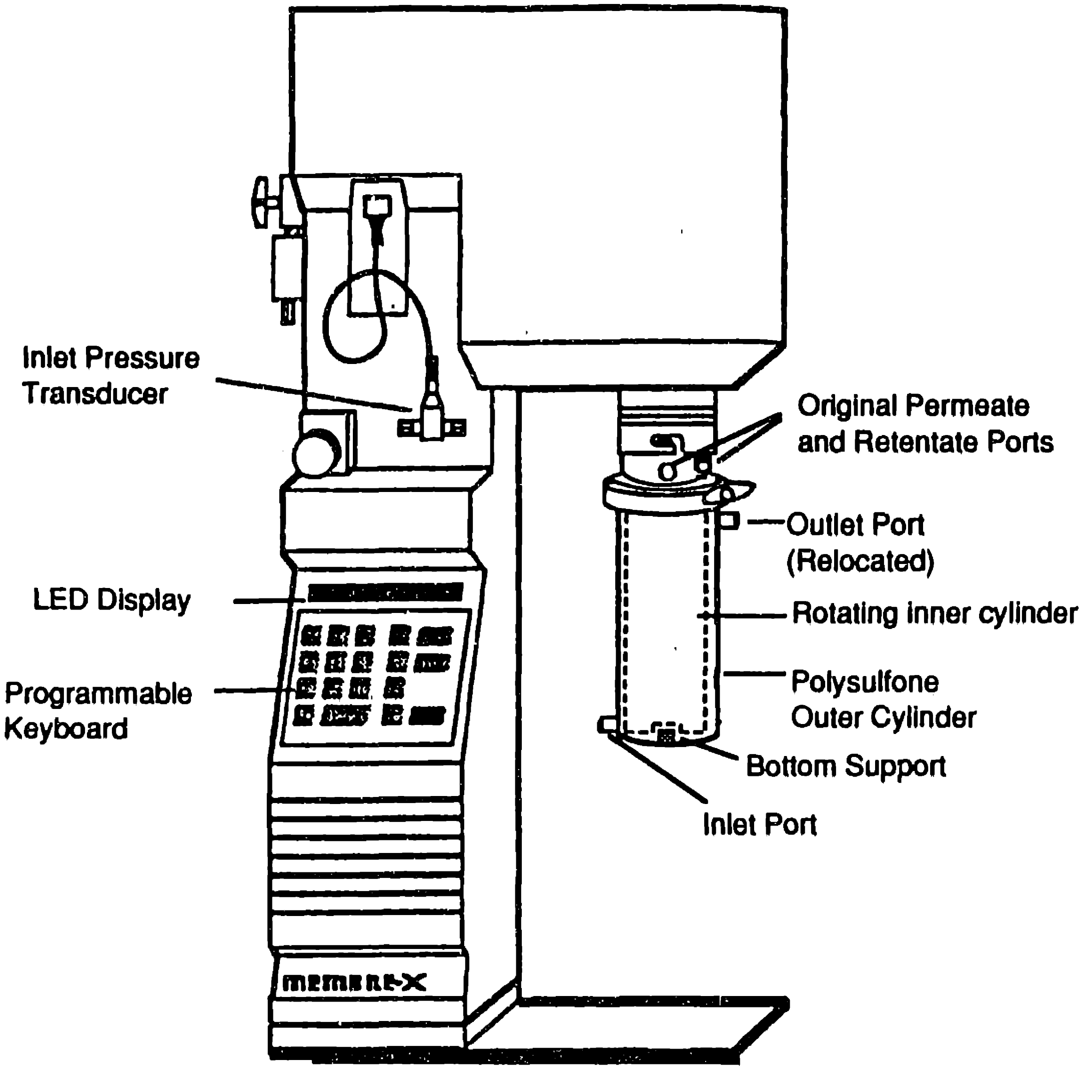

Figure 4.1 - Vortex flow reactor from modified Membrex® filtration unit.

ambient air or water bath temperature on the thermistor reading. The probe temperature reading corresponds to the temperature reading from a mercury thermometer within 0.1° C.

Outer cylinders of varied diameters were obtained by machining the commercially available Membrex cylinders. To decrease dead zones, the outlet (retentate) port was repositioned from the head cap to the outer cylinder wall, opposite the inlet. Because the commercially available cylinders had a large amount of cylinder wobble, the outer cylinders

Inner Cylinder Diameter

Outer Cylinder	4.45 cm			4.21 cm			3.81 cm			4.69 cm		
	$\frac{b}{r_i}$	$\frac{L}{b}$	critical Re_θ	$\frac{b}{r_i}$	$\frac{L}{b}$	critical Re_θ	$\frac{b}{r_i}$	$\frac{L}{b}$	critical Re_θ	$\frac{b}{r_i}$	$\frac{L}{b}$	critical Re_θ
4.90 cm	0.101	75	137	0.164	49	112	0.286	31	90.9	0.045	161	199
5.19 cm	0.166	46	111	0.233	35	97.5	0.362	25	84.6			
5.76 cm	0.294	26	90	0.368	22	84.3						

Table 4.1 Dimensions of inner and outer cylinders.

were modified by removing the raised platform and inserting a metal pin at the bottom of the cylinder. The pin contacts the rotating inner cylinder by a graphite bearing. Inner cylinders of varied diameters were machined from polypropylene. The dimensions of the available 17 cm long cylinders are shown in Table 4.1. Table 1 also includes critical rotational Reynolds numbers for the cylinders; these numbers are calculated using the stability criteria for Taylor-Couette flow with no axial flow (Taylor, 1923). These cylinders provided gap ratios ranging from 0.045 to 0.51 and aspect ratios from 17.4 to 370. An additional set of longer cylinders with length of 25.2 cm, inner cylinder diameter of 5.35 cm and an outer cylinder diameter 6.23 cm was also made, providing an gap ratio of 0.16 and an aspect ratio of 57.

The inner and outer cylinders described above were used for the residence time distribution (RTD) experiments and for the reactive membrane experiments but were found to be unacceptable for the particle VFR experiments. It was discovered that any narrow clearance between the cylinders caused extensive breakage of the particles even at low rotation rates. Both the cylinders with the metal pin and graphite bearing (used in the RTD studies and membrane experiments) and the cylinders with the platform support (used in the commercial filtration unit) were judged unacceptable for operation with the suspended particles. Outer cylinders of clear acrylic and of polysulfone were machined to create a flat bottom (i.e. no bottom support). The inner cylinders used in the previous RTD and membrane experiments (inner diameters of 3.81, 4.21 and 4.45 cm) were modified to have a flat bottom by sealing the graphite bearing with silicone rubber. The gap on the bottom between the cylinders was approximately 2mm. The particles were retained in the reactor by a 40 μm woven nylon mesh (Tetko) on the reactor outlet; the effective surface area of the mesh was 2 cm^2.

4.2 Residence Time Distribution Experiments

Axial dispersion is determined from residence time distribution studies. The experimental setup is shown in Figure 4.2. Most of the experiments used the inner and outer cylinders shown in Table 4.1. The end effect experiments used the longer set of cylinders (length of 25.2 cm); the experiments with particles used the cylinders with no bottom support. The working fluid in all experiments was deionized water or water and glycerol. Fluid enters through a port at the base of the annulus and exits from the top port, opposite the inlet. The flow rate was varied to provide axial Reynolds numbers between 0.5 and 30. All experiments were performed at room temperature (298 ± 3 K); at high rotation rates a water bath was used to maintain temperature. At the initiation of each run, a tracer of either 5×10^{-5} M blue dextran (Sigma D5751; 2,000,000 MW) or 0.14 M sodium benzoate was injected into the annulus via a 4-way chromatography valve. The particle RTD experiments used STREAMLINE SP (sulphopropyl) silica/agarose particles, with the blue dextran tracer. The particles were restrained in the reactor with a nylon mesh at the VFR outlet.

All tubing, including the sample loop, had an inner diameter of 1.5 mm. Both the injection sample and hold-up volume (tubing volume before and after annulus) were held to a minimum, less than 1% of the annulus volume. The outlet concentration of the tracer was measured with a flow-through UV spectrophotometer (Pharmacia) at a wavelength of 280 nm. Data from the spectrophotometer was monitored by a strip chart recorder and was collected on a computer for further analysis. Flow rates were determined by timing the change in mass on an electronic balance with a stopwatch.

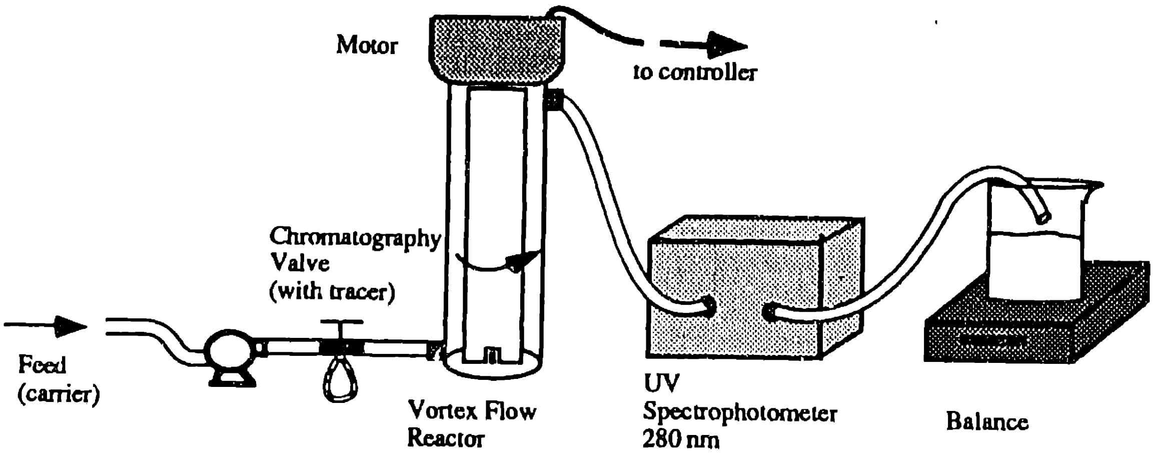

Figure 4.2: Experimental setup for residence time distribution studies.

4.3 Mass Transfer to Suspended Particles

Water-benzoic acid was chosen as the model system to study mass transfer to suspended particles. Benzoic acid is a convenient system because it is a solid at room temperature, sparsely soluble in water, non-hazardous and easily detected by a UV spectrophotometer. Since small uniform particles of benzoic acid are not commercially available, small particles were made by melting, solidifying and grinding benzoic acid in a laboratory mill (Thomas-Wiley Laboratory Mill Model 4). The particles were selected by sieving with 350 μm and 100 μm screens followed by fluidization with a saturated benzoic acid solution in a 1 cm diameter column. The effective particle diameter ($d_p = 6V_S/A_S$) was obtained from the pressure drop across a packed bed. In the experiments, saturated benzoic acid ran through a packed bed of benzoic acid particles and a water manometer was used to gauge the pressure. The pressure drop was measured within 0.1 cm of water (9.8 Pa); the bed length was measured within 0.1 cm. The void fraction, ε, was determined from the dry particle mass and packed volume. The effective particle diameter, was determined to be 135 μm by applying the Ergun equation (Bird *et al.*, 1960),

$$\frac{\Delta P}{\rho v_o^2}\frac{d_p}{L}\frac{\varepsilon^3}{1-\varepsilon} = 150\frac{\mu(1-\varepsilon)}{\rho d_p v_o} + 1.75 \tag{4.1}$$

where ΔP is the pressure drop across the bead, L is the length of the packed bed, v_o is the fluid velocity. An example of results from a pressure drop experiment is shown in Figure 4.3.

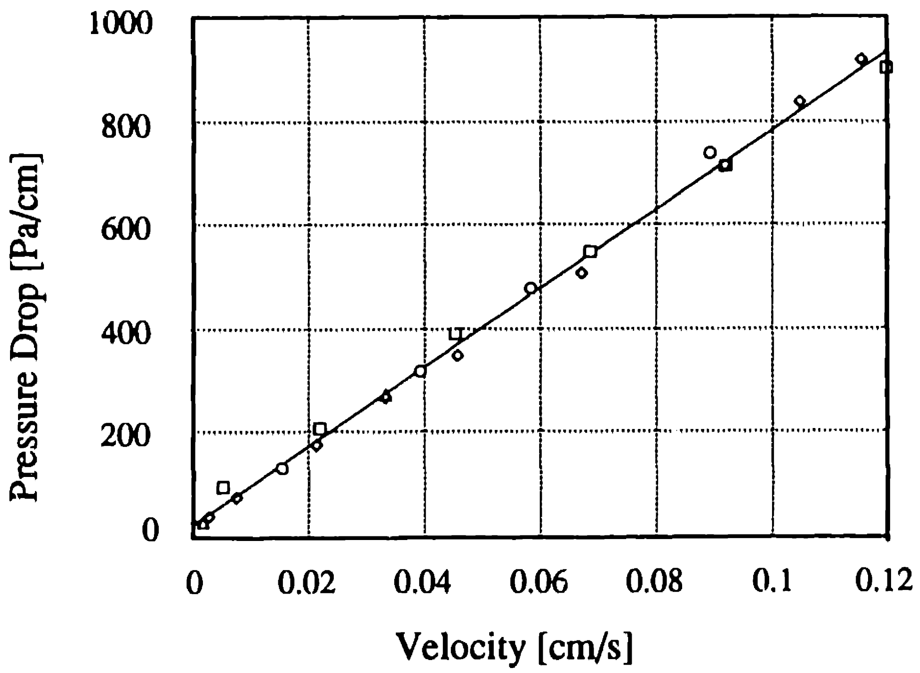

Figure 4.3 - Pressure drop across packed bed of benzoic acid particles.

All mass transfer experiments were performed in 0.01 vol% Triton X-100. The surfactant was necessary to prevent agglomeration of the small particles. Experiments on mass transfer with large benzoic acid particles in packed columns showed no dependence of mass transfer on surfactant concentration. Similar benzoic acid/surfactant experiments by Gondo and coworkers (1968) showed that the presence of a surfactant changed the mass transfer rate by less than 5%.

The mass transfer experiments used the vortex flow reactor set up described in Section 4.1. Most of the mass transfer experiments were performed with inner cylinder of 4.21 cm and outer cylinder of 4.90 cm. In one set of experiments the inner and outer radii were varied to provide gap ratios from 0.10 to 0.51. The rotation rate and flow rate were set to vary the Taylor number from 300 to 3000 and the axial Reynolds number varied from 4 to 45.

Experiments were performed in either a batch or a continuous mode as shown in Figure 4.4. All experiments were performed with the VFR in a horizontal orientation except where noted. In the batch experiments, particles suspended in saturated benzoic acid were injected into the upper port at the start of the run. Special care was taken to ensure that the solids were equally suspended and that the samples were representative. In batch runs using low rotation rates, a high rotation rate was initially applied for a few seconds to evenly distribute the particles. Then the VFR was return to the test conditions and a sample was withdrawn to determine initial concentration. At short time intervals, samples were withdrawn through the lower port and immediately filtered with a 0.22 μm syringe filter (Millex-GS). A water reservoir was connected to the top of the reactor to keep air from entering the system upon sample withdrawal. The sample was then diluted 20 fold and analyzed in a UV Spectrophotometer at 250 nm using a quartz cuvette. At this wavelength, the contribution of the 0.01% Triton to the absorbance is negligible.

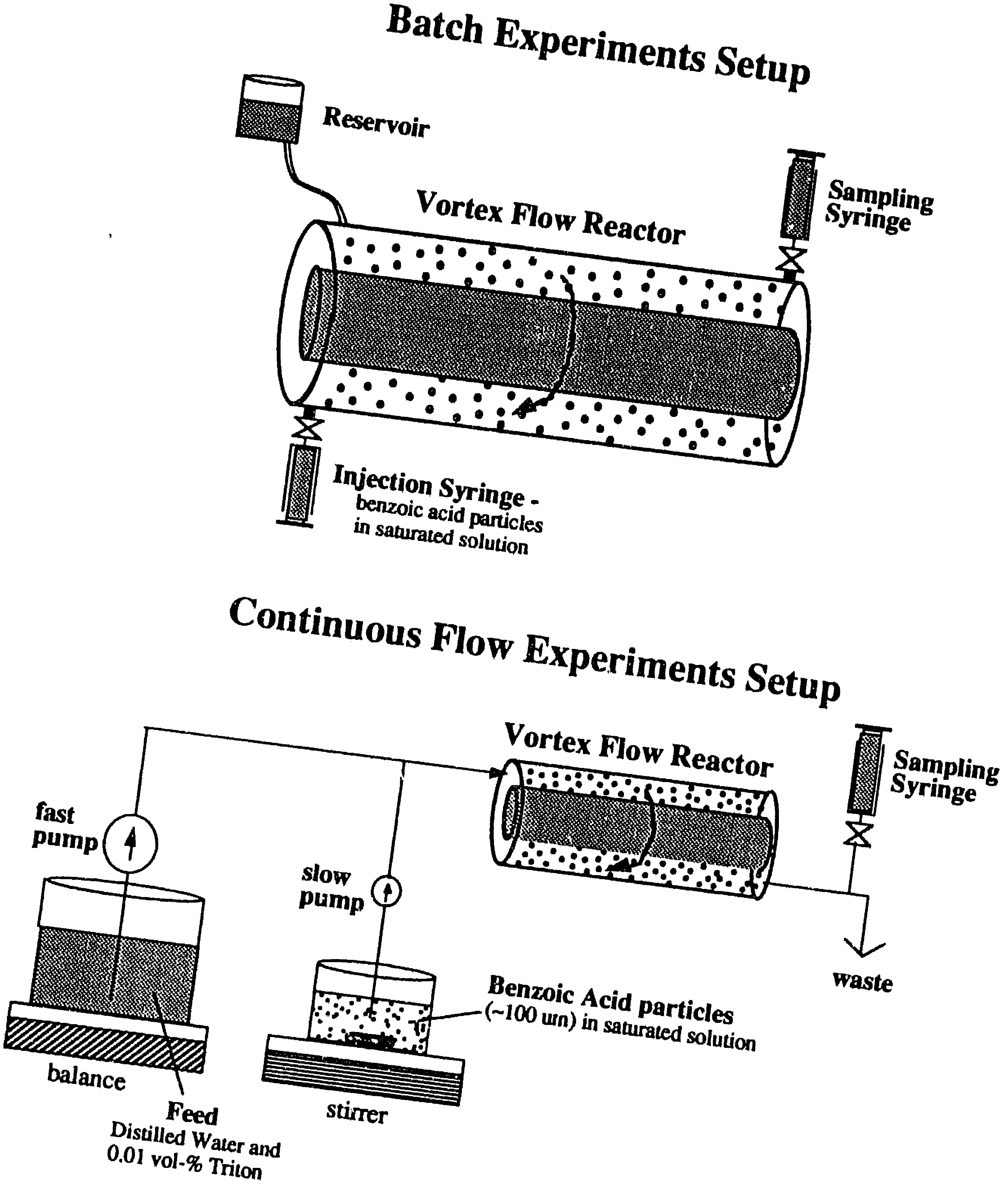

Figure 4.4: Experimental set-ups for mass transfer studies of benzoic acid dissolution.

During the batch experiments, it was discovered that a vertical orientation caused a higher mass transfer rate at the bottom of the VFR which may have been cause by an uneven particle distributions. Therefore, all continuous experiments were performed with a horizontal orientation of the VFR to providing a uniform axial distribution of particles. Note that in the continuous mass transfer studies the particles exit the reactor whereas in the model validation studies and the RTD studies, the VFR is in a vertical orientation and the particles are retained at the outlet. The continuous experiments utilized two pumps feeding into the reactor. The fast pump fed a 0.01% Triton solution from a reservoir and the slow pump fed a well-mixed solution of benzoic acid particles in saturated benzoic acid. Flow rates were determined by electronic balance and stopwatch. Each run was allowed to continue for several residence times until a steady concentration was obtained. Samples were filtered with a 0.22 μm syringe filter (Millex-GS) and the benzoic acid concentration was determined by absorbance at 250 nm.

4.4. Alkaline Phosphatase Immobilization

4.4.1 Soluble Enzyme Characterization

Alkaline phosphatase was chosen as the model enzyme for model verification studies because the enzyme is readily available, has a colorimetric assay, and exhibits Michaelis-Menton kinetics above pH=9.0 (Bretaudiere and Spillman, 1983). The enzymatic reaction is

$$\text{4-NPP} + \text{X-OH} \xrightarrow{\text{Alkaline Phosphatase}} \text{4-NP} + \text{X-OPO}_3\text{H}_2$$

where 4-nitrophenylphosphate (4-NPP) is the substrate and the buffer containing 2-amino-2-methyl-1-propanol (X-OH) functions as a phosphate acceptor. Because the phosphate acceptor is in 20 to 1000 fold excess, its concentration is assumed to be constant and the reaction rate is dependent solely upon the substrate concentration. The assay is conducted by incubating 1.35 ml of 2-amino-2-methyl-1-propanol (AMP) buffer with 0.1 ml of 240 mM 4-NPP in a water bath for at least 5 min. The reaction is initiated by addition of 0.05 ml of the alkaline phosphatase sample. The increase of the reaction product (4-nitrophenyl) is monitored at a wavelength of 406 nm for 3 min. The extinction coefficient for the product is 1.88 $mM^{-1}mm^{-1}$. For the conditions described above with a 1 cm path length cuvette, the activity in the sample is given by

$$\text{Activity (U/ml)} = 1.596\ \Delta A_{406}/\Delta t \tag{4.2}$$

where $\Delta A_{406}/\Delta t$ is the change of absorbance at 406 nm per minute. One unit of activity is defined as the amount of enzyme needed to hydrolyze 1.0 μmole of p-nitrophenyl phosphate per minute.

Two types of alkaline phosphatase were used in the immobilization experiments: a low purity lyophilized powder of alkaline phosphatase with activity of 3 Units/mg solid (Sigma Type I, Calf Intestine P3877), and a high purity ammonium sulfate suspension of alkaline phosphatase with activity of 600 U/mg (Sigma Type XXX, Calf Intestine P4028). The protein content of the low activity lyophilized powder was determined to 0.2 mg protein/mg solid, as determined by the bicinchoninic protein assay with bovine serum albumin standards (cf. Section 4.4.2). Therefore, the activity per unit protein was 15 U/mg protein. The ammonium sulfate suspension was dialyzed overnight with three buffer changes prior to use. All chemicals were obtained from Sigma. The substrate stock of 240 mM 4-NPP in water was prepared in batches, distributed in 1 ml aliquots, and then frozen. Because the 4-NPP solution is light and temperature sensitive, it was stored in the refrigerator or on ice during the experiments.

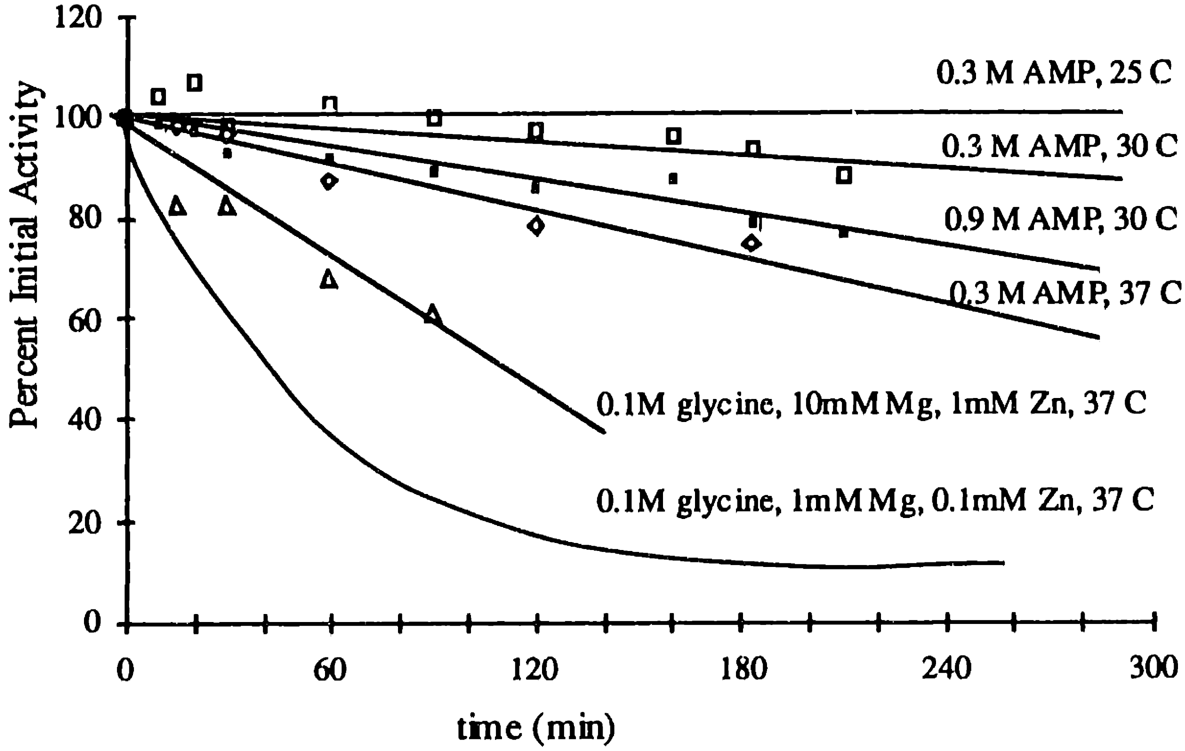

Figure 4.5 - Deactivation rates of soluble alkaline phosphatase.

After initial experiments with immobilized alkaline phosphatase revealed problems with enzyme deactivation, the soluble enzyme was examined to determine optimal buffer composition. It was known that zinc and magnesium are essential for enzyme stability but that impurities in the AMP can chelate these metal ions (Bretaudiere and Spillman, 1983). Therefore, several experiments were conducted varying the concentrations of AMP, metal ions and other buffering agents. The results from some of these studies are shown in Figure 4.5. All of the AMP buffers in the graph used a metals concentration of 2mM Mg^{+2}, 1mM Zn^{+2} and 2mM N-(2-hydroxyethyl) ethylene-diamine triacetic acid trisodium salt dihydrate (HEDTA) and pH=10.4. The HEDTA serves as a metals buffer to regulate the concentrations of free zinc and magnesium ions. The minimum deactivation rate was found for a buffer containing 300 mM 2-amino-2-methyl-1-propanol at 25 C. A plot of the observed reaction rate versus temperature for soluble alkaline phosphatase is shown in Figure 4.6. It is interesting to note that in increasing the temperature from 25 C to 30 C the reaction rate increases about 20% while the deactivation rate increases 500% (from 0.7%/hour to 3.6%/hour). The K_m of the alkaline phosphatase was determined experimentally to be 3.2 mM by measuring the reaction rate at different substrate concentrations. An interesting consequence of the high K_m is that immobilized enzyme studies could be run at 0.1 mM and be well within the first order limit of the enzyme (c.f. (3.14)). In addition, the absorbance of 0.1 mM of product is 1.88 AU, which is in the linear response range of the spectrophotometer.

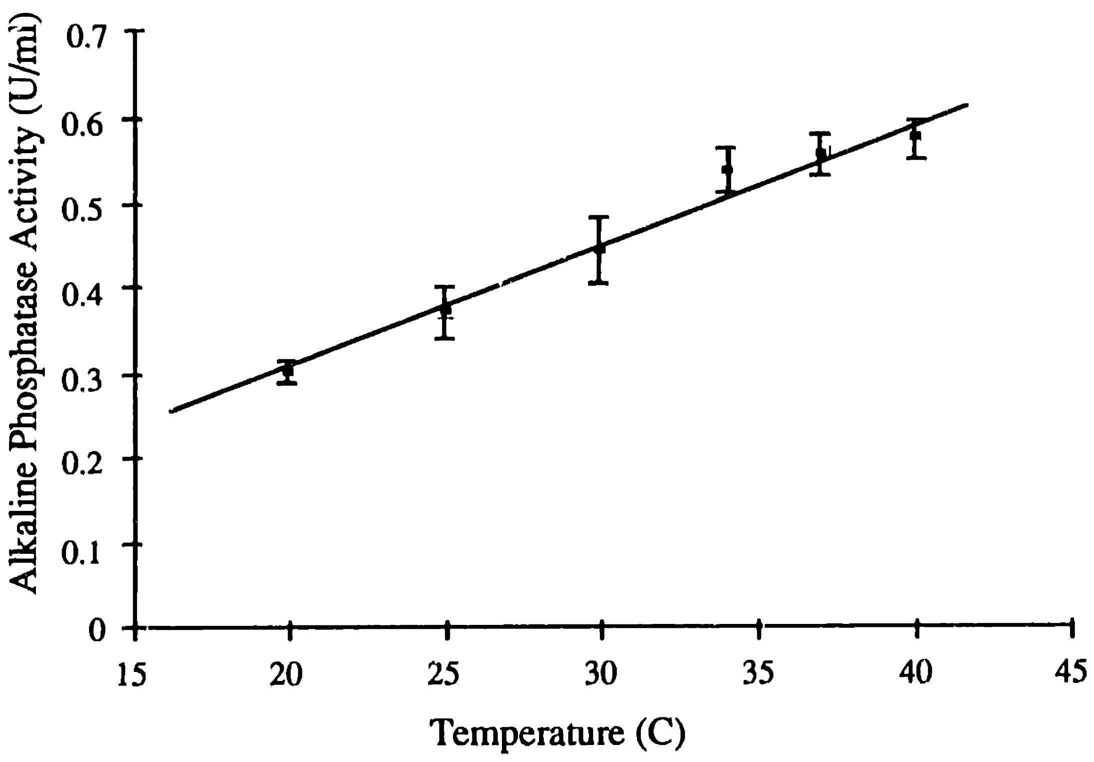

Figure 4.6 - Soluble alkaline phosphatase activity as a function of temperature.

4.4.2 Immobilization on Azlactone - Polyethylene Membranes

Alkaline phosphatase was immobilized on azlactone functionalized polyethylene membranes, obtained from 3M. The chemistry for the reaction is presented in Figure 4.7. The azlactone group is a cyclic anhydride which ring-opens upon reaction with a primary amine, such as lysine (Coleman *et al.*, 1990). The opened ring provides a stable spacer-arm of 4 atoms. The reaction occurs quickly; on polymeric beads with the same chemistry, the reaction was essentially complete in 1-2 hours (Coleman *et al.*, 1990). The membranes used in the model validation experiments had a thickness of 61 µm, a maximum pore size of 0.52 µm, a porosity of 68%, and a dry density of 0.303 g/cm^3 (Gagnon, 1993). The membranes contained 8.2% azlactone by weight corresponding to an active site density of 0.18 mmol/cm^2.

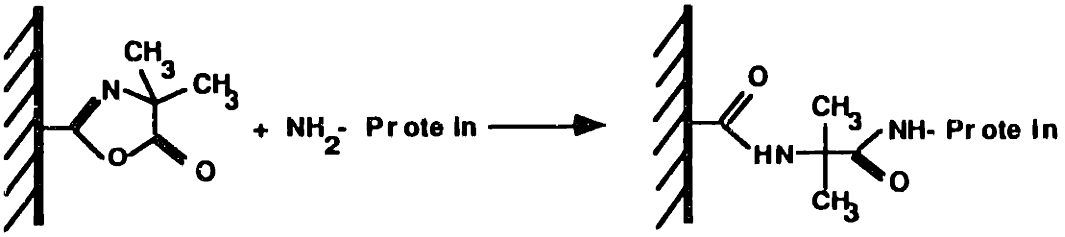

Figure 4.7 - Azlactone reaction with primary amine to yield covalently bound protein.

Because a high surface enzymatic activity is required in model validation experiments, an extensive set of experiments were conducted to optimize the immobilization procedure. Variables which were studied include coupling buffer, salt concentration, volume of coupling solution, length of coupling, ethanolamine wash concentration, presence of substrate and membrane prewashing. The immobilization on azlactone membranes involves three steps: coupling, quenching and washing. The basic procedure is outlined below, variations were used during process development. In some experiments, blanks were produced using identical immobilization procedures except for the coupling buffer which contained no enzyme.

Coupling Step

A 6.3mm circle of membrane, cut with a hole punch, was placed in a microcentrifuge tube with 50μl of coupling buffer containing protein in 25 mM Phosphate (pH=8) and 0.6M $Na_2 SO_4$. The tube was mixed continuously on a lab vortexer for one hour at which time the excess liquid was removed for later analysis. Experiments 1 through 6 used the low purity alkaline phosphatase described above, whereas experiment 7 used the high purity alkaline phosphatase.

Quench Step

After coupling, 100μl of 3M ethanolamine (pH=9.0) was added to the tube to block residual azlactone groups, and mixed for 5 minutes. This ethanolamine was discarded and an additional 1ml of ethanolamine was added, was mixed for 1 hour, and was discarded.

Wash Step

The membrane was washed consecutively with Tris (tris(hydroxymethyl)-amino methane) buffers (pH=8.0); each wash consisted of 1ml of buffer mixed for 5 minutes and removed. The wash steps were as follows: 2 washes with Tris buffer, 2 washes with Tris buffer containing 1M NaCl, 2 washes with Tris buffer. No activity was detected in the second high salt wash.

Activity Analysis

Alkaline phosphatase activity of the immobilized membrane disks was determined in a similar manner to the soluble enzyme assay presented in Section 4.4.1. Membranes with immobilized alkaline phosphatase were placed in a cuvette along with a micro-stir bar and brought to assay conditions of 0.9M 2-amino-2-methyl-1 propanol, 16mM NPP, 2mM magnesium sulfate, 1mM zinc sulfate, 2mM N-(2-hydroxyethyl) ethylenediamine triacetate (HEDTA). The cuvettes were stirred continuously in a water bath at 30° C; and the absorbance at 406 nm was read periodically. The reaction was continued until at least 15 data points were obtained to calculate kinetic rate. The activity of the samples was calculated by the formula

$$\text{Activity (U/cm}^2\text{)} = 0.0532\ \Delta A_{406}/\Delta t\ \left(\frac{\text{Volume in cuvette}}{\text{Membrane surface area}}\right) \qquad (4.3)$$

where $\Delta A_{406}/\Delta t$ is given in (AU/min). Kinetic experiments on immobilized membranes were performed by placing the membrane in a small beaker with a stir bar. Successive aliquots of NPP were added to vary the substrate concentration. Samples were removed from the beaker, read in the spectrophotomer and returned to the beaker. The rate (μmol/min/cm^2) was calculated from (4.3) for each substrate concentration.

Protein Analysis

Determination of soluble and membrane proteins were performed by the bicinchoninic acid (BCA) method (Smith et al., 1985; Stich, 1990) using chemicals from Pierce. The assay measures the color change upon the coupling of bicinchoninic acid to reduced copper ions. The reaction scheme is outlined in Figure 4.8. Unlike other protein assays, the BCA method does not directly bind a dye to the protein. Instead, the color change is due to the protein reacting with of soluble copper ions which in turn react with the dye. Because the color change occurs in the soluble phase, the reaction can be used for determination of both soluble and immobilized proteins.

Assays of soluble enzyme followed the standard assay protocol (Pierce). The working solution was prepared by mixing 50 parts of Reagent A (containing sodium carbonate, sodium bicarbonate, bicinchoninic acid and sodium tartrate in 0.2 N NaOH) with one part of Reagent B (4% copper sulfate). The reaction was initiated by adding 1 part of sample to 20 parts of working reagent. The test tubes were incubated for 30 min at 37 C and then immersed in a water bath at room temperature. After cooling for 5 minutes, 200μl of liquid from each sample was transferred to microplate well. The microplate was read immediately at 562 nm. Samples were done in triplicate whenever possible. Total protein for the membranes was determined by comparison with bovine serum albumin (BSA) standard curves.

Membranes were assayed in a similar manner. The reaction proceeded as above but instead of the soluble enzyme sample, the equivalent volume of buffer was added along with the membrane and a micro-stir bar. The membranes were stirred throughout the incubation and cooling times. The total protein was calculated using the soluble BSA standards (Pierce) as a reference. Note that ethanolamine pre-quench experiments and the high activity alkaline phosphatase immobilizations used blank membranes to correct for total protein bound. The blank membranes, produced as described above, provided an indication of the contribution of the azlactone/polyethylene support to color change.

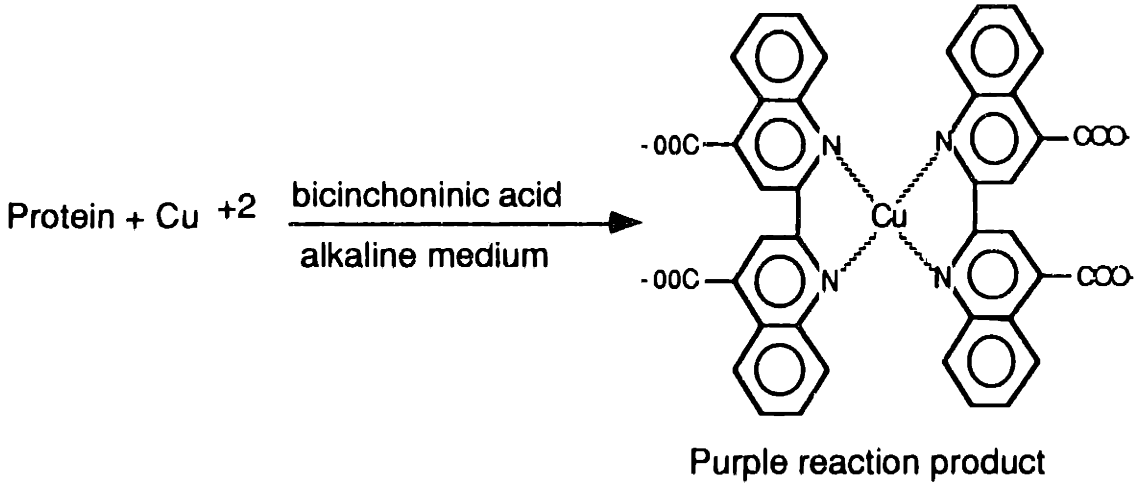

Figure 4.8 - Reaction scheme for the bicinchoninic acid protein assay.

4.4.3 Immobilization on Agarose

Immobilized Enzyme Particles

Initial tests of the immobilization method used Biogel 50-100 mesh agarose particles (Biorad). Subsequent experiments to study immobilization protocols and VFR behavior used STREAMLINE™ DEAE particles (Pharmacia). The latter is an composite material of agarose and crystalline quartz (silica) containing a DEAE (diethylaminoethyl) anion exchange functionality. It was expected that the DEAE would not interfere with the enzymatic reaction as at the pH of 10.4 used in the experiments the DEAE group has little net charge (Scopes, 1987). However, later studies showed that the DEAE particles had a much higher adsorption of the product (4-nitrophenol) than either underivatized particles or particles with a sulphopropyl (SP) cation exchange group. The equilibrium adsorption capacity of the agarose/silica particles with 0.1 mM nitrophenol is shown in Table 4.2. The DEAE resin adsorbed 0.1mM reactant (4-nitrophenol phosphate) at a capacity of 0.2 μmol/ml particles. Because of the significant adsorption of product and reactant to the DEAE particles, experiments showing the transient response of the VFR used the underivatized STREAMLINE particles.

Solid Support	Equilibrium Adsorption Capacity of 0.1 mM Nitrophenol
STREAMLINE DEAE	0.7 μmol/ml
STREAMLINE SP	0.02 μmol/ml
STREAMLINE underivatized	0.04 μmol/ml

Table 4.2 - Equilibrium adsorption capacity of 0.1 mM nitrophenol with STREAMLINE particles

The STREAMLINE particles were used in the VFR experiments because of their high density of around 1.2 g/ml. The high density is necessary for the particles to sufficiently settle in the VFR. The DEAE and SP materials are commercially available; the underivatized material was a gift from Pharmacia. The base material of the particles is macroporous, cross-linked agarose with 6% crystalline quartz material (Pharmacia, 1993). The particles have a wide pH stability ranging from 3 to 14. The agarose/silica gel matrix has a density of around 1.9 g/ml as determined by achieving neutrally buoyant particles in a cesium chloride solution. The particles range in size from 100 to 300 µm with a mean particle size of 200 µm. The volume of the particles was measured by placing in a graduated centrifuge tube and spun for at least 5 minutes at a centrifugation force of 350 g. The interstitial void fraction of the centrifuged packed bed was determined to be $\varepsilon = 0.30$ by the partitioning of 2,000,000 MW blue dextran (Sigma) into the particles.

Immobilization Protocol

The procedure for immobilizing alkaline phosphatase on agarose was adapted from a method by Basheeruddin et al. (1985). Prior to coupling, the immobilized enzyme support was placed in a column and washed with at least 30 volumes of deionized water. The gel was then transferred to a small flask or a large centrifuge tube using the minimum of water necessary to transfer all of the particles. Next, 0.6 ml of either a 35 mg/ml or a 100 mg/ml solution of cyanogen bromide (pH = 11) was added for each 1.0 ml of gel. The gel was shaken periodically by hand or by vortexing and was monitored for pH and temperature. The pH was kept close to 11 by dropwise addition of 2M NaOH. If the temperature increased 5 C above the initial (ambient) temperature, ice was added directly into the reaction mixture. The reaction was run until the pH stopped changing, about 15 to 20 minutes. The gel then was placed in a column and washed with at least 20 volumes of 0.1M sodium carbonate/bicarbonate buffer pH=9.0. After washing, the gel was transferred to a centrifuge tube, excess liquid was removed and alkaline phosphatase in bicarbonate buffer was added (approximately 1 ml enzyme solution for each 2 ml gel). The coupling step occurred overnight on an orbital mixer at 4 C. After coupling, the gel was washed with at least 20 volumes each of 0.1M bicarbonate buffer, 0.1M bicarbonate/1M NaCl buffer, and 0.1M bicarbonate buffer. Enzymatic activity of the wash solution was checked at the end of the salt wash.

Assay conditions for the immobilized alkaline phosphatase were similar to those for the soluble enzyme and for the immobilized membranes. The gel was first washed in AMP buffer, then a small amount of gel (0.1 to 0.5 ml) was centrifuged in a graduated microcentrifuge tube for 5 minutes and the volume was recorded to the nearest increment of 0.025 ml. The gel was transferred to a cuvette and conditions in the cuvette were adjusted to 3 ml of 0.9M 2-amino-2-methyl-1 propanol, 16mM NPP, 2mM magnesium sulfate, 1mM zinc sulfate, 2mM N-(2-hydroxyethyl) ethylenediamine triacetate (HEDTA) at 30 C. Some assays, later in the process development, were performed with 0.3M AMP buffer and at 25 C. The cuvette was placed in a water bath where stirred with a small microstir bar (2mm by 7mm). With this size stir bar, the gel could be well suspended in the cuvette with no damage to the particles, as observed under a microscope. Larger stir bars caused significant particle breakage. To read a sample, the cuvette was removed from the stirplate/water bath and the gel was allowed to settle for 15-30 seconds. The reaction was monitored at 406 nm with a reference wavelength of 510 nm. The reference wavelength was necessary to account for any particles which did not settle. The reaction was continued until at least 15 data points were obtained to calculate kinetic rate. Duplicate experiments performed on the same batch of immobilized enzyme showed that the assay procedure is reproducible within 5 to 10 %.

4.5 Particle Visualization Studies

Particle visualizations studies were performed with the clear acrylic outer cylinder with no bottom support ($r_o = 2.45$ cm). The inner cylinders used in Table 4.1 (diameters of 3.81, 4.21 and 4.45 cm) were modified to have a flat bottom by using silicone rubber to cover the graphite bearing. The gap on the bottom of the reactor between the cylinders was approximately 2mm. The particles were retained in the reactor by a 40 μm woven nylon mesh (Tetko) on the reactor outlet; the effective surface area of the mesh was 2 cm^2.

Dark blue particles were obtained by mixing bromophenol blue with the DEAE STREAMLINE particles. The DEAE resin strongly binds bromophenol blue which is a free acid; the capacity was found to be 75 mg/ml gel. The binding is partly hydrophobic as evidenced by the elution conditions. Whereas only a small amount of bromophenol blue was eluted from the gel with a basic high salt solution of 1M NaOH/ 1M NaCl, all of the dye was eluted with a basic hydrophobic solution of 50% ethanol and 1M NaOH.

The reactor was operated by setting a flow rate and rotation rate and noting the position of the particles at equilibrium. The regions of good fluidization were judged by when the particles were completely distributed along the axial length. Particle damage was assessed under a light microscope. During operation, the first sign of broken particles occurs when the flow rate through the VFR decreases, indicating a clogged outlet filter. At this point, or at the end of a non-fouling run, the VFR was disassembled and the particles were observed under the microscope. Both the fast and slow settling particles were examined. In general, the filter would clog when any slow settling particles (actually broken particle debris) were present. At this point, about 1 in 20 particles in the fast settling fraction would show signs of damage. In a non-fouling experiment, there was no sign of non-settling particle debris. The fast settling fraction would show damage to about 1 in 100 particles, which is similar to the unused material.

4.6 Model Validation Studies

The objective of the model verification studies was to compare experimental data from a VFR with immobilized enzyme to model predictions. Steady state and dynamic response experiments were conducted both for immobilized alkaline phosphatase on membranes and on suspended particles. In the steady state experiments, a constant feed containing substrate was used. The flow rate and the rotation rate were set and the VFR was allowed to reach steady state before changing operating conditions. In the dynamic experiments, a valve on the feed was switched at the start of a run to change from buffer with no substrate to buffer with substrate. The VFR was run with substrate until steady state was achieved at which time the feed was again changed to buffer without substrate and the reactor was allowed to reequilibrate.

All experiments used a substrate concentration of 0.1 mM NPP which is in the first order reaction limit for alkaline phosphatase. Reaction progress was continuously monitored by a spectrophotometer at 406 nm with a reference wavelength of 510 nm. The reference wavelength was necessary to correct for changes to the baseline due to air or debris entering the flow-through cuvette.

In both the membrane and particle experiments, enzymatic activity declined over time. The loss of activity was described as an exponential decay process, $k' = k'_o \exp^{-k_d t}$. The deactivation rate, k_d was determined from a set of reference experiments performed at a specific conditions and run periodically throughout the course of the experiments. Two types of reference experiments were used: batch and continuous. The continuous experiments were performed in the steady state configuration described above. The batch experiments used a high flow rate (130 ml/min) and total recycle. After the product left the VFR, it passed through the cuvette and the pump and was returned into the reactor.

Conversion per pass was kept low (<1% per pass) such that the concentration within the VFR would be constant in the axial direction. Because of the high flow rates used, the batch set-up was used only with the membrane experiments.

Immobilization of alkaline phosphatase to the membrane proceeded as outlined in Section 4.4. The azlactone membranes were secured to the inner rotating surface by silicone rubber prior to immobilization. The immobilization, quench and wash steps took place in the VFR at low rotation rates. The membrane experiments used an inner cylinder diameter of 4.45 cm and an outer cylinder diameter of 4.90 cm. Because high variation in enzymatic activity was found between small samples taken from different locations of the same membrane (standard deviation around 20%), kinetics were determined for the whole membrane through the reference experiments in the VFR. The particle experiments used cylinders of diameters of 4.21 and 4.90 cm. The alkaline phosphatase particles were prepared and assayed as described above. The kinetics were determined by assaying independent samples (i.e. particles from the same immobilization batch) in cuvettes prior to the run. Therefore, the kinetics were determined independently from the VFR in the particle experiments whereas the kinetics were determined in the VFR for the membrane experiments.

4.7 Protein Adsorption Experiments

Protein adsorption in the VFR was demonstrated using bovine serum albumin (BSA) adsorption on anion exchange particles. The anion exchange resin was a composite agarose-silica DEAE (diethylaminoethyl) material (Pharmacia, STREAMLINE DEAE). The experiments used a VFR with cylinder diameters of 4.21 cm and 4.90 cm. At the start of the experiments, the particles were placed in the VFR and were equilibrated with 50 mM Tris (tris(hydroxymethyl)-amino methane) buffer, pH=7.5. Then a 2 mg/ml solution of

BSA (Sigma #7030) was continuously pumped through the VFR at a constant flow rate and rotation rate. The protein in the reactor outlet was observed by continuous monitoring with a spectrophotometer at 280 nm. The protein solution was fed into the VFR until the outlet protein concentration reached at least 90% the inlet concentration and the UV absorbance remained relatively constant. Following the adsorption, the BSA bound to the anion exchange particles was removed by passing a 0.5M NaOH, 1M NaCl solution through the VFR until no absorbance at 280 nm was detected. After cleaning the particles, the VFR was once again equilibrated with Tris buffer in preparation for another adsorption experiment.

Chapter 5 -

Mass Transfer in Taylor-Couette Vortex Flow

Mass transfer often provides the limit on the performance and productivity of a reactive system. A major goal in characterizing the vortex flow reactor is to elucidate the relationship between mass transfer and reactor operational parameters. Mass transfer in the VFR occurs in three directions - between two vortices (e.g.. dispersion), between a vortex and the active surface, and within the porous support matrix. Of these three mass transport mechanisms, only diffusion within the porous support is independent of the reactor operation. Both mass transfer to the active surface and dispersion between vortices are a function of the reactor design and the operating conditions. By understanding the relationships between mass transfer and the geometric and operational parameters, the VFR may be systematically designed, scaled-up and optimized for any reaction.

Previous researchers have studied many aspects of mass transfer in Taylor-Couette flow. Dispersion (or mass transfer between vortices) has received moderate attention in the published literature. Most previous studies have focused on operation at extreme high or low rotation rates, typically without axial flow and without regard to the effect of reactor geometry. The results from prior studies are not sufficient to predict dispersion over the full operational range of the VFR. Therefore, further experiments were necessary to characterize dispersion in the VFR. The procedure for these experiments are presented in Section 4.2 and the results are presented in the following section.

Mass transfer to the active surface of the VFR is actually two problems, corresponding to the two VFR configurations (Figure 1.1). Mass transfer to the cylinder walls has been well described in the literature and is mathematically described by equation (2.14). As mass transfer to suspended particles had not previously been characterized, this subject was examined experimentally. The experimental techniques are presented in Section 4.3, and the experimental results are shown in Section 5.2. The experiments characterize mass transfer as a function of rotation rate, axial flow rate and geometry. The description of mass transfer to suspended particles presented in Section 5.2 is not complete because the mass transfer correlation does not include all physical and geometric parameters. However, enough experimental work is presented to show that mass transfer to the particle surface is very fast and consequently is negligible for nearly all VFR operation.

5.1 Axial Dispersion in Taylor-Couette Vortex Flow

As discussed in Section 2.5.3, mixing in Taylor-Couette flows occurs in three directions; the rate of circumferential and radial mixing is fast compared to the rate of axial mixing. Consequently, axial dispersion is the dominant parameter in designing reactive vortex flow systems. A common goal in reactor design is to approach plug flow by maximizing mixing in the cross-sectional (radial and circumferential) directions while minimizing mixing in the axial direction. Plug flow operation maximizes conversion for all reactions where the reaction rate decreases with increased reactant conversion (Carberry, 1976). Taylor-Couette vortex flow behaves as a plug flow reactor at low rotation rates and low axial flow rates (Kataoka *et al.*, 1975; Pudjiono *et al.*, 1992). As the rotation rate increases and the vortices become more turbulent, the axial dispersion also increases. The axial dispersion coefficient, which describes the deviation from plug flow, is essential in predicting conversion in the VFR.

Although the dispersion coefficient has been related mathematically to physical parameters in spatially periodic systems such as Taylor-Couette flow (Brenner, 1980; Shapiro and Brenner, 1988; Iosilevskii *et al.*, 1993), solving these equations involves complicated numerical calculations requiring detailed knowledge of the velocity profile. The calculations are feasible when the velocity profile is relatively simple, such as for Taylor vortex flow operating just above the critical rotation rate and without axial flow. However, the calculations become intractable for typical operation of the VFR where the high rotation rates and axial flow produces an exceedingly complicated velocity profile. Therefore, description of axial dispersion in the VFR in this thesis will employ semi-empirical analysis of experimental data.

The objective of the following studies was to study experimentally and describe mathematically axial dispersion in vortex flow for a wide range of operational parameters (rotation rate, axial flow rate) and design parameters (reactor geometry). Axial dispersion is determined from analysis of residence time distribution (RTD) experiments with a non-reactive tracer. Section 5.3 explains how the dispersion coefficient from the non-reactive tracer studies are used to describe dispersion in the VFR with reaction. Axial dispersion is studied for gap ratios ranging from 0.04 to 0.38, for axial Reynolds numbers ranging from 0.5 to 30, and for rotation rates of 4 to 200 times the critical rotation rate. A new method of residence time distribution analysis is presented, and its limitations are discussed. The correlation derived from this experimental study describes dispersion as a function of the operational and geometric parameters.

5.1.1 Data Analysis

As discussed in Section 3.1, transport of a non-reactive tracer in Taylor-Couette flow can be described by the one-dimensional convective dispersion equation (3.2) in the long-term limit. The solution to (3.2) for the residence time distribution studies under the boundary conditions (3.5) is given by (3.6). The long-term limit is satisfied when:

(1) The length of the test section is large compared to the vortices (i.e. large aspect ratio).

(2) The tracer is well mixed within the vortex in the radial and azimuthal directions on a time scale that is short compared to transport in the axial direction.

Since transport in the axial direction occurs both by convection and dispersion, both of these time scales must be greater than the time scale for mixing in an individual vortex. Violations of the long term limit can occur in operation of the VFR; examples are given below.

The solution to the one-dimensional equation (3.6) is in terms of an unknown coefficient, the Peclet number, *Pe*. from which the dispersion coefficient is extracted. As the equation is non-linear in *Pe*, a criterion must be chosen to determine the best Peclet number. The traditional method of analyzing residence time distribution curves is the method of moments in which the variance, σ^2, is calculated from the experimental normalized concentration versus time curve. For a closed-vessel boundary conditions, the variance is related to the dispersion coefficient by (Levenspiel, 1972)

$$\sigma^2 = \frac{2}{Pe} - \frac{2}{Pe^2}(1 - \exp(-Pe)) . \tag{5.1}$$

The variance is calculated from the experimental data by

$$\sigma^2 = \int_0^\infty (\bar{t} - 1)^2 \bar{C} d\bar{t} \bigg/ \int_0^\infty \bar{C} d\bar{t} \tag{5.2}$$

where $\bar{t}$ is the time normalized by the residence time and $\bar{C}$ is the outlet reactor concentration. Because of the time-squared term in (5.2), the variance tends to be heavily weighted by the long-time data in the tail of the curve. At high dispersion, analysis of the RTD curves by the method of moments tends to produce erroneous results due to the high sensitivity of the variance to small baseline fluctuations.

An alternative method of analysis employs the coefficient of quartile variation, Q, a statistical parameter defined as (Beyer, 1981)

$$Q = 100 \frac{t_{3/4} - t_{1/4}}{t_{3/4} + t_{1/4}} \tag{5.3}$$

where $t_{1/4}$ and $t_{3/4}$ are, respectively, the times for one-quarter and three-quarters of the RTD curve to emerge. The coefficient of quartile variation, like the variance, is a measure of the distribution curve width. The coefficient is not heavily weighted by data in the tail of the curve as it relies upon the zero-moment of the distribution curve (i.e. area under the curve), rather than the second moment (5.2). The coefficient has been previously used to describe other distribution curves with long tails, such as particle size distributions (Davis and Hunt, 1986).

Numerical integration of (3.6) over time for the first and third quartiles provide a relationship between Q and Pe, as shown in Figure 5.1. During data analysis, Q is determined from the experimental data. Then, the best-fit Peclet number is obtained from iteratively adjusting the value of Pe and integrating (3.6) until the calculated and experimental coefficients of quartile variation match. A simpler but somewhat less exact method of calculating the Peclet number obtains the value of Pe from Figure 5.1.

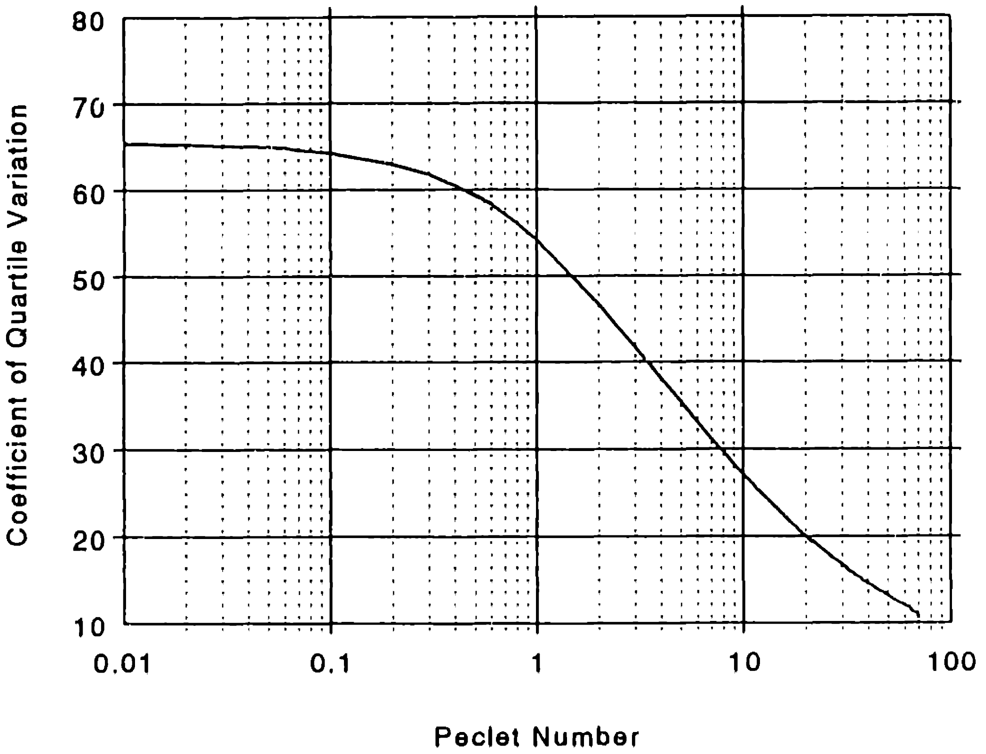

Figure 5.1: Relationship between the coefficient of quartile variation and the Peclet number for residence time distribution curves described by (3.6).

The analyzed RTD curves show that the method of quartile variation yields a more reproducible value for the Peclet number than the method of moments. Figure 5.2 shows a comparison of the two methods for high and low Pe curves. Experimental data is

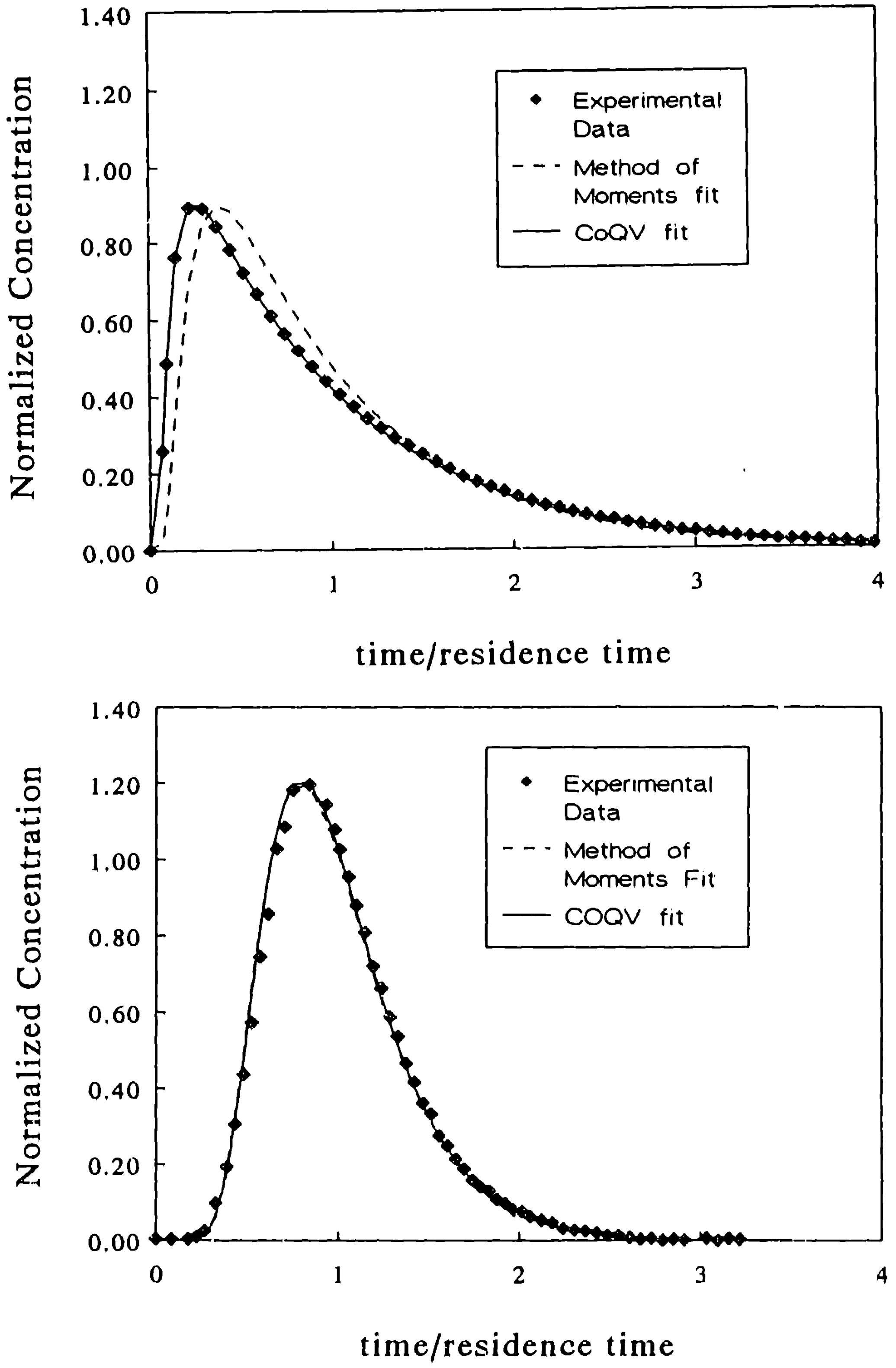

Figure 5.2: Comparison of Method of Quartile Variation and Method of Moments. Top graph is high Peclet number case: $Pe_{MOM} = 11.9$, $Pe_{CoQV} = 12.2$. Bottom graph is low Peclet number case: $Pe_{MOM} = 1.65$, $Pe_{CoQV} = 0.80$.

plotted with curves reconstructed from equation (3.6) and *Pe* determined as described above. As evident in Figure 5.2, the two methods provide similar *Pe* (and thus dispersion coefficients) for high *Pe*; the method of quartile variation provides a much better fit at low *Pe*. For $Pe>5$, the variation in the calculated Peclet number from the two methods is typically less than 10%. Above $Pe=0.05$, Peclet numbers calculated from duplicate runs and analyzed by the method of quartile variation were reproducible to within 10%. Below $Pe=0.05$, the Peclet number cannot be accurately determined, due to numerical limitations.

In the operational ranges studied, two areas of violation of the one-dimensional assumption were observed. Both violations concern the time scale for axial transport relative to mixing in individual vortices. At low rotation rates, especially in vessels with a large annular gap, the RTD curves show signs of incomplete azimuthal mixing. As seen in Figure 5.3, periodic spikes occur on the RTD curves, indicating inhomogeneity in the azimuthal direction. Although the data still fit fairly well to the dispersion model, they were not used in further analysis.

The second violation of the one-dimensional assumption occurs at high axial flow rate. As seen in Figure 5.4, the sharp breakthrough and decay of the RTD curve does not fit the dispersion model. The case of high axial flow rate corresponds to a violation of the "long-term limit" where the tracer does not have sufficient time to sample both the fast and slow moving velocity streamlines. Because the time scale for convection varies as L/u, this problem can be circumvented by either lowering the axial velocity or increasing the length of the annulus. These trends were observed experimentally.

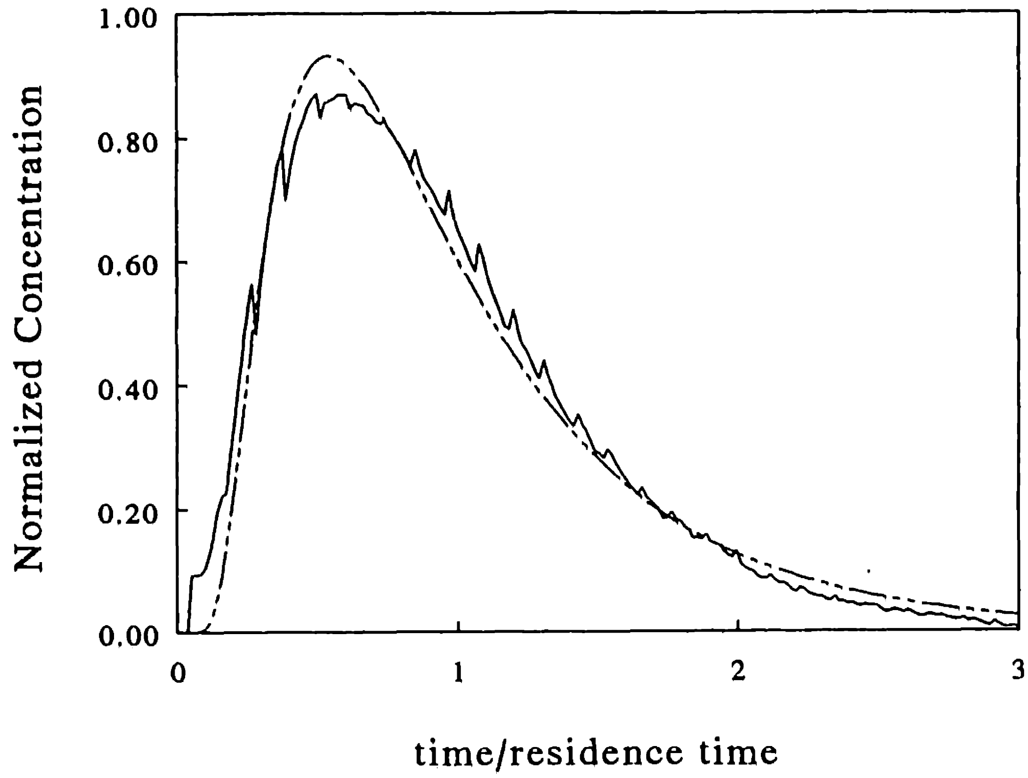

Figure 5.3: Residence time distribution curve for incomplete azimuthal mixing. Periodic spikes are seen in the reactor outlet concentration but curve still fits general shape predicted by (3.6).

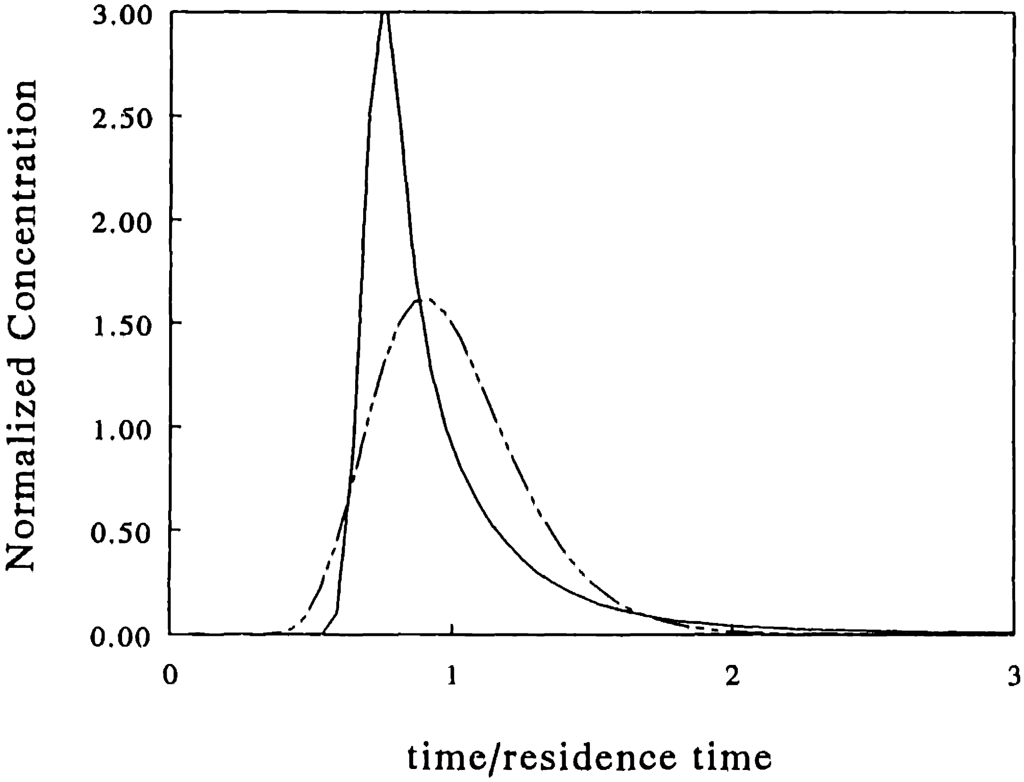

Figure 5.4: Residence time distribution curve for incomplete radial mixing. Outlet curve emerges early and has long tail indicating channeling.

5.1.2 Results

The calculated dispersion coefficients, ranging from 0.01 to 10 cm^2/s, are several orders of magnitude greater than the molecular diffusivity of approximately $8x10^{-8}$ cm^2/s (Granath, 1958) thus indicating the importance of convection in the reactor. Several series of experiments were undertaken to establish the dependency of dispersion on the geometric and operational parameters.

Effect of tracer diffusion coefficient

Tracers of blue dextran ($D = 8x10^{-8}$ cm^2/s) and sodium benzoate ($D = 8x10^{-6}$ cm^2/s) were used to determine if diffusion plays a role in transport. The experiments were conducted using a large gap ratio ($b/r_i=0.36$) at low rotation rates and low axial flow rate of $Re_z = 0.6$. The operational conditions are in the laminar vortex region where intermixing between vortices is minimal. Although the diffusion coefficients varied by a factor of 100, there is no difference in the axial dispersion, as shown in Figure 5.5. The results indicate that diffusion has no effect on axial dispersion throughout the experimental regions studied.

Effect of gap ratio

To determine the effect of the gap ratio on dispersion, nine sets of experiments were conducted at a constant axial Reynolds number, $Re_z = 5.0$. Each set used a different combination of inner and outer cylinders and spanned a wide range of angular Reynolds numbers, Re_θ. The results, shown in Figure 5.6, indicate that dispersion is a strong function of Re_θ and has little dependence on the gap ratio. Regression of the data provides $D^*{\sim}(b/r_i)^{-0.28}$ with $R^2= 0.96$.

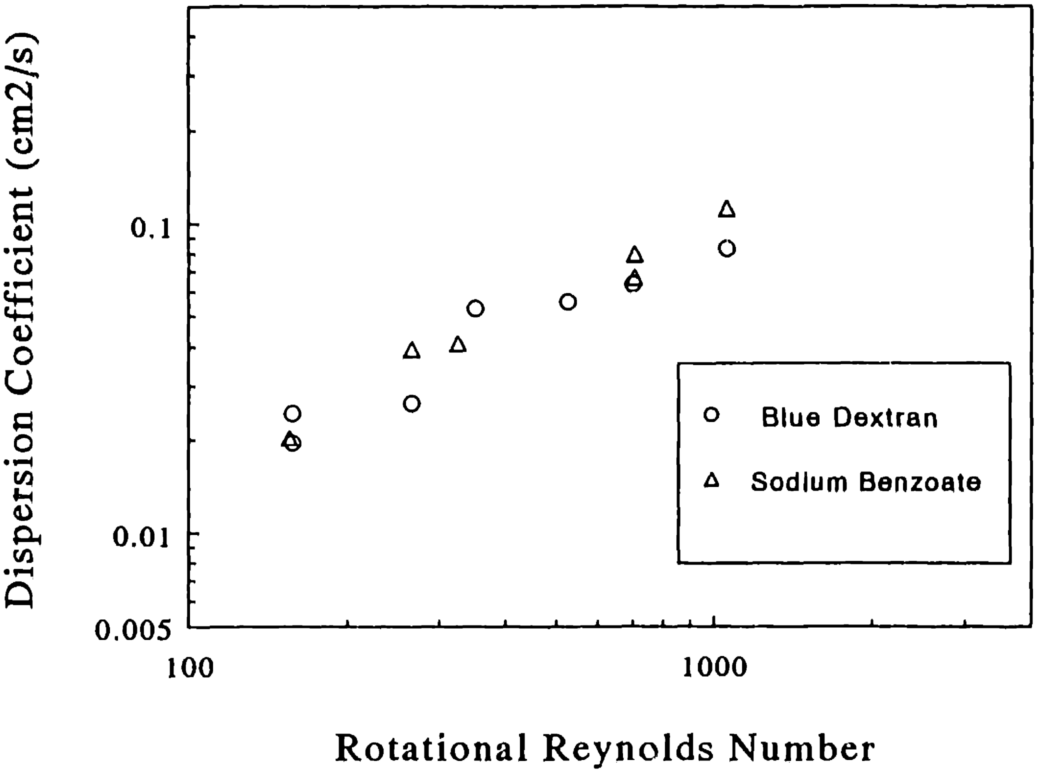

Figure 5.5: Effect of tracer diffusion coefficient on axial dispersion.

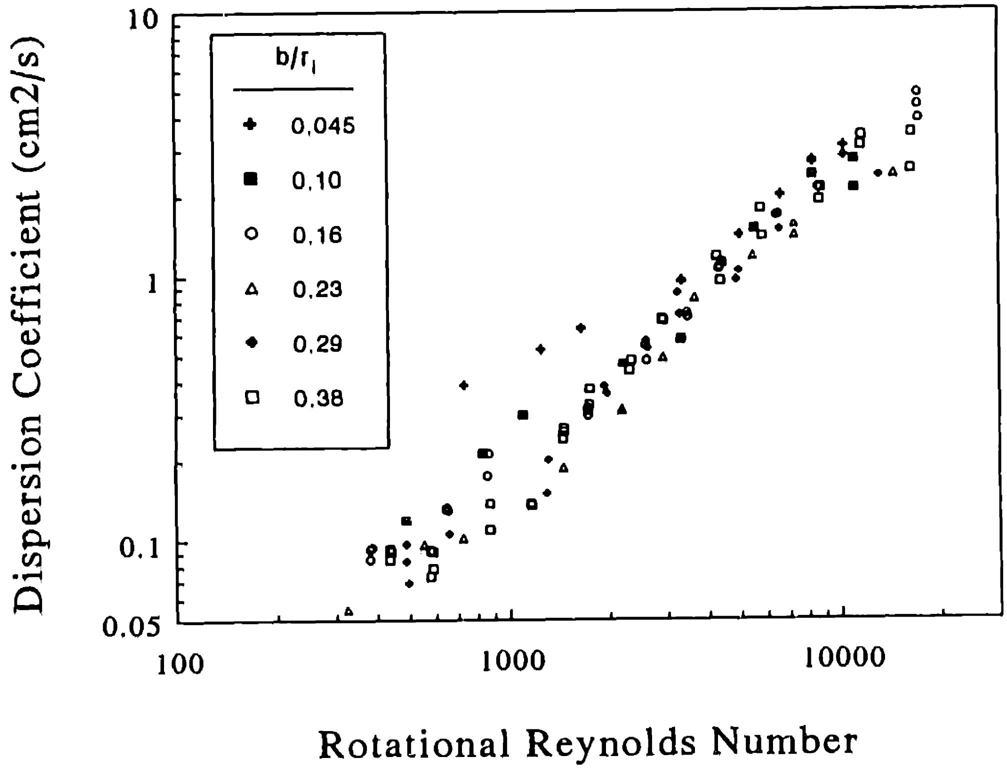

Figure 5.6: Effect of gap ratio on axial dispersion.

End effects

Dispersion experiments were conducted in a long reactor to determine if end effects have a significant influence on the measured dispersion coefficients. The cylinder used was approximately 50% longer than those in the previous experiments. Figure 5.7 shows no discrepancies between dispersion coefficients obtained from long and short cylinders with the same gap ratios, thus indicating that end effects are negligible in the region studied.

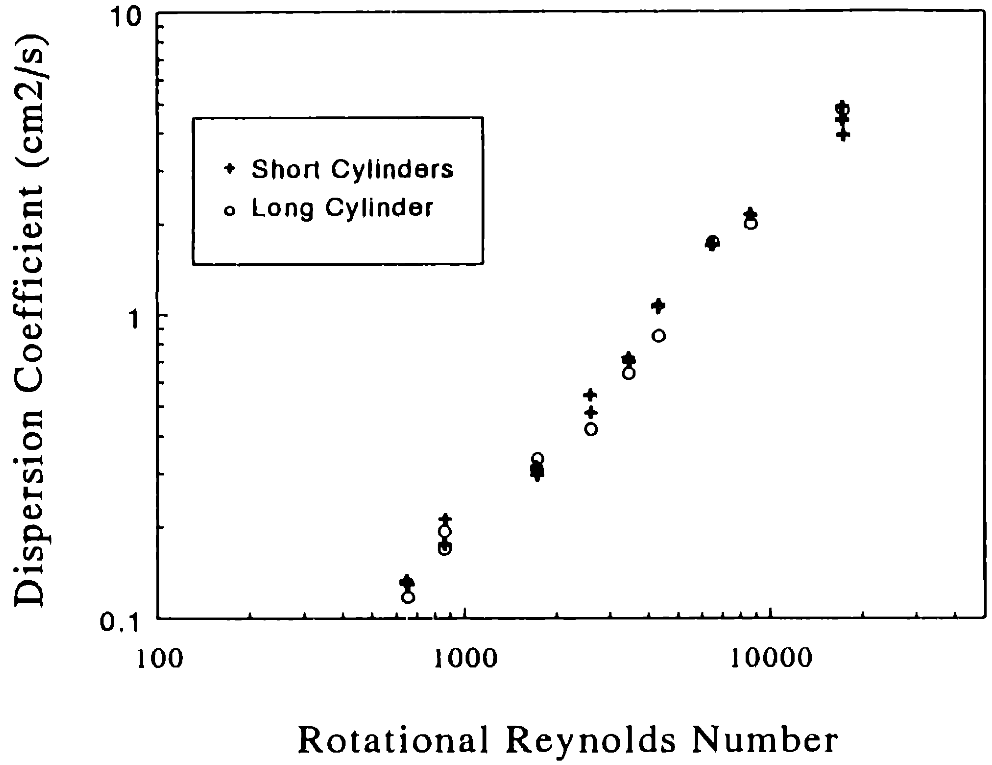

Figure 5.7: Effect of cylinder length on axial dispersion. Short cylinder is 16.9 cm long with gap ratio = 0.164, long cylinder is 25.2 cm long with gap ratio of 0.164.

Effect of Operational Parameters

To determine the effect of Re_θ and Re_z on dispersion, sets of dispersion experiments were performed with Re_z ranging from 0.5 to 30. The data reveal that dispersion is primarily dependent upon Re_θ with little dependence on Re_z. Regression of the data at each of the axial Reynolds numbers, shown in Table 5.1 provides Re_θ exponents ranging from 0.9 to 1.1. When the data are regressed together, the relationship

$$D^* \propto (b/r_i)^{-0.28} Re_\theta^{1.05} Re_z^{0.17} \tag{5.4}$$

fits the data with an average error of 17%. The regression fit is plotted against the data in Figure 5.8. The equation in dimensionless form can be written as:

$$Pe^{-1} = 7.2x10^{-3} (b/r_i)^{-0.28} Re_\theta^{1.05} Re_z^{-0.83} (2b/L) \tag{5.5}$$

Re_z	Coefficient	Exponent
0.50	$3.9x10^{-5}$	1.11 ± 0.06
1.1	$6.9x10^{-5}$	1.05 ± 0.04
2.5	$9.7x10^{-5}$	1.05 ± 0.03
8.0	$1.3x10^{-4}$	1.02 ± 0.03
15	$1.6x10^{-4}$	1.00 ± 0.03
30	$3.0x10^{-4}$	0.92 ± 0.03

Table 5.1: Regression parameters from dispersion experiments.

Effect of viscosity

While viscosity appears in the Reynolds numbers in (5.5) it was not used as a variable in developing the correlation. Therefore, the effect of viscosity provides an opportunity for independent verification of the correlation. Figure 5.9 shows the experimental values and correlation predictions for RTD studies using Re_z = 5 and glycerol-water solutions of

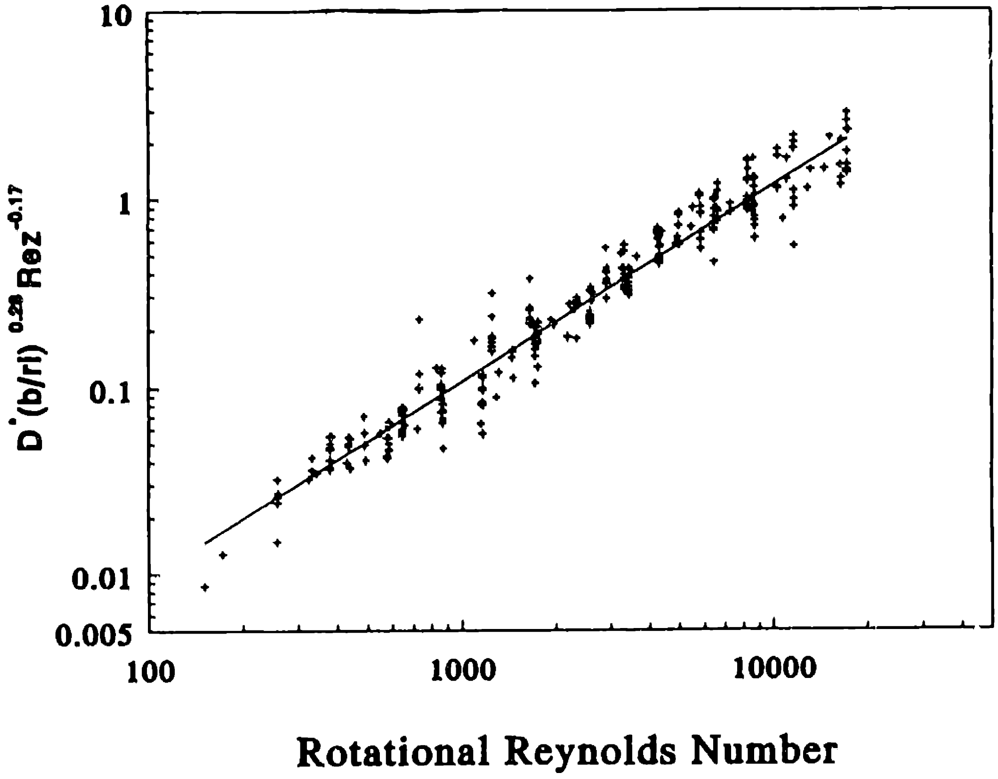

Figure 5.8: Regression fit of all dispersion data.

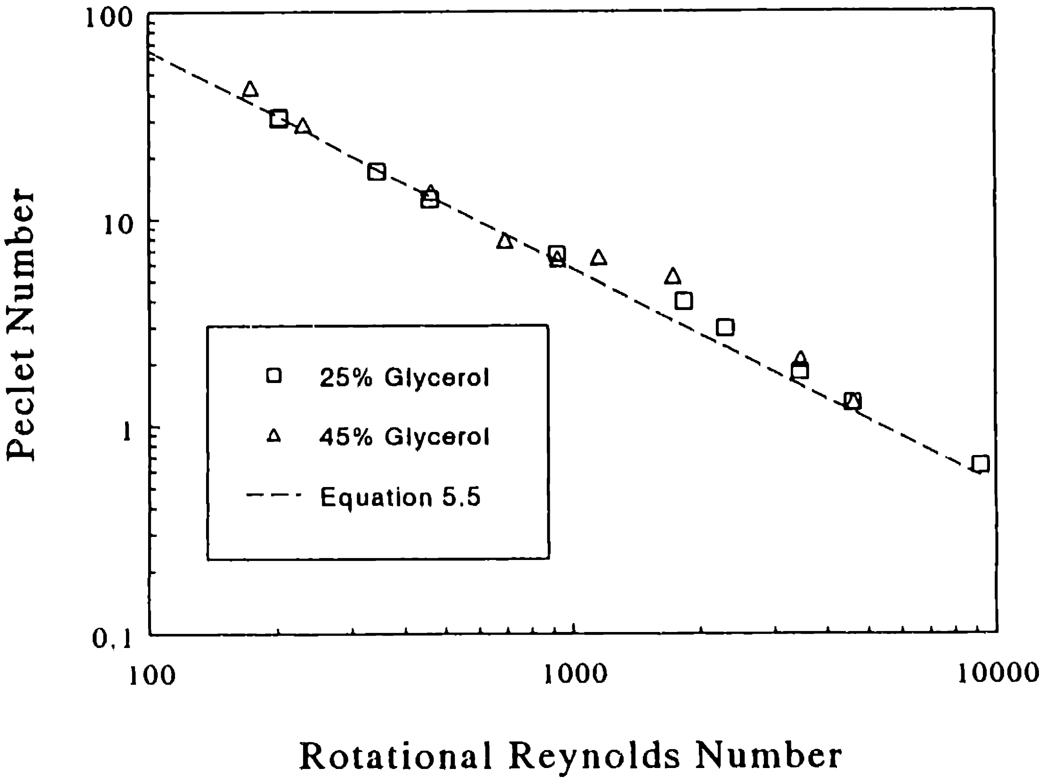

Figure 5.9: Effect of viscosity on axial dispersion.

25% and 45% with kinematic viscosities of 1.8 and 3.7 cm^2/s, respectively. Good agreement is found between the data and the correlation; the average error is 17%.

Effect of suspended particles

Residence time distribution (RTD) experiments were conducted with particle volume fractions of $f = 0, 0.035, 0.14$ and 0.35 to determine if dispersion properties in the VFR varied with the presence of suspended particles. The experiments used anion exchange agarose/silica particles with a sulphopropyl functionality in a 10 mM sodium phosphate buffer and with a blue dextran tracer (MW = 2,000,000). The volume of particles was determined by measuring the volume of the centrifuged particles and by assuming a void fraction of 0.30. This value, representing the intraparticle voids in the packed bed, was determined by a mass balance after mixing a known concentration of blue dextran with a known volume of particles and centrifuging. The velocity,

$$U = U_S/(1-f) \tag{5.6}$$

was obtained from the superficial (observed) velocity, U_S, and was used in determining the residence time and the axial Reynolds number. In general, all of the RTD curves with suspended particles showed very good agreement with the expected concentration profile (3.6); there were no indications of channeling or tailing in the experimental curves.

Dispersion coefficients determined for RTD experiments are shown in Figure 5.10; these experiments used a modified axial Reynolds number of 10 (i.e. axial Reynolds number using the superficial velocity) and cylinders of diameters 4.21 and 4.90 cm. The solid line represents the dispersion equation predicted by (5.5). Figure 5.10 shows that the dispersion coefficients for experiments with $f = 0.035$ and 0.14 are not significantly different from those of $f = 0$ particles but are about 20% higher than the dispersion coefficients predicted from the correlation. The dispersion for the highest particle loading (*f* = 0.35) is somewhat greater than the other particle loadings and appears to go through a minimum at 100 RPM. Also, it should be noted that operation with *f* = 0.35 was constrained to below 300 RPM. Above this rotation rate enough particles broke to clog the outlet mesh.

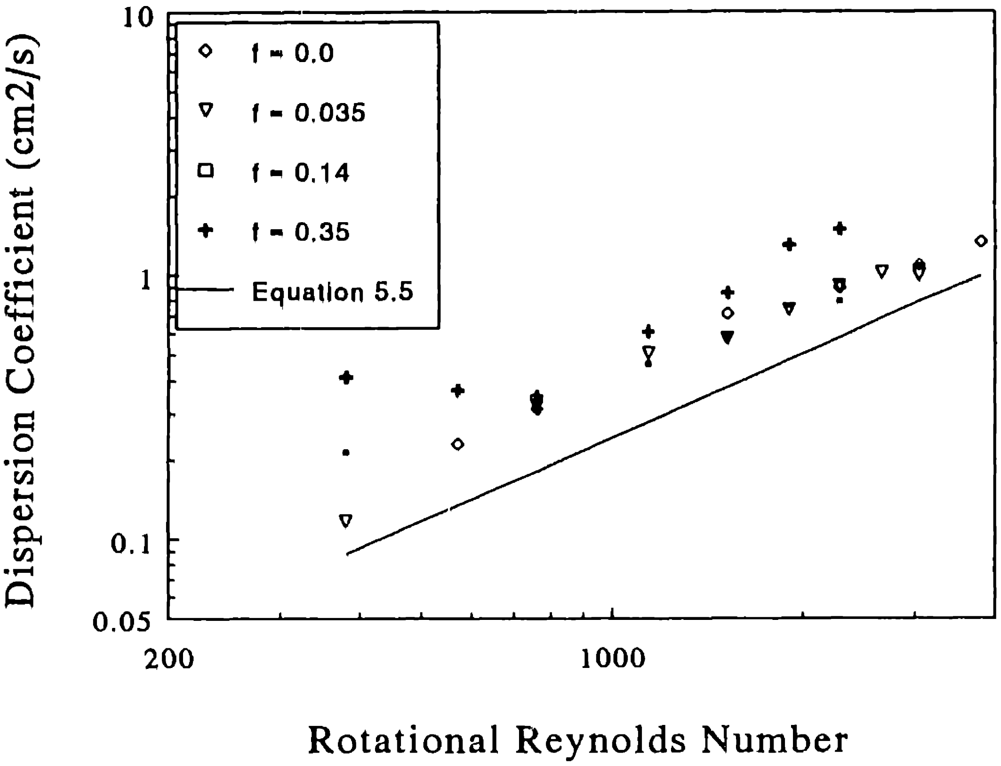

Figure 5.10: Dispersion coefficients from RTD studies with particles in the VFR. Solid line represents dispersion correlation from equation (5.5).

5.1.3. Discussion

The dispersion correlation described by equation (5.5), provides a basis for design and scale-up of vortex flow systems over a wide operating range. The operational range is known to cover several flow regimes of Taylor-Couette flow including laminar, wavy and turbulent vortices. Although the vortex structures in the three flow regimes are very different, no sudden change or discontinuity in dispersion was evident to signify a change in flow pattern or the onset of turbulence. The lack of a sharp transition is reflective of the gradual change in hydrodynamics as the vortices become increasingly turbulent.

The effect of tracer diffusivity on dispersion provides insight to the vortex structure. These experiments were performed at a low axial Reynolds number of 0.6 and with a wide gap geometry of $b/r_i \approx 0.4$ where laminar vortices are known to exist (Gu and Fahidy, 1985). If the vortex cells are truly laminar and non-overlapping, transport between cells can only occur by diffusion across the vortex boundaries. Theory of dispersion in spatially periodic systems (Rosenbluth et al., 1987) predicts that in this case D^* should vary as $(D\, u_v\, b)^{1/2}$ where u_v is the characteristic vortex velocity. Therefore, a 10-fold increase in dispersion is expected, due to the 100-fold increase in the diffusion coefficient. Instead dispersion is independent of the diffusion coefficient, as seen in Figure 5.5. If the value of $(D\, u_v\, b)^{1/2}$ is estimated by using the maximum velocity in the vortex of $u_v = \omega r_i$, the theoretical value of the dispersion coefficient is found to be at least one order of magnitude lower than the experimentally measured D^*. These findings suggest a convective interchange across the vortex boundaries, possibly caused by the small applied axial flow.

An interesting possibility for future work is to examine axial dispersion at very low rotation rates and with no axial flow. The experiments would require precisely machined cylinders with internal probes for measuring the tracer. According to theory of spatially periodic systems, dispersion should vary with the square root of the diffusivity. This relationship between dispersion and diffusion has been shown experimentally in spatially periodic Rayleigh - Bénard cells (Solomon and Gollub, 1988). Similar experiments should be able to relate dispersion in Taylor vortex flow to the theoretical predictions. Furthermore, results of the dispersion experiments could be compared to calculations utilizing the Macrotransport Theory (cf. Section 3.1) and the known velocity profile.

In addition to being independent of tracer diffusivity, the interchange between vortices is not significantly affected by the presence of a small amount of particles. There was no significant difference between the dispersion coefficients for particle loadings of up to 14% ($f = 0.14$). However, the dispersion coefficients in these experiments are higher than those predicted by the correlation (5.5). It is suspected that the higher dispersion coefficients are due either to cylinder wobble or to end effects in the reactor. Although end effects were determined to be negligible in the dispersion experiments without particles, the cylinders used in the particle experiments have a much larger dead volume at the bottom of the reactor which may cause the increased dispersion. In addition, because the inner cylinder has no bottom support an uneven rotation occurs which may increase dispersion. Experiments with better designed cylinders could easily test the two hypotheses. Although increased dispersion resulted at the highest particle loadings ($f = 0.35$), the VFR still exhibits good dispersion properties. In comparison to published literature (Chung and Wen, 1968), dispersion in the VFR is found to be comparable or lower than dispersion in traditional fluidized bed reactors at the same axial Reynolds number. In addition, the loading of $f = 0.35$ in the VFR is higher than typical operation of fluidized beds using the same particles (Pharmacia, 1994) which tend to have a 2 to 5 fold bed expansion, corresponding to particle volume percents of approximately 12 to 30%. The high particle loadings in the VFR, along with good dispersion and mass transfer properties (discussed in Section 5.2) make the VFR a viable alternative to a traditional fluidized bed.

It is difficult to compare the results from the present dispersion study with those of other authors as most of the prior work used a different range of rotational Reynolds numbers and no axial flow. Both Tam and Swinney (1987) and Enokida *et al.* (1989) in their studies on axial dispersion in Taylor-Couette flow without axial flow fit the dispersion coefficient to the equation

$$D^{*} = ATa^{B} \; .$$

The exponent B was found to be 0.81 in Enokida's study and to range from 0.69 to 0.86 in Tam and Swinney's work; these exponents are slightly lower than the corresponding value of $B = 1.05$ obtained from (5.5). The magnitude of the measured dispersion coefficients is consistent between this study and previous works. Studies of axial dispersion without axial flow yielded dispersion coefficient varying from 0.5 to 8 cm^2/s (Tam and Swinney, 1987), from 0.1 to 9 cm^2/s (Enokida *et al.*, 1989) and from 0.3 to 9 cm^2/s (Crookenwit, 1953). In comparison, the dispersion coefficients in this work range from 0.01 to 10 cm^2/s.

Enokida and coworkers (1989) additionally examined axial dispersion in Taylor-Couette flow with axial flow. A different form of the correlation was used where the increase in dispersion upon introduction of axial flow is assumed to be proportional to the axial velocity. The correlation fit the data with an error of approximately 25%. The data from their experiments are suspect as it is likely that the long term limit assumed in the one-dimensional model was violated because of the high axial flow rates. The axial Reynolds numbers used in the experiments, ranging from 60 to 250, are much higher than in this study.

Nearly a 1000 fold difference is obtained between dispersion coefficients at the highest and lowest rotation rates examined. For the current vessel, this corresponds to near plug flow performance at the lowest rotation rates and stirred tank (CSTR) performance at the highest rotation rates. Unlike other solid-liquid reactors (i.e. traditional fluidized bed, tubular reactors) dispersion in the Taylor-Couette system is primarily independent of flow rate. This is a useful feature for reactor control as the extent of reaction can be adjusted independently of the flow rate. Of course, an additional consideration in performance of a reactive vortex flow system is mass transfer to the active surface. The problem of external mass transfer is addressed in the following section.

5.2 Mass Transfer to Suspended Particles

Mass transfer to the active surface, or external mass transfer, can have a great impact on reactor performance. Maximum productivity of a solid-liquid reaction is obtained when the external mass transfer rate is much faster than the reaction rate. In the other limit when the reaction rate is much faster than the mass transfer rate, the reaction and reactor performance become mass transfer limited. In this case, the reactor performance can only be improved by increasing the mass transfer rate; increasing the catalytic enzyme loading has no effect. By quantifying external mass transport in the VFR, the reactor may be engineered to optimize performance. The variables which effect mass transport to the suspended particles are the physical parameters, such as gap ratio and particle diameter, and the operational parameters such as rotation rate and axial velocity. The following section examines the effect of the Taylor number, axial Reynolds number, particle density and gap ratio on mass transfer to suspended particles in the VFR. The effect of the particle size and viscosity is obtained by analogy from published literature on mass transfer in fluidized beds.

5.2.1 Data Analysis

A mass transfer correlation can be obtained with the aid of dimensional analysis. In a non-reacting vortex flow system, there are 10 variables (viscosity, fluid density, particle density, diffusion coefficient, rotation rate, gap width, axial velocity, particle diameter, inner cylinder radius, mass transfer coefficient) and 3 dimensions (time, length, mass). It will be assumed that the mass transfer coefficient is independent of concentration. According to the pi-theorem (Bird *et al.*, 1960), mass transfer can be described with 10-3=7 dimensionless variables. A convenient grouping is

$$Sh_p = \frac{k_{mt} d_p}{D} = \alpha Ta^a Sc^b Re_z^c \left(\frac{d_p^3 g}{v^2}\right)^d \left(\frac{\rho_p - \rho_L}{\rho_L}\right)^e \left(\frac{b}{r_i}\right)^f \tag{5.7}$$

where Sh_p is the Sherwood number based on particle diameter. The Schmidt number exponent is set to $b=1/3$ in accordance with the heat-mass transfer analogy for boundary layers (Bird *et al.*, 1960). Five unknown exponents remain which must be correlated to experimental data.

The mass transfer coefficient k_{mt} is determined by analysis of the data from the benzoic acid dissolution studies, described in Section 4.3. A mass balance yields

$$\frac{d\overline{C}}{dt} = \frac{k_{mt}}{V_l} A_s(t)(C_{sat} - \overline{C}(t)) \tag{5.8}$$

where C_{sat} is the concentration of saturated benzoic acid in water (i.e. concentration at the particle surface), $\overline{C}$ is the bulk liquid concentration, V_l is the liquid volume and $A_s(t)$ is the surface area of the benzoic acid particles. Equation (5.8) is used to describe the behavior of both the continuous and batch experiments. In the batch experiments, t represents time from the start of the experiment; in the continuous experiments, $t = z/U$ is the residence time in the vessel at position z. It is assumed that liquid and solid dispersion are negligible in the continuous experiments. This assumption is valid as the overall conversion in the experiments is kept low (typically less than 60%) such that reactor performance is essentially independent of dispersion.

The initial surface area of the benzoic acid particles is determined from the pressure drop across a packed column (cf. Section 4.3). Although the particles are not spherical, the mass transfer is expected to be independent of particle shape (Shen *et al.*, 1985). The surface area is assumed to decrease as a sphere upon benzoic acid dissolution. The relationship between the particle size and reactor concentration is obtained from a mass balance between the dissolved benzoic acid and the particles

$$V_l(\bar{C}(t)-\bar{C}(0)) = M_s(0)-M_s(t) = M_s(0)\left(1-\left(\frac{d_p(t)}{d_p(0)}\right)^3\right) \tag{5.9}$$

where $M_s = N_p\,\rho_p\,\pi\,d_p^3/6$ is the total mass of the solid benzoic acid particles of density ρ_p, and number N_p, and effective particle diameter d_p. By substituting the relationship,

$$\frac{d_p(t)}{d_p(0)} = \sqrt{\frac{A_s(t)}{A_s(0)}}\ , \tag{5.10}$$

into (5.9) the expression

$$A_s(t) = A_s(0)\left(1+\frac{V_l}{M_s(0)}(\bar{C}(t)-\bar{C}(0))\right)^{2/3} \tag{5.11}$$

is obtained relating the surface area to known parameters. Equation (5.8) and (5.11) are numerically integrated over time to obtain the concentration profile. For a batch experiment, the mass transfer coefficient is determined from a least squares fit of the experimental concentration versus time curve. The mass transfer coefficient from a continuous experiment is determined from the steady state concentration.

5.2.2 Results

The suspended benzoic acid particles were used in both batch and continuous mass transfer studies. The experiments proved to be difficult to conduct reproducibly due to the nature of the two phase (solid-liquid) system. In general, the measured mass transfer coefficients were reproducible within approximately 25%. Except where noted, all experiments were performed in the horizontal orientation of the VFR, which provided more reproducible results than the vertical orientation. All experiments, except those varying reactor geometry, used a gap ratio of 0.164.

Effect of Geometry

Batch experiments were performed to determine the effect of reactor geometry on mass transfer. The gap ratio was varied from 0.10 to 0.51 by using different inner and outer cylinders. All experiments used a constant modified Taylor number of 1880. The results, shown in Figure 5.11, indicate that mass transfer varies as $(b/r_i)^{-1.1}$ with $R^2 = 0.99$.

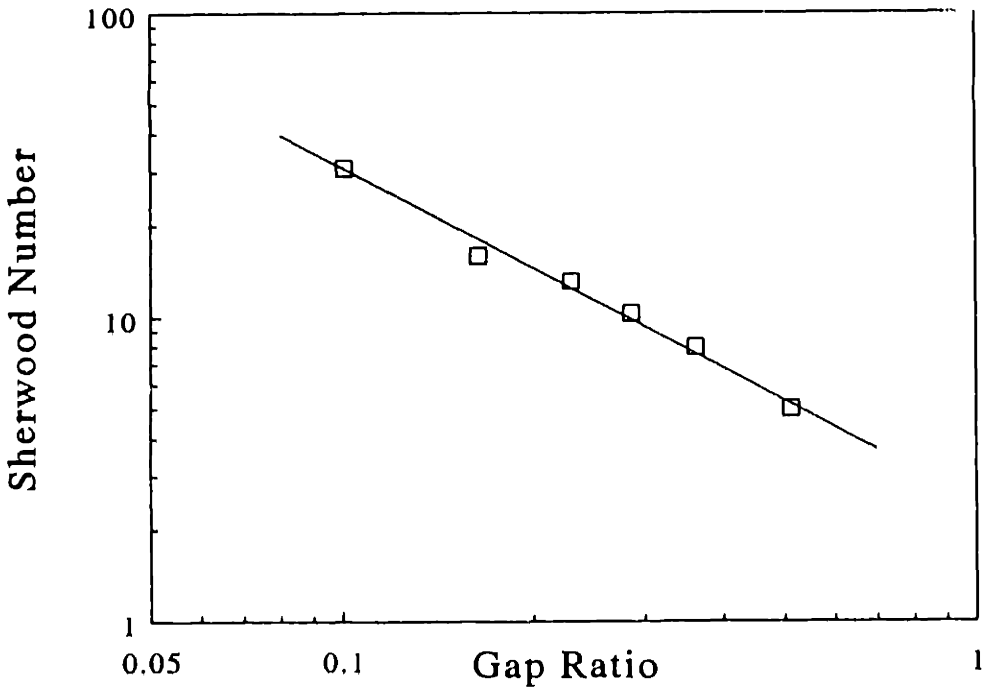

Figure 5.11: Effect of reactor geometry on mass transfer to suspended benzoic acid particles.

Effect of Particle Density

The effect of particle density was examined through mass transfer experiments using a neutrally buoyant solution of 29% calcium chloride. The densities of the solution and the solids are equal at 1.27 g/cm^3; the viscosity of the solution is 0.032 g/cm·s. The diffusion coefficient for benzoic acid in 29% calcium chloride is estimated to be 2.4x10^{-6} cm^2/s by using the Stokes-Einstein relationship (Bird *et al.*, 1960) which states that the diffusivity is inversely proportional to the viscosity. The experiments with neutrally buoyant particles were conducted in batch, using both the horizontal and vertical configurations. The results are plotted in Figure 5.12, along with results from similar mass transfer experiments using benzoic acid in water. The Sherwood number is normalized by $Sc^{1/3}$ to account for the differences in the fluid properties.

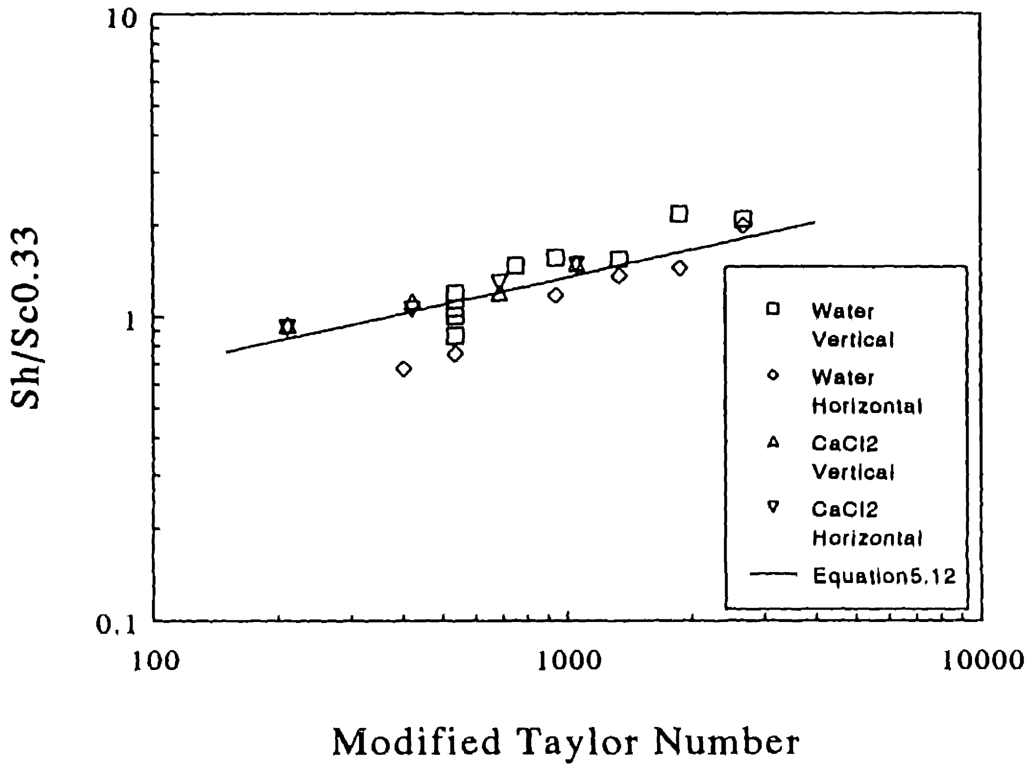

Figure 5.12: Effect of particle and fluid density on mass transfer of suspended benzoic acid particles in batch VFR (both vertical and horizontal configurations). Data includes benzoic acid particles in water and in a neutrally buoyant solution of 29% $CaCl_2$. Line is regression fit for all data.

Several points are evident from the results in Figure 5.12. Primarily, the magnitude of the normalized mass transfer does not vary significantly between benzoic acid dissolution in water or in calcium chloride indicating that mass transfer is independent of the particle and fluid density difference. As a first estimate, the exponent e in (5.7) may be set to zero. While more experiments using calcium chloride solutions of different densities would be necessary to verify this finding, the relationship provides a preliminary estimate for determining mass transfer in the VFR.

The second feature in Figure 5.12 is the effect of VFR orientation on mass transfer. In the neutrally buoyant system, mass transfer is independent of VFR orientation. This result is expected as the particles do not settle under the influence of gravity. In the benzoic acid-water studies, mass transfer is higher in the vertical set-up than in the horizontal set-up. The higher mass transfer in the vertical set-up may be due to particles settling to the reactor bottom and causing higher mass transfer near the bottom port where the samples are withdrawn. Alternatively, the higher mass transfer may be due to particles settling across the high velocity vortex boundaries. As the particles pass through the vortex boundary, they could experience a small region of high velocity gradients and enhanced mass transfer. The correct mechanism for the increased mass transfer in the vertical reactor could be distinguished by using internal probes (i.e. conductivity probes) located at the top and bottom of the VFR.

The final feature of Figure 5.12 is the slope of the lines. Table 5.2 presents a least squares fit of the individual data sets and of the combined data. The slopes of the lines for the benzoic acid-water system are higher than those of the neutrally buoyant system. The higher slopes may be due to a heavy weighting of questionable data points at low rotation rates. The mass transfer coefficients at the lowest rotation rates may be artificially low due to particles settling out of the vortices to the walls or to the bottom of the VFR. Particles on the walls were observed in some of the benzoic acid-water batch runs at low rotation rates but were not a problem in the continuous flow experiments as the axial flow helps to resuspend the particles. The slope of the combined data for the batch runs is 0.38; this line is plotted in Figure 5.12. Although there is much scatter about the line, all except 3 of the data points fall within the experimental error of 25%.

Mass Transfer Fluid	VFR Orientation	Best Fit Slope
Water	Vertical	0.49
Water	Horizontal	0.57
29% $CaCl_2$	Vertical	0.27
29% $CaCl_2$	Horizontal	0.30
ALL DATA		0.38

Table 5.2 - Regression parameters for batch mass transfer experiments.

By combining the results of Figures 5.11 and Figure 5.12 mass transfer of the benzoic acid particles in a batch VFR may be described by

$$Sh_p = 0.014 Ta_m^{0.38} Sc^{0.33} \left(\frac{b}{r_i} \right)^{-1.1} . \tag{5.12}$$

In the following sections, a similar correlation is developed for a continuous VFR.

Effect of Rotation Rate

Figure 5.13 shows the results of continuous flow mass transfer experiments using benzoic acid and water in the horizontal VFR configuration. The Sherwood number is plotted against modified Taylor number for constant axial Reynolds number. For Re_z= 7 and 28, the slopes from the regression fits are 0.35 and 0.32, with R^2 values of 0.96 and 0.97, respectively. The slopes are in close agreement with the slope of 0.38 in the batch mass transfer correlation (5.12). Consequently, mass transfer in the continuous flow VFR can be described to vary as $Ta_m^{0.35}$.

Effect of Axial Flow

The effect of axial flow on mass transfer was examined by varying the axial flow rate at constant modified Taylor number. Figure 5.14 shows the results of two sets of experiments at modified Taylor numbers of 355 and 1875. The slopes of the lines are equal to 0.37 and 0.38 for Ta_m of 355 and 1875, with R^2 values of 0.89 and 0.99, respectively. These results indicate that mass transfer varies as $Re_z^{0.37}$.

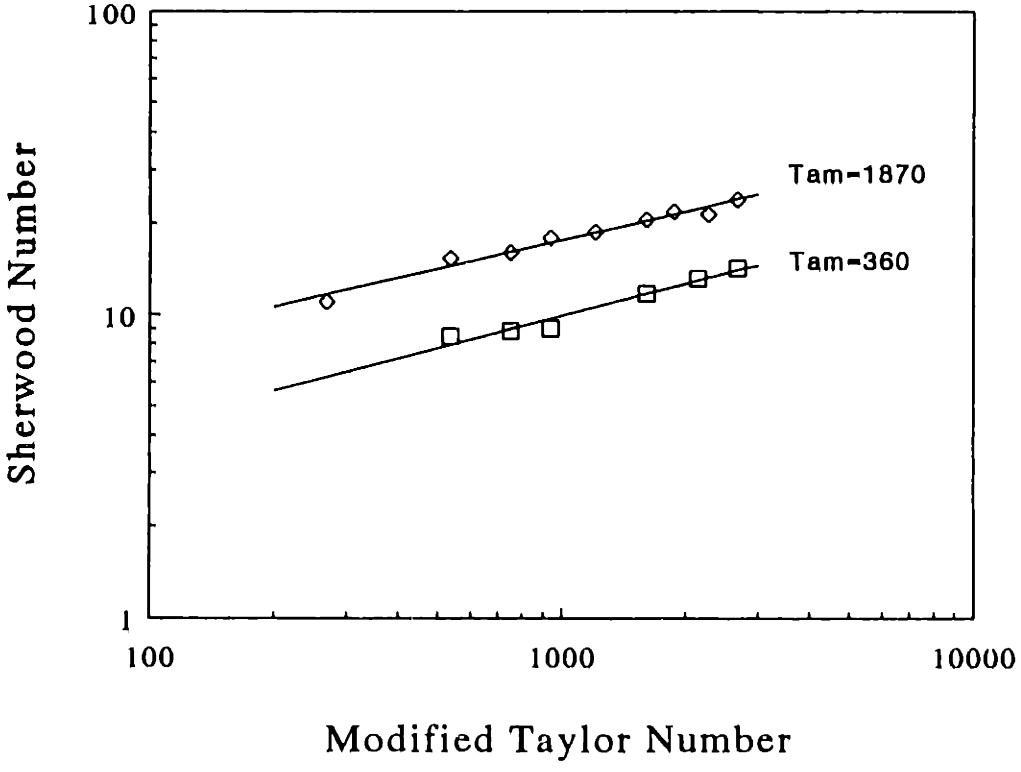

Figure 5.13: Effect of rotation rate on mass transfer to suspended benzoic acid particles.

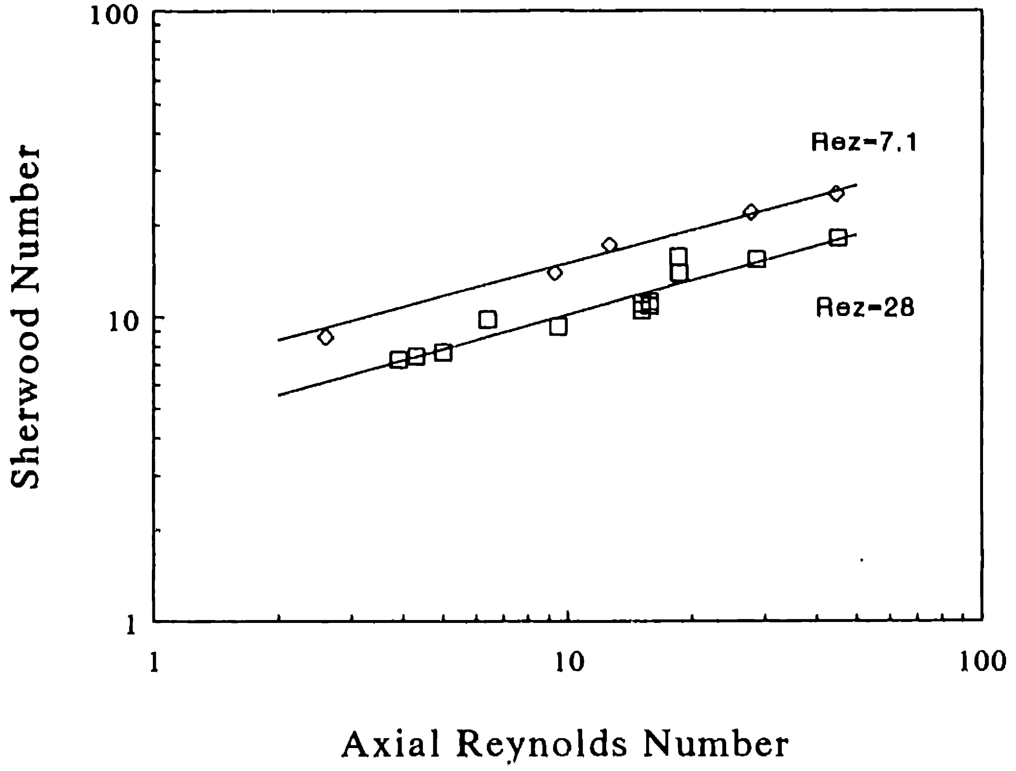

Figure 5.14: Effect of axial flow rate on mass transfer to suspended benzoic acid particles.

Effect of Particle Size

By combining the results of the data in Figures 5.11 through 5.14, mass transfer to suspended benzoic acid particles in a continuous VFR can be described by

$$Sh_p = 0.006 Ta_m^{0.35} Re_t^{0.37} Sc^{0.33} \left(\frac{b}{r_i} \right)^{-1.1} . \tag{5.13}$$

This correlation accounts for all parameters in (5.7) except for the geometric parameter, $d_p^3 g / v^2$. The geometric dependence could not easily be accounted for experimentally, as the benzoic acid particles were a mixture of non-uniform, non-symmetrical particles.

The dependence of particle size on mass transfer can be estimated by reviewing mass transfer correlations in traditional fluidized beds. Two types of correlations are prevalent for describing mass transfer to particles in fluidized beds (Tournie *et al.*, 1979). The first type explicitly uses the void fraction, or degree of bed expansion. The second form uses the dimensionless group $d_p^3 g/\nu^2$. Because the void fraction is a function of the axial flow in traditional fluidized beds but not in the VFR, the second form is preferable.

In a study of mass transfer from irregularly shaped particles, Shen et al. (1985) found the mass transfer coefficient to be independent of both particle size and shape. In a separate work, Tournie et al. (1979) found the mass transfer coefficient to vary as $d_p^{-0.04}$. These results suggest that the mass transfer coefficient is independent of particle size for traditional fluidized beds. In analogy, the mass transfer coefficient for the VFR can be estimated to be independent of particle size by setting $d = 1/3$ in (5.7).

If the assumed particle size relationship is incorporated into (5.12), the expression

$$Sh_p = 5 \times 10^{-3} Ta_m^{0.38} Sc^{0.33} \left(\frac{b}{r_i} \right)^{-1.1} \left(\frac{d_p^3 g}{\nu^2} \right)^{0.33} \tag{5.14}$$

is obtained for mass transfer to suspended particles in a batch VFR. The expression

$$Sh_p = 2 \times 10^{-3} Ta_m^{0.35} Re_z^{0.37} Sc^{0.33} \left(\frac{b}{r_i} \right)^{-1.1} \left(\frac{d_p^3 g}{\nu^2} \right)^{0.33} \tag{5.15}$$

describes mass transfer to suspended particles in a continuous VFR. Because the Sherwood number contains a factor of d_p, setting the mass transfer coefficient independent of the particle size makes Sh proportional to d_p in (5.14) and (5.15).

5.2.3 Discussion

The correlations presented in (5.14) and (5.15) allow estimation of mass transfer to (or from) suspended particles in the VFR. The experimental range was Ta_m=300 to 3000 and b/r_i = 0.10 to 0.51 with Re_z= 4 to 45 in the continuous studies. Because of the high experimental uncertainties in the benzoic acid dissolution studies these correlations are only valid to about 25%. Further refinement of the correlations requires a more reproducible experimental method. One approach is to monitor mass transfer with internal probes, such as conductivity probes, so samples would not need to be withdrawn from the reactor. In addition, the assumptions regarding particle shape, size and density need to be verified to further increase the confidence in the correlations. Although the data from the neutrally buoyant system reveal that the effect of particle density is negligible, there is not enough data to extrapolate this relationship outside of the particle and liquid densities studied here ($\Delta\rho/\rho_l = 0$ to 0.27). The correlations should be valid for the model validation experiments as the density of the agarose silica particles ($\rho_p \approx 1.2$) is close to the density of the benzoic acid particles ($\rho_p = 1.27$). Also, further experiments need to be done with particles of defined geometry to validate the assumed effect of particle size on mass transfer. A different mass transfer system should be used because of the irregularities in the benzoic acid particles.

The ideal mass transfer model is large (> 100 μm) solid (non-porous) particles with a surface that dissolves, adsorbs or reacts. One possible mass transfer model is non-porous benzoic acid particles. The non-porous particles are made from a labor intensive process of machining molds for spherical particles, filling the molds with melted benzoic acid, and cooling the particles. Particles could be made of different sizes by partial dissolution. Alternatively, future experiments could use commercial ion exchange particles. Unfortunately, solid commercial particles are typically small (< 5 μm) and large particles of the size of interest (>100 μm) are porous. The effect of particle size on mass transfer could be examined through experiments using small non-porous ion exchange particles. However, the mass transfer from small particles may not be representative of larger ones. Under certain conditions, large porous particles may be used to analyze mass transfer. In the limit of irreversible first order kinetics, the overall kinetic rate is represented by (3.27). In this case, the effects of mass transfer and reaction can be separated by recognizing that k_{int} is constant for a given immobilized enzyme and that k_{mt} is a function of operating conditions. A set of data collected for different operating conditions can be regressed to obtain the parameter k_{int} and the dependence of k_{int} on the operating condition. The limit of first order kinetics occurs for desorption and for reaction or adsorption with low substrate concentrations. The limit of irreversibility occurs for low reverse reactions, such as for adsorption at low loading on the solid support or for desorption at high loading. In an attempt to examine a different mass transfer system, experiments were conducted in the VFR using the agarose-silica anion exchange particles adsorbing bromophenol blue at low dye concentration. However, the mass transfer-adsorption rate was too fast to measure; all of the dye immediately bound the particles. Future experiments could use a larger adsorbing molecule (such as a protein) to slow down external mass transfer to a measurable rate.

There are very few studies on mass transfer in Taylor-Couette flow to compare with the results presented above. Kataoka *et al.*(1975) published results of a few particles dissolution studies in their paper on mixing in Taylor-Couette flow. The experiments used large molded benzoic acid particles (0.125 cm) in a neutrally buoyant solution of 50% sucrose. The values of $Sh/Sc^{1/3}$ they obtained ranged form 0.8 to 2.4, in close agreement with the values of 0.6 to 2.0 shown in Figure 5.12. Koenig *et al.*(1954) examined mass transfer and adsorption in a counter-current ion exchanger. They made many assumptions in determining the mass transfer coefficients including plug flow and irreversible adsorption.; deviations from these assumptions were lumped into the mass transfer coefficient. Thus, the reported mass transfer coefficient was not the same parameter as described by (5.8) but rather an overall parameter indicating adsorber performance. The magnitude of the mass transfer coefficients, ranging from 1.5×10^{-3} to 4.0×10^{-2} cm/s are comparable to those in the current study. In contrast to the present study, the mass transfer coefficient was found to decrease with increasing rotation rate. This finding is most likely due to lumping the dispersion effects into an effective mass transfer coefficient. Whereas the studies presented in this chapter indicate that increasing the rotation rate causes subsequent increases in the dispersion coefficient and the mass transfer coefficient, the increased dispersion may cause a net decrease in the overall adsorber performance.

The correlation for mass transfer in the continuous VFR (5.15) can be compared to mass transfer in traditional fluidized beds. For example, Shen et al. (1985) found the mass transfer coefficient in a fluidized bed to vary as

$$k_{ml} = 2.4918 \times 10^{-3} U^{0.2664} d_p^{-0.0242} \quad . \tag{5.16}$$

The mass transfer coefficients predicted from (5.16) range from 1.0×10^{-4} to 1.9×10^{-3} cm/s for the fluid velocities used in the continuous VFR experiments. The actual mass transfer coefficients, ranging from 3.0×10^{-3} to 1.6×10^{-2} cm/s, are an order of magnitude higher than those predicted by (5.16). Thus, it can be seen that the VFR provides higher mass transfer than the traditional fluidized bed. This result is to be expected since a VFR with no rotation is simply an annular fluidized bed. Unfortunately, due to the current VFR configuration this limit could not be experimentally tested. The inlet and outlet ports are not evenly distributed and channeling occurs without rotation.

Similar to the dispersion studies, the above investigation of mass transfer to suspended particles in the VFR utilizes a macroscopic approach which does not consider the complicated hydrodynamics of Taylor-Couette vortex flow. Mass transfer from a suspended particle is a function of particle location in the vortex, the local velocity profile and the particle motion. Several forces act on the particles including gravitational, centripetal, lift and drag forces. Studies of particle motion and location may aid in describing mass transfer to suspended particles. Theoretical and experimental studies have described the equilibrium position (Halow and Wills, 1970a, 1970b) and the mass transfer rate (Acrivos, 1980) of the suspended particles in simple Couette flow. Similar studies in Taylor-Couette flow may provide insight into the mass transfer mechanism from the suspended particles.

Chapter 6 -

Mathematical Model Simulations

In this section, the information on mass transfer from Chapter 5 is incorporated into the mathematical model presented in Chapter 3 for the purpose of examining VFR operation through model simulations. Three unknown coefficients are necessary to solve the model's equations - the dispersion coefficient, the overall reaction rate and the average velocity. The average velocity is an operational parameter and can easily be measured. The overall reaction rate is a function of the external mass transfer, the internal mass transfer and the intrinsic kinetics; the internal mass transfer and intrinsic kinetics may be determined in experiments which are independent of operation in the VFR. Only the axial dispersion and the external mass transfer rate are dependent on the operational and design parameters of the VFR. The respective relationships are summarized in Table 6.1.

The effect of the major operational parameters on mass transport can be examined from the information in Table 6.1. The performance of the VFR depends upon the relationships between the reaction kinetics, external mass transfer resistances and dispersion. Changing the operational parameters often has offsetting effects. For example, increasing the rotation rate causes higher external mass transfer but also higher dispersion. The higher mass transfer tends to increase conversion in the VFR while the higher dispersion tends to decrease conversion. These counteracting effects are discussed below for different reaction rate limits.

Transport Property and Correlation	**Dependence on:**	
	Axial Flow Rate	**Rotation Rate**
(5.5) Axial Dispersion $Pe^{-1} = 7.2x10^{-3}(b/r_i)^{-0.28} Re_\theta^{1.05} Re_z^{-0.83} (2b/L)$	low	high
(2.14) Mass Transfer to the Wall $Sh = 0.5\, Ta^{0.5}\, Sc^{1/3}$	none	moderate
(5.15) Mass Transfer to Suspended Particles $Sh_p = 2 \times 10^{-3} Ta_m^{0.35} Re_z^{0.37} Sc^{0.33} \left(\frac{b}{r_i}\right)^{-1.1} \left(\frac{d_p^3 g}{\nu^2}\right)^{0.33}$	moderate	moderate

Table 6.1: Summary of transport properties and correlations for the vortex flow reactor.

6.1 Particle VFR Simulations

Model simulations were performed to predict the general effect of operational and design parameters on conversion in a VFR containing suspended immobilized enzyme particles. These simulations assume a steady state, irreversible first order reaction. Equation (3.11) was solved with inputs of overall reaction rates, dispersion coefficient (Peclet number) and velocity coefficient. The average fluid velocity U was used for the mean species velocity

U^* while the dispersion coefficient and the external mass transfer coefficient were calculated from (5.5) and (5.15), respectively. Many of the simulations presented in this section use a high enzymatic reaction rate which is typically associated with internal mass transfer limitations and high Damkohler numbers. However, since the simulations examine steady state operation, the nonreactive coefficients for the dispersion coefficient and the mean fluid velocity can be used in the model. In addition, the overall reaction parameter K^* is related to the intrinsic reaction rate and the external mass transfer coefficient as described in Section 3.3.

Simulations of VFR performance help to illustrate the impact of operational and design parameters on reactor conversion. Figure 6.1 shows such an example. The lines on the graph show the locus of rotation rates and axial flow rates where constant conversions ranging from 86 to 98% are obtained. The simulation conditions are r_i = 2.225 cm, b = 0.38 cm, Sc = 1000, k_{int} = 0.08 s^{-1}, f = 0.20, d_p = 200 μm, and t_r = 4 min. Higher conversions are obtained when operating below a constant conversion line and lower conversions are obtained when operating above the line. For a fair comparison, the simulations were conducted at constant residence time. As a consequence, higher axial Reynolds numbers correspond to longer reactor lengths. The simulations were performed in the kinetically limited regime where the ratio of the surface kinetic rate to external mass transfer rate, $k_{int}V_s/k_{mt}A_s$, ranges from 0.01 to 0.1. The operating lines of constant conversion in Figure 6.1 demonstrate the balance between mass transfer and dispersion in the VFR. In this example, nearly any axial flow rate may be chosen and the rotation rate adjusted correspondingly to provide the desired reactor conversion. This flexibility of operation in the VFR is unlike traditional solid-liquid bioreactors where only one operational parameter (axial flow rate) defines conversion. In the VFR, there are two important control parameters - axial flow rate and rotation rate. The extra degree of control is useful in operations where the feed composition or the flow rate may change with time.

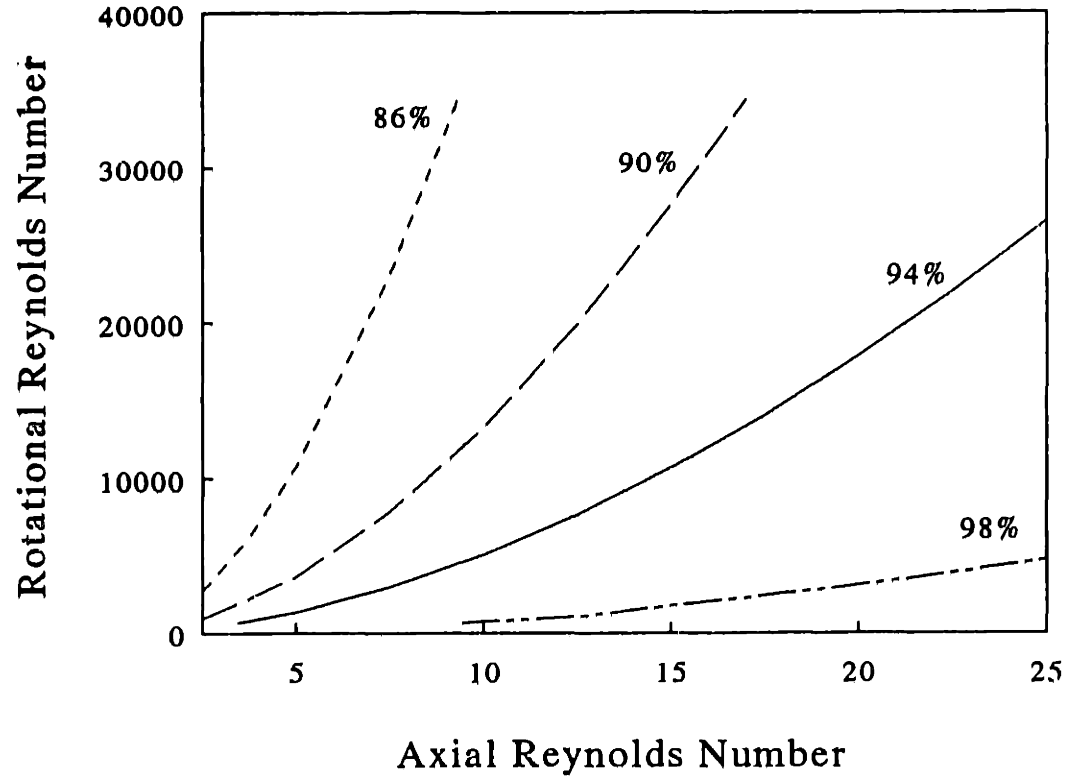

Figure 6.1: Constant conversion operating curves for a VFR containing suspended immobilized enzyme particles. VFR contains a constant amount of enzyme per unit volume; the residence time is kept constant by varying the reactor volume with Re_z Operating parameters are: $r_i = 2.225$ cm, $b = 0.38$ cm, $Sc = 1000$, $k_{int} = 0.08\ s^{-1}$, $f = 0.20$, $d_p = 200\ \mu m$, $t_r = 4$ min.

A controllable and constant level of conversion is critical in some applications such as in an extracorporeal reactor. Traditional bioreactors, such as a hollow fiber or fluidized bed reactors, are less controllable as the flow rate is the sole operating parameter effecting conversion.

Simulations further help to better understand the simultaneous transport phenomena in the VFR. For example, both dispersion and external mass transfer increase with increasing rotation rate. The increased dispersion tends to lower reactor conversion whereas the increased mass transfer tends to increase conversion. These offsetting effects

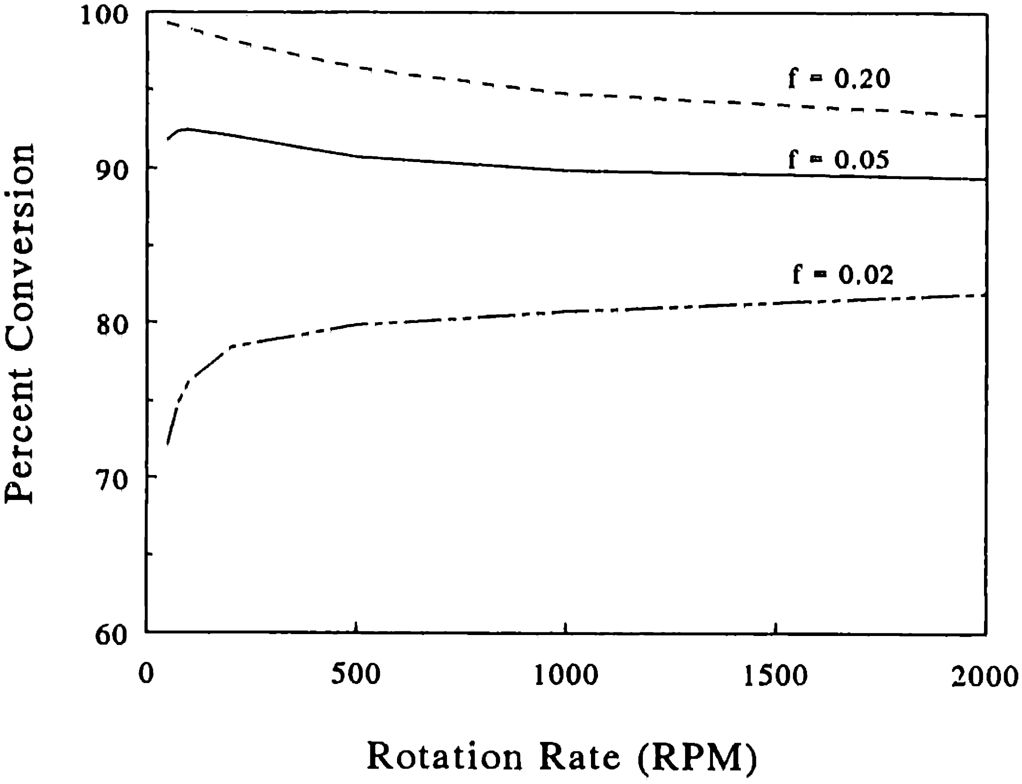

Figure 6.2: Conversion *vs.* rotation rate for kinetically limited ($f = 0.20$, $k_{int} = 1.0\ s^{-1}$), mass transfer limited ($f = 0.02$, $k_{int} = 10\ s^{-1}$) and intermediate ($f = 0.05$, $k_{int} = 4.0\ s^{-1}$) regimes. VFR contains a constant amount of enzyme distributed on differing amounts of surface area. Operating parameters are: $r_i = 2.225$ cm, $b = 0.225$ cm, $Sc = 1000$, $d_p = 200\ \mu m$, and $t_r = 1$ min.

are apparent in Figure 6.2, which shows three sets of simulations. A constant amount of enzyme is used in the three simulations with different total surface areas, or volume fraction of particles. The effect of the operational parameters in both the kinetic and mass transfer limited regimes is evident in Figure 6.2. The simulation conditions are $r_i = 2.225$ cm, $b = 0.225$ cm, $Sc = 1000$, $d_p = 200\ \mu m$ and $t_r = 1$ min. The top line ($f = 0.20$) shows kinetic limitations; in this case, the ratio of the surface kinetic rate to external mass transfer rate, $k_{int}V_s/k_{mt}A_s$, ranges from 0.2 to 0.8. As the rotation rate increases, conversion decreases due to increased dispersion. Since the reaction is kinetically limited due to the large surface area, the increasing mass transfer has a negligible effect on the conversion. The bottom line ($f = 0.02$) shows mass transfer limitations where the ratio of surface kinetic rate to external mass transfer rate varies from 2.1 to 7.6. As the rotation rate increases, mass transfer and conversion increase. The middle line ($f = 0.05$) shows the competing effects of mass transfer and dispersion. In this case, the surface kinetic rate and the external mass transfer rate are approximately equal. A slight maximum followed by a decline in conversion is seen with increasing rotation rate. Even though the conversion is almost constant over the entire range of rotation rates in this case, the second parameter of axial flow can be adjusted to change the reactor performance.

Predictions from the model simulations are useful in evaluating the performance potential of VFR applications. The model is a powerful tool capable of predicting reactor conversion for a wide range of operating conditions; the only additional experimental data necessary is the intrinsic kinetics. Chapters 7 and 8 present experiments validating the mathematical model and the predictions shown above. In Appendix A, the model is used further to predict the best design and operating condition for a heparinase reactor.

6.2 Wall VFR Simulations

This section explores the effects of mass transfer and reaction in a VFR containing immobilized enzyme on one or both of the cylinder walls. As above, the simulations use (3.11) to calculate the overall conversion and assume a steady state, irreversible first order reaction. The dispersion coefficients were determined by (5.5) and the external mass transfer coefficient were determined from (2.14) for the given operating parameters.

The effects of rotation rate and axial flow rate in a VFR containing immobilized enzyme on the wall is shown in Figure 6.3. These "isoconversion curves" show the operating conditions necessary to obtain constant conversions of 86%, 90% and 94%. The simulation conditions are r_i= 2.225 cm, b = 0.225 cm, Sc = 1000, k_{int}= 0.1 s^{-1} and t_r = 15 min; the immobilized enzymatic membranes are located on both the inner and outer cylinders and have a thickness of 60 μm. As in Figure 6.1, the length and volume of the reactors were adjusted proportionally to the axial Reynolds number to provide a constant residence time. The simulation conditions are primarily in the kinetics limited regime where the ratio of the surface kinetic rate to external mass transfer rate, $k_{int}V_s/k_{mt}A_s$, ranges from 0.07 to 0.6. Figure 6.3 again illustrates the flexibility of the VFR; both the rotation rate and the axial flow rate may be adjusted to provide the desired reactor performance.

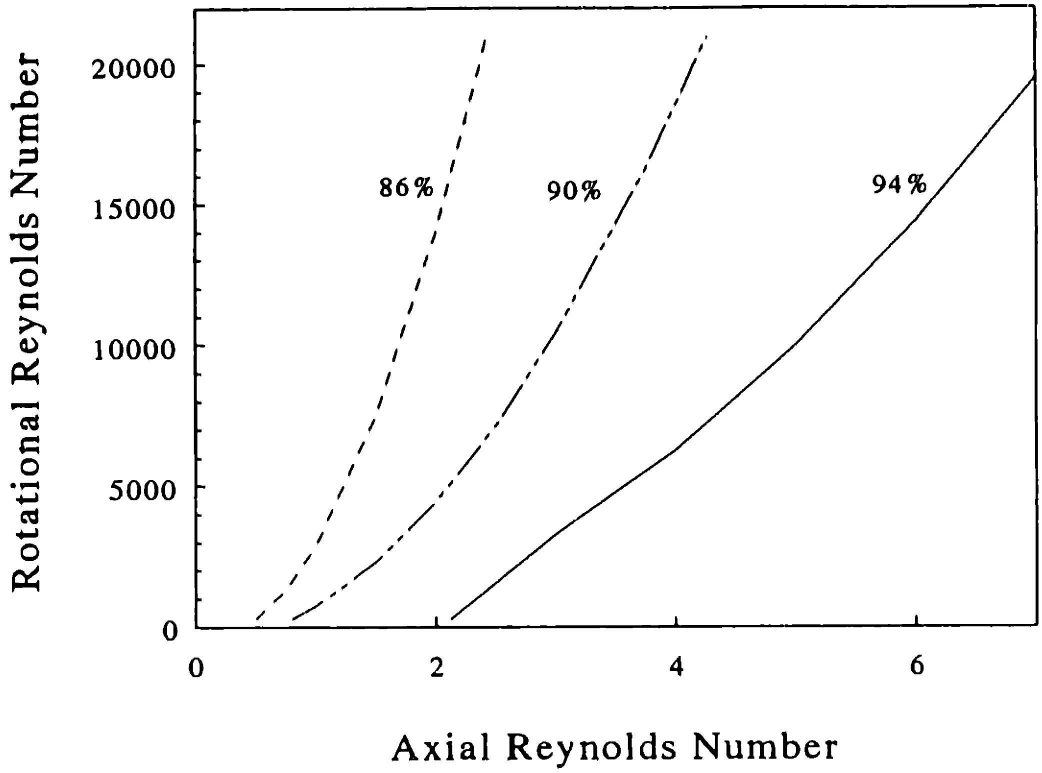

Figure 6.3: Constant conversion operating curves for a VFR with membrane on both cylinder walls. VFR contains a constant amount of enzyme per unit volume; residence time is kept constant by varying reactor volume. Operating parameters are: r_i= 2.225 cm, b = 0.225 cm, Sc = 1000, k_{int}= 0.1 s^{-1}, t_r = 15 min and membrane thickness= 60 μm.

Figure 6.4 shows the tradeoff between dispersion and external mass transfer resistances for a VFR with constant volume and a constant amount of enzyme on the cylinder walls. The simulations are in the "intermediate kinetic regime" where surface reaction rates and external mass transfer rates are comparable; the ratio of the surface kinetic rate to external mass transfer rate ranges from 0.25 to 1.8. The simulation conditions are r_i= 2.225 cm, b = 0.225 cm, Sc = 1000, k_{int}= 0.3 s^{-1} and V_l = 66 ml. The immobilized enzymatic membrane is 60 μm thick and is located on the inner rotating cylinder.

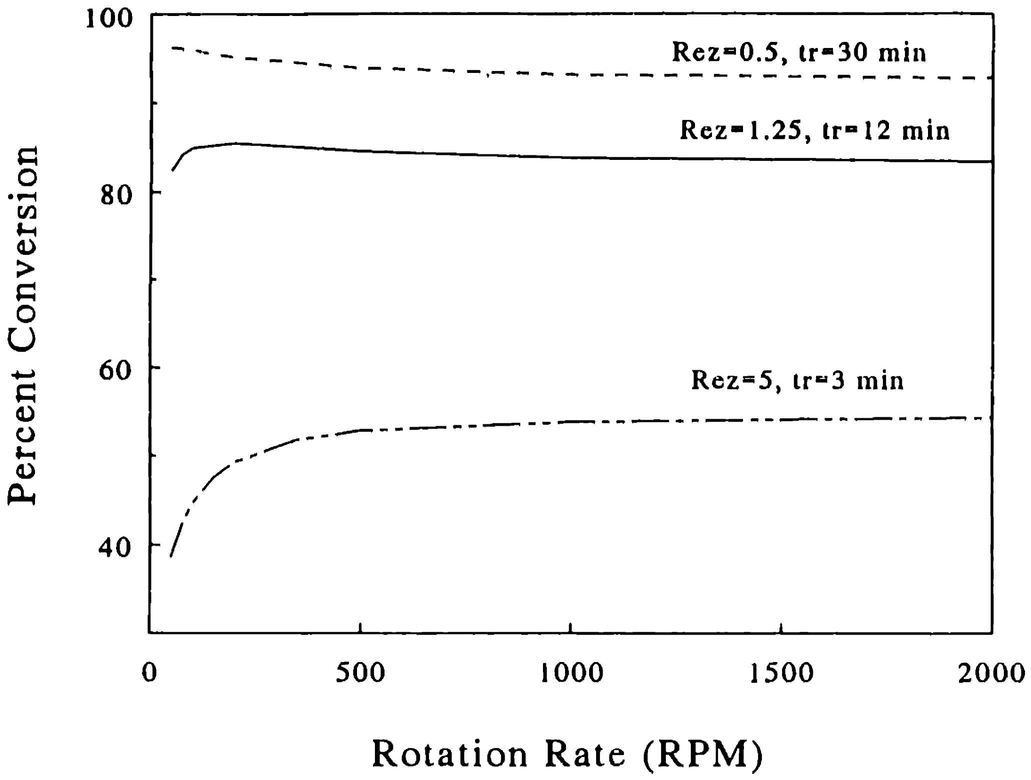

Figure 6.4: Conversion *vs.* rotation rate for VFR with membrane on inner rotating cylinder. The VFR has a constant volume; axial Reynolds numbers and residence times change between cases. Operating parameters are: r_i= 2.225 cm, b = 0.225 cm, Sc = 1000, k_{int}= 0.3 s^{-1} and V_l = 66 ml.

Figure 6.4 appears to show the same effects of mass transfer and kinetic limitations observed in Figure 6.2. However, the difference between kinetic and mass transfer limited regimes in Figure 6.1 is due to a change in the total amount of surface area while the difference in Figure 6.4 is due to a change in dispersion properties. At the shortest residence time (t_r = 3 min, Re_z=5), the effect of the mass transfer limitations is evident at low rotation rates; the conversion increases dramatically with increasing rotation rate. Because of the short residence times and high velocity in this case, the Peclet numbers are large and performance is near plug flow even with increased rotation rate when the dispersion increases. Consequently, the effect of the increased mass transfer with rotation rate dominates. In the low Reynolds number cases (Re_z= 0.5), the effect of the increased dispersion with increasing rotation rate dominates; the effect is a net decrease in conversion. In the intermediate case (Re_z= 1.25), the mass transfer and dispersion effects balance to provide a near constant level of conversion.

The tradeoffs between increasing external mass transfer and dispersion can be further illustrated by comparing the simulation results in Figure 6.4 to the limits of no axial mixing (PFR) and of total axial mixing (CSTR). Figure 6.5 shows the results of the Re_z = 1.25 and 5 simulations from Figure 6.4 along with the corresponding limits for a plug flow reactor and a continuous stirred tank reactor. The CSTR and PFR conversion are determined using the same kinetics and mass transfer rates as in the VFR simulations; only the dispersion properties are varied. As expected, the PFR conversion is higher than the CSTR conversion, and in both cases conversion increases with increased rotation rate due to higher mass transfer. From Figure 6.5, the conversion in the VFR can be seen to be near the PFR limit at low rotation rates. As the rotation rate increases there is a concomitant increase in axial mixing and the performance tends toward the CSTR limit. By comparing VFR performance to the limiting dispersion cases, Figure 6.5 helps illustrate the balance between mass transfer and dispersion in the VFR.

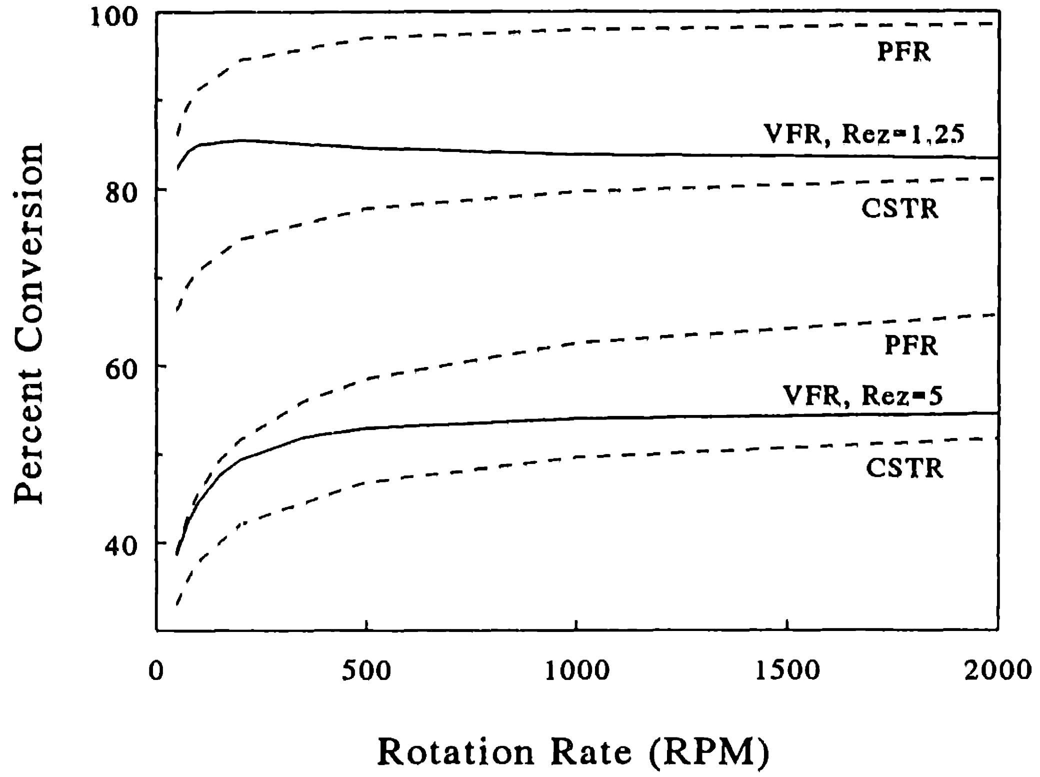

Figure 6.5: Comparison of VFR performance with plug flow reactor (PFR) and continuous stirred tank reactor (CSTR) performance. Solid lines are VFR simulations from Figure 6.4.

The simulations in Figure 6.4 are similar to the model validation experimental results presented in Chapters 7 and 8. In these experiments, a solid support containing immobilized enzyme is introduced into the VFR and the reactor is operated at various rotation rates and axial flow rates. The goal of the model validation experiments is to confirm the model presented in Chapter 3. With a valid mathematical model of the VFR, further simulations may be performed to design or optimize vortex flow reactors for any desired application.

Chapter 7 -

Characterization of a VFR with an Immobilized Alkaline Phosphatase Membrane

This chapter examines a vortex flow reactor containing immobilized alkaline phosphatase on the inner rotating cylinder. Results are presented for experiments in optimization of the alkaline phosphatase immobilization procedure and for operation of the VFR with the immobilized alkaline phosphatase membranes. The experimental results from the VFR containing immobilized enzyme show good agreement with model predictions and demonstrate some of the features of the VFR discussed in Chapter 6.

7.1 Immobilization of Alkaline Phosphatase on Azlactone Functionalized Membranes

Alkaline phosphatase was immobilized on azlactone functionalized polyethylene membranes, using the general procedure presented in Section 4.4.2. Enzymatic activity and protein content were determined by the procedures described in Section 4.4.2. Unless noted all experiments used low purity alkaline phosphatase (3 U/mg solid). Because a high surface activity was required for the model validation experiments, the immobilization procedure was optimized with respect to the immobilization parameters. The experiments focused on methods to increase enzymatic activity during the coupling step or to decrease enzyme inactivation during the quench step. The effect of coupling buffer, protein concentration, length of coupling and presence of ethanolamine were examined. Each set of experiments, presented below, alter a single immobilization parameter and examine its effect on total bound protein and enzymatic activity. The experimental results indicate that the only factors which have a significant effect on the amount of alkaline phosphatase bound to the azlactone membranes are protein concentration in the coupling buffer and length of coupling step.

7.1.1 Effect of Ethanolamine Quench

Early in the immobilization experiments it was asked whether the ethanolamine quench step was the cause of the low alkaline phosphatase membrane activity. The experiments examining the effect of the ethanolamine quench used a coupling procedure of 100 μl of 0.2 mg/ml alkaline phosphatase (3 U/mg solid) in 25 mM phosphate buffer (pH=8.0), 0.8 M Na_2SO_4 added to a 6.3 mm disk of membrane and mixed for 1 hour. As the data in Table 7.1 show, the concentration of ethanolamine in the quench step had no impact on the protein bound or on alkaline phosphatase activity. Separate experiments (not shown in Table 7.1) found no difference in the activity of immobilized alkaline phosphatase membranes with or without the ethanolamine wash.

7.1.2 Effect of Coupling Solution and Coupling Time

It was expected that the concentration of salt in the coupling solution would have a great impact on the amount of enzyme bound to the membranes. Previous work with immobilized protein on azlactone activated beads (Coleman *et al.*, 1990) found up to ten-fold increases in bound protein when using high concentrations of sodium sulfate in the

[Ethanolamine] (M)	Bound Protein ($\mu g/cm^2$)	Activity (10^{-3} Units/cm^2)
0.1	5.7	1.8
0.5	3.9	1.9
1.0	----	1.3
3.0	6.9	1.8

Table 7.1 - Effect of ethanolamine concentration during quench step.

Buffer Salts / Concentration	Coupling Solution Volume (μl)	Bound Protein ($\mu g/cm^2$)	Activity (10^{-3} Units/cm^2)
Phosphate/150mM NaCl	100	9.8	11.2
Phosphate/3M NaCl	100	7.1	10.3
Carbonate/0.6M Na_2SO_4	50	4.3	6.6
Phosphate/0.6M Na_2SO_4	50	14.3	9.30
Phosphate/0.6M Na_2SO_4	100	10.0	10.5
Phosphate/0.6M Na_2SO_4	200	9.7	8.6

Table 7.2 - Effect of salt concentration and volume of buffer in coupling step.

coupling solution. The results in Table 7.2 compare the effects of coupling buffer composition and volume on activity and bound protein. All experiments in Table 7.2 used a coupling procedure of 5 mg/ml alkaline phosphatase for 1 hour. The salt solution of 0.6 M Na_2SO_4 was chosen for this and for other studies because higher salt concentrations caused partial precipitation of the alkaline phosphatase. As the data in Table 7.2 indicates, both activity and bound protein are found to be independent of buffer salts or volume of coupling solution.

The percent of the bound protein which is active can be estimated from the information in Table 7.2. The enzyme preparation has an activity of 3.0 U/mg solid or 15 U/mg protein (cf. Section 4.4.1). Therefore, a membrane with 10 μg protein/cm^2 and 100% active protein would have an activity of 0.150 U/cm^2. The actual activity of the membranes is only around 0.010 U/cm^2 indicating that about 7% of the bound protein is active. In general, the activity of the immobilized membranes made from the low purity alkaline phosphatase ranged from 5 to 10% of the possible activity as calculated from the bound protein. The low activity retention may be due to binding of the active site or to loss of conformation upon binding. Experiments were performed to examine the effect of protecting the active site with a substrate or an inhibitor. Coupling in phosphate, which is an alkaline phosphatase inhibitor, was compared to coupling in a carbonate buffer at the same pH. The results in Table 7.2 indicate a slightly higher activity of coupling with the phosphate buffer as compared to the carbonate buffer. However, later studies revealed no difference in enzymatic activity between the two coupling buffers. The carbonate buffer was predominately used in later experiments as it was not possible to accurately assay the coupling solution activity in phosphate buffer due to the phosphate inhibition. Experiments were also performed using 80mM of the substrate (p-nitrophenyl phosphate) in the coupling solution. No significant difference was seen between the enzymatic activity with or without the substrate.

The effect of coupling time was examined through experiments using 50 μl of 5 mg/ml enzyme in phosphate buffer (pH=8.0) with 0.6 M Na_2SO_4. The coupling was done at room temperature, except for the 24 hour sample, which was run for 4 hours at room temperature followed by 20 hours at 4°C. As seen in Table 7.3, the activity and the bound protein remains relatively constant for the first four hours and increases about 25% at 24 hours. The results are similar to the work of Coleman *et al.* (1990) who studied immobilization of proteins to azlactone activated beads and found that the reaction was essentially complete in 1-2 hours with a slight increase in coupling (about 10%) at 24 hours.

Coupling Time (hour)	Bound Protein ($\mu g/cm^2$)	Activity (10^{-3} Units/cm^2)
1.0	6.7	6.8
2.0	10.5	7.7
4.0	9.7	6.7
24.0	18.1	10.0

Table 7.3 - Effect of coupling time on alkaline phosphatase immobilization.

7.1.3 Effect of Protein Concentration

The next set of experiments examined the effect of protein concentration in a low salt environment (25 mM phosphate buffer, pH=8.0 with 150 mM NaCl). The experiments used a coupling solution of 100 µl for 1 hour and wash of 0.5M ethanolamine. The results are presented in Table 7.4. The increase of activity upon increasing enzyme concentration is easily seen; there is a seven-fold increase in activity between the lowest and highest concentrations. A relationship between bound protein and enzyme concentration is not as obvious. As discussed below, this is likely due to error in the protein analysis. The enzymatic assay, on the other hand, is much more reproducible and can determine accurately small concentrations of active alkaline phosphatase.

The same dependence of increasing activity by increasing protein concentration is seen in experiments using high purity alkaline phosphatase (600 U/mg protein), shown in Table 7.5, where a 30-fold increase in activity is observed between the lowest and highest concentrations of protein in the coupling solution. All experiments in Table 7.5 used a coupling step with 50 µl of 0.6M Na_2SO_4 in sodium carbonate buffer (pH=8.0) for 1 hour and a quench step of 3.0 M ethanolamine for 1.5 hour. The effect of increasing activity

[Alkaline Phosphatase] (mg/ml)	Bound Protein ($\mu g/cm^2$)	Activity (10^{-3} Units/cm^2)
0.2	9.9	1.7
0.4	5.8	2.9
1.0	5.6	2.9
5.0	9.8	11.2

Table 7.4- Effect of protein concentration using low purity alkaline phosphatase.

Membrane Sample #	Protein in Coupling Solution (μg/ml)	Bound Protein Uncorrected (μg/cm^2)	Bound Protein Corrected (μg/cm^2)	Membrane Activity (mU/cm^2)
7A-1	8.4	8.25	1.90	29.1
7A-2	8.4	9.69	3.34	28.3
7A-3	8.4	11.09	4.74	16.4
7A-4	8.4	5.51	-----	35.1
Average =		*8.6 +/- 2.1*		*27.2 +/- 2.4*
7B-1	75.2	7.50	1.15	201
7B-2	75.2	13.6	7.25	117
7B-3	75.2	8.29	1.94	149
7B-4	75.2	6.43	0.08	128
Average =		*9.0 +/-2.8*		*149 +/- 38*
7C-1	205	13.6	7.21	921
7C-2	205	12.0	5.65	743
7C-3	205	18.1	11.70	654
7C-4	205	15.0	8.65	837
Average =		*14.7 +/- 2.2*	*8.3 +/- 2.2*	*789 +/- 116*
Blank-1	0	6.33		
Blank-2	0	6.52		
SDS Blank-3	0	5.79		
Unreacted	0	3.79		
Unreacted	0	4.19		

Table 7.5 - Results from immobilization of high purity alkaline phosphatase on azlactone functionalized membranes.

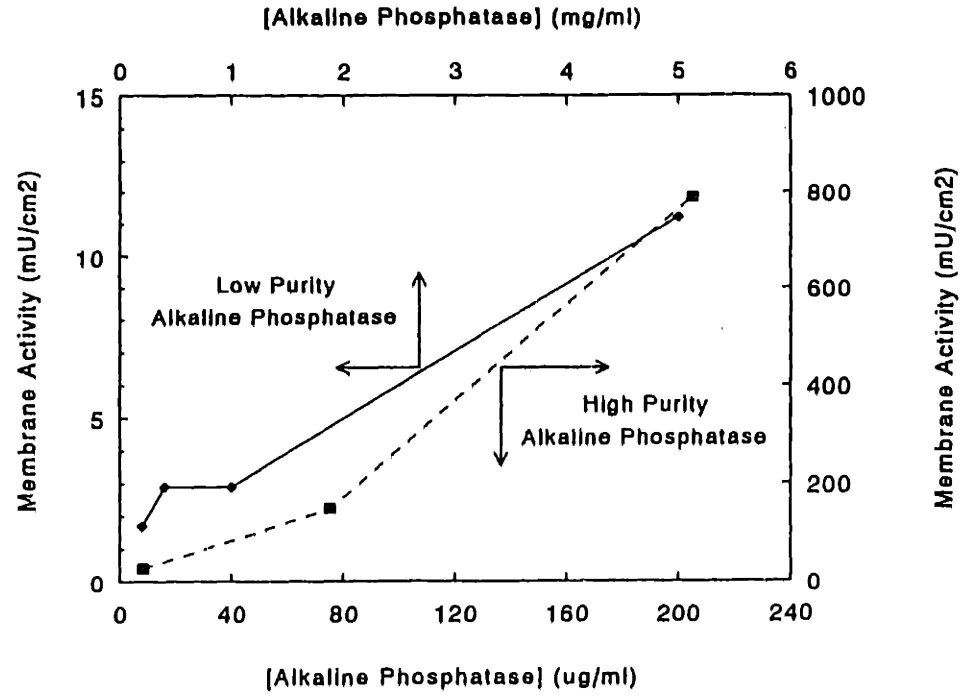

Figure 7.1 - Effect of protein concentration on bound protein and immobilized alkaline phosphatase activity.

with protein concentration can be seen in Figure 7.1 which contains the data from Tables 7.4 and 7.5.

After assaying for activity, the membranes in Table 7.5 were used for experiments to determine protein concentration. The first two membranes in each data set in Table 7.5 were assayed for protein in the usual manner. Samples suffixed in -3 and -4 were treated with 1% sodium dodecyl sulfate (SDS) for 4 hours at 37°C and washed three times in SDS prior to assaying for protein. No noticeable difference was found between the protein content of the SDS treated and untreated membranes indicating no appreciable noncovalently bound protein. The corrected protein, reported in Table 7.5, is obtained by subtracting off the membrane "blanks" from the uncorrected protein. Note that the blank membranes (reacted with ethanolamine) and the unreacted membranes (no ethanolamine) both have significant reaction in the bicinchoninic acid protein assay, corresponding to 6.4 $\mu g/cm^2$ and 4.0 $\mu g/cm^2$, respectively. The high value of the blank causes large errors in calculating the amount of protein bound to the membrane. While the enzymatic activities of duplicate membranes are reproducible within 25%, the bound protein measurement is not reproducible at lower protein concentrations (i.e. experiments 7A and 7B) and is reproducible only within 30% at high concentrations of bound protein.

When a relatively high amount of protein is bound to the membrane, the bicinchoninic assay provides a valid order-of-magnitude estimation of bound protein as seen by a comparison of two methods to determine bound protein. Table 7.6 reports the percent protein of the initial coupling solution bound to the membrane as determined directly by the bicinchoninic protein assay on the membrane and indirectly by a material balance. The membrane assay uses the corrected protein bound (from Table 7.5) and the known initial concentration and volume of the coupling solution. The material balance uses the difference between the protein content of the coupling solution before and after immobilization. As Table 7.6 shows, both methods give similar results for membranes 7C-1 through 7C-4 indicating that approximately 20% of the protein in the coupling solution was bound to the membrane.

Membrane Sample #	Percent Protein Bound Membrane Assay	Material Balance
7C-1	21.9	18.8
7C-2	17.1	21.2
7C-3	35.5	17.6
7C-4	26.3	21.2

Table 7.6 - Comparison of percent protein bound on membranes using membrane assay and material balance methods.

A calculation of the active enzyme of the membrane indicates that approximately 5 to 15% of the bound protein is active. The calculation compares the experimentally obtained enzymatic activity to the maximum activity as determined from the bound protein concentration and the initial soluble activity of 600 U/mg protein. The low activity could be caused by the active site binding the solid support in such a way as to be inaccessible to the substrate. Another possible explanation for the low activity is multipoint attachment and loss of conformation caused by the high surface concentration of azlactone. This hypothesis is examined in the experiments described below.

7.1.4 Effect of Ethanolamine Prewashes

Despite the efforts described above to increase membrane activity, little improvement was seen through variation of the operational parameters. The experiments in this section used ethanolamine to partially deactivate the azlactone groups with the intention of lessening deactivation caused by multipoint attachment. In the first experiment, the membranes were "pre-quenched" with ethanolamine for 1 hour prior to coupling using varied ratios of ethanolamine to azlactone. In the second experiment, the coupling step occurred in the presence of both protein and ethanolamine. All experiments were run in triplicate with a coupling procedure of 5 mg/ml alkaline phosphatase for 1 hour in 0.6 M sodium sulfate, 0.1 M bicarbonate buffer. The activity assays for the second experiment (ethanolamine during coupling) were performed at 25 C instead of 30 C.

The most obvious feature of the results, presented in Table 7.7, is that the presence of ethanolamine has little effect on total membrane activity except at very high ethanolamine concentrations where the total activity decreases. No obvious difference in the bound protein was seen within each set of runs. The second feature of the data is that all the experiments, including the control without ethanolamine, had an activity about 25% higher

Ratio Ethanolamine:Azlactone	Ethanolamine Before or During Coupling?	Activity (mU/cm^2)	Average Activity (mU/cm^2)	Average Corrected Protein (μg/cm^2)
1:10	Before	14.6, 8.4, 13.6	12.2	9.8
1:1	Before	4.2, 9.7, 9.0	7.6	7.1
10:1	Before	9.0, 14.3, 4.7	9.3	7.1
0	--------	11.0, 7.4, 11.3	9.9	5.1
1:100	During	7.4, 12.9, 9.8	10.0	4.9
1:10	During	8.9, 12.2, 8.6	9.9	4.6
1:1	During	7.0, 8.8, 5.6	7.2	3.7
10:1	During	8.6, 7.4, 12.0	9.3	4.6
100:1	During	8.5, 9.7, 7.0	8.4	4.4
1000:1	During	10.5, 5.6, 6.5	7.5	3.7
10000:1	During	8.3, 4.0, 8.6	6.9	4.2

Table 7.7 - Results from experiments with ethanolamine added before coupling or present during coupling.

than the experiments shown in Tables 7.1 through 7.4. The higher activity can be attributed to these experiments using a different starting alkaline phosphatase material with approximately a 25% higher activity of 3.9 Units/mg solid.

The results presented in Table 7.7 do not rule out the possibility of multipoint attachment causing the low activity retention of the immobilized enzyme. While the experiments summarized in Table 7.7 examined different levels of azlactone functionality by varying the concentration of ethanolamine, the azlactone activity was not determined quantitatively. Quantitative measurements of the azlactone functional density before and after the immobilization procedure can be made using Fourier Transform Infra Red (FTIR) Spectroscopy (Gagnon, 1993). Such measurements may aid in relating the azlactone surface density to the alkaline phosphatase activity on the membrane.

7.1.5 Kinetic Studies

Kinetic studies were performed on several of the immobilized azlactone membranes to determine the Michaelis constant, K_m. The studies used the experimental procedure described in Section 4.4.2. Mass transfer resistances inside the membrane were considered in determining the values of K_m for the low and high purity alkaline phosphatase membranes. The Thiele modulus was used to assess internal diffusion limitations within the membranes. The observable Thiele modulus is defined as (Bailey and Ollis, 1977):

$$\Phi = \frac{rw^2}{D_{eff}C} \tag{7.1}$$

where r is the observed volumetric reaction rate, w is the membrane thickness and D_{eff} is the effective diffusion coefficient of the substrate, as given by (3.4b). The observable Thiele modulus in (7.1) contains only observable parameters and is independent of reaction order. The effective diffusion coefficient is estimated to be 1.6×10^{-6} cm^2/s by knowing the porosity of 0.68 and membrane thickness of 61µm (Gagnon, 1993), and by assuming a soluble diffusivity of 7×10^{-6} cm^2/s and a tortuosity of 3. For first-order kinetics, a simple relationship (3.22) exists between the effectiveness factor and the Thiele modulus. However, no analytical expression relates η and Φ for non-linear Michaelis-Menton kinetics; the effectiveness factor is determined graphical from Figure 7.2.

The kinetic constants K_m and V_{max} can be determined for Michaelis-Menton kinetics (3.13) by plotting $1/rate$ vs. $1/C$; the slope of the line is K_m/V_{max} and the intercept is $1/V_{max}$. The rate used in the plot is the intrinsic kinetic rate. If internal mass transfer resistances are negligible, the intrinsic kinetic rate and the observed kinetic rate are the same. Since the effectiveness factor for the highest enzymatic loading on the low purity alkaline phosphatase membranes (0.015 Unit/cm^2) ranges from 0.95 to 1.00, internal mass transfer resistances are negligible for all membranes in these studies coupled with the low purity alkaline phosphatase. Consequently, the K_m was determined by plotting 1/*observed rate* vs. $1/C$ as described above. A K_m value of 3.3 mM was found in good agreement the K_m of 3.2 mM for the soluble enzyme.

Calculation of the Thiele modulus for immobilized membranes using high purity alkaline phosphatase (experiment 7B) reveals significant mass transfer limitations. In order to determine the kinetics parameters V_{max} and K_m, it was first necessary to find the intrinsic reaction rate by using the effectiveness factor. The intrinsic reaction rate, or rate without mass transfer limitations, is equal to the observed rate divided by the effectiveness factor. A summary of this calculation, which uses (7.1) and Figure 7.2 is presented in Table 7.8. A plot of the inverse of the intrinsic rates in Table 7.8 vs. $1/C$ gave a K_m of 2.2 mM for the membranes made from the high purity alkaline phosphatase.

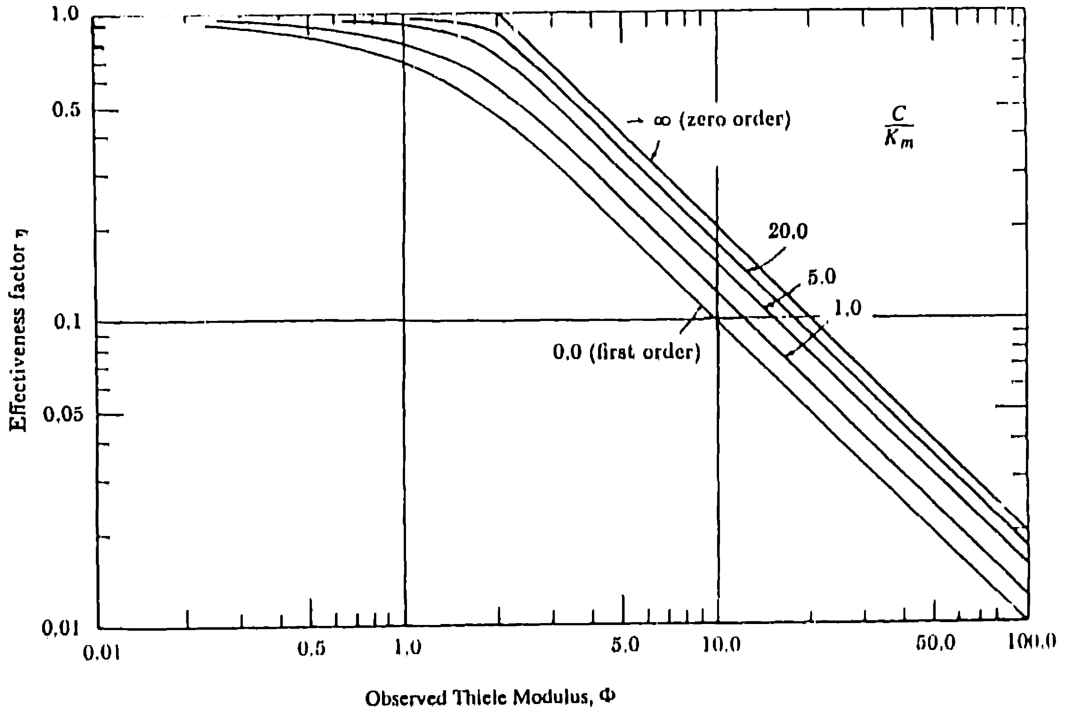

Figure 7.2 - Relationship between observed Thiele modulus, Φ, and effectiveness factor for Michaelis-Menton kinetics in a porous membrane. Curves are for different values of C/K_m. (Adapted from Satterfield, 1970)

NPP Conc. (mM)	Observed Rate (μmol/min)	Thiele Modulus	Effectiveness Factor	Intrinsic Rate (μmol/min)
0.20	2.4×10^{-3}	2.74	0.23	4.8×10^{-3}
0.50	5.4×10^{-3}	1.68	0.50	10.4×10^{-3}
2.0	18.9×10^{-3}	1.45	0.52	30.4×10^{-3}
5.0	31.8×10^{-3}	0.976	0.82	38.8×10^{-3}
16.5	50.9×10^{-3}	0.473	1.00	50.9×10^{-3}

Table 7.8 - Summary of kinetic experiments and analysis of internal mass transfer limitation for membrane 7 B-1

The K_m values of 2.2 and 3.3 mM obtained for the high and low purity alkaline phosphatase membranes, respectively, insures that the model validation experiments, run at 0.1 mM, are in the first-order reaction limit. An interesting point is that the membranes with the highest activity (Table 7.5, experiment 7C) show mass transfer limitations under all conditions. At the assay conditions of 16 mM, the effectiveness factor is 0.1; under the model validation experimental conditions of 0.1 mM substrate concentration, the effectiveness factor is predicted to be only 0.015. As the substrate is only able to access a small fraction of the membrane volume, much of the enzymatic capacity is unused. In contrast, the membranes in experiment 7A show no internal mass transfer limitations at the assay conditions or at a substrate concentration of 0.1 mM. Consequently, if full utilization of the enzymatic capacity of the immobilized membrane is desired, lower membrane activities should be used. However, if the enzyme deactivates over time and a steady performance is desired, a higher membrane activity is desired. In internally mass transfer limited membranes, the decrease in enzyme activity is partially offset by a decrease in internal mass transfer resistances. Therefore, the observed reaction rate will decrease slower in membranes with high enzymatic activity which are internally mass transfer limited than in membrane with low activity which are not mass transfer limited.

7.1.6 Discussion of Immobilization Results

Several trends become evident from study of alkaline phosphatase immobilized membranes studied here. First, the membranes bind between 4 and 15 $\mu g/cm^2$ of alkaline phosphatase, independent of most of the experimental parameters. The total amount of protein bound is lower than the 25-60 $\mu g/cm^2$ obtained in previous work where Protein A and immunoglobulin G were covalently attached to the membranes (Gagnon and Coleman, 1994). The amount of protein bound on the membranes also can be compared to protein bound on azlactone functionalized beads (Coleman et al., 1990) by a pore surface area basis. Using a pore surface area of 15 m^2/g and a density of 0.303 g/cm^3 (Gagnon, 1993), the protein bound in the membrane ranged from 0.14 to 0.54 g/m^2. In comparison, the protein bound to the azlactone functionalized beads ranged from 1.4 to 2.0 g/m^2. Although the protein binding is lower than may have been expected from previous work, the protein activity obtained in these experiments was sufficient enough to use the membranes for the model validation studies. However, a more efficient procedure may be needed for immobilizing heparinase or other enzymes of interest in the VFR.

The second observation is the effect of operational parameters on immobilized alkaline phosphatase activity. The activity was found to be independent of buffer salts in the coupling buffer, volume of the coupling buffer and partial azlactone deactivation by ethanolamine. The length of the coupling step had a slight effect in increasing membrane activity. The largest influence on membrane activity is the concentration of protein in the coupling solution. As seen in Figure 7.1, increasing the protein concentration dramatically increased the activity of the bound protein for both the low and high activity alkaline phosphatase starting materials. Because of this effect, high concentrations of protein were used in preparing the membranes for the model validations experiments in Section 7.2.

An additional trend which is apparent from the experiments is the inconsistency of results from the bicinchoninic protein assay. Duplicate sample gave very different results, especially if the membranes contained low amount of bound protein. In addition, membranes without protein had a significant reaction in this assay. Subtracting out the contribution from the "blank membranes" resulted in high experimental error. Theoretically, the bicinchoninic assay should work well with these membranes. The method has been used previously to assay protein covalently bound to other particles (Stich, 1990; Coleman et al., 1990). Results from the assay have been shown to correlate well with protein determined from radioactive labeling (Coleman et al., 1993). The irreproducibility in the results is most likely due to the high background contribution from the azlactone or membrane support. External mass transfer limitations may also contribute to experimental error. Even though every effort was made to vigorously stir the membranes throughout the assay, differences in mass transfer to the membrane surface may have affected the results. Similar external mass transfer limitation could also contribute to the variation between the measured activities of the immobilized enzyme membranes.

The protein assay does provide a rough estimate of the total protein bound. From the assay results, it is possible to estimate the activity retained on the membrane as ranging from 4 to 15%. The activity retention is low compared to work of other researchers (Basheeruddin *et al.*, 1985) who retained 54% of immobilized alkaline phosphatase activity upon immobilization through amine groups via cyanogen bromide activation. Loss of activity upon immobilization can be due to several factors including blocking or disruption of the catalytic site or binding sites. This mechanism was examined by immobilization in the presence of the substrate (nitrophenyl phosphate) and an inhibitor (phosphate). No significant difference between activity was observed in the samples containing nitrophenyl phosphate or phosphate buffer. Low immobilized enzyme activity also may be due to multipoint attachment of the protein to the solid support causing loss of conformation. When this mechanism was studied by partial deactivation of azlactone groups with ethanolamine, no effect of azlactone deactivation on total enzymatic activity was observed. Further experiments are needed to distinguish the mechanism for the low activity of immobilized alkaline phosphatase.

7.2 Model Validation Experiments Using a VFR with an Immobilized Enzymatic Membrane

In this section, the mathematical model is validated through VFR experiments using immobilized alkaline phosphatase membranes on the inner rotating cylinder. Both the dynamic response and the steady state behavior of the VFR are experimentally examined. The dynamic response experiments demonstrate the dispersion behavior in a VFR with reaction. In particular, the experiments indicate the validity of the model assumption that dispersion with reaction is the same as that without reaction. The steady state experiments compare the predicted conversion with the experimental results. The model predictions use no fitted parameters; the model inputs are the transport properties from the correlations in Chapter 5 and the kinetic parameters determined in separate experiments. The steady state experiments reveal the effects of external mass transfer and dispersion on reactor performance, and show how performance can be adjusted by varying the operational parameters of axial flow rate and rotation rate.

The model validation experiments used the experimental set-up described in Section 4.6. The procedure for immobilizing alkaline phosphatase to the membrane is outlined in Section 4.4.3. All experiments used the high purity alkaline phosphatase with a concentration of 0.1 mg/ml protein in the coupling buffer. Both the dynamic and steady state experiments used an inner cylinder of 4.45 cm and an outer cylinder of 4.90 cm.

Deactivation of the membrane bound alkaline phosphatase was a serious problem in the steady state experiments. The rate of deactivation was slow enough such that the enzymatic activity could be considered constant throughout the length of a run, but fast enough to decrease between consecutive runs. Therefore, reference runs were periodically conducted through the course of the experiments to track enzyme deactivation in the steady state experiments. Although deactivation of the enzyme occurred in the dynamic response experiments, it was not necessary to characterize because the experimental data are normalized to the percent of the final conversion.

7.2.1 Dynamic Response Membrane Experiments

The results of the dynamic response experiments (ranging from 100 to 800 RPM) are shown in Figure 7.2. The data shows both the rise of the product concentration with the introduction of substrate and the fall of the product concentration with the return to buffer. The model predictions, which are represented on the graphs by solid lines, are calculated from (3.11), using the dispersion coefficient from (5.5) and the external mass transfer coefficient from (2.14). The model accurately describes the rate of rise and fall of the product. The slight time lag evident in a few of the model curves is likely due to a small overestimation in the measured volume of the reactor and tubing. To compare the influence of dispersion on reactor behavior, Figure 7.3 shows the first half of the step change data for the experiments at 100 and 800 RPM. The curve for 100 RPM has a longer time lag before the emergence of the product and a sharper rise than the curve at 800 RPM,

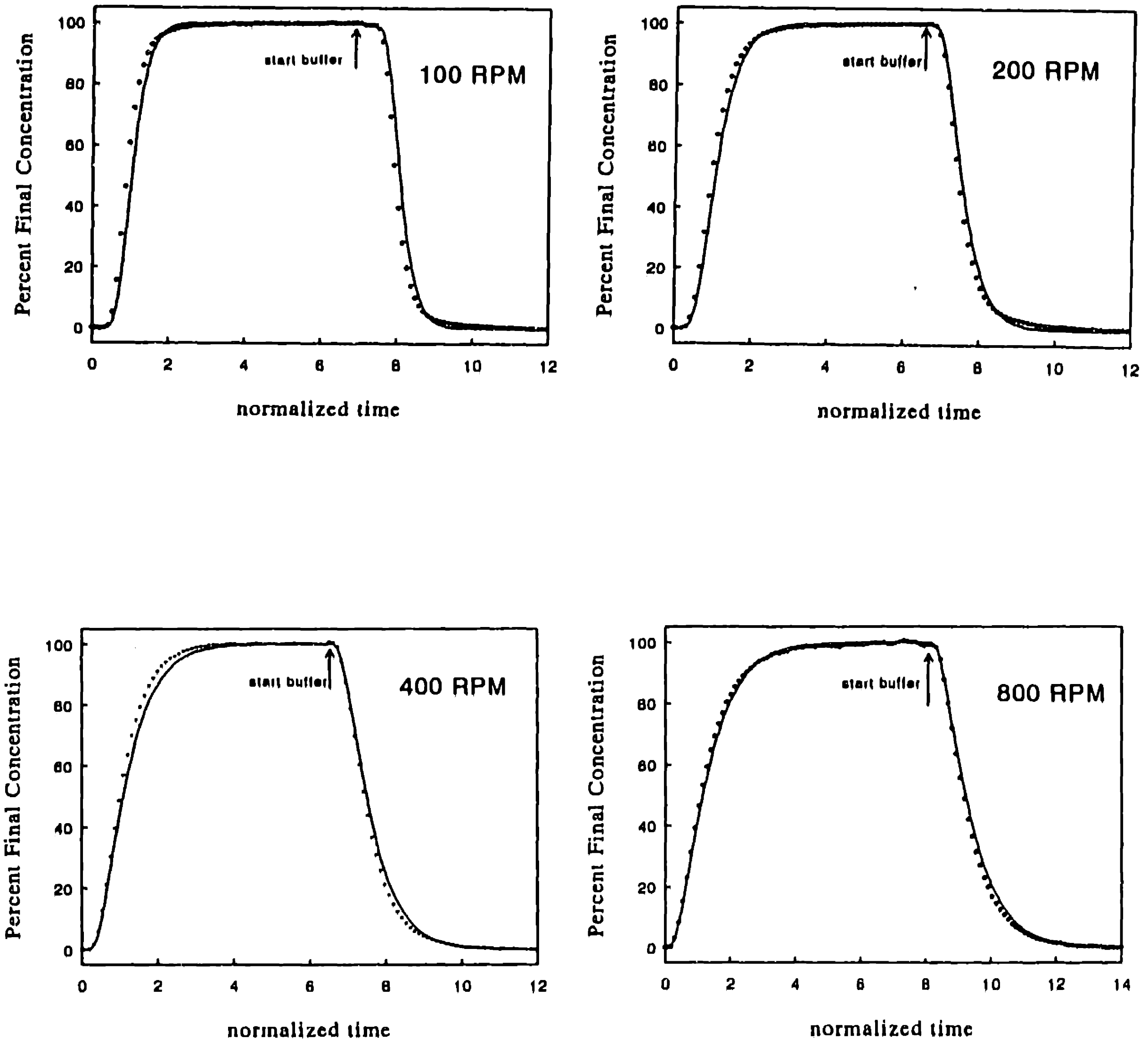

Figure 7.3 - Dynamic response experiment in VFR containing immobilized alkaline phosphatase on the inner cylinder. All curves have $Re_z = 5$, rotation rate is as labeled. Solid line is model prediction (3.11), points are experimental data.

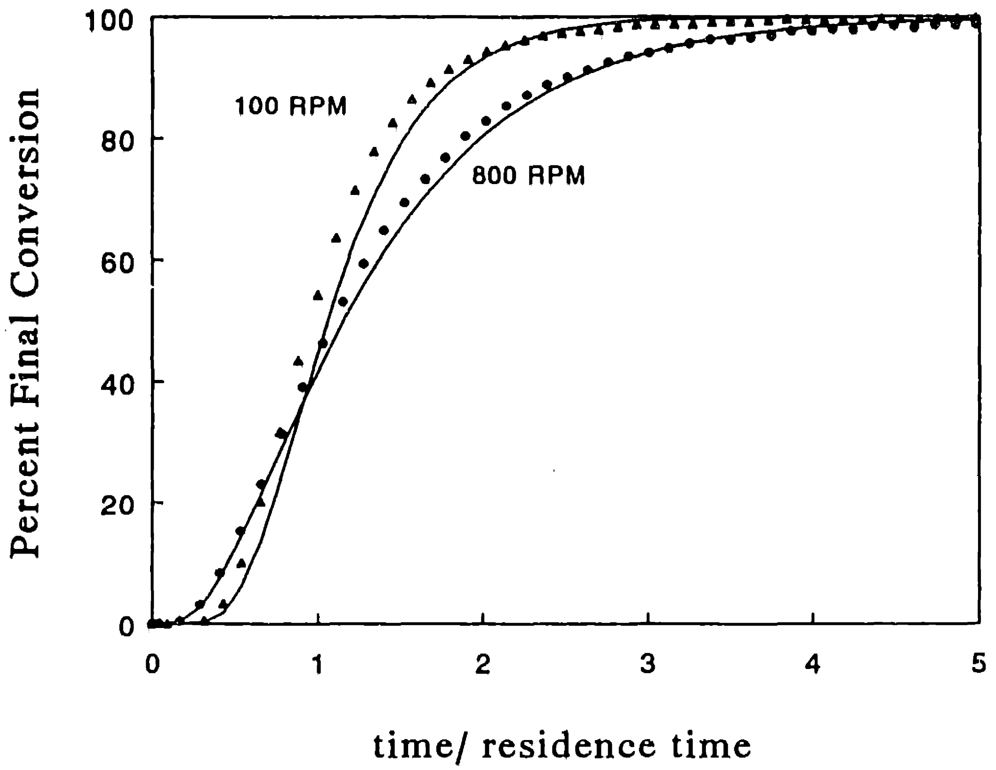

Figure 7.4 - Comparison of dynamic response curves in VFR with immobilized alkaline phosphatase membrane. Experimental conditions are $Re_z = 5$, 100 and 800 RPM.

indicating a lower dispersion. The trend of increasing dispersion with increasing rotation rate is observed consistently for all of the experiments shown in Figure 7.2.

The good agreement with the experimental results and the model indicates that the assumptions made in the model development are valid. In particular, the data is consistent with the assumption that the dispersion coefficient for the reactive case is the same as for the non-reactive tracer. As discussed in Chapter 3, the independence of dispersion on reaction rate is expected if the internal mass transfer is faster than either the intrinsic reaction rate or the external mass transfer rate. This assumption can be checked by estimating the characteristic times for reaction, diffusion to the support, and transport to the surface of the membrane. The time for diffusion is estimated by

$$t_{Diff} = \frac{w^2}{D_{eff}} \quad , \tag{7.2}$$

which is equal to approximately 23 s for the membranes used in these experiments. The characteristic reaction time is the inverse of the rate constant based on the volume of the solid support or

$$t_{rxt} = \frac{1}{k'}\frac{V_s}{V_l} \quad . \tag{7.3}$$

The first order kinetic constant for the membrane was approximately 0.005 s^{-1}, corresponding to $t_{rxt} = 4.3$ s. Since $t_{Diff} >> t_{rxt}$ there are significant internal mass transfer limitations in the membranes used for the dynamic response experiments. The same result can be obtained by calculating the Thiele modulus and effectiveness factor as described in Section 3.3. Even though the internal mass transfer rate is slower than the intrinsic kinetic rate, the model assumptions are still valid if internal mass transfer is faster than external mass transfer. The time scale for external mass transfer can be estimated by

$$t_{mt} = \frac{\delta}{k_{mt}} \tag{7.4}$$

where δ is the external mass transfer boundary layer thickness. By using the relationship $k_{mt} = D/\delta$ given by film theory (Cussler, 1984), the expression

$$t_{mt} = \frac{D}{{k_{mt}}^2} \tag{7.5}$$

is obtained relating the time for external mass transfer to known parameters. For the conditions used in the dynamic response experiments, t_{mt} ranges from 30 to 300s. Thus, it can be seen that the time for diffusion in the membrane is comparable or less than the time for mass transport to the active surface. Consequently, even though there are internal mass transfer limitations in the membrane, the model works well in predicting the dynamic response to a step change input. Chapter 8 provides examples of experiments where the dynamic response cannot be described by the transport model due to a slow diffusion rate through the agarose/silica particles.

7.2.2 Steady State Membrane Experiments

Steady state experiments were conducted using an immobilized alkaline phosphatase membrane on the inner rotating cylinder. The purpose of the experiments was to examine the effects of mass transfer and dispersion in the VFR. Unlike the dynamic response experiments which only examine the dispersion behavior in the reactor, the steady state experiments examine both the effects of external mass transfer and dispersion on overall conversion. Two sets of steady state experiments were conducted using the immobilized alkaline phosphatase membranes. Enzyme deactivation was significant in both experimental sets. The first set of experiments used a reference condition of 400 RPM and Re_z= 5.0 in continuous operation. The second set of experiments used a batch configuration with 400 RPM as a reference condition. In both cases, the kinetic and deactivation rates were obtained from the reference runs. The reference run data and the fit for the exponential decay are shown in Figure 7.5 for the two experiments. The deactivation rate for the first experimental set (top graph) was 0.0294 hr^{-1} and the first-order kinetic constant at initial time was $k'(0)$=0.214 min^{-1}. The deactivation rate and initial first-order kinetic constant for the second experimental set are k_d = 0.0175 hr^{-1} and $k'(0)$ = 0.0714 min^{-1}. Note that the deactivation rate is slightly higher for the first set of experiments which was run at 30 C than for the second set which was conducted at 25 C. Also, both deactivation rates are less than the deactivation rate of the soluble enzyme of 0.037 hr^{-1} at 30 C. A much higher surface activity was obtained in the first experimental

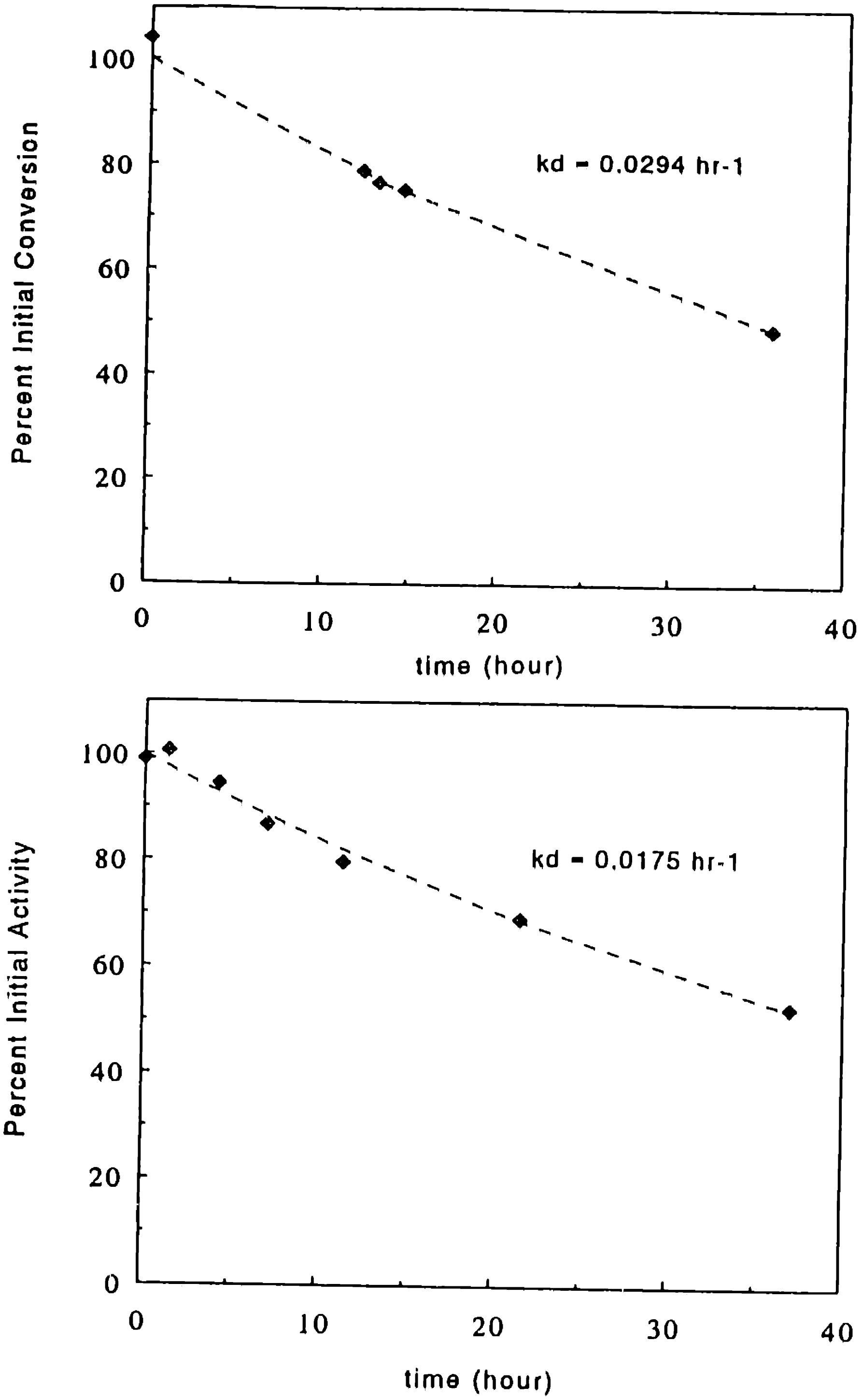

Figure 7.5 - Reference runs for membrane VFR experiments used to determine deactivation of immobilized alkaline phosphatase membranes with time. Top graph is for continuous membrane experiment #1, run in continuous mode (400 RPM, $Re_z = 5$, 30 C). The deactivation rate is 0.0294 hr^{-1}, the kinetic rate is 0.214 min^{-1}. Bottom graph is for continuous membrane experiment #2, run in a batch mode (400 RPM, 25 C). The deactivation rate is 0.0175 hr^{-1}, the kinetic rate is 0.0714 min^{-1}.

set than in the second. The ratio of the surface reaction rates to the mass transfer rate ranges from 0.5 to 1.3 for experiment set #1 and from 0.08 to 0.3 in experiment set #2. Therefore, experiment set #2 is always in the kinetically limited regime and experiment set #1 is the intermediate regime where external mass transfer and kinetics are comparable.

The results for the continuous membrane experiments are presented in Figures 7.6 and 7.7. The data is plotted along with the model predictions. The solution to the model equation (3.12) uses the Peclet number calculated from (5.5), the mass external transfer coefficient calculated from (2.14) and the experimentally determined kinetic and deactivation constants described above. Thus, there are no fitted parameters in the model predictions. As evident in Figures 7.6 and 7.7, the model shows excellent agreement with the experimental data. In addition, the experimental results reveal some of the effects of operational parameters on conversion . The effect of axial Reynolds number is easily seen; an increase is conversion is obtained with a decrease in axial Reynolds number due to the longer residence time in the VFR. The effect of mass transfer limitations can be seen in the data at higher axial Reynolds number in Figures 7.6 and 7.7 where an increasing rotation rate increases the mass transfer to the active surface and thus raises the conversion. The increased conversion is smaller than seen in many of the model simulations presented in Chapter 6 due to the relatively low surface reaction rates. The effect of dispersion is also evident upon changing the rotation rate. The data for Re_z=0.5 in Figure 7.7 clearly shows this feature; the increase in rotation rate causes a concomitant increase in dispersion thus lowering the overall conversion in the VFR. The offsetting effects of mass transfer and kinetics can be seen for the $Re_z = 0.5$ data in Figure 7.6 where increasing the rotation rate causes an initial increase in conversion followed by a gradual decrease in conversion.

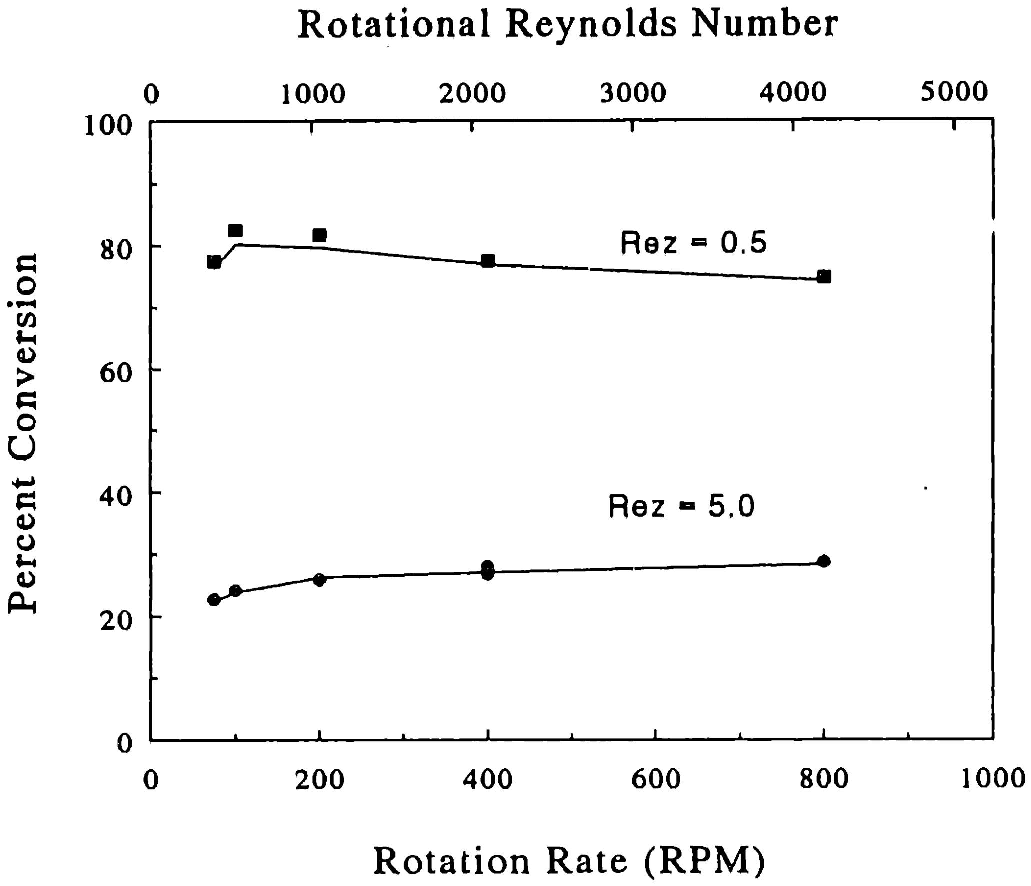

Figure 7.6 - Results from continuous membrane experiment #1 with alkaline phosphatase immobilized on inner cylinder. Points are experimental data and solid lines are model predictions.

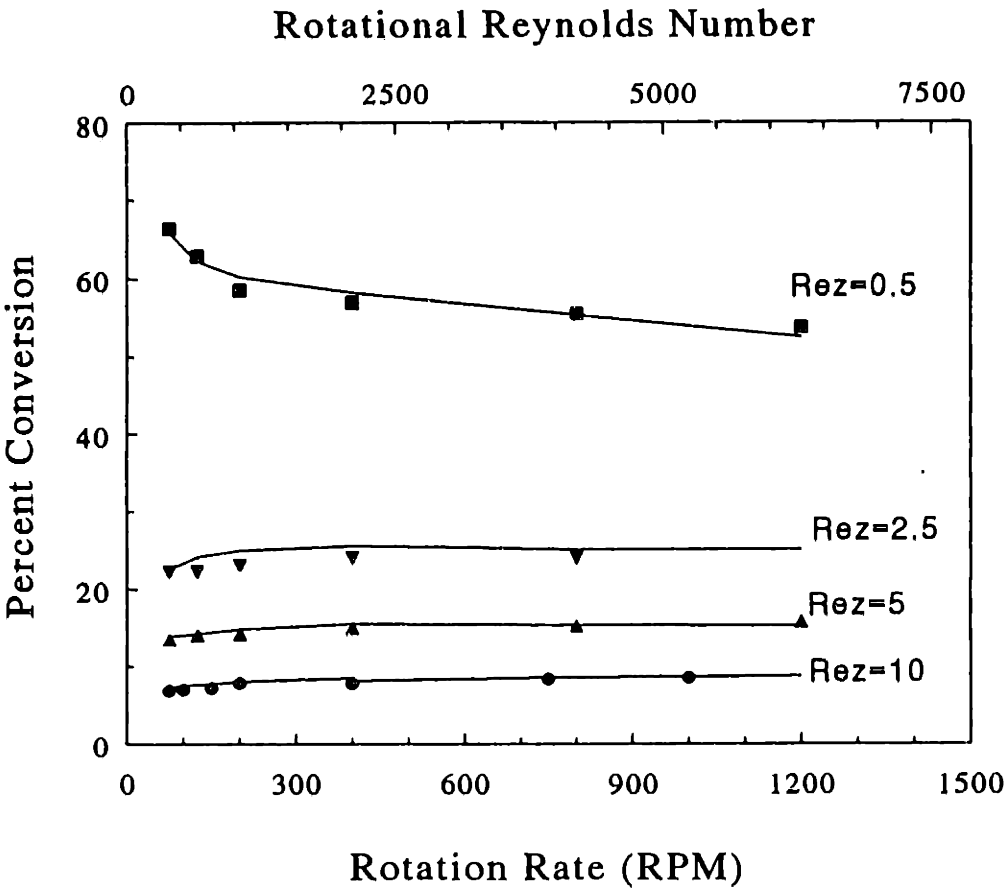

Figure 7.7 - Results from continuous membrane experiment #2 with alkaline phosphatase immobilized on inner cylinder. Points are experimental data and solid lines are model predictions.

7.2.3 Discussion of Membrane VFR Experiments

The experiments presented above demonstrate the validity of the mathematical model developed to describe the vortex flow reactor with immobilized enzyme on the cylinder walls. In general, the model predictions compare very well with both the dynamic response and steady state experimental results. The model is able to successfully determine conversion in the VFR with no fitted parameters. The only inputs to the model equations are the operating parameters and the experimentally determined kinetic constants.

The experiments further illustrate the effect of the operating parameters on mass transfer, dispersion and overall conversion in the VFR. As anticipated by the model simulations described in Chapter 6, conversion in the VFR is influenced by both external mass transfer and dispersion effects. In the experiments presented above, the major determinant of the extent of reaction in the VFR is the residence time as set by the axial flow rate. The rotation rate may be adjusted independently to further define the reactor conversion. The effect of the rotation rate in raising or lowering the conversion depends upon many factors including mass transfer rate, kinetic rate and extent of conversion. The mathematical model provides a relatively simple tool to predict the effect these complex factors have on reactor performance. The model is useful in optimizing conversion in existing processes or in designing reactors for new processes. An example of reactor design is presented in Appendix A, where the model is used to predict operation of a vortex flow reactor for heparin neutralization by immobilized heparinase.

Chapter 8 -

Characterization of a Vortex Flow Reactor Containing Suspended Particles

This chapter discusses the performance of a vortex flow reactor containing immobilized enzyme particles and adsorbent particles. Particle visualization studies are presented which define the acceptable operating regions for a VFR containing suspended particles. Operation of the VFR with immobilized enzyme particles is examined both for steady state and dynamic response experiments. The mathematical model of the VFR is validated through comparison of these experimental results and the model predictions. In addition, the utility of the VFR as an adsorber is demonstrated through experiments studying protein adsorption on ion exchange particles.

8.1 Particle Visualization Studies

It was necessary to determine the acceptable operational range for the VFR prior to performing experiments with suspended particles. Therefore, particle visualization studies were conducted to determine regions of good fluidization of the agarose/silica particles. The experiments used clear acrylic cylinders and low volume fractions ($f < 0.05$) of

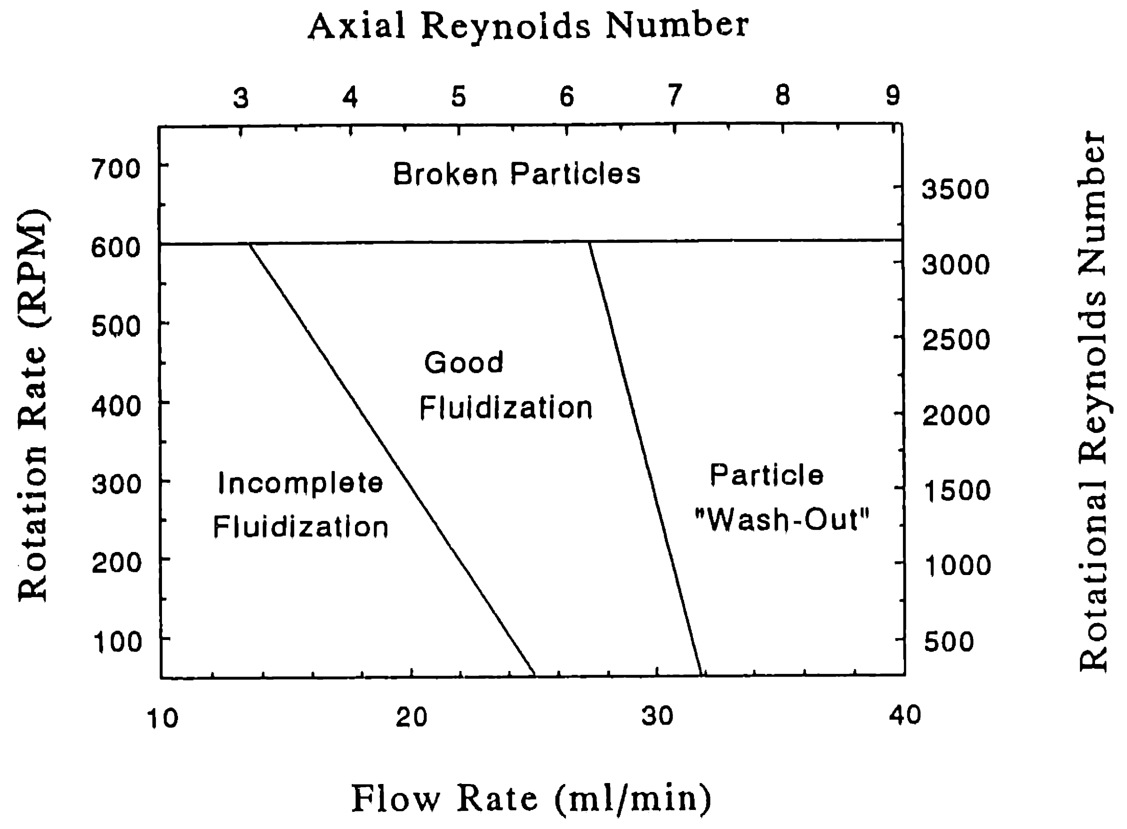

Figure 8.1 - Fluidization regimes of agarose/silica particles, d_i= 4.45 cm and d_o = 4.90 cm, b = 0.225 cm.

agarose-silica particles. The particles were colored dark blue by binding bromophenol blue to the DEAE agarose-silica particles.

Figure 8.1 shows the operating regimes for a VFR with an inner cylinder diameter of 4.45 cm and outer cylinder diameter of 4.90 cm. In the region marked "Good Fluidization" the blue particles appear to be distributed along the entire length of the VFR. At lower flow rates or at lower rotation rates the majority of the particles rest on the bottom of the VFR and only a few particles rise up the annulus. In the region marked "Particle Wash-Out", the particles gather at the top of the annulus; the particles do not really leave the annulus as they are retained by the mesh on the reactor outlet. It should be noted that the operating regions outlined in Figures 8.1 are not exact but rather based on visual observations of when the particles appear to occupy the entire vortex length. Differences in the axial distribution of the particles may still exist in the regions marked "good fluidization". Additionally, the particle distribution found in the incomplete fluidization region and in the particle wash-out region may be sufficient to operate the VFR.

As indicated in Figure 8.1, above 600 RPM a catastrophic failure occurs and all of the particles rapidly break into small pieces. The limit of 600 RPM seems to be independent of inner cylinder diameter and gap ratio; the same upper limit of 600 RPM is found for all inner cylinder diameters. If the particle breaking mechanism was shear, the limiting rotation rate would be dependent on the gap ratio. Instead, it is likely that the breakage is caused by cylinder wobble. Since the inner cylinders used in this study have no bottom support, they tend to rub against the outer cylinder at high RPM. The upper rotation rate limit in Figure 8.1 could be raised by using a non-shearing cylinder support at the bottom of the reactor. In contrast, shear may be responsible for particle damage at high particle loading. As explained in the residence time distribution experiments with suspended particles (cf. Section 5.1.2), volume fractions greater than 0.35 caused enough broken particles so as to clog the outlet filter. Therefore, VFR operation in this work was constrained below 300 RPM with high particle loading.

Figures 8.2 and 8.3 show the fluidization regimes for a VFR with an outer cylinder diameter of 4.90 cm and inner cylinders diameters of 4.21 and 3.81 cm, respectively. The graphs show many of the same features found in Figure 8.1. In general, the flow rate required to evenly suspend the particles decreases with increasing rotation rate. The rotation of the inner cylinder provides a secondary mechanism for particle fluidization; the mechanism has a stronger influence in the wider gaps. Figure 8.3 demonstrates that for the widest gap of 0.545 cm, no applied axial flow is required to suspended all of the particles at high enough rotation rates (>250 RPM). The suspension of particles by shear is not

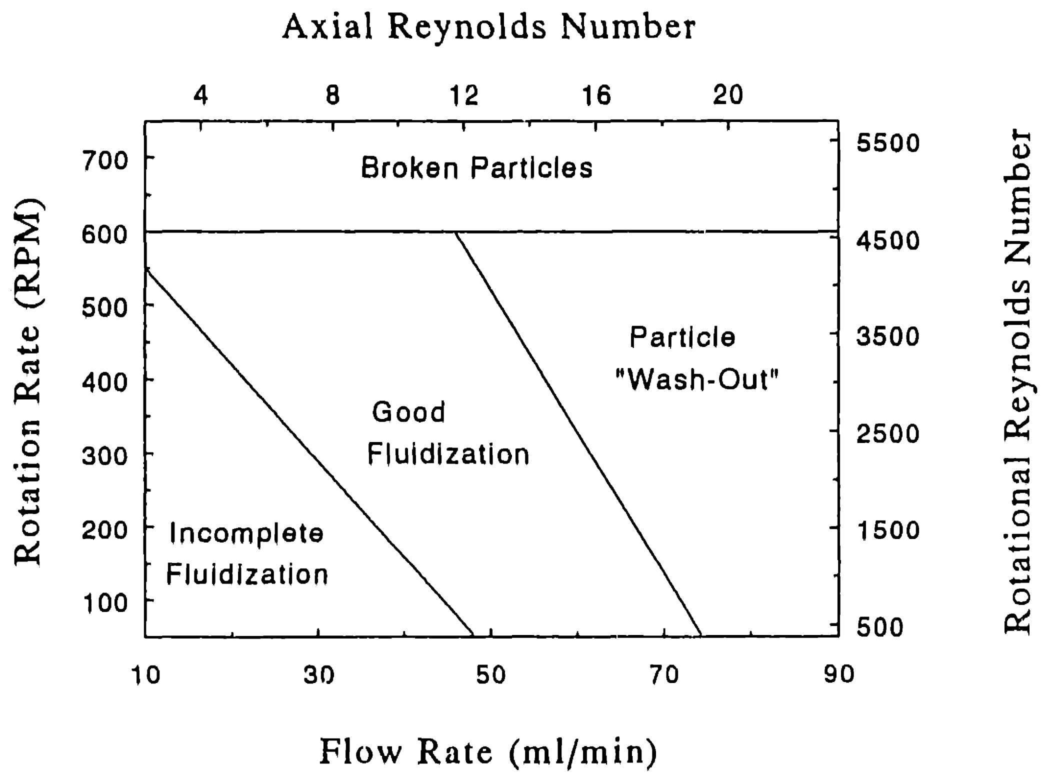

Figure 8.2 - Fluidization regimes of agarose/silica particles, d_i= 4.21 cm, d_o = 4.90 cm and b = 0.35 cm.

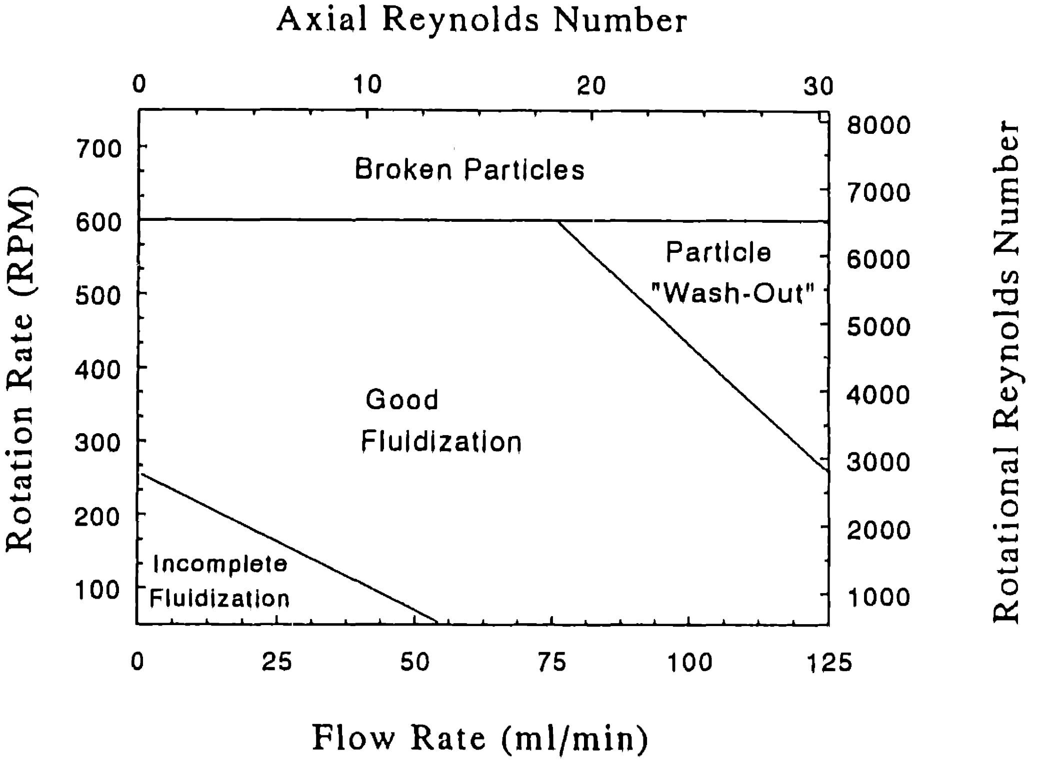

Figure 8.3 - Fluidization regimes of agarose/silica particles, d_i= 3.81 cm, d_o = 4.90 cm and b = 0.55 cm.

unique to Taylor-Couette vortex flow; Leighton and Acrivos (1986) found a similar phenomena in laminar Couette flow.

The fluidization regimes for different geometries in the VFR can be compared by examining the velocities required to suspend the particles. Table 8.1 shows the maximum velocity for good fluidization over the range of rotation rates studied. The fluidization velocities range from 0.14 to over 0.28 cm/s. The fluidization velocities for b=0.345 and 0.545 cm are comparable while the lower velocities are found for the b=0.225 cm case. The lower velocities for the smallest gap are likely due to wall effects as the particles are approximately 10% of the gap width. In comparison with the experimentally determined velocities, the Stokes settling velocity (Bird *et al*, 1960) for the agarose/silica particles (calculated from the mean particle size of 200 μm and the density of 1.2 g/cm^3) corresponds to an settling velocity of 0.44 cm/s. Thus, the maximum operational velocities are approximately 30% to 60% the theoretical settling velocity. These results are similar to those of Olin *et. al* (1954) who studied particle settling rates in a counter-current Taylor flow ion exchanger. Their experimentally determined settling velocity are approximately 30% to 100% of the Stokes settling velocity, in good agreement with the current study.

Diameter Inner/Outer Cylinders (cm)	Gap Width (cm)	Axial Velocity (cm/s)
3.81/4.90	0.545	0.16 to > 0.28
4.21/4.90	0.345	0.17 to 0.28
4.45/4.90	0.225	0.14 to 0.16

Table 8.1 - Maximum fluidization velocities for suspended particles in the VFR.

8.2 Model Validation Experiments Using a VFR with Suspended Immobilized Enzyme Particles

8.2.1 Immobilization Results

Alkaline phosphatase was immobilized on agarose and agarose-silica particles according to the procedure described in Section 4.4.3. A summary of the immobilization results is presented in Table 8.2. For a cyanogen bromide concentration of 35 mg/ml, the composite agarose-silica particles had much lower coupling efficiency than the plain agarose particles. Therefore, a higher cyanogen bromide concentration of 100 mg/ml was used to achieve a reasonable enzyme loading. The lower coupling efficiency may be from a reduction in available active sites in the agarose-silica material, either due to the presence of the silica or due to a higher degree of crosslinking. Kinetic studies conducted with the alkaline phosphatase immobilized on plain agarose show a K_m of 4.2 mM, which is slightly higher than the K_m of 3.2 mM for the soluble enzyme. When alkaline phosphatase was coupled to the agarose/silica DEAE gel, the apparent K_m was found to be 6.8 mM. The higher K_m value is likely due to binding of the product by the agarose/silica matrix. As seen in Table 4.2, the agarose-silica DEAE particles strongly bind the reaction product (nitrophenol).

Table 8.2 also presents the observed Thiele modulus for a substrate concentration of 0.1 mM; the calculation uses (7.1) with $w=d_p/6$ and assumes that the particles have a diameter of 200 μm, a porosity of 0.8, and a tortuosity of 2. The Thiele modulus indicates that mass transfer is negligible ($\Phi < 0.3$) except for the highest enzymatic loading of $k' = 4.8$ min^{-1} where slight internal mass transfer limitations are evident. Because internal mass transfer resistances are negligible, VFR experiments conducted with these immobilized enzyme particles will fit within the mathematical model's limitations.

Solid Support	Cyanogen Bromide (mg/ml)	Enzyme Concentration (U/ml)	1st order rate constant (min^{-1})	Observed Thiele Modulus
Agarose	35	100	2.8	0.19
Agarose-Silica DEAE	35	20	0.006	0.0004
Agarose-Silica DEAE	35	100	0.14	0.009
Agarose-Silica DEAE	100	100	2.6	0.17
Agarose-Silica Underivatized	100	100	4.8	0.32
Agarose-Silica Underivatized	100	100 †	3.4	0.22

† All experiments used low purity lyophilized alkaline phosphatase (3.9 U/mg) except last data set which used high purity alkaline phosphatase in a ammonium sulfate suspension.

Table 8.2 - Summary of results from immobilization of alkaline phosphatase on agarose and on agarose-silica particles.

8.2.2 Dynamic Response Experiments

Step change experiments were conducted in a VFR with suspended immobilized enzyme particles with the purpose of examining the dynamic response of the reactor and of comparing the VFR response to the model predictions. The experimental used the setup described in Section 4.6, cylinders of diameters of 4.21 cm and 4.90 cm, and an operating temperature of 25 C. The model predictions were calculated from (3.11) using the dispersion coefficient from (5.5) and the external mass transfer coefficient from (5.15).

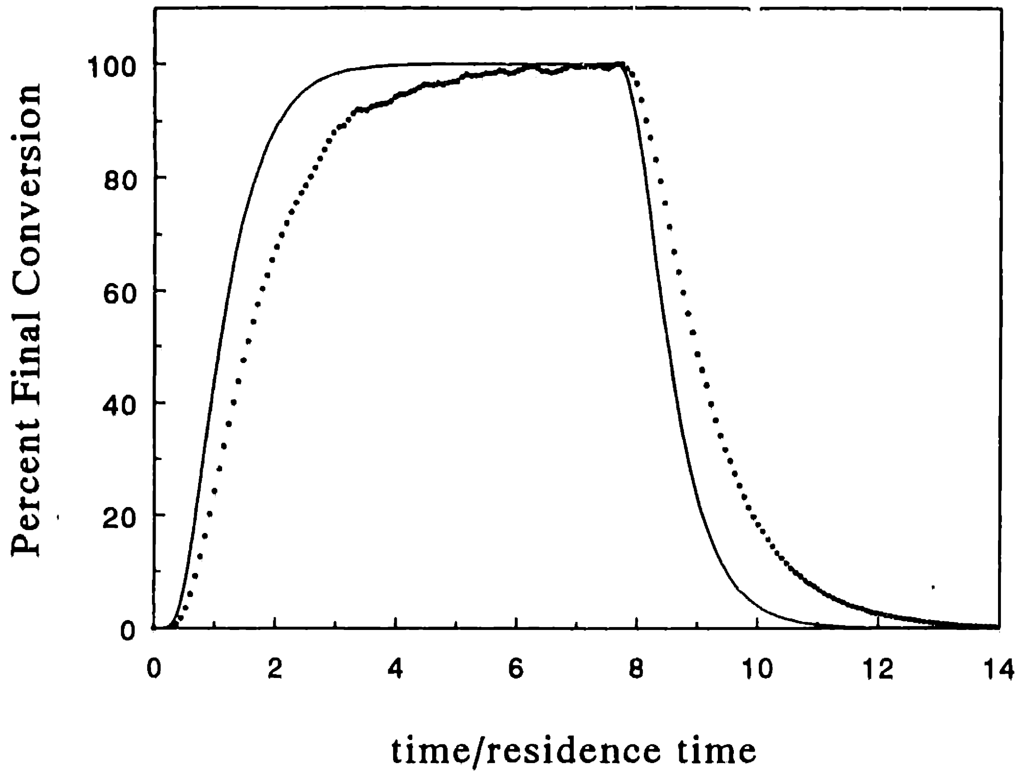

Figure 8.4 - Dynamic response experiment using immobilized alkaline phosphatase on DEAE agarose-silica particles. Operating conditions are Re_z=10.8, Re_θ=1520 (200 RPM), f=0.14.

The first set of dynamic response experiments used the DEAE agarose-silica ion exchange resin as an immobilization support and a particle loading of f = 0.14. The kinetic constant for gel was approximately 1.2 min^{-1}. As seen by comparison with the data in Table 8.2, internal mass transfer resistance are negligible at this kinetic rate. Figure 8.4 presents the experimental results and model predictions for a dynamic response experiment operating at Re_z=10.8 and Re_θ = 1520 (200 RPM). The predicted curve in Figure 8.4 is much earlier than the experimental curve. This effect was found consistently among the step change experiments using the DEAE resin and is considered to be due to adsorption of the product to the agarose/silica particle. As noted in Table 4.2, the DEAE resin has an equilibrium capacity of 0.7 μmol/ml for 0.1 mM of the reaction product (nitrophenol). The lag seen in Figure 8.4 is due to product adsorption. At initial times, the nitrophenol produced from the alkaline phosphatase reaction binds the DEAE and thus the product does not emerge from the VFR and is not measured on the spectrophotometer. Eventually, the agarose-silica DEAE particles reach equilibrium with the product and steady-state is obtained. About 8 residence times were required to reach steady state, as compared to the typical response of 4 to 6 residence times without product adsorption. Following the reintroduction of buffer into the VFR, the bound nitrophenol is slowly eluted from the particles, causing the lag in the measured nitrophenol concentration upon returning to the baseline. The amount of bound nitrophenol can be estimated by integrating the area between the curves over time. The experiment shown in Figure 8.4 had a final nitrophenol concentration of 0.04 mM and a corresponding amount of bound nitrophenol of approximately 0.2 μmol/ml, in reasonable agreement with the equilibrium data in Table 4.2.

To avoid the problem of product adsorption, the dynamic response experiments were repeated using the underivatized agarose-silica particles, which have negligible adsorption of nitrophenol. The experimental results for Re_z=5 and varied rotation rates are shown in Figure 8.5. The kinetic constant, determined by fitting the final steady-state conversion, was approximately 0.8 min^{-1}; internal mass transfer resistances are negligible at this kinetic rate. Because the shape of the normalized curve is independent of the kinetic rate, the experimental and model data are plotted as a percent final conversion. As seen in Figure 8.5, the model correctly describes the rise and fall of the product concentration. The effect of dispersion can be seen by comparing the dynamic response curves at the different rotation rates. The curves at the lower rotation rates have a longer time lag and a sharper rise than the curves at the higher rotation rates. This effect is due to increasing axial dispersion with increasing rotation rate. Figure 8.6 illustrates the effect of axial flow rate on dispersion for a constant rotation rate of 300 RPM (Re_θ=2280). The dynamic response

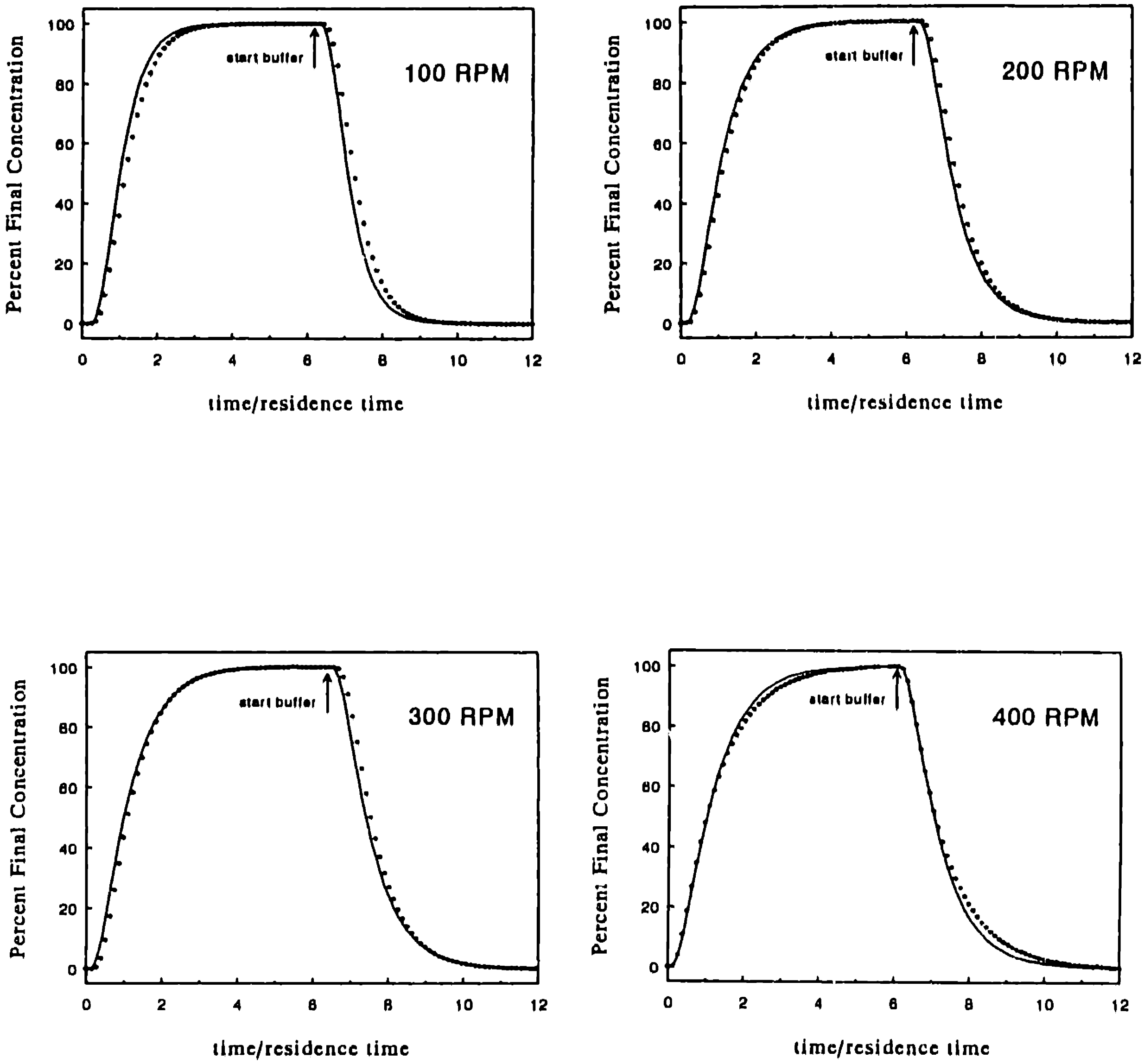

Figure 8.5 - Dynamic response experiments in VFR containing immobilized alkaline phosphatase on underivatized agarose-silica particles. All curves have Re_z=5 and f=0.20, rotation rate is as labeled. Solid line is model prediction (3.11), points are experimental data.

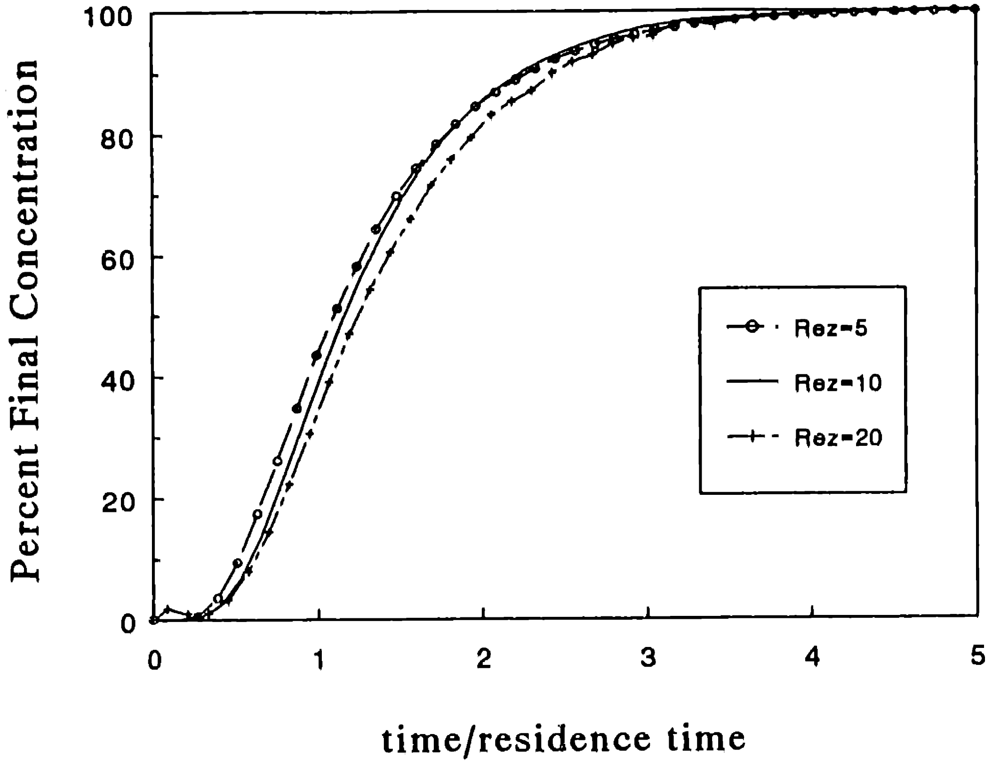

Figure 8.6 - Dynamic response experiment using varied axial Reynolds numbers. The VFR contains immobilized alkaline phosphatase on DEAE agarose-silica particles. Operating conditions are Re_θ=2280 (300 RPM), and f=0.20.

curves for the three axial Reynolds numbers are almost identical, indicating that the axial flow rate has only a slight effect on the dispersion in the VFR.

The dynamic response experiments in Figure 8.5 illustrate that the dispersion properties in the VFR can be predicted by the mathematical model. As seen in Figure 8.4, the dynamic response experiments are sensitive in isolating effects which are inconsistent with the model assumptions. In the example of the DEAE particles, adsorption occurred simultaneously with reaction resulting in disagreement between the experiment and model results. Adsorption with or without simultaneous reaction can be included in the model by adding additional reaction terms for the adsorption and desorption rates. The adsorption parameters could be obtained through independent experiments thus avoiding unnecessary fitted parameters. It is expected that once included, good agreement would result between experimental and model predictions.

Another problem anticipated to cause deviation from the predicted dynamic response is internal mass transfer limitations. All experiments in this section showed negligible internal mass transfer limitation. However, it is expected that a poor dynamic response curve would be observed for immobilized enzyme particles with large internal mass transfer limitations. The effect of internal mass transfer limitations on the dynamic response is further discussed in the protein adsorption experiments presented in Section 8.3.

8.2.3 Steady State Experiments

Steady state experiments were conducted using immobilized enzyme particles in the VFR. Whereas the dynamic response experiments presented above isolate the dispersion effects in the reactor, the steady state experiments examine the effects of external mass transfer and dispersion on overall conversion in the VFR. The experiments used alkaline phosphatase immobilized on the DEAE particles. Although the product binds to the DEAE particles, the experimental data is acceptable as long as true steady state was achieved. Therefore, the experiments were run for a longer time (about 8-9 residence times) to allow equilibrium to be achieved with the adsorption reaction.

Results from the steady state experiments are shown in Figure 8.6. The model predictions from (3.12) use the dispersion coefficient calculated from (5.5), and the mass transfer coefficient calculated from (5.15). The initial first order kinetic constant of 1.9 min^{-1} was determined by assaying a small sample of particles in a cuvette prior to the VFR experiments (cf. Section 4.4.3). The enzymatic deactivation rate was determined to be

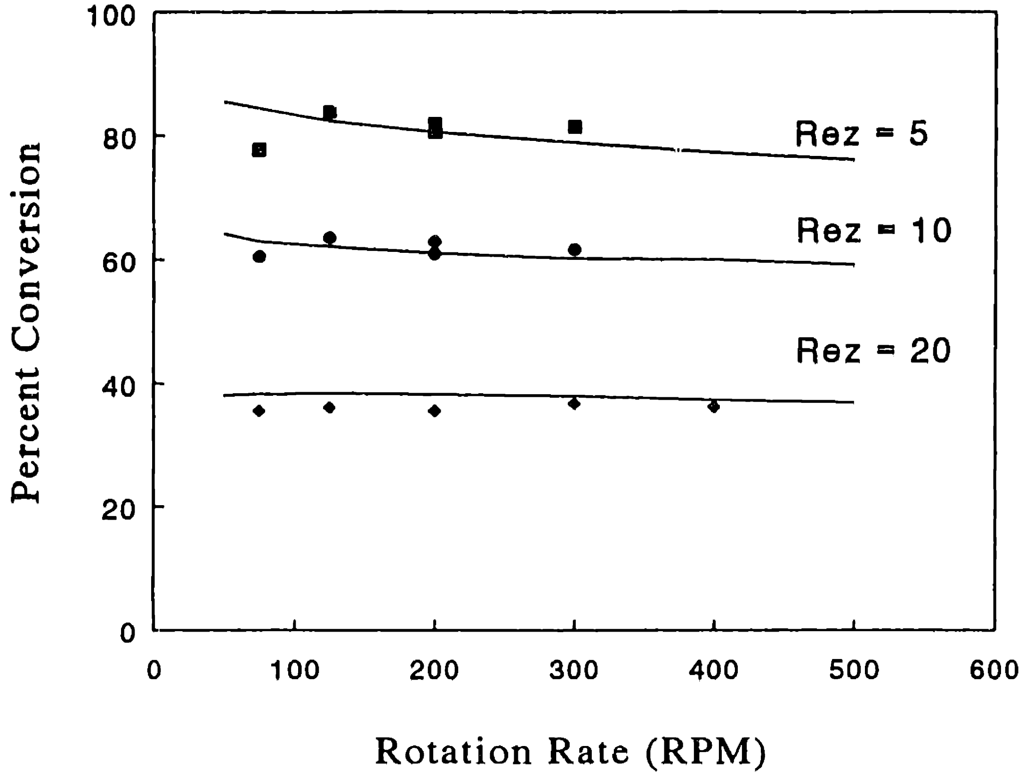

Figure 8.7 - Results from steady state experiments in a VFR containing alkaline phosphatase immobilized on agarose-silica particles with f=0.14.

0.019 hr^{-1}, through reference runs at Re_z=10, and Re_θ=1520 (200 RPM). In general, the model predictions show excellent agreement with the experimental data. The deviation between the model predictions and experimental results seen at the lowest rotation rate of 75 RPM can be attributed to incomplete mixing in the radial direction leading to channeling. The effect of channeling was seen in the corresponding residence time distribution curves at 75 RPM; the concentration profiles exhibited a sharp rise and a long tail not characteristic of the dispersion equation.

While the experimental results in Figure 8.7 show good agreement with the model predictions, they do not reveal many of the effects of operating parameters highlighted in the VFR simulations in Chapter 6. Slight dispersion effects are seen for the Re_z =5 data where the conversion decreases with increasing rotation rate. In general, however, conversion is constant with changing rotation rate; axial flow (i.e. residence time) is the primary factor in reactor conversion. One reason for small variation of conversion with rotation rate is the constraint on rotation rates between 100 and 500 RPM with this VFR design. However, the primary reason for the independence of conversion from rotation rate is the fast mass transfer to the particle surface. Some of the most interesting features of the VFR occur when the reactor is external mass transfer limited or near external mass transfer limitations. For the particles in these experiments, the ratio of the external mass transfer to the surface reaction rate was between 40 and 70. Consequently, nearly a 100-fold increase in particle activity is required to demonstrate the effects of external mass transfer resistances in a VFR containing immobilized alkaline phosphatase. Achieving such high particle activity is not only experimentally difficult, but also is complicated by internal mass transfer resistances. For simultaneous reaction and diffusion into a particle, the maximum reaction rate is limited by the internal diffusion rate. Figure 8.8 illustrates the effect of increasing enzyme loading on observed reaction rate. The observed kinetic rate incorporates the internal mass transfer resistances and is calculated from $k_{int}=k'\eta$, using (3.26b) and the particle properties specified previously. The reaction rates corresponding to the kinetic rates of $k_{int}=1.9$ min^{-1} obtained for the experiments in Figure 8.7 are indicated in Figure 8.8. Over a 500 fold increase in enzymatic loading (Units/ml gel) is necessary to obtained the 40-fold increase in surface reaction rate required to make the reaction rate and mass transfer rate comparable. Since these high enzymatic loadings are unlikely to be achieved with this enzyme it is expected that external mass transfer resistances will always be negligible for immobilized alkaline phosphatase on the agarose-silica particles. Different enzymes with higher specific activities may induce external mass transfer limitations in the VFR.

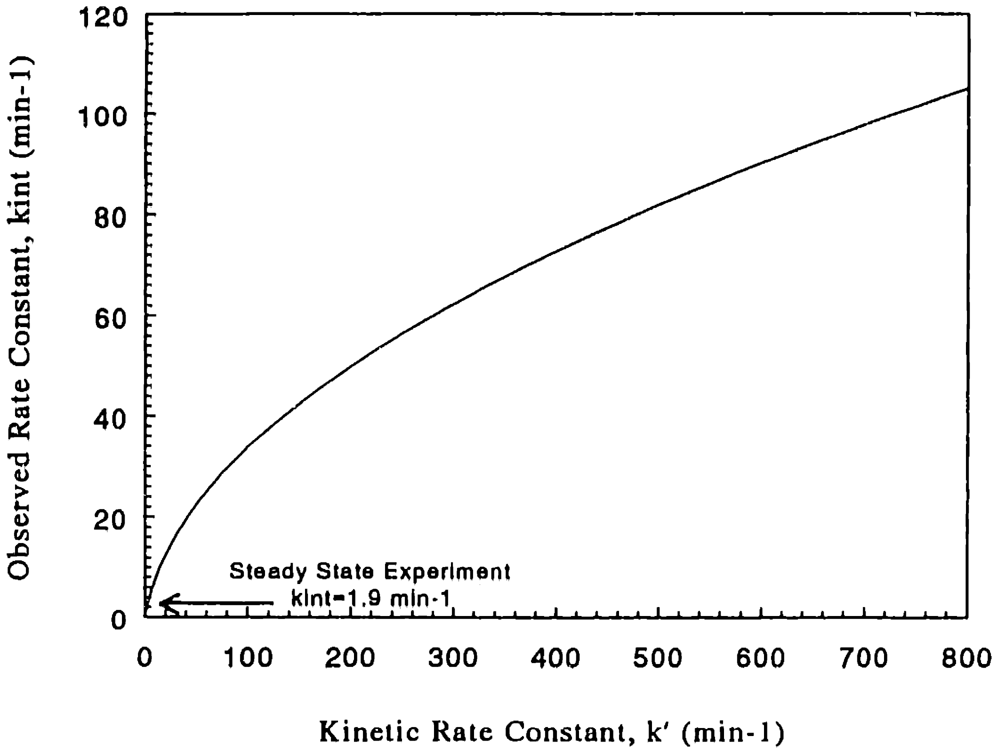

Figure 8.8 - Effect of increasing intrinsic reaction rate constant on observed reaction rate constant for agarose-silica particles (d_p=200 μm, D_{eff} = 2.8x10^{-6} cm^2/s). The kinetic rate obtained in the steady state experiments of 1.9 min^{-1} is indicated with the arrow.

Several alternative approaches are available to examine external mass transfer limitations in a VFR containing immobilized enzyme particles. In general, to see the effects of external mass transfer resistances the effective surface reaction rate must be comparable or higher than the external mass transfer rate. One method to obtain high surface reaction rates is to use an enzyme with a faster kinetic rate. Another approach is to use smaller particles. Although a small particle will have a lower surface reaction rate than a large particle with the same volumetric reaction rate, the small particle will have lower internal mass transfer resistances and thus a higher effectiveness factor. Since the external mass transfer rate is assumed to be independent of particle size (c.f. Section 5.2.2), smaller sized particles may be useful to demonstrate external mass transfer resistances. One drawback of using smaller particles in the VFR is the settling velocity. Lower flowrates or higher particle densities would be required to properly fluidize the particles.

8.3 Protein Adsorption in the VFR

One of the foreseen applications of the VFR is adsorption from biological process streams. Such applications include adsorption of a product from a cell homogenate and continuous removal of a product or a waste from a cell culture. In this section, adsorption in a VFR is examined using a model system of bovine serum albumin (BSA) adsorption on anion exchange particles.

The adsorption experiments used a continuous feed of BSA into a VFR containing adsorbent particles to generate a "break-through" curve. The protein solution was fed into the reactor until the particles were saturated with BSA and the concentration of the protein in the outlet stream approached the inlet concentration. In ideal operation, all protein introduced is bound to the particles until saturation is reached at which time the outlet concentration changes from zero to that of the inlet concentration. In real operation, the protein begins to break through the reactor outlet before saturation. The resulting concentration versus time curve is indicative of both the protein capacity of the particles and the non-idealities of the dynamic adsorption behavior.

The results from the protein adsorption experiments with f=0.21 and Re_z= 5 are shown in Figure 8.9. The curves plot the fraction of the inlet protein concentration in the reactor outlet (C/Co) against the normalized time. The time axis is also equivalent to the total amount of protein introduced into the reactor, shown on the graph as (mg BSA/ml adsorbent). The two curves in Figure 8.9 show a very similar dynamic response. The

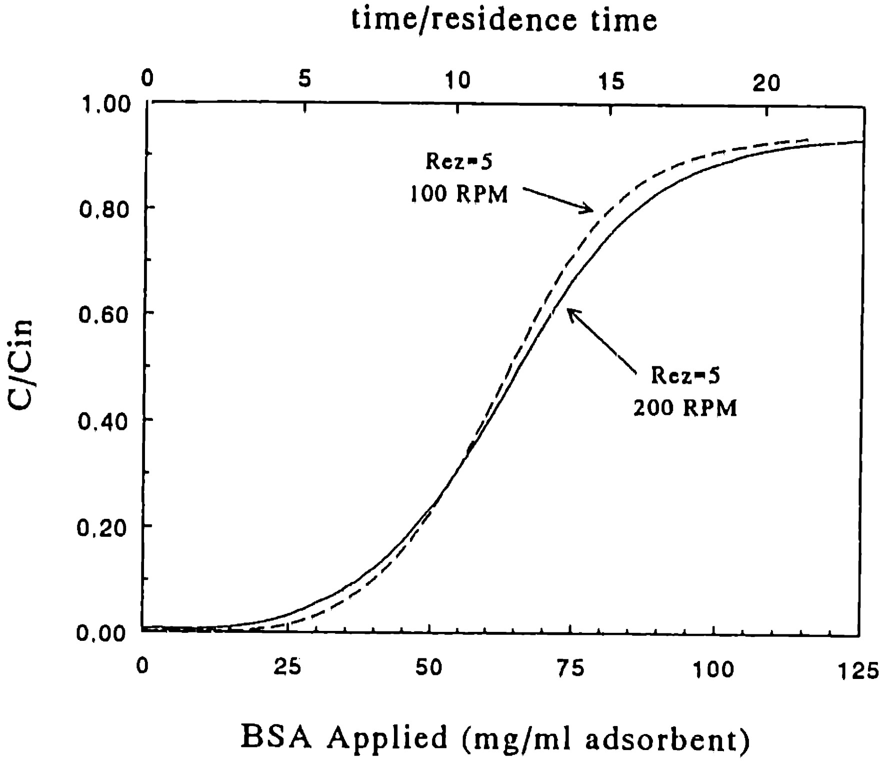

Figure 8.9 - Protein adsorption breakthrough curves with variable rotation rates. Experiments used f=0.21 and Re_z =5.

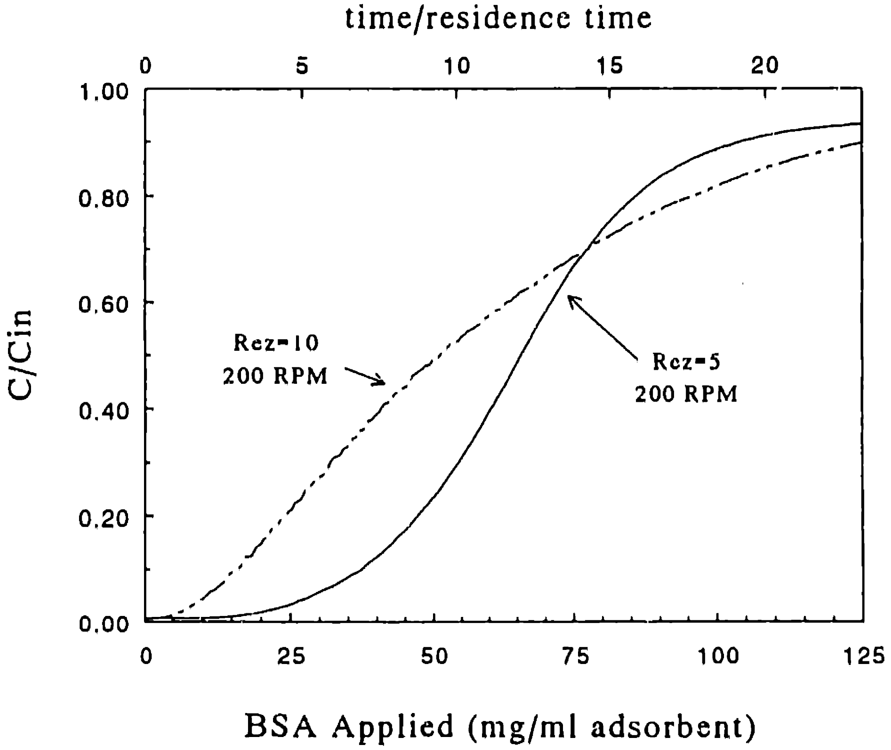

Figure 8.10 - Protein adsorption breakthrough curves with varying axial velocity. Experiments used f=0.21 and Re_θ= 1520 (200 RPM).

slight sharpening of the curve at 100 RPM as compared to the curve at 200 RPM can be attributed to the decrease in dispersion in the reactor. In general, the curves show the same characteristic sigmoidal shape as evidenced in the dynamic response curves for the immobilized enzyme particles (Figure 8.6). In contrast, Figure 8.10 shows data from Re_z=5 and 200 RPM plotted along with the previous curve at Re_z=5 and 200 RPM. The data from the Re_z=10 experiments does not follow the behavior expected from the known dispersion properties of the VFR. As seen in Figure 8.6, the outlet profiles with reaction (or adsorption) are expected to be relatively independent of the axial flow rate. Instead, in Figure 8.10, a much greater degree of dispersion and a poorer reactor performance is evident at higher axial flow rates. The explanation for this behavior is internal mass transfer limitations in the particles. In the previous immobilized enzyme experiments, internal mass transfer limitations were negligible and the dynamic response was well described by the model equations. With the case of protein adsorption, the assumption of no internal mass transfer limitations made in the model development is violated, therefore the apparent dispersion is no longer the same as in the non-reactive case. In formulating the model equations, it was assumed that the concentration gradients within the particles do not vary with time. In other words, when the concentration at the surface of the particle changes, the particles instantly equilibrate. This assumption is acceptable when internal mass transfer rate is faster than the intrinsic reaction rate but breaks down when internal mass transfer is the limiting rate. In the internal mass transfer limited regime, protein introduced into the VFR takes time to diffuse into the pores of the solid particles. At higher axial flow rates, the protein does not have enough time to penetrate into the particles prior to being removed by convection, therefore an earlier breakthrough of protein is observed.

By understanding the consequences of internal mass transfer limitations, one can better design a VFR for adsorption operations. In column chromatography, internal mass

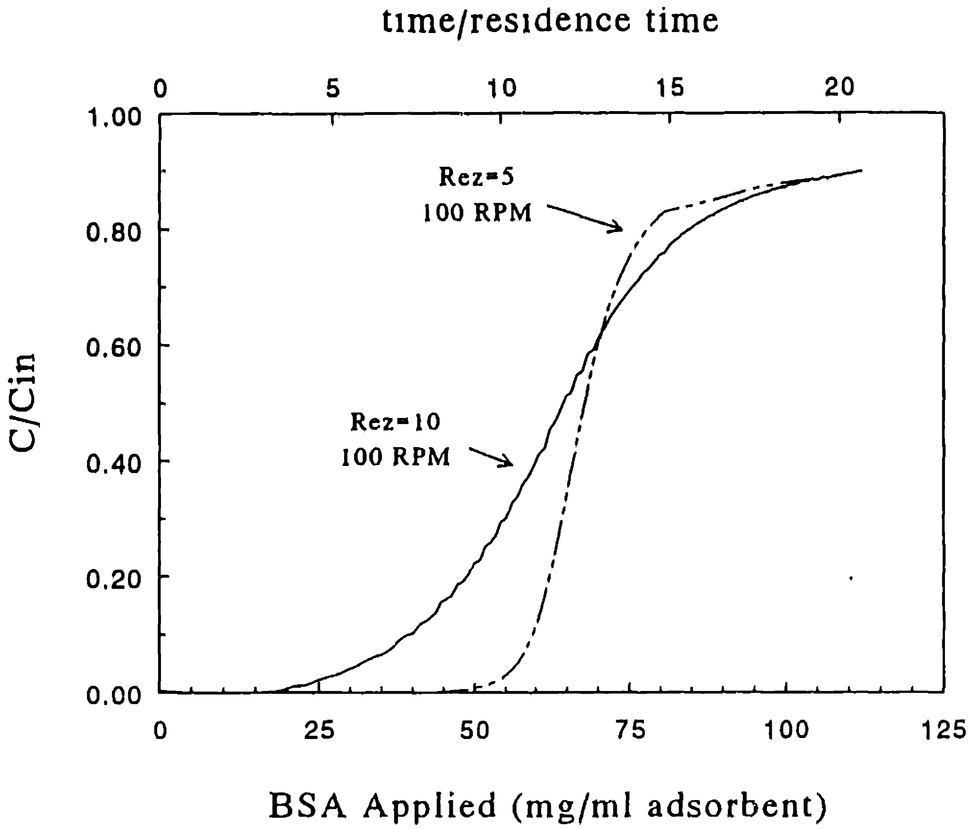

Figure 8.11 - Protein adsorption breakthrough curves at high particle loading Experiments use f=0.48, Re_{θ}=760 (100 RPM).

transfer limitations are circumvented either by increasing the time for convection (i.e. by lowering the flow rate or by using a longer column), or by decreasing the time for diffusion additional operational parameter of particle volume fraction which may be adjusted to improve reactor performance. An example of breakthrough curves with f=0.48 is shown in Figure 8.11. The experiments used the same axial Reynolds numbers as in Figure 8.10 and a rotation rate of 100 RPM. As can be seen in Figure 8.11, increasing the volume fraction of particles and thus the available surface area greatly improved reactor performance. The curve at Re_z=5 shows excellent dispersion properties. Under these conditions approximately 80% of the ion exchange capacity was utilized before losing protein in the outlet stream. The low degree of dispersion evident in the Re_z=5 case is typically characteristic of a packed bed operation. However, since the VFR is a fluidized bed it has the advantage of being able to process solids-containing process streams. The high particle loadings of up to 50% are greater than those achievable in conventional fluidized beds. Pharmacia (1994) reports the minimum and nominal fluidization velocities of these particles in a conventional fluidized bed corresponds to 2 and 3 fold bed expansions, or volume fractions of approximately 0.3 and 0.2, respectively. By operating at higher particle fractions, the VFR can provide improved adsorption performance, even with an internally mass transfer limited process.

8.4 Discussion of VFR with Suspended Particles

This chapter has presented experimental results for suspended immobilized enzyme and ion exchange particles in the VFR. The experiments with immobilized alkaline phosphatase show good agreement with the model thus validating the mathematical model. Operation in the external mass transfer limited regime was not examined due to the extremely high enzymatic loading required. It is unlikely that such high immobilized enzyme loadings can be obtained for either alkaline phosphatase or heparinase.

In addition to demonstrating the success of the model in describing VFR operation, the results in this chapter also point out the model limitations. In the dynamic response experiments on anion exchange particles, the effect of product adsorption onto particles was noticed through a comparison of the experimental results and the predictions of the model which neglected adsorption. Internal mass transfer resistances were evident in the protein adsorption experiments by examining the effect of axial flow rate on the reactor performance. The mathematical model does not yet account for these effects of adsorption and internal mass transfer limitations. Future work can focus on extending the current model, presented in Chapter 3, to these phenomena.

The results presented in this chapter not only support the mathematical model but also demonstrate the utility of the VFR with suspended particles as an immobilized enzyme reactor and as an adsorber. The good dispersion properties and high particles loadings of up to f=0.50 make the VFR an attractive alternative to a traditional fluidized bed. The work in this chapter further suggests optimal operating conditions for the VFR. Since external mass transfer resistances are negligible, the best performance is achieved at low rotation rates. The rotation rate must be high enough to provide Taylor-Couette flow with good radial mixing (i.e. about 100 RPM for the current design). By using the low rotation rates, the best dispersion properties are obtained with the lowest particle breakage.

Chapter 9 -

Conclusions

This thesis presents work on characterization of a vortex flow reactor and demonstrates applications of the reactor to immobilized enzymatic reactions and adsorptive separations. The specific steps and conclusions from this thesis are outlined below.

1.) A mathematical model using a one-dimensional dispersion reaction equation was developed to describe the complicated hydrodynamic and reaction behavior in Taylor-Couette vortex flow. The model uses only macroscopic transport and reaction parameters, which can be measured or independently determined. The modeling approach assumes that the dispersion and solute velocity with reaction are the same as in the nonreactive case. This assumption is valid as long as the system is not rate limited by diffusion through the solid support; experiments of protein adsorption in the VFR illustrate the consequences a violating the internal mass transfer assumption.

2.) Axial dispersion in Taylor-Couette vortex flow was quantified over a wide range of reactor geometries and operating conditions. A new method of fitting the residence time distribution curves employing the coefficient of quartile variation was successfully used in the experiments, particularly in fitting curves with high amounts of dispersion where the traditional method of moments gave erroneous results. The correlation for axial dispersion,

$$Pe^{-1} = 7.2x10^{-3}(b/r_i)^{-0.28} Re_\theta^{1.05} Re_z^{-0.83} (2b/L) \ ,$$

was developed over the operating range of Re_z=0.5 to 30, b/r_i=0.045 to 0.37, and rotation rates of 4 to 200 times the critical rotation rates. While other researchers have previously examined axial dispersion in Taylor vortices, most studies did not use axial flow and none systematically examined all relevant operational and geometric parameters. The dispersion correlation developed in this work is an important tool for the design of vortex flow systems.

3.) Mass transfer to the cylinder wall was found to be described by the consensus correlation,

$$Sh = 0.5\ Ta^{0.5}\ Sc^{0.33} \ .$$

This relationship was found by compiling the experimental results of several independent researchers. The correlation was incorporated into the mathematical model and subsequently was used in determining mass transfer resistances to immobilized enzyme located on the inner cylinder wall.

4.) Mass transfer to suspended particles in the vortex flow reactor was examined by dissolution of solid benzoic acid particles. The expression

$$Sh_p = 5 \times 10^{-3} Ta_m^{0.38} Sc^{0.33} \left(\frac{b}{r_i}\right)^{-1.1} \left(\frac{d_p^3 g}{\nu^2}\right)^{0.33}$$

was obtained for mass transfer to suspended particles in a batch VFR. The expression

$$Sh_p = 2 \times 10^{-3} Ta_m^{0.35} Re_z^{0.37} Sc^{0.33} \left(\frac{b}{r_i}\right)^{-1.1} \left(\frac{d_p^3 g}{\nu^2}\right)^{0.33}$$

was found to describe mass transfer to suspended particles in a continuous VFR. The experimental range was Ta_m=300 to 3000 and b/r_i = 0.10 to 0.51 with Re_z= 4 to 45 in the continuous studies. Previously, only a few researchers had examined mass transfer from suspended particles in Taylor-Couette flow; none had presented a comprehensive examination of varying the operational parameters. The correlations presented above provide a method for estimatation of the external mass transfer rate to suspended particles. By using these correlations, it was determined that external mass transfer resistances are negligible for the immobilized enzyme experiments presented here and for all except extremely high immobilized enzyme loadings.

5.) The studies with immobilized alkaline phosphatase both validated the mathematical model predictions and demonstrated the utility of the VFR as an immobilized enzyme reactor. The dynamic response experiments proved to be a sensitive method to demonstrate that under the correct model limitations, the dispersion with reaction was the same as that without reaction. In the steady state experiments, the mathematical model was able to correctly predict VFR conversion using no fit parameters. Through the immobilized enzyme experiments and model simulations, it is possible to see the effects of external mass transfer, dispersion and residence time on reactor conversion. These factors are controlled by two adjustable parameters - axial flow rate and rotation. The conversion in the reactor can be adjusted by altering either of these parameters. In contrast, the flow rate is the only adjustable parameter in traditional bioreactors such as fluidized beds or hollow fiber reactors.

6.) The utility of the vortex flow reactor as an adsorber was demonstrated through protein adsorption on anion exchange particles. Because of the high volume fractions of particles possible in the VFR (up to f=0.50), the reactor can exceed traditional fluidized bed performance and approach packed bed performance.

Chapter 10-

Recommendations for Future Research

This thesis presents a systematic characterization of the vortex flow reactor and demonstrates applications of the VFR in immobilized enzymatic reaction and protein adsorption. Through this work, many questions have arisen regarding transport phenomena and applications of the VFR. The unresolved questions and suggested approaches to answering them are presented below. This section also includes new directions for research on vortex flow reactors and their applications.

Refining the Transport Correlations

This thesis uses a semi-empirical approach to quantify transport in the VFR. Further work using the same approach can strengthen and extend the correlations. For example, both experiments for mass transfer to particles and for axial dispersion in the VFR were conducted using a relatively small reactor with gap widths ranging from $b = 0.10$ to 0.65 cm. The experiments could be repeated on a larger vortex flow unit to validate the correlations for reactor scale-up.

In addition, further work on mass transfer to suspended particles could increase the reliability of the correlations. The experiments presented in Chapter 5 do not vary the particle diameter and only examine two different fluid densities. Additional studies could verify the assumed dependence on particle size and refine the relationship between fluid density and mass transfer. Mass transfer experiments using large, uniformly sized, non-porous particles with an active surface would provide the best mass transfer system. Unfortunately, this type of particle is not commercially available. As mentioned in Section 5.2.3, experimental results from mass transfer studies using small non-porous particles could be extrapolated to larger diameters. Alternatively, the mass transfer experiments could use large porous ion exchange particles in the limit of initial adsorption or desorption. A third alternative is to use large particles with a solid core and a porous, active shell. Such particles were first designed by Horvath and Lipsky (1967) for column chromatography and have been more recently used by Goetz *et al.* (1991) in magnetically stabilized fluidized beds. The particles used in the fluidized bed experiments had a thin layer of silica covering the nickel particles. Such particles could be used in the VFR for ion exchange experiments to elucidate the relationship between external mass transfer and particle size. Because of the thinness of the active layer, the internal mass transfer rate should be negligible and the adsorption should be externally mass transfer limited. Alternatively, it may be possible to coat benzoic acid or some other dissolving solid on the particles for use in dissolution studies.

Examining Transport Fundamentals

One of the drawbacks of the semi-emperical analysis is that the resulting correlations do not reflect the fundamentals hydrodynamics of the system. Nevertheless, the axial dispersion and mass transfer to suspended particles experiments provide some insight into vortex hydrodynamics. For example, the axial dispersion was found to be independent of the diffusion coefficient and the presence of suspended particles indicating convective exchange over the vortex boundaries. The convection mixing is likely due to the small applied axial flow. The question which arises is if the convective exchange occurs without axial flow. Theory of spatially periodic systems predicts that dispersion in laminar Taylor vortices (without axial flow) should vary as $D^{1/2}$ (Rosenbluth *et al.*, 1987). This theory could easily be tested with a well machined set of cylinders and internal probes to measure concentration with time. The experimental apparatus must be long enough such that end effects are negligible and that the long term limit in the dispersion formulation is satisfied (i.e. mixing is complete in the radial and circumferential directions). Since the velocity profile for Taylor Vortex flow is known, the results from these experiments could further be compared to predictions from macrotransport theory (Brenner, 1980).

Another interesting result emerged from the batch mass transfer experiments where about a 35% higher mass transfer rate was found in the vertical set-up as compared to the horizontal reactor set-up. This effect could be due either to a higher concentration of particles at the reactor bottom, or to a difference in mass transfer mechanisms between the two orientations. The possibility of a non-uniform particle distribution may be examined by measuring the mass transfer rates at the top and the bottom of the VFR using internal probes. The second possible explanation is increased transport due to the settling of particles through the vortex boundaries in the vertical orientation. No easy test is evident, but in this case the mass transfer should be proportional to the particle motion in the axial direction through the vortex boundaries. Particle transport may be examined by visually observing the spread of colored particles upon their injection into the VFR with the reactor in the vertical and horizontal orientations.

Extending the Mathematical Model

One of the simplest and most useful areas of future work is extending the mathematical model to non-linear kinetics, such as Michaelis-Menton enzyme kinetics and Langmuir-Hinshelwood type adsorptions. Conversion in the VFR can be predicted for non-linear kinetics by solving the one-dimensional transport equation using a finite difference method. As discuss in Section 3.2, it is logical to use the non-reactive dispersion coefficients and velocities in the model equations under the limit of low Damkohler number (i.e. negligible internal mass transfer resistances). Because internal mass transfer resistances are more likely to be negligible for immobilized enzymatic reaction than for protein adsorption, the first comparisons of model and experimental data should use an enzyme with Michaelis-Menton kinetics. Alternatively, enzymes with substrate or product inhibition could be used in validating the model predictions.

Protein adsorption adds another degree of difficulty to the model equations. In immobilized enzymatic reactions, all particles are considered equivalent and movement of particles within the reactor is not important. In adsorption however, the amount of protein bound to the particle is a function of time and also may be a function of particle position. If the particles do not mix, as in a packed bed, the particles at the reactor entrance have a higher loading than those at the outlet. Because particle loading varies with time and possibly position, an additional transport equation is required to describe the system. The two transport equations for substrate in solute and bound to the particles must be solved simultaneously.

Furthermore, internal mass transfer limitations are likely to be present in the case of protein adsorptions, due to the high concentration of adsorbent in the particles (i.e. fast reaction rate) and the low diffusion coefficients of the proteins. It may be possible to circumvent this problem by adsorbing a small =- molecule such as a peptide or a small protein like lysozyme (14,000 MW). By solving the coupled solute and particle transport equations described above, the breakthrough curves such as those shown in Section 8.4 can be predicted using the nonreactive dispersion and velocity parameters.

Although the current model formulation is not capable of predicting dispersion and mean velocity for the internal mass transfer limited case, the conversion can be estimated for the limits of plug flow (PFR) operation and well-stirred (CSTR) operation. The internal diffusion equation can be solved together with the mass balance equations for either a CSTR or PFR. Note that the particles are assumed to be well mixed in a CSTR and totally non-mixed in a PFR. The analysis of PFR and CSTR operation provides the upper and lower bounds of performance in the VFR.

Exploring VFR Applications

This thesis presents studies of the VFR in enzymatic reaction using immobilized alkaline phosphatase and in protein adsorption using bovine serum albumin on ion exchange particles. The alkaline phosphatase and albumin were model systems chosen strictly for the purposes of validating the mathematical model and demonstrating reactor performance. The next step in continuing this work is to use the VFR with more complex or "real" biological feed streams.

Protein purification experiments should be conducted using a cell homogenate to demonstrate the ability of the VFR to simultaneously purify and clarify a complex protein mixture. In another application, the VFR could be attached to a bioreactor to provide continuous removal of cell culture products or wastes. One specific difference between the model system of albumin adsorption and the real applications is the density and viscosity of the feed streams. Higher viscosity and higher fluid densities will require lower flow rates to correctly suspend particles within the VFR. For the suspended particles, the maximum axial velocity is expected to be 30-60% of Stokes settling velocity. This rule of thumb for the vortex flow reactor may be validated by running particle visualization experiments using a transparent fluid with high viscosity, such as glycerol or polyethylene glycol solutions. The operational limitations of a membrane reactor are expected to be independent of feed properties.

The final application of interest for the VFR is an extracorporeal reactor. The following appendix outlines calculations for an immobilized heparinase reactor for heparin neutralization in blood. The mathematical model represented in this thesis is capable of predicting reactor performance. The remaining issues lie in the physical design of the extracorporeal reactor. The VFR used in these experiments is made of materials which are not blood compatible including polysulfone, polypropylene, graphite, and rubber. A new set of cylinders will need to be constructed which are made of a blood compatible material. Once complete, blood damage will need to be tested in reactor both in the presence and absence of immobilization support. As mentioned in the appendix, the current particles are not dense enough to handle the high flow rates associated with the desired operational parameters. An alternative immobilization support may need to be developed. Finally, the immobilization chemistry for heparinase either on particles or on a membrane will need to be examined to achieve sufficient enzymatic capacity for effective heparin neutralization.

Nomenclature

Symbols:

A_s = surface area of solid support
$b = r_o - r_i$ = gap width
c_p = heat capacity
C_s = surface concentration
C_{sat}= saturation concentration
$\bar{C}$ = dimensionless concentration (Chapter 5)
$\bar{C}$ = concentration in bulk fluid (Chapter 3)
d_i = inner cylinder diameter
d_o = outer cylinder diameter
d_p = diameter of particle
D^* = dispersion coefficient
D^*_{nr} = non-reactive dispersion coefficient
D = diffusion coefficient
D_{eff} = effective diffusivity
E = enzyme activity
f = particle volume fraction (except in Chapter 2)
f = friction factor (Chapter 2)
F_g = Taylor number correction factor given by (2.1b)
g = gravitational constant
h = heat transfer coefficient
G = torque
$j_D' = \frac{k_s}{wr_i} Sc^{0.644}$ =mass transfer parameter
k' = intrinsic reaction rate constant
k_c = thermal conductivity
k_d = enzyme deactivation rate
k_{mt} = external mass transfer coefficient
k_l = microtransport reaction parameter
K^* = macrotransport reaction coefficient
K_m = Michaelis constant
l = characteristic length of solid support
L = length of reactor
M = mass
Q = coefficient of quartile variation
P = parameter, given by (2.1c)
ΔP = pressure drop
r = length in radial direction
r_i = inner radius
r_o = outer radius
R = reaction or adsorption rate
t = time
$\bar{t}$ = dimensionless time
t_r = residence time
S = specific activity
T = temperature
U = mean fluid axial velocity
U^* = mean solute velocity
U_S = superficial axial velocity
u_v = characteristic vortex velocity
V_l = liquid volume
V_{max} = maximum volumetric kinetic rate
V_s= volume of solid support
v_o= fluid velocity
w = membrane thickness

Dimensionless Numbers:

$\mathrm{Bi} = \frac{k_{mt} w}{D_{eff}}$ = Biot number

$\mathrm{Da} = \frac{k' l^2}{D_{eff}}$ = Damkohler number

$\mathrm{Gr} = \frac{b^3 \beta\, g\, \Delta T}{\nu^2}$ = Grasholf number

$\mathrm{Nu} = \frac{2b\, h}{k_c}$ = Nusselt number

$\mathrm{Nu}^* = \frac{r_i \ln(r_o/r_i)\, h}{k_c}$ = alt. Nusselt number

Nu_{cond} = Nusselt number for conduction

$\mathrm{Pe} = \frac{U\, L}{D^*}$ = Peclet number

$\mathrm{Pr} = \frac{\mu\, c_p}{k_c}$ = Prandtl number

$\mathrm{Re}_z = \frac{u_{avg}\, 2b}{\nu}$ = axial Reynolds number

$\mathrm{Re}_r = \frac{2\omega\, r_i^2}{\nu}$ =tangential Reynolds number (based on radius)

$\mathrm{Re}_\theta = \frac{\omega\, r_i\, 2b}{\nu}$ = tangential Reynolds number

$\mathrm{Sc} = \frac{\nu}{D}$ = Schmidt number

$\mathrm{Sh} = \frac{k_s\, 2b}{D}$ = Sherwood number

$\mathrm{Sh}_d = \frac{k_s\, d_i}{D}$ = Sherwood number (based on inner cylinder diameter)

$\mathrm{Sh}_p = \frac{k_s\, d_p}{D}$ = Sherwood number (based on particle diameter)

$\mathrm{Ta} = \frac{\omega b}{\nu}\left(\frac{b}{r_i}\right)^{0.5}$ = Taylor number

Ta_{cr} = critical Taylor number

$\mathrm{Ta}^* = \frac{2\, r_i^2\, b^4}{r_o^2 - r_i^2}\left(\frac{\omega}{\nu}\right)^2$ = alternate Taylor number

$\mathrm{Ta}_m = \mathrm{Ta}/F_g$ = modified Taylor number

Greek Symbols:

β = thermal coeff. of vol. expansion

δ = boundary layer thickness

ε = void fraction

$\phi = \frac{V_p}{A_p}\sqrt{k/D_{eff}}$ = Thiele modulus

$\Phi = \frac{R\, w^2}{D_{eff}\, C}$ = observed Thiele modulus

γ_w = shear rate at wall

η = effectiveness factor

λ = vortex pair height

μ = absolute viscosity

ν = kinematic viscosity

ω = rotation rate (rad/s)

ρ = density (of liquid)

ρ_L = liquid density

ρ_p = particle density

σ^2 = variance

τ = tortuosity (except in Chapter 2)

τ = shear stress (Chapter 2)

τ_{pois} = shear stress for Poiseuille flow

References

Abdallah, Y. A. G. and Coney, J. E. R., 1988, Adiabatic and Diabatic Flow Studies by Shear Stress Measurements in Annuli with Inner Cylinder Rotation. *J. Fluids Engng* 110, 399-405.

Abu-Reesh, I. and Kargi, F., 1989, Biological Responses of Hybridoma Cells to Defined Hydrodynamic Shear Stress. *J. Biotechnol.* 9, 167-178.

Acrivos, A., 1980, A Note on the Rate of Heat or Mass Transfer from a Small Particle Freely Suspended in a Linear Shear Field. *J. Fluid Mech.* **98**, 299-304.

Afeyan, N.B., Gordon, N.F. and Cooney, C.L., 1989, Mathematical Modelling of the Continuous Affinity-Recycle Extraction Purification Technique. *J.Chromat.* 478, 1-19.

Aoki, H., Nohira, H. and Arai, H., 1967, Convective Heat Transfer in an Annulus with an Inner Rotating Cylinder. *Bull. JSME* 10, 523-532.

Aris, R., 1956, On Dispersion of a Solute in a Fluid Flowing Through a Tube. *Proc. R. Soc.* 235, 67-77.

Arvia, A. J. and Carozza, J. S. W., 1962, Mass Transfer in the Electrolysis of $CuSO_4$-H_2SO_4 in Aqueous Solutions under Limiting Current and Forced Convection Employing a Cylindrical Cell with Rotating Electrodes. *Electrochim. Acta* 7, 65-78.

Astill, K. N., 1964, Studies of the Developing Flow Between Concentric Cylinders with the Inner Cylinder Rotating. *J. Heat Transfer* 86, 383-392.

Astill, K. N., Ganley, J. N. and Martin, B. W., 1968, The Developing Tangential Velocity Profile for Axial Flow in an Annulus with a Rotating Inner Cylinder. *Proc. R. Soc.* A307, 55-69.

Balakrishnan, M., Agarwal, G. P. and Cooney, C. L., 1993, Study of Protein Transmission through Ultrafiltration Membranes. *J. Membrane Sci.* 85, 111-128.

Ball, K. S., Farouk, B. and Dixit, V. C., 1989, An Experimental Study of Heat Transfer in a Vertical Annulus with a Rotating Inner Cylinder. *Int. J. Heat Mass Transfer* 32, 1517-1527.

Bailey, J. E. and D. F. Ollis, 1977, *Biochemical Engineering Fundamentals*. McGraw Hill, New York.

Basheeruddin, K., V. Rothman and S. Margolis, 1985, Immobilzed *E. Coli* Alkaline Phosphatase; Its Properties, Stability, and Utility in Studying the Dephosphorylation of Proteins. *Appl. Biochem. Biotechnol.* **11**, 133-140.

Beaudoin, G. and Jaffrin, M. Y., 1987, High Efficiency Plasmapheresis Using Rotating Membrane Device. *Life Support Syst.* 5, 273-278.

Beaudoin, G. and Jaffrin, M. Y., 1989, Plasma Filtration in Couette Flow Membrane Devices. *Artif. Organs* 13, 43-51.

Becker, K. M. and Kaye, J., 1962a, The Influence of a Radial Temperature Gradient on the Instability of Fluid Flow in an Annulus with an Inner Rotating Cylinder. *J. Heat Transfer* 84, 106-110.

Becker, K. M. and Kaye, J., 1962b, Measurements of Diabatic Flow in an Annulus With an Inner Rotating Cylinder. *J. Heat Transfer* 84, 97-105.

Belfort, G., Mikulasek, P., Pimbley, J. and Chung, K. Y., 1993a, Diagnosis of Membrane Fouling Using a Rotating Annular Filter: 1. Cell Culture Media. *J. Membrane Sci.* 77, 1-22.

Belfort, G., Mikulasek, P., Pimbley, J. M. and Chung, K. Y., 1993b, Diagnosis of Membrane Fouling Using a Rotating Annular Filter. 2. Dilute Particle Suspensions of Known Particle Size. *J. Membrane Sci.* 77, 23-39.

Bennett, J. A. R. and Lewis, J. B., 1958, Dissolution Rates of Solids in Mercury and Aqueous Liquids: The Development of a New Type of Rotating Dissolution Cell. *AIChE J.* 4, 418-422.

Bernstein, H., Lund, D., Randawa, M., Yang, V.C., Harmon, W. and Langer, R., 1987, Extracorporeal Enzymatic Heparin Removal Using a Sheep Dialysis Model. *Kidney Int.* 32, 452-463.

Bernstein, H. and Langer, R., 1988, *Ex Vivo* Model of an Immobilized-Enzyme Reactor. *Proceedings of the National Acadamy of Science* 85, 8751-8755.

Beyer, W. H., 1981, *CRC Standard Mathematical Tables* . CRC Press, Boca Raton.

Bird, R. B., W. E. Stewart and E. N. Lightfoot, 1960, *Transport Phenomena* . John Wiley & Sons, New York.

Bjorklund, I. S. and Kays, W. M., 1959, Heat Transfer Between Concentric Rotating Cylinders. *J. Heat Transfer* 81, 175-186.

Brenner, H., 1980a, A General Theory of Taylor Dispersion Phenomena. *PhysicoChem. Hydrodynam.* 1, 91-123.

Brenner, H., 1980b, Dispersion Resulting From Flow Through Spatially Periodic Porous Media. *Phil. Trans. R. Soc.* A 297, 81-133.

Bretaudiere, J.-P. and T. Spillman, 1983, Alkaline Phosphatases, in *Methods of Enzymatic Analysis* eds. Bergmeyer, J. and Grassl, M.). pp. 75-92, Verlag Chemie, Deerfield Beach, FL.

Bühler, K., Coney, J. E. R., Wimmer, M. and Zierep, J., 1986, Advanaces in Taylor Vortex Flow: A Report on the Fourth Taylor Vortex Working Party Meeting. *Acta Mech.* 62, 47-61.

Buijs, A. and Wesselingh, J.A., 1980, Batch Fluidized Ion-Exchange Column for Streams Containing Suspended Particles. *J.Chromat.* 201, 319-327.

Burns, M.A. and Graves, D.J., 1985, Continuous Affinity Chromatography Using a Magnetically Stabilized Fluidized Bed. *Biotechnol. Prog.* 1, 95-103.

Carberry, J.J., 1976, *Chemical and Catalytic Reaction Engineering* . McGraw-Hill, New York.

Chandrasekhar, S., 1958, The Stability of Viscous Flow Between Rotating Cylinders. *Proc. R. Soc.* A246, 301-311.

Chandrasekhar, S., 1960, The Hydrodynamic Stability of Viscid Flow Between Coaxial Cylinders. *Proc. Natn. Acad. Sci. U.S.A.* 46, 141-143.

Chandrasekhar, S., 1961, *Hydrodynamic and Hydromagnetic Stability* . Clarendon Press, Oxford.

Chandrasekhar, S., 1962, The Stability of Spiral Flow Between Rotating Cylinders. *Proc. R. Soc.* A265, 188-197.

Chung, S. F. and C. Y. Wen, 1968, Longitudinal Dispersion of Liquid Flowing Through Fixed and Fluidized Beds. *AIChE J.* **14**, 857-866.

Chung, K. C. and Astill, K. N., 1977, Hydrodynamic Instability of Viscous Flow Between Rotating Coaxial Cylinders with Fully Developed Axial Flow. *J. Fluid Mech.* 81, 641-655.

Coeuret, F. and Legrand, J., 1980, Mass Transfer at the Walls of a Couette-Type Cell with Small Gaps in the Laminar Vortex Regime. *J. Appl. Electrochem.* 10, 785-788.

Coeuret, F. and Legrand, J., 1981, Mass Transfer at the Electrode of Concentric Cylindrical Reactors Combining Axial Flow and Rotation of the Inner Cylinder. *Electrochim. Acta* 26, 865-872.

Cohen, S. and Moalem Maron, D., 1983, Experimental and Theoretical Study of a Rotating Annular Flow Reactor. *Chem. Engng J.* 27, 87-97.

Coleman, P. L., M. M. Walker, D. S. Milbrath, D. M. Stauffer, J. K. Rasmussen, L. R. Krepski and S. M. Heilmann, 1990, Immobilization of Protein A at High Density on Azlactone-Functional Polymeric Beads and Their Use in Affinity Chromatography. *J.Chromat.* **512**, 345-363.

Coles, D., 1965, Transition in Circular Couette Flow. *J. Fluid Mech.* 21, 385-425.

Coney, J. E. R. and Simmers, D. A., 1979, A Study of Fully-Developed, Laminar, Axial Flow and Taylor Vortex Flow by Means of Shear Stress Measurements. *J. Mech. Engng Sci.* 21, 19-24.

Crank, J., 1975, *The Mathematics of Diffusion* . Clarendon Press, Oxford.

Croockewit, P., Honig, C. C. and Kramers, H., 1955, Longitudinal Diffusion in Liquid Flow Through an Annulus Between a Stationary Outer Cylinder and a Rotating Inner Cylinder. *Chem. Engng Sci.* 4, 111-118.

Cussler, E.L., 1984, *Diffusion: Mass Transfer in Fluid Systems* . Cambridge University Press, New York.

Dankwerts, P. V., 1952, Continuous Flow Systems, Distribution of Residence Times. *Chem. Engng Sci.* 2, 1-13.

Datta, S. K., 1965, Stability of Spiral Flow Between Concentric Circular Cylinders at Low Axial Reynolds Number. *J. Fluid Mech.* 21, 635-640.

Davis, M. W. and Weber, E. J., 1960, Liquid-Liquid Extraction Between Rotating Concentric Cylinders. *Ind. Engng Chem.* 52, 929-934.

Davis, R. H. and T. P. Hunt, 1986, Modeling and Measurement of Yeast Flocculation. *Biotechnol. Progress* 2, 91-97.

DeStefano, A. M. R. P., Aguirre, E. and Llorens, H., 1991, Ultrafiltration as an Alternative to Chemical Clarification in Cane Juice Polarization Analysis. *J. of Assoc. of Sugar Cane Technol.* 88-95.

DiPrima, R. C., 1960, The Stability of a Viscous Fluid Between Rotating Cylinders with an Axial Flow. *J. Fluid Mech.* 9, 621-631.

DiPrima, R. C. and Swinney, H. L., 1981, Instabilities and Transition in Flow Between Concentric Rotating Cylinders, in *Hydrodynamic Instabilies and the Transition to Turbulence* (eds. Swinney, H. L. and Gollub, J. P.). pp. 139-180, Springer-Verlag, New York.

Donnelly, R. J., 1991, Taylor-Couette Flow: The Early Days. *Phys. Today* 32-39.

Donnelly, R. J. and Fultz, D., 1960, Experiments on the Stability of Spiral Flow Between Rotating Cylinders. *Proc. Natn. Acad. Sci. U.S.A.* 46, 1150-1154.

Donnelly, R. J. and Simon, N. J., 1960, An Empirical Relation for Supercritical Flow between Rotating Cylinders. *J. Fluid Mech.* 7, 401-418.

Eagles, P. M., 1974, On the Torque in Wavy Vortices. *J. Fluid Mech.* 62, 1-9.

Eisenberg, M., Tobias, C. W. and Wilke, C. R., 1954, Ionic Mass Transfer and Concentration Polarization at Rotating Electrodes. *J. Electrochem. Soc.* 101, 306-319.

Eisenberg, M., Tobias, C. W. and Wilke, C. R., 1955, Mass Transfer at Rotating Cylinders. *Chem. Engng Prog. Symp. Series* 51, 1-16.

Eklund, A. and Simonsson, D., 1988, Enhanced Mass Transfer to a Rotating Cylinder Electrode with Axial Flow. *J. Appl. Electrochem.* 18, 710-714.

Ellison, B. T. and Schmeal, W. R., 1978, Corrosion of Steel in Concentrated Sulfuric Acid. *J. Electrochem. Soc.* 124, 524-531.

Enokida, Y., Nakata, K. and Suzuki, A., 1989, Axial Turbulent Diffusion in Fluid between Rotating Coaxial Cylinders. *AIChE J.* 35, 1211-1214.

Fenstermacher, P. R., Swinney, H. L. and Gollub, J. P., 1979, Dynamical Instabilities and the Transition to Chaotic Taylor Vortex Flow. *J. Fluid Mech.* 94, 103.

Fischel, R. J., Fischer, H., Shatzel, A., Lange, W. P., Cahill, D., Gervais, D. and Ascher, N. L., 1988, Couette Membrane Filtration with Constant Shear Stress. *Trans. Am. Soc. Artif. Intern. Organs* 34, 375-385.

Flower, J. R. and Macleod, N., 1969, The Radial Transfer of Mass and Momentum in Axial Fluid Stream between Coaxial Rotating Cylinders - II The Analogy between Mass and Momentum Transfer in Streams Containing Secondary Flows. *Chem. Engng Sci.* 24, 651-662.

Flower, J. R., Macleod, N. and Shahbederian, A. P., 1969, The Radial Transfer of Mass and Momentum in Axial Fluid Stream between Coaxial Rotating Cylinders- I Experimental Measurements. *Chem. Engng Sci.* 24, 637-650.

Freed, L.E., Vunjak-Novakovic, G.V., Drinker, P.A. and Langer, R., 1993a, Bioreactor Based on Suspended Particles of Immobilized Enzyme. *Annals Biomedical Engineering* 21, 57-65.

Freed, L.E., Vunjak-Novakovic, G.V., Bernstein, H., Cooney, C.L. and Langer, R., 1993b, The Kinetics of Immobilized Heparinase in Human Blood. *Ann. Biomed. Engng* 21, 67-76.

Gabe, D. R., 1974, The Rotating Cylinder Electrode. *J. Appl. Electrochem.* 4, 91-108.

Gabe, D. R. and Walsh, F. C., 1983, The Rotating Cylinder Electrode: A Review of Development. *J. Appl. Electrochem.* 13, 3-22.

Gagnon, D., 1993, *Personal Communication.*.

Gagnon, D. and Coleman, P. L., 1994, Azlactone-Grafted Microporous Membranes. *207th American Chemical Soceity Meeting* (San Diego, CA).

Gardiner, S. R. M. and Sabersky, R. H., 1978, Heat Transfer in an Annular Gap. *Int. J. Heat Mass Transfer* 21, 1459-1466.

Gaylor, J. D. S. and Smeby, L. C., 1976, The Taylor-Vortex Membrane Oxygenator: Design Analysis Based on a Predictive Correlation for Oxygen Transfer, in *Physiological and Clinical Aspects of Oxygenator Design* (eds. Dawids, S. G. and Engell, H. C.). pp. 65-76, Elsevier/North-Holland, Amsterdam.

Gazley, C., 1958, Heat-Transfer Characteristics of a Rotational and Axial Flow Between Concentric Cylinders. *Trans. Am. Soc. Mech. Engrs* 80, 79-90.

Goetz, V., Remaud, M., and Graves, D. J., A Novel Magnetic Silica upport for Use in Chromatographic and Enzymatic Bioprocessing. *Biotechnol. Bioengng* 37, 614-622.

Goldinger, W., Rebsamen, E., Brandli, E. and Ziegler, H., 1986, Dynamische Mikro-und Ultrafiltration in der Biotechnologie. *Tech. Rdsch. Sulzer* 3, 10-12.

Gordon, N.F., Tsujimura, H. and Cooney, C.L., 1990, Optimization and Simulation of Continuous Affinity-Recycle Extraction (CARE). *Bioseparation* 1, 9-21.

Gorman, M. and Swinney, H. L., 1982, Spatial and Temporal Characteristics of Modulated Waves in the Circular Couette System. *J. Fluid Mech.* 117, 123-142.

Gravas, N. and Martin, B. W., 1978, Instability of Viscous Axial Flow in Annuli Having a Rotating Inner Cylinder. *J. Fluid Mech.* 86, 385-394.

Grutzner, J. B. and P. J. Pellechia, 1990, Vortex Stabilized Electrophoretic Separation Apparatus. *U.S. Patent 4,900,421.*

Grutzner, J. B., Patrick, E. A., Pellechia, P. J. and Vera, M., 1988, The Continuously Rotated Cellular Reactor. *J. Am. Chem. Soc.* 110, 726-728.

Gu, Z.-H. and Fahidy, T. Z., 1982, Electrolytic Mass Transport at a Rotating Outer Cylinder Electrode with Developing Axial Flow in the Annulus. *J. Appl. Electrochem.* 12, 659-667.

Gu, Z. H. and Fahidy, T. Z., 1985a, Characteristics of Taylor Vortex Structure in Combined Axial and Rotating Flow. *Can. J. Chem. Engng* 63, 710-715.

Gu, Z. H. and Fahidy, T. Z., 1985b, Mass Transport in the Taylor-Vortex Regime of Rotating Flow. *Chem. Engng Sci.* 40, 1145-1153.

Gu, Z. H. and Fahidy, T. Z., 1985c, Visualization of Flow Patterns in Axial Flow Between Horizontal Coxial Roating Cylinders. *Can. J. Chem. Engng* 63, 14-21.

Gu, Z. H. and Fahidy, T. Z., 1986, The Effect of Geometric Parameters on the Structure of Combined Axial and Taylor-Vortex Flow. *Can. J. Chem. Engng* 64, 185-189.

Guihard, L., Coeuret, F., Legrand, J., Fahidy, T. Z. and Gu, Z. H., 1989, Circumferential Mixing in the Taylor-Couette Reactor, in *Electrochemical Enginnering 1989*, The Institution of Chemical Engineers, Loughborough University.

Haas, F. C. and Nissan, A. H., 1961, Experimental Heat Transfer Characteristics of a Liquid in Couette Motion and with Taylor Vortices. *Proc. R. Soc.* 1961, 215-226.

Hallstrom, B. and Lopez-Levia, M., 1978, Description of a Rotating Ultrafiltration Module. *Desalination* 24, 273-279.

Halow, J. S. and G. B. Wills, 1970a, Experimental Observations of Sphere Migration in Couette Systems. *Ind. Eng. Chem. Fundam.* 9, 603-607.

Halow, J. S. and G. B. Wills, 1970b, Radial Migration of Spherical Particles in Couette Systems. *AIChE J.* **16**, 281-286.

Hansoon, M. A. and Martin, B. W., 1977, The Stability of Viscous Axial Flow in an Annulus with a Rotating Inner Cylinder. *Proc. R. Soc.* A352, 351-380.

Harmon, W., 1994, *Personal Communication.*

Heuser, G. and Opitz, R., 1980, A Couette Viscometer for Short Time Shearing of Blood. *Rheology* 17, 17-24.

Ho, C. Y., Nardacci, J. L. and Nissan, A. H., 1964, Heat Transfer Characteristics of Fluids Moving in a Taylor System of Vortices. *AIChE J.* 10, 194-202.

Holeschovsky, U. B. and Cooney, C. L., 1991, Quantitative Description of Ultrafiltration in a Rotating Filtration Device. *AIChE J.* 37, 1219-1226.

Holman, K.L. and Ashar, S.T., 1971, Mass Transfer in Concentric Rotating Cylinders with Surface Chemical Reaction in the Presence of Taylor Vortexes. *Chem. Engng Sci.* 26, 1817-1831.

Horn, F. J. M., 1971, Calculation of Dispersion Coefficients by Means of Moments. *AIChE J.* 17, 613.

Horvath, C., and Lipsky, S. R., 1967, *J. Chromatogr. Sci.* 7, 109.

Howell, J. A., Fredrickson, A. G. and Tsuchiya, H. M., 1966, Optimal and Dynamic Characteristics of a Continuous Photosynthetic Algal Gas Exchanger, in *Nuclear Engineering Part XVI* (Ed. (eds. Hill, F. B., Walker, C. A., Raines, G. E. and Dryden, C. E.). pp. 56-68, American Institute of Chemical Engineers, New York.

Iosilevskii, G., Brenner, H., Moore, C. M. V., and Cooney, C. L., 1993, Mass Transport and Chemical Reaction in Taylor-Vortex Flows with Entrained Catalytic Particles: Application to a Novel Class of Immobilized Enzyme Biochemical Reactors. *Phil. Trans. R. Soc.,* A 345, 259-294.

Ivory, C. N., Gobie, W. A. and Koegler, W. S., 1992, High Performance Preparative Electrophoresis. *AIChE Annual Meeting (Miami Beach)*, Abstract 91c.

Jaffrin, M. Y., 1989, Innovative Processes for Membrane Plasma Separation. *J. Membrane Sci.* 44, 115-129.

Janes, D. A., Thomas, N. H. and Callow, J. A., 1987, Demonstration of a Bubble-Free Annular-Vortex Membrane Bioreactor for Batch Culture of Red Beet Cells. *Biotechnol. Techniques* 1, 257-262.

Jiang, S. C., Thurmond, J. M., Pichard, S. L. and Paul, J. H., 1992, Concentration of Microbial Populations from Aquatic Environments by Vortex Flow Filtration. *Marine Biol. Prog. Ser.* 80, 101-107.

Jones, C. A., 1981, Nonlinear Taylor Vortices and Their Stability. *J. Fluid Mech.* 102, 249-261.

Kappesser, R., Cornet, I. and Grief, R., 1971, Mass Transfer to a Rough Rotating Cylinder. *J. Electrochem. Soc.* 118, 1957-1959.

Kataoka, K., 1975, Heat-Transfer in a Taylor Vortex Flow. *J. Chem. Engng Japan* 8, 271-276.

Kataoka, K., 1986, Taylor Vortices and Instabilities in Circular Couette Flows, in *Encyclopedia of Fluid Mechanics* (Ed. by Cheremisinoff, N. P.). pp. 236-274, Gulf Publishing, Houston.

Kataoka, K., Bitou, Y., Hashioka, K., Komai, T. and Doi, H., 1984, Mass Transfer in the Annulus between Two Coaxial Rotating Cylinders, in *Heat and Mass Transfer in Rotating Machinery* (eds. Metzger, D. E. and Afgan, N. H.). pp. 143-153, Hemisphere, New York.

Kataoka, K., Doi, H. and Hongo, T., 1975, Ideal Plug-Flow Properties of Taylor Vortex Flow. *J. Chem. Engng Japan* 8, 472-476.

Kataoka, K., Doi, H. and Komai, T., 1977, Heat/Mass Transfer in Taylor Vortex Flow with Constant Axial Flow Rates. *Int. J. Heat Mass Transfer* 20, 57-63.

Kataoka, K. and Takigawa, T., 1981, Intermixing over Cell Boundary between Taylor Vortices. *AIChE J.* 27, 504-508.

Kaye, J. and Elgar, E. C., 1958, Modes of Adiabatic and Diabatic Fluid Flow in an Annulus With an Inner Rotating Cylinder. *Trans. Am. Soc. Mech. Engrs* 753-763.

Koenig, W. W., Olin, J., Babb, A. L. and McCarthy, J. L., 1954, Continuous Countercurrent Ion Exchange: II. Mass Transfer Rates in Spinner Columns. *Chem. Engng Prog. Symp. Series* 50, 111-121.

Kroner, K. H., 1987, Enzym-Abtrennung aus Zellhomogenaten mit dem Biodruckfilter. *Bioengng* 36-46.

Kroner, K. H. and Nissinen, V., 1986, Recent Studies with Dynamic Filtration of Microbial Suspensions using an Axially Rotating Filter, in *5th International Symposium Synth. Membr. in Science and Industry* .

Kroner, K. H. and Nissinen, V., 1987, Dynamic Filtration Studies with Cell Homogenates, in *4th European Congress on Biotechnology* (eds. Neijssell, O. M., van der Meer, R. R. and Luyben, K. C. A. M.). pp. 475-478, Elsevier Science Publishers, Amsterdam.

Kroner, K. H. and Nissinen, V., 1988, Dynamic Filtration of Microbial Suspensions Using an Axially Rotating Filter. *J. Membrane Sci.* 36, 85-100.

Kroner, K. H., Nissinen, V. and Ziegler, H., 1987, Improved Dynamic Filtration of Microbial Suspensions. *Bio/Technol.* 5, 921-926.

Krueger, E. R. and DiPrima, R. C., 1964, The Stability of a Viscous Fluid Between Rotating Cylinders with an Axial Flow. *J. Fluid Mech.* 19, 528-538.

Kurusz, C., 1986, *6th Annual Meeting of Pathophysiology and Extracorporeal Technology*, San Diego, CA.

Lathrop, D. P., Fineberg, J. and Swinney, H. L., 1992a, Transition to Shear-Driven Turbulence in Couette-Taylor Flow. *Phys. Rev. A* 46, 6390-6405.

Lathrop, D. P., Fineberg, J. and Swinney, H. L., 1992b, Turbulent Flow between Concentric Rotating Cylinders at Large Reynolds Number. *Phys. Rev. Lett.* 68, 1515-1518.

Leighton, D. and A. Acrivos, 1986, Viscous Resuspension. *Chem. Engng Sci.* 41, 1377-1384.

Legrand, J. and Coeuret, F., 1984, Circumferential Mixing in One-Phase and Two-Phase Taylor Vortex Flows. *Chem. Engng Sci.* 41, 47-53.

Legrand, J. and Coeuret, F., 1987, Transfert de matiere liquide-paroi et hydrodynamique de l'ecoulement de Couette-Taylor-Poiseuille biphasic. *Can. J. Chem. Engng* 65, 237-243.

Legrand, J., Coeuret, F. and Billon, M., 1983, Structure Dynamique et Transfert de Matiere Liquide-Paroi Dans Le Cas De L' Ecoulement Laminaire Tourbillonnaire de Couette-Poiseuille. *Int. J. Heat Mass Transfer* 26, 1075-1085.

Legrand, J., Dumargue, P. and Coeuret, F., 1980, Overall Mass Transfer to the Rotating Inner Electrode of a Concentric Cylindrical Reactor with Axial Flow. *Electrochim. Acta* 25, 669-673.

Levenspiel, O., 1972, *Chemical Reaction Engineering* . John Wiley & Sons, New York.

Lieberherr, J., 1978, Scherfiltration in Ringsplat, PhD Thesis, ETH, Zurich.

Linhardt, R.J.,Grant, A., Cooney, C.L. and Langer, R., 1982, Differential Anticoagulent Activity of Heparin Fragments Prepared Using Microbial Heparinase. *J. Biol. Chem.* 257(13), 7310-7313.

Livingston, A. G. and Noble, J. B., 1993, Mass Transfer in Liquid-Solid Fluidized Beds of Ion Exchange Resins at Low Reynolds Numbers, *Chem. Engng Sci.*, 48(6), 1174-1178.

Lohse, D. and Linhardt, R., 1992, Purification and Characterization of Heparin Lyases from *Flavobacterium heparinum*, *J. Biol. Chem.* 267, 243-247.

Lopez-Levia, 1979, Ultrafiltration in Rotary Annular Flow, MSc Thesis, Lund University, Sweden.

Lopez-Levia, M., 1980a, Prediction of Permeate Fluxes in UF/RO Systems. *Polym. Sci. Technol.* 13, 269-281.

Lopez-Levia, M., 1980b, Ultrafiltration at Low Degrees of Concentration Polarization: Technical Possibilities. *Desalination* 35, 115-128.

Macleod, N. and Ruess, T., 1975, The Radial Transfer of Mass to an Axial Stream of Liquid between Coaxial Rotating Cylinders. *Chem. Engng Sci.* 30, 235-242.

Majumdar, A. K. and Spalding, D. B., 1977, Numerical Computation of Taylor Vortices. *J. Fluid Mech.* 81, 295-304.

Marcus, P. S., 1984a, Simulation of Taylor-Couette Flow. Part 1. Numerical Methods and Comparison with Experiment. *J. Fluid Mech.* 146, 45-64.

Marcus, P. S., 1984b, Simulation of Taylor-Couette Flow. Part 2. Numerical Results for Wavy-Vortex Flow with One Travelling Wave. *J. Fluid Mech.* 146, 65-113.

Maycock, R. L., 1949, *United States Patent 2474006*.

Mendler, N., Mottaghy, K., Shröck, R., Schmid-Schönbein, H. and Sebening, F., 1976, A Fluid Oxygenator Using Shear Flow Dispersion of Blood in Fluorocarbon, in *Physiological and Clinical Aspects of Oxygenator Design* (eds. Dawids, S. G. and Engell, H. C.). pp. 119-128, Elsevier/North-Holland, Amsterdam.

Mered, M., Dadson, A., Lowe, B., Figueroa, C., Cohen, D. and Rice, C., 1992, Comparison of Commercially Available Cell Culture Recycle Systems: Application to Large Scale Continuous Perfusion Fermentation, *International Biotechnology Symposium*, (Washington, DC).

Miller, R. L., Fredrickson, A. G., Brown, A. H. and Tsuchiya, H. M., 1964, Hydromechanical Method to Increase Efficiency of Algal Photosynthesis. *Ind. Engng Chem. Proc. Des. and Develop.* 3, 134-143.

Mizushina, T., 1971, The Electrochemical Method in Transport Phenomena, in *Advances in Heat Transfer* (eds. Irvine, T. F. and Hartnett, J. P.). pp. 87-161, Academic Press, New York.

Mizushina, T., Ito, R., Kataoka, K., Nakajima, Y., & Fukada, A., 1971, Velocity Distribution of Taylor Vortex Flow in an Annulus Between Rotating Coaxial Cylinder, *Kagaku Kogaku,* 35, 1116-1121.

Moalem Maron, D., 1983, Theoretical Analysis of Concentration Distribution in a Multicomponent Rotating Stream. *Israel J. Technol.* 21, 125-133.

Mottaghy, K. and Hanse, H. J., 1985, Effect of Combined Shear, Secondary and Axial Flow of Blood on Oxygen Uptake. *Chem. Engng Commun.* 36, 269-279.

Nakabayashi, K., Yamada, Y. and Kishimoto, T., 1982, Viscous Frictional Torque in the Flow Between Two Concentric Rotating Rough Cylinders. *J. Fluid Mech.* 119, 409-422.

Ney, W. O. and Lochte, H. L., 1941, Columns for Liquid-Liquid Extraction. *Ind. Engng Chem.* 33, 825-828.

Ohashi, K., Tashiro, K., Kushiya, F., Matsumoto, T., Yoshida, S., Endo, M., Horio, T., Ozawa, K. and Sakai, K., 1988, Rotation-Induced Taylor Vortex Enhances Filtrate Flux in Plasma Separation. *Trans. Am. Soc. Artif. Intern. Organs* 34, 300-307.

Olin, J., Koenig, W. W., Babb, A. L. and McCarthy, J. L., 1954, Continous Countercurrent Ion Exchange: I. Resin Particle Settling Rates in Spiner Columns. *Chem. Engng Prog. Symp. Series* 50, 103-110.

Ouyang, Q., Boissonade, J., Roux, J.C. and Kepper, P.D., 1989, Sustained Reaction-Diffusion Structures in an Open Reactor. *Phys. Lett. A* 134, 282-286.

Paul, J. H., Jiang, S. C. and Rose, J. B., 1991, Concentration of Viruses and Dissolved DNA from Aquatic Environments by Vortex Flow Filtration. *Appl. Environ. Microbiol.* 57, 2197-2204.

Pharmacia BioProcess Technology AB, 1993, *Data File - Expanded Bed Adsorption.*

Pudjiono, P. I., Tavare, N. S., Garside, J. and Nigam, K. D. P., 1992, Residence time distribution from a continuous Couette flow device. *Chem. Engng J.* 48, 101-110.

Pungor, E.J., Afeyan, N.B., Gordon, N.F. and Cooney, C.L., 1987, Continuous Affinity-Recycle Extraction: A Novel Protein Separation Technique. *Bio/Technol.* 5, 604-608.

Rebsamen, E., 1983, Fundamentals and Engineering Concept of a Pressure Filter for Dynamic Filtration. *Tech. Film Appl. Oper. Genie Chim. Colloq. Int.* 489-510.

Rebsamen, E., Goldinger, W., Scheirer, W. and Merten, O.-W., 1985, Use of a Dynamic Filtration Method for Separation of Animal Cells,*7th General Meeting of European Society for Animal Cell Technology* , (Baden/Vienna).

Rolchigo, P. M., August, 1992, Vortex Flow Perfusion , *International Biotechnology Symposium,* (Washington, DC).

Rolchigo, P. M., Raymond, W. and Hildebrandt, J., 1988, The Improved Control of Ultrafiltration with the Use of Vaorticular Hydrodynamics with Ultra-Hydrophilic Membranes, *AIChE Annual Meeting*, (Washington, DC).

Satterfield, C. N., 1970, *Mass Transfer in Heterogeneous Catalysis*. Kriegar Publishing, Malabar, FL.

Schlichting, H., 1955, *Boundary -Layer Theory* . McGraw-Hill, New York.

Scopes, R. K., 1987, *Protein Purification; Principles and Practice* . Springer-Verlag, New York.

Shapiro, M. and H. Brenner, 1986, Taylor Dispersion of Chemically Reactive Species: Irreversible First-Order Reactions in Bulk and on Boundaries. *Chem. Engng Sci.* 41, 1417-1433.

Shapiro, M. and H. Brenner, 1988, Dispersion of a Chemically Reactive Solute in a Spatially Periodic Model of a Porous Medium. *Chem. Engng Sci.* 43, 551-571.

Shen, G. C., C. J. Geankoplis and R. S. Brodkey, 1985, A Note on Particle-Liquid Mass Transfer in a Fluidized Bed of Small Irregular-Shaped Benzoic Acid Particles. *Chem.Engng Sci.* **40**, 1797-1802.

Sherwood, T. K., Brian, P. L. T. and Fisher, R. E., 1967, Desalination by Reverse Osmosis. *Ind. Engng Chem. Fund.* 6, 2-12.

Sherwood, T. K. and Ryan, J. M., 1959, Mass Transfer to a Turbulent Fluid With and Without Chemical Reactions. *Chem. Engng Sci.* 11, 1959.

Shirkhanzadeh, M., 1987, A Rotating Cylinder Electrode for Corrosion Studies Under Controlled Heat Transfer Conditions. *Corrosion* 43, 621-623.

Shoendorfer, D., 1987, *U. S. Patent 4,675,106* .

Shooneman, F., 1988, Use of a New Plasma Separation Membrane for Plasma Donation; Technical and Biological Results. *Artif. Organs* 12, 526-529.

Short, J. F. and Twigg, G. H., 1951, Laboratory Liquid-Liquid Extraction Column, *Ind. Engng Chem.* 43, 2932-2933.

Simmers, D. A. and Coney, J. E., 1979a, The Effect of Taylor Vortex Flow on the Development Length in Concentric Annuli. *J. Mech. Engng Sci.* 21, 59-64.

Simmers, D. A. and Coney, J. E. R., 1979b, A Reynolds Analogy Solution for the Heat Transfer Characteristics of Combined Taylor Vortex and Axial Flow. *Int. J. Heat Mass Transfer* 22, 679-689.

Simmers, D. A. and Coney, J. E. R., 1980, Velocity Distributions in Taylor Vortex Flow with Imposed Laminar Axial Flow and Isothermal Surface Heat Transfer. *Int. J. Heat Fluid Flow* 2, 85-91.

Sinevic, V., Kuboi, R. and Nienow, A. W., 1986, Power Numbers, Taylor Numbers and Taylor Vortices in Viscous Newtonian and Non-Newtonian Fluids. *Chem. Engng Sci.* 41, 2915-2923.

Singh, P. C. and Mishra, P., 1980, Mass Transfer to Newtonian and Non-Newtonian Fluids from a Rotating Cylinder. *Chem. Engng Sci.* 35, 1657-1666.

Smith, G. P. and Townsend, A. A., 1982, Turbulent Couette Flow Between Concentric Cylinders at Large Taylor Number. *J. Fluid Mech.* 123, 187-217.

Smith, P. K., R. I. Krohn, G. T. Hermanson, A. K. Mallia, F. H. Gartner, M. D. Provenzano, E. K. Fujimoto, N. M. Goeke, B. J. Olson and D. C. Klenk, 1985, Measurement of Protein Using Bicinchoninic Acid. *Anal. Biochem.* **150**, 76-85.

Snyder, H. A., 1962, Experiments on the Stability of Spiral Flow at Low Axial Reynolds Numbers. *Proc. R. Soc.* A265, 198-214.

Snyder, H. A., 1969, Change in Wave-Form and Mean Flow Associated with Wavelength Variation in Rotating Couette Flow. Part 1. *J. Fluid Mech.* 35, 337-352.

Solomon, T. H. and J. P. Gollub, 1988, Passive Transport in Steady Rayleigh-Benard Convection. *Phys. Fluids* **31**, 1372-1378.

Sorour, M. M. and Coney, J. E. R., 1979a, The Characteristics of Spiral Vortex Flow at High Taylor Numbers. *J. Mech. Engng Sci.* 21, 65-71.

Sorour, M. M. and Coney, J. E. R., 1979b, The Effect of Temperature Gradient on the Stability of Flow between Vertical, Concentric, Rotating Cylinders. *J. Mech. Engng Sci.* 21, 403-409.

Stich, T. M., 1990, Determination of Protein Covalently Bound to Agarose Supports Using Bicinchoninic Acid. *Anal. Biochem.* **191**, 343-346.

Strong, A. B. and Carlucci, L., 1976, An Experimental Study of Mass Transfer in Rotating Couette Flow with Low Axial Reynolds Number. *Can. J. Chem. Engng* 54, 295-298.

Stuart, J. T., 1958, On the Non-linear Mechanics of Hydrodynamic Stability. *J. Fluid Mech.* 4, 1-21.

Stuart, J. T., 1986, Taylor-Vortex Flow: A Dynamical System. *SIAM Rev.* 28, 315-342.

Tachibana, F. and Fukui, S., 1964, Convective Heat Transfer of the Rotational and Axial Flow between Two Concentric Cylinders. *Bull. JSME* 7, 385-391.

Tachibana, F., Fukui, S. and Mitsumura, H., 1960, Heat Transfer in an Annulus with an Inner Rotating Cylinder. *Bull. JSME* 3, 119-123.

Tam, W. Y. and Swinney, H. L., 1987, Mass Transport in Turbulent Couette-Taylor Flow. *Phys. Rev. A* 36, 1374-1381.

Tam, W.Y., Vastano, J.A., Swinney, H.L. and Horsthemke, W., 1988, Regular and Chaotic Chemical Spatiotemporal Patterns. *Phys. Rev. Lett.* 61, 2163-2166.

Taylor, G. I., 1923, Stability of a Viscous Liquid Contained between Two Rotating Cylinders. *Phil. Trans. R. Soc.* A 223, 289-343.

Taylor, G. I., 1935, Distribution of Velocity and Temperature Between Concentric Cylinders. *Proc. R. Soc.* 151, 494-512.

Taylor, G. I., 1936, Fluid Friction Between Rotating Cylinders: I- Torque Measurements. *Proc. R. Soc.* A 157, 546-564.

Taylor, G. I., 1953, Dispersion of Soluble Matter in Solvent Flowing Slowly Through a Tube. *Proc. R. Soc.* A 219, 186-203.

Thomas, N. H. and Janes, D. A., 1987, Fluid Dynamic Considerations in Airlift and Annular Vortex Bioreactors for Plant Cell Culture. *Ann. N.Y. Acad. Sci.* 506, 171-189.

Tobler, W., 1979, Dynamic Filtration - the Engineering Concept of the Escher Wyss Pressure Filter. *Filtrn & Separn* Nov/Dec, 630-633.

Tobler, W., 1982, Dynamic Filtration: Principle and Application of Shear Filtration in An Annular Gap. *Filtrn & Separn* July/Aug, 329-332.

Tsai, Y., Sobsey, M. D., Sangermano, L. R. and Palmer, C. J., 1993, Simple Method of Concentrating Enteroviruses and Hepatitis A Virus from Sewage and Ocean Water for Rapid Detection by Reverse Transcriptase-Polymerase Chain Reaction. *Appl. Environ. Microbiol.* 59, 3488-3491.

Tramper, J., Williams, J. B., Joustra, D. and Vlak, J. M., 1986, Shear Sensitivity of Insect Cells in Suspension. *Enzyme Microb. Technol.* 8, 33-36.

Turkson, A. K., Mikhlin, J. A. and Weber, M. E., 1989a, Dynamic Membranes. I. Concentration Effects on Reflection Coefficient and Specific Resistance of Bovine Serum Albumin "Gel" Layer. *Sep. Sci. Technol.* 25, 31-44.

Turkson, A. K., Mikhlin, J. A. and Weber, M. E., 1989b, Dynamic Membranes. II. Determination of Optimum Formation Conditions and Electrofiltration of Bovine Serum Albumin with a Rotating Module. *Sep. Sci. Technol.* 24, 1261-1291.

van Hemert, I. P. A. and Tiesjema, R. H., 1987, Safety Aspects of Closed-System Filtration and Ultrafiltration in Vaccine Production. *Swiss Biotech* 5, 13-18.

Vera, M. and Grutzner, J. B., 1986, The Taylor Vortex: The Measurement of Viscosity in NMR Samples. *J. Am. Chem. Soc.* 108, 1304-1306.

Vigo, F. and Uliana, C., 1986, Influence of the Vorticity at the Membrane Surface on the Performances of the Ultrafiltration Rotating Module. *Sep. Sci. Technol.* 21, 367-381.

Vigo, F., Uliana, C. and Lupino, P., 1985, The Performance of a Rotating Module in Oily Emulsions Ultrafiltration. *Sep. Sci. Technol.* 20, 213-230.

Wendt, F., 1933, Turbulente Stromungen zwishchen zwei rotierenden konaxialen Zylindern. *Ing.-Arch.* 4, 577-595.

Westerterp, K. R. and P. Landsman, 1962, Axial Mixing in a Rotating Disk Contactor - I Apparent Longitudinal Diffusion. *Chemical Engineering Science* 17, 363-372.

Wiener, R. J., Hammer, P. W., Swanson, C. E. and Donnelly, R. J., 1990, Stability of Taylor-Couette Flow Subject to an External Coriolis Force. *Phys. Rev. Lett.* 64, 1115-1118.

Yacoub, N. and Moalem Maron, D., 1984, Analysis of Centrifugal Annular Reactor with Radial Flow. *Chem. Engng Sci.* 39, 313-318.

Yagi, S. and T. Miyauchi, 1953, On the Residence Time Curves of the Continuous Reactors. *Kagaku Kogaku* 17, 382-386.

Yang, V. C., Lindhardt, R. J., Bernstein, H., Cooney, C. L., and Langer, R., 1985, Purification and Characterization of Heparinase from *Flavobacterium heparinum*. *J. Bio. Chem.* 260, 1849-1857.

Zimmerman, J., 1994, *Personal Communication.*

Appendix A -

Design Calculations for a VFR with Immobilized Heparinase

An area of great interest for future research is the development of a VFR containing immobilized heparinase for effective neutralization of heparin with minimal blood damage. Heparin is a non-homogeneous highly-sulfated polysaccharide commonly used as an anticoagulant in extracorporeal therapy. Upon completion of therapy, it is desired to reverse the action of heparin to prevent hemorrhaging; protamine titration is typically used for this purpose. However, application of protamine can cause serious side-effects, some leading to death (Kurusz, 1986). An alternative to protamine administration is to enzymatically degrade heparin with heparinase. Heparinase, a 43 kDa enzyme isolated from *Flavobacterium heparinum*, cleaves heparin into fragments that have little or no anticoagulant activity (Linhardt *et al.*, 1982). Extracorporeal reactors containing immobilized heparinase have been shown to be effective at removing heparin *in vitro* (Freed *et al.*, 1993a,b) and *in vivo* (Bernstein *et al.*, 1987).

The VFR is expected to work well as an immobilized heparinase extracorporeal reactor because of its good transport properties and its proven biocompatibility. The biocompatibility of the vortex flow systems with blood has been demonstrated through extensive studies on blood plasmapheresis and on blood oxygenation in vortex flow, as discussed in Section 2.1. The VFR also provides excellent mass transfer and axial dispersion properties which help to maximize conversion. Furthermore, by offering two independent adjustable control parameters (axial flow rate and rotation rate), conversion may be more controllable than other traditional bioreactors such as hollow fiber, packed bed or fluidized bed reactors.

A.1 Reactor Specifications

The immobilized heparinase reactor is being considered for treatment in two applications where bleeding is a severe threat: acute dialysis and extra-corporeal membrane oxygenation (ECMO) in infants. As the reactor specifications for both cases are similar, a single reactor may be designed to suit both procedures. Regional heparinization is desired, where heparin is added prior to the extracorporeal device and neutralized prior to return to the patient. Typical blood flow rates are 300-400 cm^3/min for dialysis and 200-300 cm^3/min for ECMO in infants (Harmon, 1994). In both cases, an immobilized heparinase reactor volume with blood volume of 200 cm^3 or less is desired. The goal is to neutralize over 90% of the heparin entering the immobilized heparinase reactor (Harmon, 1994).

In addition to the amount of heparin neutralized, the design of a VFR extracorporeal reactor must consider the shear induced by the rotating cylinder. The shear rate in Taylor-Couette vortex flow can be expressed by (2.3). In the reactor designs presented here, the maximum shear rate is limited to 20,000 s^{-1} which has been shown cause negligible blood hemolysis (Heuser and Opitz, 1980; Fischel et al., 1988).

In this appendix, conversion in a VFR with immobilized heparinase is predicted using the mathematical model developed in Chapter 3 and using the transport correlations presented in Chapter 5. Heparinase in human blood is described by first-order reaction kinetics with $k'/E = 0.0028$ cm^3/U min (Freed et al., 1993b). The first order assumption is possible since the clinically relevant heparin concentrations of 2-25 μg/cm^3 are 6 to 75 times lower than the Michaelis constant for immobilized heparinase in buffer of K_m = 150 μg/cm^3. In these calculations, 1 Unit of heparinase is defined as the amount of enzyme necessary to degrade 1 mg heparin/hour. An alternative scale for heparinase activity uses International Units (IU) which are defined as the amount of enzyme causing 1 μmol of double bonds to be broken per minute. Experiments reveal that there are approximately 75 Units of heparinase per IU (Yang, 1985). The kinematic viscosity of blood is assumed to be 0.04 g/cm s, the diffusivity of heparin in blood is estimated to be 1.2×10^{-6} cm^2/s (Bernstein and Langer, 1988) and the activity of pure heparinase is assumed to be 15,000 U/mg (Lohse, 1992). The assumptions regarding heparinase capacity on the solid supports are taken from previous laboratory experience with heparinase or other enzymes

By using the known heparinase kinetics and the model equations described in the thesis, it is possible to predict performance in the VFR for any reactor geometry, operating conditions, and enzymatic loading. The calculations presented below solve the steady-state equation (3.12) using the dispersion coefficient from (5.5), and the mass transfer coefficient from the cylinder wall (2.14) or the mass transfer coefficient from suspended particles (5.15).

A.2 Design for a VFR with Suspended Immobilized Heparinase Particles

This section examines the performance of a VFR with immobilized heparinase particles using the mathematical model and reactor specifications outlined above. The first step in designing the reactor is to estimate the activity of the immobilized heparinase. Previous experiments immobilizing heparinase on underivatized agarose-silica particles (Pharmacia STREAMLINE, d_p~200 μm) obtained heparinase activities up to 1000 U/ml gel (packed bed volume) or 1400 U/ml particles (Zimmerman, 1994). This value is an observed activity, incorporating both internal mass transfer limitations and intrinsic kinetics. The immobilization efficiency, defined as the total observed heparinase activity over the soluble heparinase activity before immobilization, ranged from about 6 to 15%. These particles had approximately 0.09 mg/ml of active protein which is comparable to the alkaline phosphatase loading of approximately 0.05 mg/ml active protein.

The effectiveness factor for the immobilized heparinase may be calculated using (3.26b). Figure A.1 shows the observed reaction rate vs. the heparinase loading (i.e. amount of active heparinase per ml particles with no internal mass transfer resistances) for three different particle diameters. Note that the observed particle activity of 1400 U/ml described above is equivalent to a heparinase loading of 3000 U/ml. The observed particle activity can be increased by either increasing the amount of bound heparinase or by increasing the specific activity of the enzyme. However, because of internal mass transfer limitations, increasing the heparinase loading has diminishing returns on the observed activity. As seen in Figure A.1, higher observed activities can be obtained by using smaller particles which have lower internal mass transfer resistances. The limit of the particle diameter is ultimately constrained by the ability to retain the particles while passing the

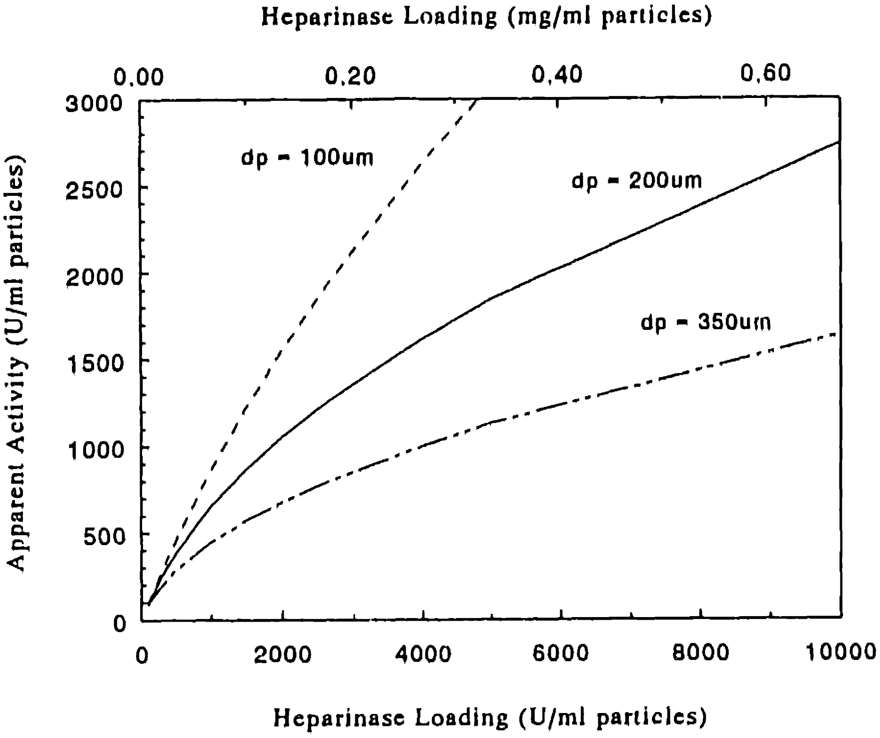

Figure A.1 - Effect of internal mass transfer limitations on observed activity for agarose-silica particles of 100, 200 and 350 μm. The heparinase loading represents the amount of active heparinase (U or mg) per ml particles with no internal mass transfer resistances.

blood cells. One advantage of internal mass transfer limitations is a lowered observed deactivation rate. For example, a 33% decrease of activity from a heparinase loading of 3000 U/ml particles would exhibit a corresponding 22% decrease in the observed activity for the 200μm particles.

The first set of design calculations examines the effect of particle volume fraction in the VFR for a reactor with dimensions of r_d = 5.2 cm, d_o = 6.0 cm , V = 350 ml and L = 50 cm. The simulations use particle volume fractions ranging from f=0.25 to 0.5; the corresponding blood volume in the VFR ranges from V_l = 260 ml to 175 ml. Figure A.2

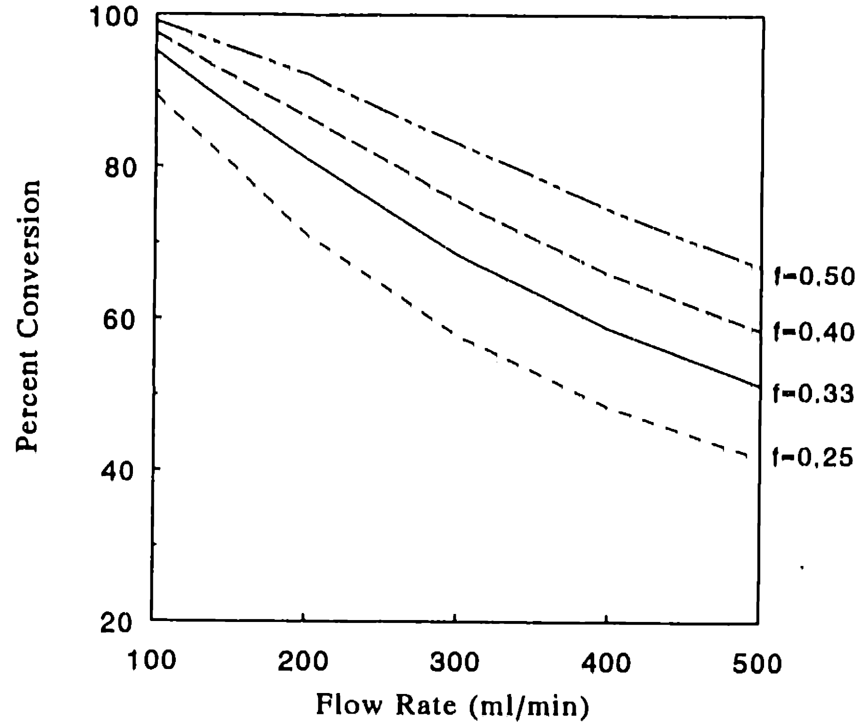

Figure A.2 - Predicted steady state conversion in a constant volume VFR containing immobilized heparinase for varied particle volume fractions and axial flow rates. Particle activity = 1400 U/ml, reactor volume = 350 ml, r_i =2.6 cm, r_o=3.0 cm, L = 50 cm.

shows the steady state conversions as a function of flow rate. The simulations use an observed particle activity of 1400 U/ml particles and a constant rotation rate of 100 RPM. Table A.1 shows an example calculation containing the intermediate parameters. As expected, the VFR conversion increases with higher particle fractions and longer residence time (i.e. slower axial flow rates). At 100 ml/min all particle loadings provide a conversion of greater than 90%. At the desired flow rates of 200-400 ml/min, the conversion falls short of the 90% goal. Conversion may be further increased by increasing the particle volume fraction, increasing the observed heparinase activity or by increasing the reactor volume and thus lengthening the residence time.

The second main operating parameter in the VFR is the rotation rate. Figure A.3 shows the overall conversion for various flow rates and rotation rates. The simulations use

HEPARINASE WORKSHEET

PARTICLE REACTOR

INPUT PARAMETERS

Design Parameters–Reactor

Do(cm)=	6
Di(cm)=	5.2
Vol liq(cm3)=	175

Design Parameters–Beads

Vol fract=	0.5
Bead diam=	0.02 cm
porosity=	0.8
tortuosity=	2

Enzymatic Parameters

Rate Const=	0.0028 cm3/U min
Loading=	3000 U/ml gel

Operating Parameters

visc(cm2/s)=	0.04
Diff(cm2/s)=	1.20E−06
Flow Rate =	5.0000 ml/s
Rotation Rat	100 RPM

****

Conversion 82.98 %

****

CALCULATED PARAMETERS

Calculated Dimensions

Gap(cm)=	0.4
GapRatio=	0.1538462
CSA (cm2) =	7.0371675
Adj CSA(cm2	3.5185838
vol/SA(cm)=	0.0033333
Surface Area	52500 cm2
res. time (s)=	35
Vol (cm3)=	350
Length(cm)=	49.7

Internal Mass Transfer

Deff=	4.800E−07
Thiele=	1.80020575
tanh(thiele)=	0.99995925
Eff. factor=	0.45265755
Obsrvd Activity=	1358
k1st,vol (min−1)	8.4
k1,surf(cm/s)	0.00046667
k1st,obs(min−1)	3.80232345
k1,s,obs(cm/s)	0.00021124

Dimensionless Numbers

P =	0.0519949
Fg =	1.1381104
Rez =	28.4205
Retheta =	272.27
Ta =	106.79
Tam =	93.834141
Pe =	234.76
dp3g/v2 =	4.9
Sh =	14.4782
Sc =	33333.333
A3wall =	1.7842
Gamma =	119.1521

External Mass Transfer

kwall (cm/s)	0.0009
kw/krxt	4.1124
PFR	83.21
CSTR	64.08

Definition – 1 U of heparinase degrades 1 mg heparin/hour

****

Wall Shear 162 s−1

****

Table A.1 - Spreadsheet showing intermediate calculations for predicted steady-state heparin conversion in the VFR with immobilized heparinase particles.

a flow rate of 200 ml/min, an observed particle activity of 1400 U/ml particles, a particle volume fraction of 0.40, and the same reactor dimensions as described above. The shear limit of 20,000 s^{-1} is reached at 2500 RPM. Figure A.3 shows the offsetting effects of dispersion and mass transfer. Upon increasing the rotation rate, a slight increase in conversion is due to the higher external mass transfer, followed by a decrease in conversion due to higher dispersion. In general, the maximum conversion is obtained between 100 to 400 RPM. To minimize shear and blood damage in the VFR it may be advantageous to operate at the lowest rotation rate of 100 RPM even if the maximum conversion is not obtained.

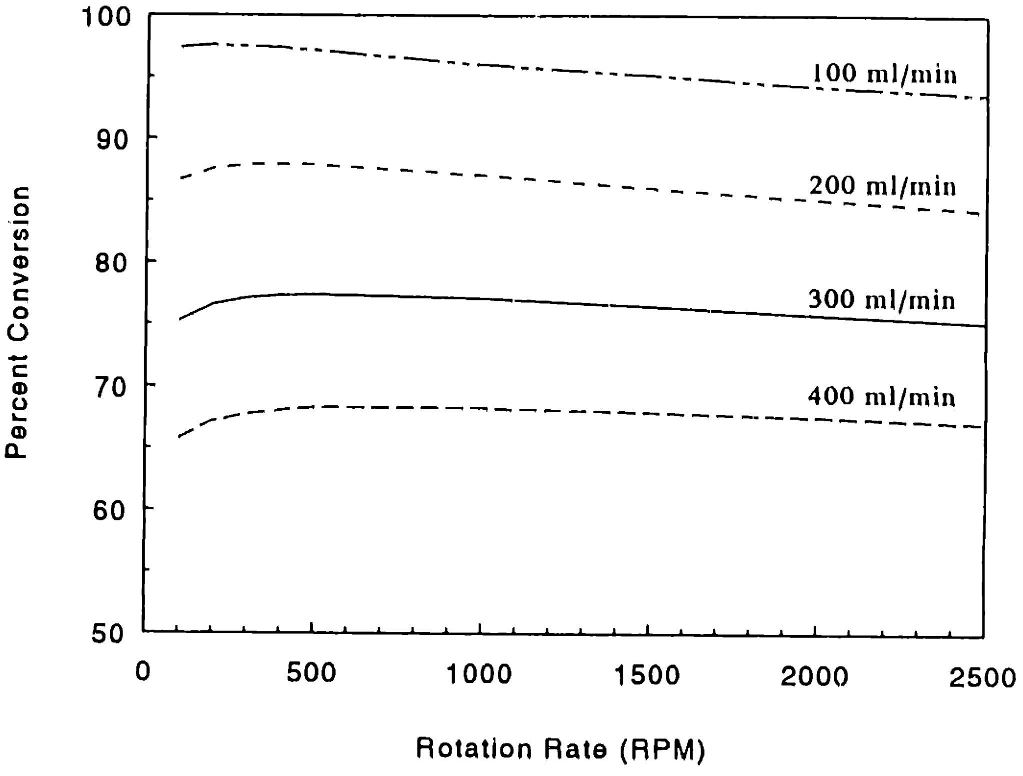

Figure A.3 - Predicted steady state conversion in a VFR containing immobilized heparinase for various flow rates and rotation rates. Particle activity = 1400 U/ml, volume fraction=0.40, flow rate=200 ml/min, reactor volume= 350 ml, r_i =2.6 cm, r_o=3.0 cm, L = 50 cm.

An important issue not addressed in the above calculations is the fluidization properties of the particles. The agarose-silica particles have a Stokes settling velocity through blood of about 0.1 cm/s. According to the particle visualization experiments in Chapter 8, suspended particles tend to be well fluidized at 30 to 60% of the Stokes settling velocity. Therefore, the corresponding maximum operating velocities for the agarose-silica particles in the VFR range from 0.03 to 0.06 cm/s. The fluid velocities in the above examples are much higher and range from 0.24 to 1.2 cm/s. Therefore, operating at these flow rates would require larger particles, higher density particles or a larger cross-sectional area (shorter reactor). To obtain the desired fluidization velocities with 200 μm particles, the current value $\Delta\rho = 0.2$ would need to be increased by 4 to 40 fold, corresponding to particle densities of 1.8 to 9.0 g/cm^3. Particles with $\rho_p = 1.8$ g/cm^3 could probably be made by increasing the silica content. Particle of higher densities could be achieved by using agarose particles with solid metal cores. For examples, the effective density of a 200 μm agarose particle with a 120 μm stainless steel core is approximately 2.6 g/cm^3; the same size particle with a 160 μm core has a density of 4.6 g/cm^3. Although the total agarose content is less in the particles with metal centers, it may be possible to obtain equivalent overall kinetic rates due to the shorter diffusion path and decreased internal mass transfer limitations.

The second option for properly suspending the particles is to increase the cross sectional area of the VFR. Calculations for four different reactor designs with the same total volume is presented in Table A.2. The cross-sectional area is varied by changing the diameter of the inner cylinder. The calculations use a reactor volume of 350 ml, a particle fraction of 0.40, a rotation rate of 100 RPM and varied flow rates. A seen in Table A.2, the conversion tends to decrease with increasing cross-sectional area. The lower conversion is due to the decreased external mass transfer from the suspended particles.

	d_i (cm)	d_o (cm)	L (cm)	Cross Sectional Area (cm^2)	100 ml/min	300 ml/min	500 ml/min
CASE 1	5.2	6.0	50	7.0	97.4 %	75.3 %	58.3 %
CASE 2	5.0	6.0	40	8.6	96.6 %	73.6 %	56.8 %
CASE 3	4.6	6.0	30	11.7	94.4 %	70.3 %	54.0 %
CASE 4	3.7	6.0	20	17.5	86.2 %	60.6 %	46.2 %

Table A.2: Predictions of steady state conversion for a VFR containing immobilized heparinase particles with flow rate=300 ml/min, rotation rate = 100 RPM, particle volume fraction = 0.40, and particle activity = 1400 U/ml.

A final alternative for improving particle fluidization involves changing the design of the reactor. In all of the above examples, it is assumed that the blood enters at the bottom of the VFR, contacts particles as it moves through the reactor, and passes through a retaining screen at top of the reactor. An alternative configuration uses a screen placed between the inner rotating cylinder and the outer cylinder. The blood flows both in the axial direction and radially through the screen, as in vortex flow filtration. Because the flow is more in the radial direction, a lower fluidization velocity should be required. In addition, this design would also increase the surface area available for the blood to pass through, thus reducing the likelihood of fouling. The drawback of the design is lower conversion due to the shorter contact time between the blood and the suspended particles. In general, as long as the particles are sufficiently fluidized, it is expected that design with the retaining screen on the outlet port will provide a better performance than the reactor with radial flow.

As seen in the above discussion, there are many different parameters which may be examined in designing a VFR with immobilized heparinase particles. Axial flow rate, particle volume and loading, and reactor geometry all expected to have a strong influence on the overall degree of heparin neutralization. Figure A.2 shows that good heparin neutralization of 80% should be obtained at particle loadings of $f = 0.5$, under clinically relevant conditions of 350 ml reactor volume and flow rate of 300 ml/min. Incremental improvements on this performance can be achieved by increasing the enzymatic activity of the particles. Another expected difficulty in developing the particle heparinase reactor is correct suspension the particles within the VFR. Future research should concentrate on enzyme immobilization and particle fluidization.

A.3 Design for a VFR with Immobilized Heparinase on the Cylinder Walls

The second type of extracorporeal VFR uses an immobilized heparinase membrane on the cylinder walls. The membrane reactor has inherent advantages over the particle VFR both in terms of reliability and compatibility. In the particle VFR, there are concerns that the outlet filter might clog or that the particles might break and exit the VFR. The membrane reactor is a much simpler design and should provide easy and reliable operation.

The capacity of the immobilized heparinase membrane is estimated using previous experience with the azlactone polyethylene membranes. The results in Chapter 7 showed that alkaline phosphatase was immobilized in the membrane at surface densities ranging from 5 to 10 $\mu g/cm^2$. Researchers at 3M (Gagnon and Coleman, 1994) have been able to obtain protein loadings of 25 to 50 $\mu g/cm^2$ for Protein A and IgG on the membranes. The surface heparinase loading of 375 U/cm^2 used in these calculations is estimated by assuming a protein loading of 50 $\mu g/cm^2$, a purified heparinase activity of 15 Units/μg, and an activity retention of 50%. It should be noted that with this enzyme activity and the assumed membrane thickness of 60 µm, the internal mass transfer resistances are small with $\eta = 0.85$.

A reactor with immobilized heparinase membranes can be directly compared to a particle reactor containing the same amount of heparinase. The particle reactor chosen for the comparison is the f=0.33 example in Figure A.1 (d_i = 5.2cm, d_o= 6.0cm and V_v = 233ml). A membrane VFR with the same dimensions and with a heparinase loading of 325 U/cm^2 has the same total enzymatic loading as the corresponding particle reactor (total heparinase in reactor of 350,000 U). However, for a rotation rate of 2500 RPM and flow rates between 100 and 500 ml/min, the predicted corresponding overall heparinase neutralization is only 13 to 45% in the membrane reactor as compared to 53 to 90% in the particle reactor. The lower conversion in the membrane VFR is due to limited mass transfer at the membrane surface; the ratio of the external mass transfer rate to the surface reaction rate is 0.10. Although mass transfer can be increased by increasing the rotation rate, the highest allowable rotation rate is limited by the shear constraint. An alternative way to increase the conversion is to increase the overall surface area.

Table A.3 presents a three reactor designs examining conversion in the VFR as a function of the membrane surface area. All reactors have a volume of 250 ml and assume a heparinase loading of 375 U/cm^2. A sample calculation is presented in Table A.4. The maximum rotation rates are used in the predictions in Table A.3 such that the shear rate is 20,000 s^{-1} in all cases. Case 3 comes the closest to meeting the desired conversion rate of 90% at the desired flow rates of 200-400 ml/min. However, the length of this reactor design (2 meters) is impractical. While it is possible to use several columns of rotating cylinders in series to achieve the same length, this design may be too expensive and cumbersome to be feasible.

	d_i (cm)	d_o (cm)	L (cm)	Cross Sectional Area (cm^2)	Rotation Rate (RPM)	100 ml/min	200 ml/min	300 ml/min	500 ml/min
CASE 1	5.2	6.0	32.5	1140	2500	47.2 %	30.2 %	22.1 %	14.3 %
CASE 2	7.6	8.0	48	2350	1600	74.5 %	54.2 %	41.8 %	28.3 %
CASE 3	3.8	4.0	200	4930	2500	98.6 %	88.4 %	76.3 %	58.0 %

Table A.3: Predictions of steady-state conversion of a VFR with immobilized heparinase on both cylinder walls. The reactor volume is 250 ml, heparinase loading is 375 U/cm^2 and membrane thickness=60 μm..

Another method of increasing the effective surface area may be to change the reactor design. Two concepts for alternative designs are shown in Figure A.4 and Figure A.5. The first design uses disks which extend from a rotating inner cylinder and/or from the stationary outer cylinder to provide increased surface area. Blood travels through the device flowing over the disk surfaces. Similar devices used as liquid-liquid extractors have high rates of mass transfer and good mixing properties (Westerterp and Landsman, 1962). As performance of the rotating disk reactor with blood is unknown, thorough biocompatibility studies would be necessary.

The second design (Figure A.5) uses a series of concentric rotating cylinder. The second inside wall is connected to innermost cylinder and rotates at the same rotation rate. The outer cylinder and its connected walls are stationary. The blood flows outward from the center annulus traveling up and down the reactor through the three annular gaps. Vortex flow is present in the first and third gaps where the inner wall is rotating; laminar

HEPARINASE WORKSHEET

MEMBRANE REACTOR

INPUT PARAMETERS

Design Parameters−Reactor

Do(cm)=	4
Di(cm)=	3.8
Vol (cm3)=	250

Design Parameters−Membrane

%inner cyl=	100
%outer cyl=	100
Membrn(cm)	0.0061
Porosity	0.68
Tortuosity	3

Enzymatic Parameters

Rate Const=	0.0028 cm3/U min
Soluble Act=	15000 U/mg
Act Enz Load	0.025 mg/cm2

Operating Parameters

visc(cm2/s)=	0.04
Diff(cm2/s)=	1.20E−06
Flow Rate =	5.0000 ml/s
Rotation Rat	2500 RPM

****

Conversion 76.33 %

****

CALCULATED PARAMETERS

Calculated Dimensions

Gap(cm)=	0.1
GapRatio=	0.0526316
CSA(cm2)=	1.2252211
Area inner=	2400.0833
Area outer=	2526.4035
res. time (s)	50
Length(cm)=	201.0448

Internal Mass Transfer

Enz. Conc=	375
Eff Diff Coefi	2.720E−07
phi	0.77363198
effect factor	0.83894725
klst,no mt(cm/s)	0.0175
klst, w/int mt	0.01468158

Dimensionless Numbers

Rez =	20.4045
Retheta =	1243.55
Ta =	285.29
Pe =	439.77
Sh =	271.6991
Sc =	33333.333
A3wall =	1.4457
Gamma =	221.3248

External Mass Transfer

kwall	0.0016
kw/krxt	0.1110
PFR	76.44
CSTR	59.11
PFR no ext MT	100.00
CSTR no ext MT	93.53

Definition − 1 U of heparinase degrades 1 mg heparin/hour

****

Wall Shear 19324 s−1

****

Table A.4 - Spreadsheet showing intermediate calculations for predicted steady-state heparin conversion in a membrane VFR.

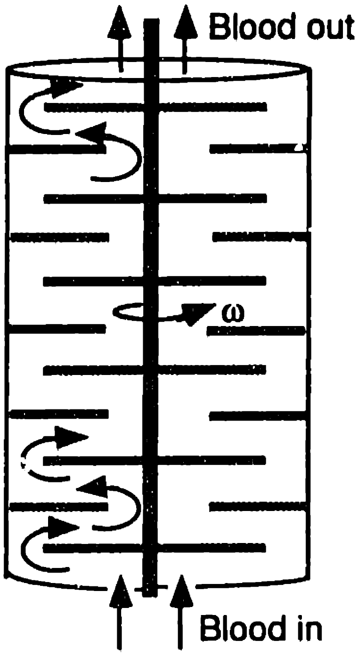

Figure A.4 - Proposed design for an immobilized heparinase extracorporeal reactor using a rotating disk contactor. The inner cylinder and connected disks rotate to provide high rates of mass transfer. Immobilized enzyme may be placed on all disks and cylindder surfaces.

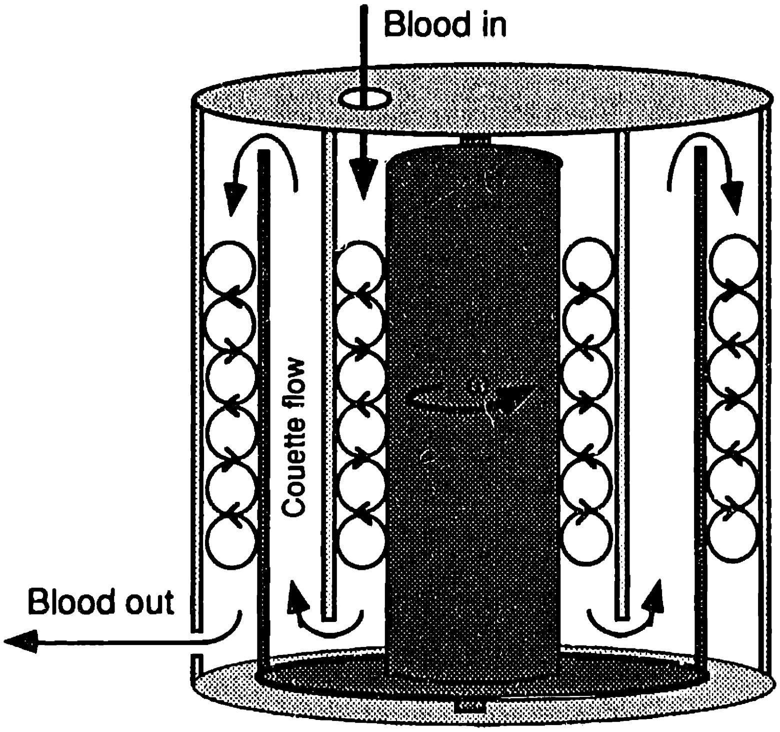

Figure A.5 - Proposed design for an immobilized heparinase extracorporeal reactor using a concentric vortex flow reactor. The inner cylinder and second inner wall are connected and rotate. Vortices occur in the innermost and outermost channels. Immobilized enzyme may be placed on all walls.

Couette flow is present in the second gap where the outer wall rotates. It is expected that in the vortex channels the mass transfer and dispersion properties of this system are the same as in the single annulus VFR. However, behavior of the complete reactor in unknown due to the non-vortex center channel. The advantage of this device over a single annulus VFR is that high surface area to volume ratios can be obtained without excessive reactor lengths. In addition, the high mass transfer rate provided by the vortices is available in two-thirds of the reactor. Further variations of this design are possible such as using more concentric cylinders, or using a counter rotating outer cylinder to induce vortices in every channel. The limitations of the device are in its construction and cost. Since the reactor will use narrow gaps (probably around 1 mm), the cylinders will need to be carefully machined to provide true rotation and not damage the blood.

The calculations for a membrane VFR containing immobilized heparinase presented in Table A.3 predict clinical relevant heparin neutralization for reactors with high surface area. Unfortunately, the dimensions of the single annulus VFR providing the required surface area are unreasonable. The alternative designs in Figures A.4 and A.5 may be successful in functioning as an extracorporeal heparinase reactor. Further work in this area should focus on validating the model predictions for the single annulus VFR and judging the performance and economics of the different reactor designs.

A.4 Conclusions

The model predictions in this appendix show that the concept of effective heparin neutralization is reasonable for both the membrane and the particle reactors. Calculations show that good heparinase neutralization rates of over 80% should be achievable at clinical conditions of 300 ml/min flow rate and reactor bloodvolumes of around 200 ml. Much experimental work is needed to validate these predictions. The estimates and parameters shown in these calculations rely upon particle and membranes with high immobilized heparinase activity. In addition, the simulations do not consider enzyme deactivation. Future work will be needed to develop and optinuize procedures for immobilizing heparinase such that the high heparinase loadings discussed above can be obtained. Additionally, for the particle reactor, further work will be needed studying particle fluidization in highly viscous fluids. For the membrane reactor, future work should focus on the external mass transfer limitations and on obtaining sufficient surface area.